ULB UNIVERSITÉ LIBRE DE BRUXELLES

beams

UNIVERSITÉ D'EUROPE

Towards Medical Flexible Instruments: a Contribution to the Study of Flexible Fluidic Actuators

Promoteur de thèse :
Prof. Pierre Lambert
Co-promoteur :
Prof. Alain Delchambre

Recherche financée par le **F.R.S. - F.N.R.S.**

Année académique 2010-2011

Dissertation originale présentée
par **Aline De Greef**
en vue de l'obtention du grade de
Docteur en Sciences de l'Ingénieur

Acknowledgements

The financial support of the following institutions is gratefully acknowledged. This work has been supported by the ULB and the FRS-FNRS. The first one employed me as a research assistant during the first year of my PhD and the second one gave me a four years grant to do my research as an "Aspirant" of the FRS-FNRS. The experimental test bench has been financed by the FRS-FNRS, the Emile Defay fund, the Jules Reyers fund and the ULB. Travel costs have been supported by the FRS-FNRS and the ULB.

I would like to thank Prof. Alain Delchambre, and Prof. Pierre Lambert. Alain Delchambre allowed me to perform this PhD in his lab and the both of them supervised my research work. Besides his precious research advice, Pierre helped me developing contacts in the Flexible Fluidic Actuators community and this led me as far as Japan, to visit a lab in Kyoto! I particularly thank the both of you for the understanding you showed towards me during a tough period of my life.

Doing a PhD is mostly a work you do alone, like a lonesome cowboy in the research Far West. However, if you look back, you realize that there were a lot of people who helped you during this long journey. Therefore, I would like to thank all the colleagues of the BEAMS department. All of them have contributed in some way or other to this work. Some helped me with the mechanical hardware (a special thank to Bruno Tartini and Salvatore Mele), others with the electronics, the informatics or the logistics but all of them contributed to the nice working atmosphere of the department.
Special thanks to Cyrille Lenders and Jean-Baptiste Valsamis. Both have been my officemates, Cyrille since the beginning and Jean-Baptiste since the mid-term of my PhD. I will miss our regular arguments and debates!
Super special thank to Cyrille who helped me a lot along all my PhD with the hardware but also through interesting discussions.

Outside your own department, there are also nice people ready to help you. Hence, I would like to thank the SAAS department, where Michel Kinnaert, Laurent Catoire and Serge Torfs always warmly welcomed me. Many thanks also to Jennifer Valcke, Laurent Engels, Aurore De Boom, etc. and to all the people who spare me some time and advised me.

I would like to acknowledge Dirk Lefeber of the VUB and Michäel De Volder of the KUL for the interesting meetings and the collaborations and/or exchanges that resulted from it. Thank you also to Prof. Satoshi Konishi and Kenichi Morimoto who organized me a wonderful visit of their lab.

Moreover, I would like to thank Andrew Watson for correcting the English of a part of my manuscript.

Special thanks to my friends and family, who supported me during these five years and especially during the last months.

Finally, THANK YOU to you Thomas, my partner, friend and first supporter! Thank you for your kind attentions, your advice, your patience, your help at every hour, your support and your love.

At the end of this adventure, I leave with scientific knowledges, a better knowledge of me,

nice acquaintances and also new friends.

Abstract

The medical community has expressed a need for flexible medical instruments. Hence, this work investigates the possibility to use "flexible fluidic actuators" to develop such flexible instruments. These actuators are driven by fluid, i.e. gas or liquid, and present a flexible structure, i.e. an elastically deformable and/or inflatable structure.
Different aspects of the study of these actuators have been tackled in the present work:

- A literature review of these actuators has been established. It has allowed to identify the different types of motion that these actuators can develop as well as the design principles underlying. This review can help to develop flexible instruments based on flexible fluidic actuators.

- A test bench has been developed to characterize the flexible fluidic actuators.

- A interesting measuring concept has been implemented and experimentally validated on a specific flexible fluidic actuator (the "Pneumatic Balloon Actuator", PBA). According to this principle, the measurements of the pressure and of the volume of fluid supplied to the actuator allow to determine the displacement of the actuator and the force it develops. This means being able to determine the displacement of a flexible fluidic actuator and the force it develops without using a displacement sensor or a force sensor. This principle is interesting for medical applications inside the human body, for which measuring the force applied by the organs to the surgical tools remains a problem.
  The study of this principle paves the way for a lot of future works such as the implementation and the testing of this principle on more complex structures or in a control loop in order to control the displacement of the actuator (or the force it develops) without using a displacement or a force sensor.

- A 2D-model of the PBA has been established and has helped to better understand the physics underlying the behaviour of this actuator.

- A miniaturization work has been performed on a particular kind of flexible fluidic actuator: the Pleated Pneumatic Artificial Muscle (PPAM). This miniaturization study has been made on this type of actuator because, according to theoretical models, miniaturized PPAMs, whose dimensions are small enough to be inserted into MIS medical instruments, could be able to develop the forces required to allow the instruments to perform most surgical actions. The achieved miniaturized muscles have a design similar to that of the third generation PPAMs developed at the VUB and present a total length of about 90 mm and an outer diameter at rest of about 15 mm. One of the developed miniaturized PPAMs has been pressurized at $p = 1$ bar and it was able to develop a pulling force $F = 100$ N while producing a contraction $\epsilon = 4$ %.
  Propositions have been made regarding a further miniaturization of the muscles.

Contents

Chapter 1

Introduction

1.1 Context of the research

Flexible instruments, i.e. instruments presenting a large number of degrees of freedom (DOFs) and able to perform snake-like movements when avoiding obstacles, can find a lot of applications in the medical field and the three following examples will bring this to light.

1. During a Minimally Invasive surgery (MIS) procedure, only a few small incisions are performed in the patient's body to insert the surgical tools and a camera for visualization. The tools manipulated by the surgeons are rigid rods, presenting four DOFs (see Fig. 1.1), sliding in trocars (which are used to keep the incisions open) and whose tips are analogous to the instruments used in open surgery [69].
   Robotically-assisted systems for MIS (such as the Zeus system or the da Vinci system) have been commercially available for about ten years. Compared to traditional MIS, the rigid rods are equipped with articulated wrists placed at their tips and which present up to two DOFs. These robotically-assisted systems brought about a lot of advantages to MIS such as a more comfortable settling of the surgeon during the operation and an improved motion precision thanks to tremor filtering and motion scaling [33].
   Nonetheless, some drawbacks remain in chest surgery such as a limited dexterity and working space. Due to these two inconveniences, the insertion points sometimes need to be replaced during the operation, to allow the surgeons to do the necessary movements and to reach the target points [69]. In [33], a surgeon trained with the Zeus system explains that this is due to the rigid rods passing between the ribs and he proposes to develop flexible instruments. In addition to this opinion, [69] gathers the views of other surgeons and engineers about the shortcomings of the existing surgical robots (notably the da Vinci system) and underlines a need for instruments presenting high mobility.

2. In the field of endoluminal surgery, where the surgical tools pass through natural orifices, a need for flexible tools is also expressed by the medical community [4].

3. Concerning catheters, which are flexible tubes inserted into vessels, [46] mentioned the need for active catheters, i.e. actuated catheters able to move their shaft, to ease their insertion. Indeed, the insertion of classical passive catheters is difficult due to the small diameter of the vessels and their complex shape (with bending, twisting and branching).

For MIS applications, instruments must have a diameter less than 10 mm [66] while the diameter of catheters can be as low as 1 mm or less [60]. Developing flexible instruments for medical applications is thus a miniaturization challenge.

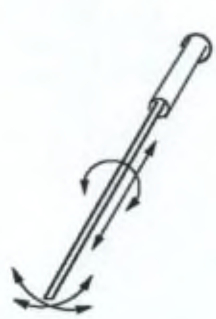

Figure 1.1: Four DOFs in Minimally Invasive Surgery: one translation, one axial rotation and two rotations around the insertion point. Figure adapted from [28].

1.2 Flexible Fluidic Actuators and aim of the thesis

"Flexible Fluidic Actuators" is the name we decided to give to actuators driven by fluid, i.e. gas or liquid, and presenting a flexible structure, i.e. an elastically deformable and/or inflatable structure. As will be shown later in more details, such actuators present interesting features regarding medical applications. Hence, the aim of the thesis is to study these actuators and to investigate whether it is interesting to use them to develop flexible instruments for medical applications.

1.3 Content and contributions of the thesis

Chapter 2 allows to become familiar with the flexible fluidic actuators. It lists the advantages and drawbacks linked to the use of these actuators, discusses about the miniaturization of the peripherics of these actuators and presents a literature review of these actuators. This review has been published (see [40]) and is the first contribution of the thesis. It shows the different design principles of these actuators and it sorts them according to their ability to stretch themselves or shorten, bend themselves or rotate. Hence, this review can help to design medical flexible instruments based on flexible fluidic actuators.

Among the interesting features linked to the use of flexible fluidic actuators, one has caught our eye. Indeed, in [79], a flexible fluidic actuator, called "the Flexible Microactuator", is presented and it is suggested that the measurements of the fluid pressure and of the volume of supplied fluid allow to determine and control the position of the actuator and the force it develops. This property, that will hereafter be referred to as the "Pressure-Volume-Force-Position principle" or "PVFP principle", means being able to determine the displacement of a flexible fluidic actuator and the force it develops without using a displacement sensor or a force sensor [79]. The PVFP principle is schematically presented in Fig. 1.2. According to us, this measuring principle can be applied to all flexible fluidic actuators whatever the actuation fluid (compressible or incompressible).
To study and implement the PVFP principle, a flexible fluidic actuator called "Pneumatic Balloon Actuator" (PBA) has been used. This actuator, invented by [50], has been selected among the actuators of the review because it has a simple design, one DOF and because it is easily manufactured. An example of such an actuator is presented in Fig. 1.3. A PBA is composed of two square layers whose materials have different rigidities, the upper layer being less rigid than the lower one. Both layers are fixed to each other along their surrounding edge and this forms a square cavity. The actuator is fixed as a cantilever and when the cavity is pressurized, the actuator free end moves upwards.

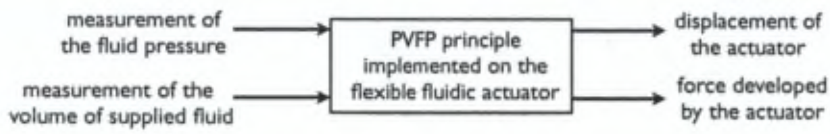

Figure 1.2: Schematic representation of the PVFP principle: according to this principle, the measurements of the fluid pressure and of the volume of supplied fluid allow to determine and control the position of the actuator and the force it develops.

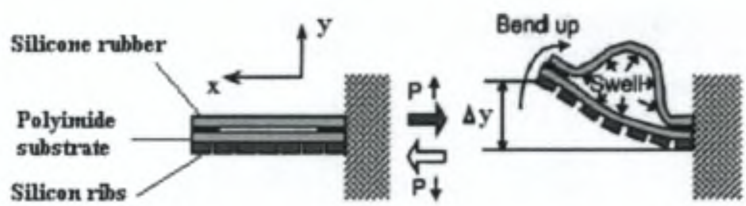

Figure 1.3: Working principle of a Pneumatic Balloon Actuator (PBA): PBA at rest and pressurized PBA on the left hand side and the right hand side, respectively.

Fig. 1.4 presents a PBA linked to a syringe-pump; the actuation fluid is air. The volume of fluid supplied to the actuator is considered to be the volume swept by the piston during its displacement; this swept volume is proportional to the piston displacement u and equals Su, where S is the syringe-pump cross-section. Therefore, the piston displacement u will be used for the PVFP principle rather than the swept volume.
When a displacement u is imposed to the piston, the inner pressure p_{in} increases and the PBA inflates and its free end A moves upwards. The vertical and horizontal displacements of this point are Δy_0 and Δx_0, respectively. Afterwards, keeping the piston position constant, if a weight w is hung from the PBA free end, the inner pressure p_{in} increases and the displacements Δy and Δx of the PBA free end decrease. According to the PVFP principle, knowing the values of p_{in} and u allows to determine the displacements of point A and the value of the weight w.

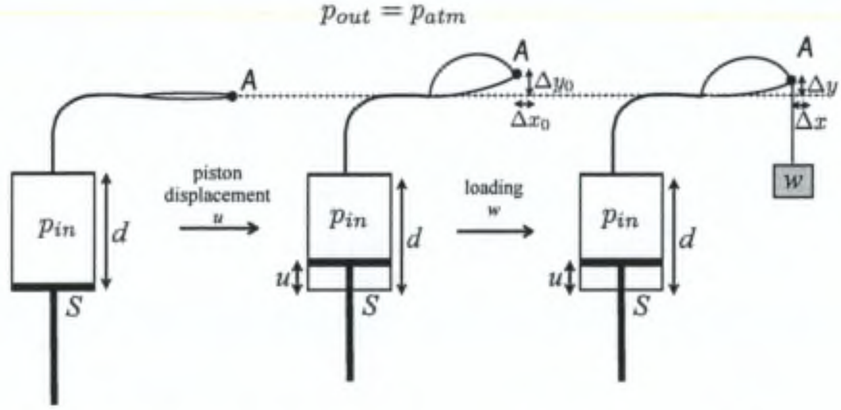

Figure 1.4: Pneumatic Balloon Actuator (PBA) linked to a syringe-pump.

PBAs have been manufactured and the PVFP principle has been successfully implemented on a PBA. To do so, experimental models of the behaviour of the PBA have been established and then used to predict the actuator displacements Δx and Δy and the load w attached from its end, on the basis of the measurements of u and p_{in}. This experimental validation of the PVFP principle on a PBA constitutes the second contribution of the thesis and it is presented in Chapter 5 as well as a discussion about the practical implementation of the PVFP principle in a targeted application.
The PVFP principle is an interesting measuring concept for applications where the space is limited and where a miniaturization effort is required. This is for example the case in Teleoperated MIS where it is necessary to measure the force applied by the tools to the organs to ensure a force feedback of good quality. Obtaining this measurement is not straightforward. Indeed, if the force sensor is placed on the tool, outside the body of the patient, the measurement will be polluted by the friction of the trocar. To solve this problem, some researchers propose to place the sensor at the end of the tool inside the body but this raises the challenge to develop a small and sterilizable force sensor [64]. Using flexible fluidic actuators to actuate the surgical tools and exploiting the PVFP principle would allow to measure the force applied to the organs without the need for a force sensor. Besides, the measurements of the fluid pressure and of the volume of supplied fluid could be performed outside the patient's body.

A 2D-model of the PBA is presented in Chapter 6; it has been built in order to better understand the physics underlying the behaviour of this actuator. The results provided by this model have been compared with the measurements performed on two PBAs. Because of the numerous assumptions on which the model rests, its quantitative results are far from the measurements performed on the prototypes and other comparisons with experimental results are needed to assess whether the qualitative results provided by the model are correct. However, this model is able to predict the bidirectional behaviour that has been experimentally noticed by different researchers on PBAs made of only one material (the upper membrane being thinner than the lower one). A PBA presenting a bidirectional behaviour moves its end upwards when it is pressurized until a given pressure level is reached and above this level, the PBA tip is moved downwards.
This model constitutes the third contribution of this thesis.

A literature review (see Table 1.1) has established that a force of about 13 N is required at the end of a surgical instrument to allow the execution of all the surgical gestures. Fig. 1.5 presents schematically a surgical instrument having a length L and a width l. F is the force applied by the organs to the tip of the surgical instrument. α is the angle of inclination of the instrument. Two actuators are located at the basis of the instrument and apply vertical downwards forces F' and F'' to the points A and B of the instrument, respectively. The actuators act one at a time: if $F' > 0$, $F'' = 0$ and when $F'' > 0$, $F' = 0$. For $L = 2l$, if α equals $\pi/2$ and if only the actuator acting on point A applies a force to the instrument, it has to develop a force $F' = 104$ N so that the instrument can develop a force $F = 13$ N at its tip. On the other hand, if α equals $\pi/6$, the actuator has to develop a force $F' = 208$ N so that the instrument can develop a force $F = 13$ N at its tip. According to theoretical models, a miniaturized Pleated Pneumatic Artificial Muscle (PPAM, see Fig. 1.6), whose dimensions are small enough to be inserted into a MIS medical instrument, could able to develop the required force of 104-208 N. Therefore, the PPAMs have been studied in order to assess their miniaturization potential. The fourth contribution of the thesis is the miniaturization work done on the PPAM, in collaboration with the Vrije Universiteit Brussel (VUB) which has developed this actuator; this is presented in Chapter 7. The achieved miniaturized muscles have a design similar to that of the third generation PPAMs developed at the VUB and present a total length of about 90 mm and an outer diameter at rest of about 15 mm. One of the miniaturized PPAMs has been pressurized at $p = 1$ bar and it was able to develop a pulling force $F = 100$ N while producing a contraction $\epsilon = 4$ %.

Source	Action	Organ	Force measurement
[36]	Piercing	Sheep heart	Max force: 0.3 N
[64]	Suturing	Rat: skin, muscle and liver tissue	Max force: 2.3 N
[83]	MIS actions: Cutting, suturing dissecting, biopsy by traction, knotting, palpation, prehension	Pelvi-trainer (in vitro), pig, human (coelioscopy, thoracoscopy)	Force range: 0.48 N to 12.86 N
[58]	Various MIS interventional tasks	Various	Force range: 0.1 N to 3 N

Table 1.1: Forces measured at the tip of the surgical tools during the execution of different surgical gestures. For source [83], the minimum value of the force range has been computed, by a torque equilibrium, from the measurement of the force applied to the handle of the tool; the maximum value of the force range is the difference between the force applied to the handle of the tool (14.34 N) and the friction in the trochar (1.48 N).

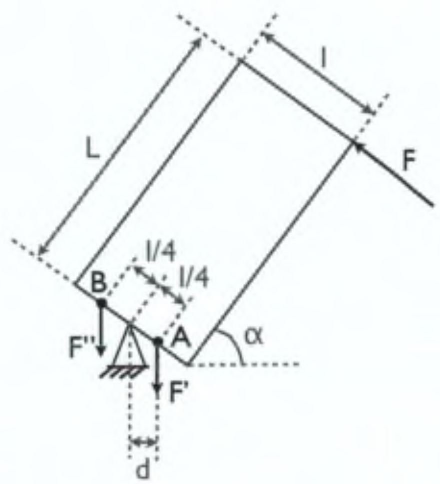

$F' > 0$ and $F'' = 0$

$F'.d = F.L$

with $d = \frac{l}{4} sin(\alpha)$

$$\boxed{F' = F\frac{4L}{l.sin(\alpha)}}$$

For $L = 2.l$ and $F = 13\ N$

1) $\alpha = \pi/2$

$\boxed{F' = 104\ N}$

2) $\alpha = \pi/6$

$\boxed{F' = 208\ N}$

Figure 1.5: The surgical instrument has a length L and a width l. F is the force applied by the organs to the tip of the surgical instrument. α is the angle of inclination of the instrument. Two actuators are located at the basis of the instrument and apply vertical downwards forces F' and F'' to the points A and B of the instrument, respectively. The actuators act one at a time: if $F' > 0$, $F'' = 0$ and when $F'' > 0$, $F' = 0$. For $L = 2l$, if α equals $\pi/2$ and if only the actuator acting on point A applies a force to the instrument, it has to develop a force $F' = 104$ N so that the instrument can develop a force $F = 13$ N at its tip. On the other hand, if α equals $\pi/6$, the actuator has to develop a force $F' = 208$ N so that the instrument can develop a force $F = 13$ N at its tip.

To study the PVFP principle and to characterize the PBAs and the miniaturized PPAMs, a test bench has been developed. It constitutes the fifth contribution of this thesis and its design and building are described in Chapter 3. This test bench is basically a syringe-pump composed of a linear motor linked to a cylinder and the output of the cylinder is linked to the actuator to be studied by a tube. When the motor moves the cylinder piston, the fluid located in the cylinder chamber and the tubes is compressed and the flexible fluidic actuator

Figure 1.6: Deflated and inflated states of a PPAM. When pressurized gas is introduced in this actuator, the membrane bulges out and contracts axially. Figure from [84].

is pressurized.

Finally Chapter 8 presents the conclusions of the thesis and the perspectives for future works.

1.4 Reading suggestion

The reader in a hurry can get the gist of this work by reading the following parts:

- Chapter 2 "Flexible fluidic actuators":
  - Advantages and drawbacks of flexible fluidic actuators: Section 2.2
  - Miniaturization of fluidic actuators peripherics: Section 2.3
  - Literature review of the flexible fluidic actuators: the introduction (Section 2.4.1), the general descriptions of the different categories of flexible fluidic actuators (the first pages of Sections 2.4.2, 2.4.3, 2.4.4 and 2.4.5) and the conclusion (Section 2.5).
- Chapter 3 "Test bench":
  - Description of the test bench: Section 3.5
  - Conclusions: Section 3.6
- Chapter 4 "Study of the PVFP principle and of the Pneumatic Balloon Actuators: Test bench particularities"
- Chapter 5 "The PVFP principle"
- Chapter 6 "Model of the Pneumatic Balloon Actuator"
- Chapter 7 "Miniaturization of Pleated Pneumatic Artificial Muscles"
- Chapter 8 "Conclusions and perspectives"

Chapter 2

Flexible fluidic actuators

2.1 Introduction

The aim of this chapter is to get familiar with the flexible fluidic actuators. These actuators are driven by fluid, i.e. gas or liquid, and present a flexible structure, i.e. an elastically deformable and inflatable structure.
Section 2.2 lists the advantages and difficulties linked to the use of these actuators while Section 2.3 discusses about the miniaturization of their peripherics (such as the valves and the flow control devices). Indeed, according to the application targeted for the flexible fluidic actuators, some miniaturization might be necessary and miniaturizing the actuators means also miniaturizing their peripherics.
Section 2.4 presents a literature review of these actuators. The goal of this review is to help to develop medical flexible instruments based on flexible fluidic actuators. Therefore, the review identifies the movement types that these actuators can generate and the design principles underlying. Hence, it presents the working principle of each actuator and also focuses on other characteristics such as the DOFs, the materials, the manufacturing process, the actuator dimensions, the actuation mode (pneumatic or hydraulic), the pressure range and the performance in terms of developed force and displacement.
Finally, conclusions are presented in Section 2.5.

2.2 Advantages and drawbacks of the flexible fluidic actuators

The fluidic actuation presents nice features regarding an application inside the human body. Indeed, it has the non-negligible advantage to prevent having energized parts, i.e. under electrical voltage, (unlike the electrostatic actuators, the piezoelectric actuators [82], the Electroactive Polymers or the electromagnetic motors when used inside the body) or high temperature parts (unlike the Shape Memory Alloys and thermal actuators) inside a patient's body; this increases the safety. As no electrical power is used, operation in presence of radioactivity or magnetic field is possible [25]. In the case of a hydraulic actuation, a sterile physiological saline solution could be used so that a leakage of the system would have no consequence on the patient's body.
One can think of miniaturizing classical piston-based fluidic actuators but it raises difficulties regarding the sealing of the chambers. O-rings and lip seals are no longer suitable [34] because small variations of the shape or size of the components (seal, seal house or piston) involve high friction or leakage. [34] proposes to use "restriction seals", i.e. small clearances between the rod and the orifice. These generate less friction and allow a compromise between the

leakage and the manufacturing accuracy; the actuator can present virtually no leakage but then tolerances in the range of 1 μm or less are required. However, to avoid leakages and friction which limit efficiency, we chose to use pressurized elastic deformable chambers, i.e. flexible fluidic actuators, as suggested by [79].
As these actuators present no relative motion of parts, static sealings can be used and this means no need for lubricants, no leakages and no wear particles; consequently these actuators could possibly operate in clean room, food or agriculture industries [25]. Besides, smooth motion and precise positioning are possible to achieve since there is no friction [79] (unlike piston-based actuators or systems actuated with cables). In the field of robotics, compliant structures have relevant additional advantages over traditional rigid body robots:

- They can handle delicate objects without causing any damage thanks to their own compliance [25]. This compliance allows them to adapt themselves to their environment during contacts [25] [67].

- Compared to traditional mechanisms made of articulated rigid parts, compliant structures allow the reduction of the number of parts necessary to perform a given task [44]. This is an interesting feature regarding miniaturization.

- When they are made of membranes, flexible structures can be very lightweight. If the instrument is actuated thanks to inflatable membranes, its volume may be reduced when the membranes are deflated. This is an interesting characteristic if the whole device has to be inserted into a small orifice.

The combination of a fluidic actuation and a flexible structure also brings advantageous properties:

- Regarding a medical application, reducing the fluid pressure lets the device loose its rigidity and lets it regain its initial shape. In emergency cases, it then allows to take the instrument out of the patient's body quickly.

- Concerning the "Flexible Microactuator" (FMA, see section 2.4.2) whose actuation is obtained by the deformation of elastic chambers, [79] said that "*By measuring the volume and pressure of an operating fluid having been supplied, the operator can learn about the posture of the actuator and the acting force; that is, it is possible to control the posture and the acting force without equipping a sensor on the distal end of the actuator.*" This remark seems to be applicable to all devices based on the same actuation principle.

Nevertheless, a fluidic actuation presents some drawbacks:

- It needs equipment such as pumps, valves and pipes that can be bulky. However, in the case of a medical application, the pump is placed outside the patient's body and will not increase the bulkiness of the instrument inside the body.

- Regarding fluidic micro-actuators, [23] mentioned different drawbacks: the pipes used to drive the fluid can present leakages and cause pressure losses which limit efficiency. Moreover, controlling pressures and debits in small sections is often more delicate than controlling electrical quantities.

- Still, an important shortcoming of flexible fluidic actuators lies in their control strategy, as explained by [25]: "*Fluidic flexible robots require sophisticated controls in order to reach accurate and repeatable positioning. Further their dynamics modeling has to fight with the deformable structure and with not conventional actuations.*"

Comparing liquids and gases, one can note that the compressibility of gases brings more compliance, leads to a more difficult study and involves thermal losses upon compression. Air is a readily available source and exhaust gases can be freely evacuated in the ambient air [71]. Finally, gases lead to more lightweight actuators and to pressure losses a hundred times smaller than for liquids [80].

2.3 Miniaturization of fluidic actuators peripherics

Regarding the miniaturization of the actuators, [71] explains that the size of the valves and of the flow control devices needs to be correspondingly reduced as the scale decreases. To answer this need, the Lee company [6] provides miniature fluidic equipments and custom miniature valves can be found in the literature, as people developing micro flexible fluidic actuators sometimes develop their own miniature valves (for example [68] and [46]). Besides, as thermal time constants decrease nicely when the scale decreases, thermo-pneumatically controlled valves can be used, in pneumatic systems, at the meso- and micro-scales [71].

2.4 Literature review of the flexible fluidic actuators

2.4.1 Introduction

This section proposes a review of the flexible fluidic actuators found in the literature. The goal of this review is to help to develop medical flexible instruments based on flexible fluidic actuators. Therefore, this review identifies the movement types that these actuators can generate and the design principles underlying. The working principle of each actuator as well as some applications are presented and the review also focuses on other characteristics such as the DOFs, the materials, the manufacturing process, the actuator dimensions, the actuation mode (pneumatic or hydraulic), the pressure range and the performance in terms of developed force and displacement. Tables 2.1 and 2.2 summary the characteristics of many actuators described in this review.

At the light of this review, it has been established that the flexible fluidic actuators can bend themselves, stretch themselves, shorten or develop a rotational motion and some of them present several DOFs. The review sorts the actuators in three categories according to their bending, rotation or stretching/shortening ability. Two different methods to achieve bending have been identified and will be described in more details later. The first technique is based on "internal chambers differently pressurized" and the other one on "anisotropic rigidity". Besides, two methods to generate a rotational motion have also been identified. The actuators based on the first technique present a structure reinforced in places (with fibres or by increasing the material thickness) in such a way that when the actuators are pressurized, their structure involves a rotation. The second method to generate a rotational motion consists in an articulated structure in which one or several flexible fluidic actuators are inserted. When the actuators are pressurized, they actuate the structure which involves a rotation.

The classification of the flexible fluidic actuators, according to the movement types they can generate, is schematically presented in Fig. 2.1.

2.4.2 Bending thanks to internal chambers differently pressurized

The devices based on this principle will hereafter be referred to as "chambers actuators". They present elongated chambers placed between two plates and the chambers are designed in such a way that when they are pressurized, their length increases or decreases. Hence, when a chamber is pressurized, its length changes while the other chambers keep their initial

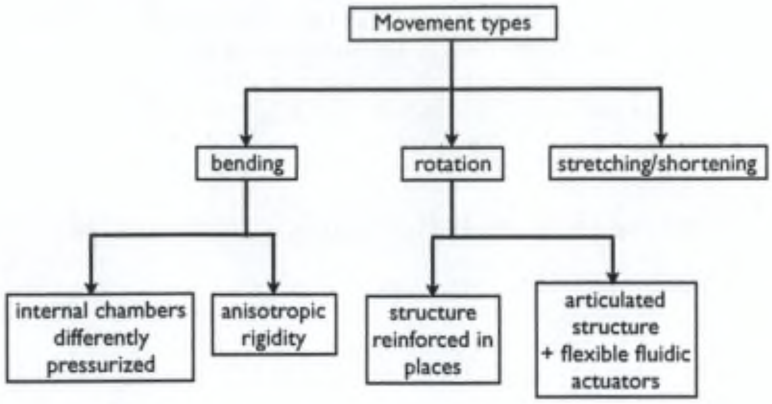

Figure 2.1: Classification of the flexible fluidic actuators according to the movement types they can generate.

length and consequently the whole device bends. According to the type of actuator, the bulging of the chambers may be hampered.
Fig. 2.2 presents a chambers actuator having three chambers and the chambers are such that they stretch themselves when they are pressurized. Hence, if chamber no. 1 is pressurized, its length increases and the device bends as shown in the figure.

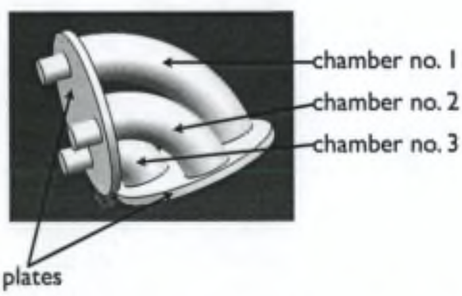

Figure 2.2: Chambers actuator presenting three elongated chambers placed between two plates. The chambers are designed in such a way that their length increases when they are pressurized. Hence, if chamber no. 1 is pressurized, its length increases while the other chambers keep their initial length and consequently the whole device bends as shown in the figure.

The chambers can be of different types (see Fig. 2.3 and 2.4):

- bellows which expand when pressurized (see no. 1 in Fig. 2.3).
  For example, a chambers actuator based on bellows has been used in a coloscope [82], a "Dextrous Underwater Manipulator" [62] and a catheter or endoscope [47].
- pneumatic artificial muscles which contract when pressurized (see no. 2 in Fig. 2.3).
  For example, a chambers actuator based on McKibben pneumatic artificial muscles has been used in the "Octarm" [57] which is a continuum manipulator.
- elastic tubes with mechanical constraints (see no. 3 in Fig. 2.3). The mechanical constraints are obtained thanks to fibres fixed to the tubes and according to the type

of mechanical constraints, the elastic tube will shorten, stretch itself, bend itself or develop a torsion motion.
For example, a chambers actuator based on such elastic tubes is used in [43] and [85].

- microballoons (see no. 4 in Fig. 2.3).
A chambers actuator based on microballoons has been used in a positioning system for a catheter [68] (see the figure illustrating no. 4 in Fig. 2.3). The balloons are pressed against the vessel walls and this allows to fix the catheter tip at a certain place in the vessel. After this is achieved, changing the balloon's size enables to change the orientation of the catheter tip.

- flexible and extensible tubes fixed to a core member (see no. 5 in Fig. 2.4).
Such a chambers actuator is presented in [59]. The core member is made of a flexible but inextensible material. The tubes are designed in such a way that when pressurized, they will extend axially but will not bulge radially. When the pressure is increased in one tube, the other tubes keep their initial length while the core member is not able to lengthen and it causes the bending of the device. Three designs A, B and C are shown in the figure illustrating no. 5 in Fig. 2.4; they are composed of one, two and three tubes, respectively.

- internal chambers in a tube (see no. 6 in Fig. 2.4). These chambers are designed in such a way that they stretch themselves when they are pressurized.
For example, the "Flexible Microactuator" of [73] presents such chambers and it will be described in more details later.

- balloons in a bellows tube (see no. 7 in Fig. 2.4). When they are pressurized, these balloons stretch themselves.
For example, the "Fluidic Bellows Manipulator" of [25] presents such chambers and it will be described in more details later.

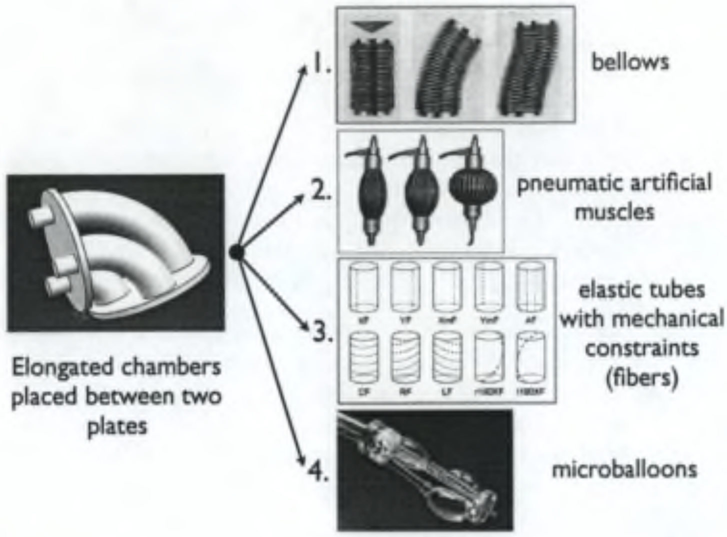

Figure 2.3: "Chambers actuators": they present elongated chambers placed between two plates and the chambers are designed in such a way that when they are pressurized, their length increases or decreases. Hence, when a chamber is pressurized, its length changes while the other chambers keep their initial length and consequently the whole device bends. These chambers can be of different types such as bellows (figure from [67]), pneumatic artificial muscles (figure from [26]), elastic tubes with mechanical constraints (figure from [43]) or microballoons (figure from [68]).

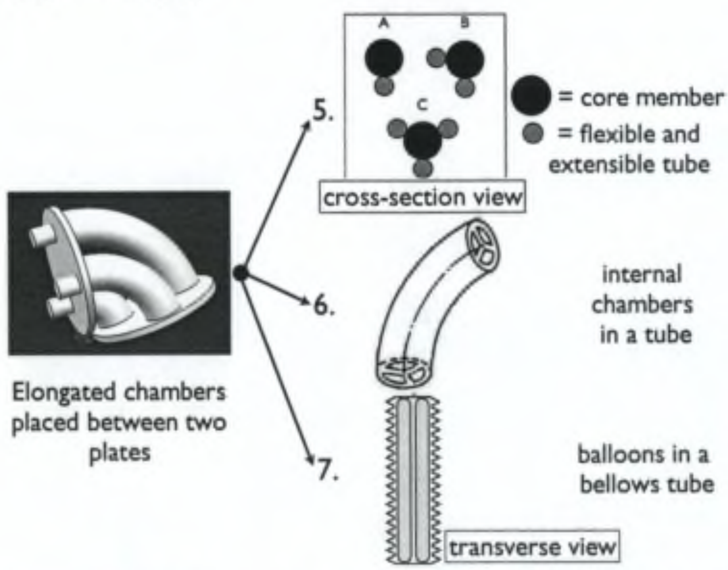

Figure 2.4: "Chambers actuators": they present elongated chambers placed between two plates and the chambers are designed in such a way that when they are pressurized, their length increases or decreases. Hence, when a chamber is pressurized, its length changes while the other chambers keep their initial length and consequently the whole device bends. These chambers can be of different types such as flexible and extensible tubes fixed to a core member (figure reproduced from [59]), internal chambers in a tube (figure adapted from [73]) or balloons in a bellows tube.

A) Example of a chambers actuator presenting internal chambers in a tube: the "Flexible Microactuator" (FMA)

In [73], [74], [75] and [72], K. Suzumori et al. describe the "Flexible Microactuator" (FMA), which is a pneumatic rubber actuator. It is a cylinder presenting three internal chambers and it is composed of silicone rubber reinforced with nylon fibres disposed in a circular direction (see Fig. 2.5). The function of these fibres is to create anisotropic elasticity in order to prevent radial deformations. When a chamber is pressurized, its length increases while the other chambers keep their initial length and consequently the cylinder bends in the direction opposite the pressurized chamber. For example, Fig. 2.6 presents a bending FMA whose chambers no. 1 and 2 are pressurized.

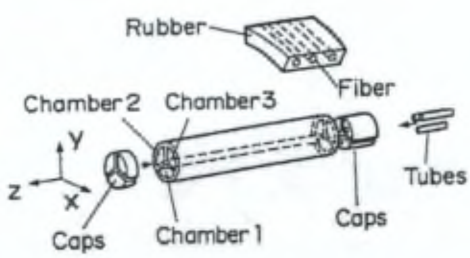

Figure 2.5: Parts of a Flexible Microactuator (FMA): it is a cylinder presenting three internal chambers and it is composed of silicone rubber reinforced with nylon fibres disposed in a circular direction. The function of these fibres is to create anisotropic elasticity in order to prevent radial deformations. Figure from [73].

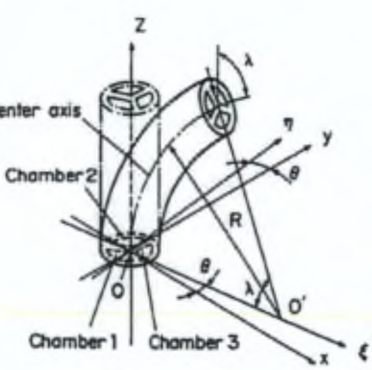

Figure 2.6: Bending Flexible Microactuator (FMA): when a chamber is pressurized, its length increases while the other chambers keep their initial length and consequently the cylinder bends in the direction opposite the pressurized chamber. The figure presents a bending FMA whose chambers no. 1 and 2 are pressurized. Figure from [73].

An electro-pneumatic (or electro-hydraulic) system is used to control the motion of the FMA and it enables to control the pressure in the chambers independently. This system comprises flexible tubes connected to the chambers and to pressure control valves.

The FMA is said to bend in any direction thanks to appropriate pressures in the chambers. Besides, it can stretch in the axial direction when the pressure is equally increased in all the chambers. Hence, an FMA has three DOFs (one stretching and two bending DOFs).

Several FMAs can be connected in series to increase the number of DOFs and FMAs have

been used to build a multi-fingered robot hand, walking robots, pipeline inspection robots, etc.
The FMAs reinforced with fibres are obtained from liquid silicone rubber and nylon fibres, by a moulding process. The small dies used for this operation are made using an electrical discharge machining process [74].
In [76] and [77], the authors wanted to miniaturize and integrate FMAs. To achieve this, the moulding process was no longer suitable and stereo-lithography was preferred. Since a product produced by stereo-lithography must be made of a single material, a new design has been developed to obtain anisotropic elasticity without fibres. This has been achieved thanks to "restraint beams" (see Fig. 2.7). These are rubber walls added to the FMA chambers to prevent the radial deformation of the actuator.

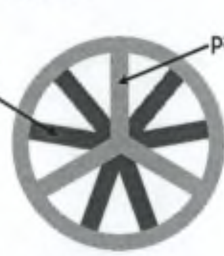

Figure 2.7: Cross-section view of a Flexible Microactuator (FMA) with two "restraint beams" in each chamber: the restraint beams are rubber walls added to the FMA chambers to prevent the radial deformation of the actuator. Hence, they allow the manufacturing of a fibreless FMA made of only one material, which can thus be processed by stereo-lithography. Figure redrawn from [76].

Another FMA fibreless design is presented in [78]. The cross-section of this FMA presents three chambers (and no restraint beams) and the shape of the cross-section has been optimized, by increasing or decreasing the material thickness in places, in order to limit radial deformation. This design has been developed to allow the manufacturing by an extrusion moulding process, which reduces the manufacturing costs in comparison with the moulding process of the fibre-reinforced FMA.

B) Example of a chambers actuator presenting two balloons in a bellows tube: the "Fluidic Bellows Manipulator"

A "Fluidic Bellows Manipulator" is presented in [25]. It comprises two vulcanized balloons placed in an elastomer bellows tube, closed at both ends (see Fig. 2.8). The bellows tube is made of an alternation of rigid and compliant rings which enable the tube to bend and stretch. A polycarbonate floating spine, stiffened by a high-strength steel sheet, separates the balloons.

To operate the device, it has to be fixed at one end while the other remains free. When a balloon is inflated with air, it expands and the floating spine shifts and takes the shape of the tube wall (see Fig. 2.9). The inflated balloon applies a force to the inner side of the device tip and generates a bending moment with respect to the neutral axis of the structure and this involves the bending of the manipulator. An equilibrium position is reached when this bending moment is balanced by the bending moments corresponding to the deformations of the floating spine and of the tube. Fig. 2.10 presents the actuator bending when one balloon is pressurized with a given pressure and when the actuator is loaded by a weight hung at its end.

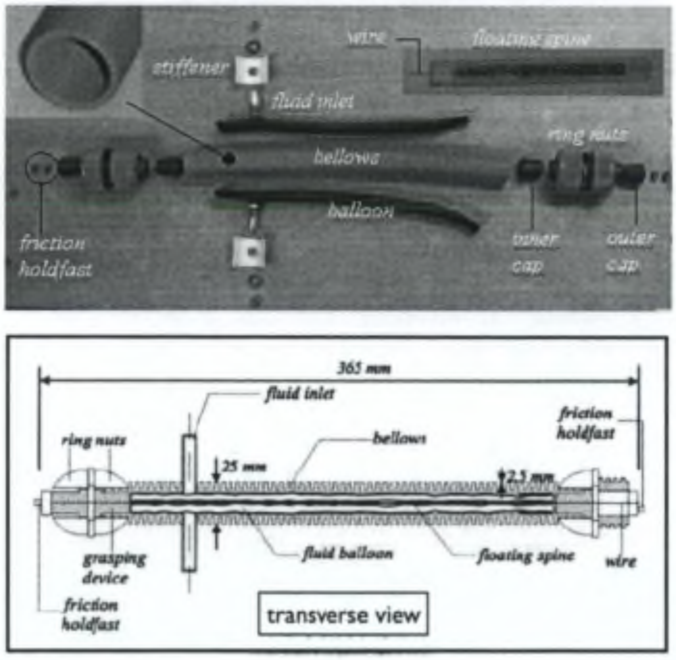

Figure 2.8: Parts of the Fluidic Bellows Manipulator: it comprises two vulcanized balloons placed in an elastomer bellows tube, closed at both ends. The bellows tube is made of an alternation of rigid and compliant rings which enable the tube to bend and stretch. A polycarbonate floating spine, stiffened by a high-strength steel sheet, separates the balloons. Upper figure from [25] and lower figure adapted from [25].

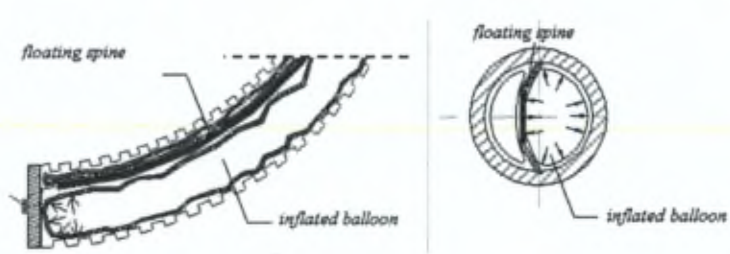

Figure 2.9: Views of the inside of the Fluidic Bellows Manipulator when it is actuated: when a balloon is inflated with air, it expands and the floating spine shifts and takes the shape of the tube wall. The inflated balloon applies a force to the inner side of the device tip and generates a bending moment with respect to the neutral axis of the structure and this involves the bending of the manipulator. An equilibrium position is reached when this bending moment is balanced by the bending moments corresponding to the deformations of the floating spine and of the tube. The left figure presents a transverse view of the actuator while the right figure presents a cross-section view. Figures from [25].

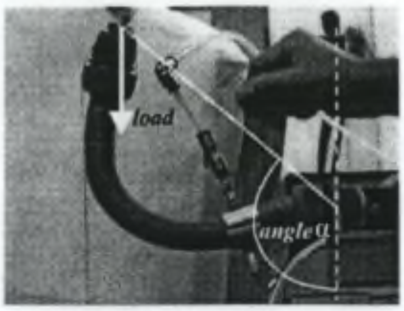

Figure 2.10: Bending Fluidic Bellows Manipulator: one balloon is pressurized with a given pressure and a given weight is hung at the end of the actuator. The bending angle α of the actuator is defined as presented in the figure. Figure adapted from [25].

2.4.3 Bending thanks to anisotropic rigidity

The devices based on this principle present an elongated shape closed at one end and an elongated area whose rigidity is higher than that of the rest of the device. This difference in rigidity is called "anisotropic rigidity". Fig. 2.11 presents such an actuator whose right side is more rigid than its left side. When the device is pressurized, the length of the stiffer area increases less than the rest of the device and consequently the device bends.

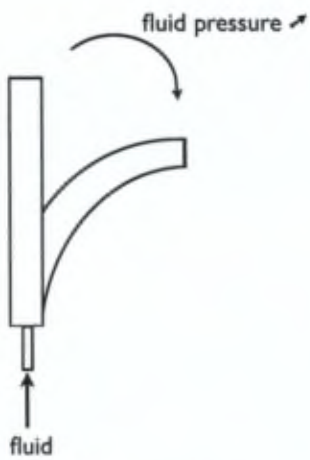

Figure 2.11: Side view of a device bending thanks to anisotropic rigidity. The right side is more rigid than the left side. When the device is pressurized, the length of the stiffer side increases less than that of the other side and consequently the device bends.

Anisotropic rigidity can be achieved by different ways (see Fig. 2.13 and 2.14):

- by using different thicknesses of material in the actuator, the thicker area being stiffer than the rest of the device (see no. 1 in Fig. 2.13).
  [42] presents an example of such an actuator.
- by using different materials presenting different rigidities (see no. 2 in Fig. 2.13).

The "Pneumatic Balloon Actuator" of [50] is such an actuator and it will be described in more details later.

- by fixing inextensible fibres or sheets to the actuator or by embedding them in its material (see no. 3 in Fig. 2.14).
  The "FMA gripper" of [74] is such an actuator and it will be described in more details later. Other examples can be found in [37] (inextensible fibre fixed to the actuator), [35] (inextensible sheet fixed to the actuator) or [85] (inextensible fibre embedded in the rubber of the actuator).

- by weakening an area of the actuator with incisions, bellows, etc (see no. 4 in Fig. 2.14).
  For example, the "Hydraulic Suction Active Catheter" presented in [60] (see Fig. 2.12) belongs to this category. It is composed of a Ti-Ni super elastic alloy structure (processed by laser ablation) and of a flexible tube (of silicone rubber) covering the Ti-Ni structure. The Ti-Ni structure consists of rings connected by "meandering beams" (see Fig. 2.12) and it creates the anisotropic rigidity of the device. The catheter is filled with water and the suction of it involves the bending of the device.

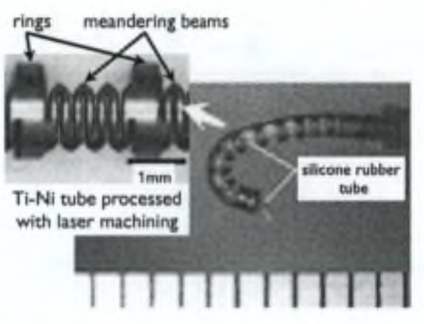

Figure 2.12: Hydraulic Suction Active Catheter: it is composed of a Ti-Ni super elastic alloy structure and of a flexible tube (of silicone rubber) covering the Ti-Ni structure. The Ti-Ni structure consists of rings connected by "meandering beams" and it creates the anisotropic rigidity of the device. The catheter is filled with water and the suction of it involves the bending of the device. Figure adapted from [60].

Concerning the "Hydraulic Forceps" of [54], it is an actuator bending thanks to the presence of incisions in its structure; it will be described in more details later. Other examples can be found in [48] and [46] (actuators bending thanks to the presence of bellows in their structure).

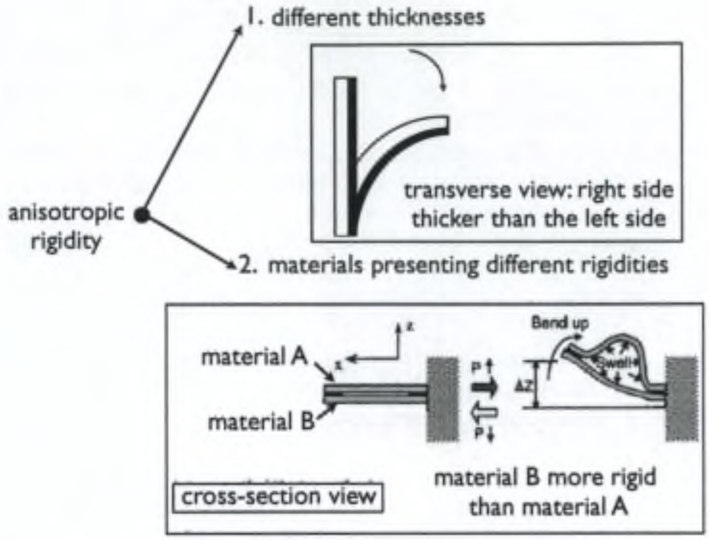

Figure 2.13: Flexible fluidic actuators bending thanks to "anisotropic rigidity". These actuators present an elongated shape closed at one end and an elongated area whose rigidity is higher than that of the rest of the device. This difference in rigidity is called "anisotropic rigidity". When the device is pressurized, the length of the stiffer area increases less than the rest of the device and consequently the device bends. Anisotropic rigidity can be achieved by different ways such as using different material thicknesses in the actuator or using different materials presenting different rigidities (figure adapted from [50]).

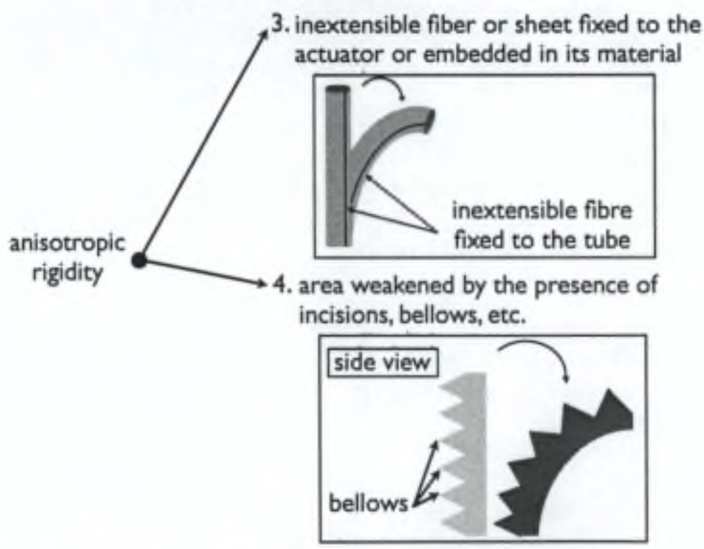

Figure 2.14: Flexible fluidic actuators bending thanks to "anisotropic rigidity". These actuators present an elongated shape closed at one end and an elongated area whose rigidity is higher than that of the rest of the device. This difference in rigidity is called "anisotropic rigidity". When the device is pressurized, the length of the stiffer area increases less than the rest of the device and consequently the device bends. Anisotropic rigidity can be achieved by different ways such as fixing inextensible fibres or sheets to the actuator or embedding them in its material or weakening an area of the actuator with incisions, bellows, etc.

A) An example of anisotropic rigidity achieved by using different materials presenting different rigidities: the "Pneumatic Balloon Actuator" (PBA)

In [50], Konishi et al. propose a "Pneumatic Balloon Actuator" (PBA). This device is fixed as a cantilever and comprises two flexible films. The upper one acts as a membrane and is a silicone rubber film while the lower one plays the role of a substrate and is a polyimide film (see the left part of Fig. 2.15). This difference in the film rigidities involves anisotropic rigidity. The films are glued to one another along their surrounding edge with silicone rubber glue and this configuration forms a cavity. When pressurized air is introduced in this cavity, the silicone rubber film inflates without supporting any bending load (like a membrane). On the other hand, the polyimide film bends due to the moment produced by the tensile forces in the membrane. This behaviour results in a large out-of-plane vertical displacement (i.e. in the y-direction in Fig. 2.15) and in a horizontal displacement (i.e. in the x-direction in Fig. 2.15) of the free end of the actuator.

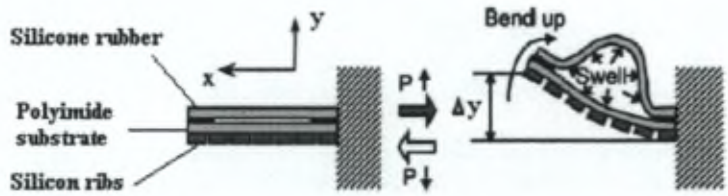

Figure 2.15: Working principle of a Pneumatic Balloon Actuator (PBA), cross-section views: PBA at rest and pressurized PBA (P = pressure) on the left hand side and the right hand side respectively. The PBA is fixed as a cantilever and comprises two flexible films. The upper one acts as a membrane and is a silicone rubber film while the lower one plays the role of a substrate and is a polyimide film. When pressurized air is introduced in the PBA, the silicone rubber film inflates without supporting any bending load and the polyimide film bends due to the moment produced by the tensile forces in the membrane. Figure adapted from [50].

In Fig. 2.15, one can notice the presence of ribs below the polyimide film. These are silicon ribs (obtained by dicing a silicon beam) glued to the substrate and aimed at preventing an unwanted swelling of the substrate and at forcing the device to bend around the z-axis of the ribs, in order to avoid an unwanted corner folding [50].
In order to miniaturize the PBA, the air compressor, that had been used, needed to be replaced and the authors considered and successfully tested a "liquid to gas" phase transformation by Joule heating, to obtain the pressure supply.
Miniaturized PBAs can be achieved thanks to micromachining. Indeed, the planar structure of the PBA suits this technique well and allows distributed micro PBA arrays to be produced in batches.
PBAs have been used to make a "ciliary motion conveyance system" in which they have to work in a co-operative way to displace an object horizontally, such as a glass plate for example. Another application is a two DOFs actuator comprising two PBAs.
In [51], Konishi et al. describe micro PBAs which have been used to actuate a micro hand. They are composed of two layers of different thicknesses made of PDMS elastomer, one of the layers presenting a cavity. When the same PDMS is used for both layers, the PBA presents a bidirectional bending motion. Indeed, when fixed as a cantilever (with the thicker layer below) and pressurized, the PBA moves its end upwards, until a given pressure level is reached; above this level, the PBA tip is moved downwards. On the other hand, a unidirectional bending motion (i.e. upwards motion only) is achieved in the case of a PBA whose layers are

made of different PDMS.

The micronsize "Balloon-Jointed Micro-fingers" presented in [56] (see Fig. 2.16) work on the same principle as the PBA. These fingers are made of two silicon parts jointed by a Parylene balloon. The balloon comprises two membranes: the upper one is free to deform while the lower one is fixed and unable to inflate. When the balloon is pneumatically pressurized, the upper membrane inflates and pulls on the silicon parts, involving the finger to close itself.

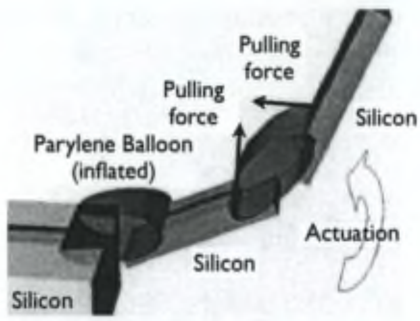

Figure 2.16: Balloon-Jointed Micro-finger: it is made of two silicon parts jointed by a Parylene balloon. The balloon comprises two membranes: the upper one is free to deform while the lower one is fixed and unable to inflate. When the balloon is pneumatically pressurized, the upper membrane inflates and pulls on the silicon parts, involving the finger to close itself. Figure from [56].

B) An example of anisotropic rigidity achieved by fixing inextensible fibres or sheets to the actuator or by embedding them in its material: the FMA Gripper

A gripper placed at the end of an FMA is presented in [74]. Fig. 2.17 shows this gripper, made of rubber-like material. It comprises an internal chamber whose four sides A, B, C and D are fibre-reinforced in the transverse direction. Besides, fibres reinforce side C in the longitudinal direction and cause anisotropic rigidity. Consequently, when the pressure is increased in the chamber, the gripper bends to side C (dashed-dotted lines in Fig. 2.17) and if an object is placed between the plate and side C, it will be gripped.

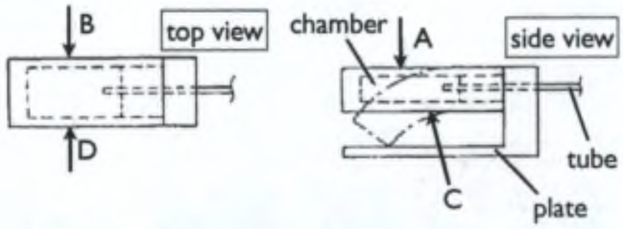

Figure 2.17: Views of the FMA Gripper: gripper at rest and pressurized gripper in continuous and dash-dotted lines, respectively. Fibres reinforce side C in the longitudinal direction. Consequently, when the pressure is increased in the chamber, the gripper bends to side C and if an object is placed between the plate and side C, it will be gripped. Figure adapted from [74].

C) An example of anisotropic rigidity achieved by weakening an area of the actuator with incisions, bellows, etc.: the "Hydraulic Forceps"

[54] presents a "Hydraulic Forceps". A forceps is a medical tool used during MIS operations "*to move tissue away from the operation field or to stretch tissue that has to be dissected*" [54].
The Hydraulic Forceps presents two tubes (see Fig. 2.18): a very flexible material is used for the inner tube, which contains water, while a stiffer material has been chosen for the outer tube. As can be seen in Fig. 2.18, small incisions have been performed in the outer tube, perpendicularly to it and these involve anisotropic rigidity. Both tips of both tubes are fixed to each other and this implies equal deformations of the tubes.

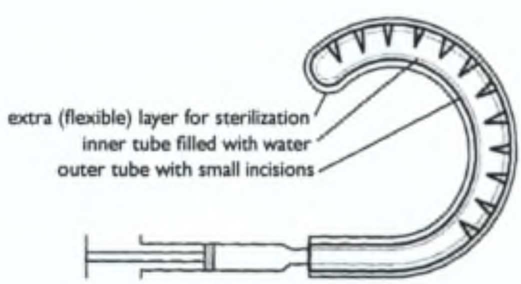

Figure 2.18: Working principle of the Hydraulic Forceps: when filled with pressurized water, the forceps curls due to the incisions in the outer tube. Figure from [54].

When the pressure of water is increased, axial and radial forces are generated. The radial forces do not participate to the bending of the device because they are applied over the total length of the tubes. On the other hand, the axial forces are applied to the end of the tubes and are at the origin of the bending. The outer tube carries most of the axial forces because its stiffness is bigger than that of the inner tube. More precisely, the axial forces are distributed only over one half of the cross-section of the outer tube because of the presence of the small incisions in the other half. This asymmetrical force distribution creates a bending moment which involves the bending of the entire device.
The forceps has been integrated in a teleoperation system with force feedback. A manipulator actuated by the surgeon's finger constitutes the master device of this system while the hydraulic forceps is its slave device. When the surgeon moves the master, the slave has to reproduce its movements, i.e. the evolution of the surgeon's finger curvature. On the other hand, force feedback aims at making the surgeon feel the forces applied to the forceps and it is obtained by measuring and introducing these forces to the master.
The principle of the forceps is said to be suitable for other (surgical) applications where the handling of soft objects is required and it could also be used for the positioning of instruments in fields such as endoscopy or robotics [54].

2.4.4 Rotation

This section presents actuators having a rotational ability. As shown in Fig. 2.19, two ways of generating a rotational motion have been found in the literature:

- Some actuators are based on a structure reinforced in places (with fibres or by increasing the material thickness) in such a way that when the actuator is pressurized, its structure involves a rotation (see no. 1 in Fig. 2.19). The "Pneumatic Rotary Soft Actuator" of [61] is such an actuator and it will be described later in more details.
- Another way to generate a rotational motion consists in an articulated structure in which one or several flexible fluidic actuators are inserted (see no. 2 in Fig. 2.19). These actuators present only one DOF, such as stretching, shortening or expanding. When the actuators are pressurized, they actuate the structure which involves a rotation. For example, an antagonistic structure in which two Pneumatic Artificial Muscles are inserted is a system belonging to this second category. This example and three others will be described later in more details.

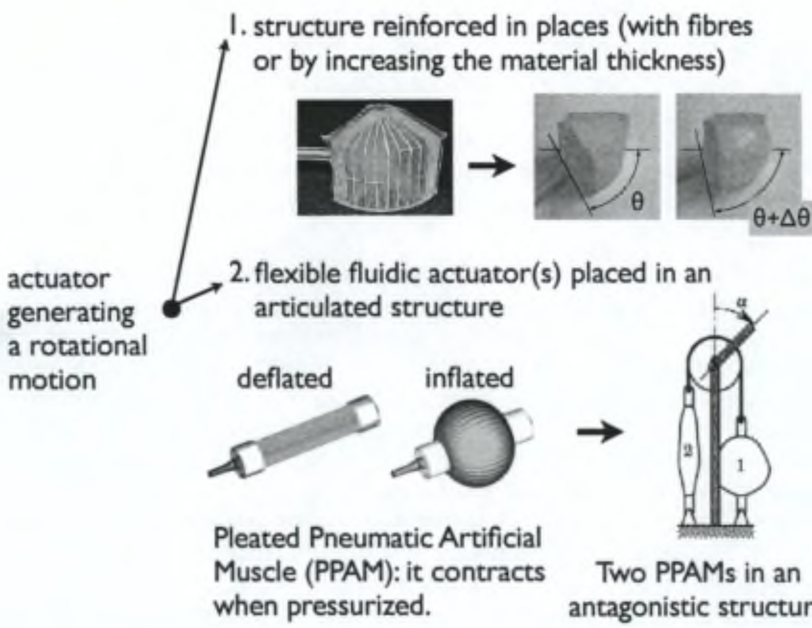

Figure 2.19: Two ways of generating a rotational motion: Some actuators are based on a structure reinforced in places (with fibres or by increasing the material thickness) in such a way that when the actuator is pressurized, its structure involves a rotation (figures from [61]). Another way to generate a rotational motion consists in an articulated structure in which one or several flexible fluidic actuators are inserted. These actuators present only one DOF, such as stretching, shortening or expanding. When the actuators are pressurized, they actuate the structure which involves a rotation. For example, an antagonistic structure in which two Pneumatic Artificial Muscles are inserted is a system belonging to this second category (figures from [84] and [31]).

A) An example of rotational motion achieved thanks to a structure reinforced in places: the "Pneumatic Rotary Soft Actuator"

In [61], a pneumatic actuator made of silicone rubber is described (see Fig. 2.20). It is called "Pneumatic Rotary Soft Actuator". This actuator acts as a rotary joint and can be used in micro-manipulators and fingers. It is composed of two side plates (see (a) in Fig. 2.21), a sector circular arc (see (b) in Fig. 2.21) and a pneumatic tube (see (c) in Fig. 2.21) which is connected to one of the side plates and which feeds the actuator with air.

Figure 2.20: Pneumatic Rotary Soft Actuator. This actuator is made of silicone rubber and fibres and it acts as a rotary joint. Figure from [61].

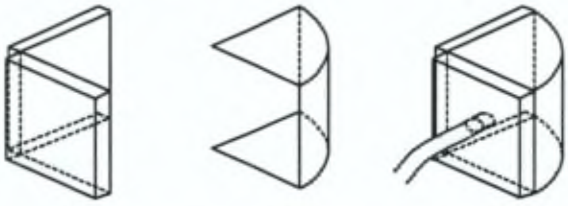

(a) (b) (c)

Figure 2.21: Parts of the Pneumatic Rotary Soft Actuator: (a) two side plates (b) sector circular arc (c) two side plates + sector circular arc + tube = complete Pneumatic Rotary Soft Actuator. Figure from [61].

The thickness of the side plates is higher than that of the sector circular arc, which is reinforced thanks to fibres placed in the radial and vertical directions (see Fig. 2.20). When the device is pressurized, the thickness of the side plates prevents them from deforming while the radial deformation of the sector circular arc is hindered by the fibres. Consequently the device expands only in the circumferential direction, its opening angle is increased and a rotation is achieved (see Fig. 2.22).

To manufacture the different components of the actuator, liquid silicone rubber is poured into metal moulds and left to harden. Two additives, a hardener and a diluent (called "RTV thinner"), are mixed in the rubber. Changing the quantity of the diluent allows to control the stiffness obtained after hardening.
Two pressurized tubes and a rotary soft actuator have been used as phalanxes and joint, respectively, to construct a soft finger. Changing the inner pressure of the tubes allows to modify the compliance of the finger. A soft hand comprising three soft fingers has also been developed and has allowed to grip objects moving in arbitrary directions, objects presenting different shapes and easily deformable objects.

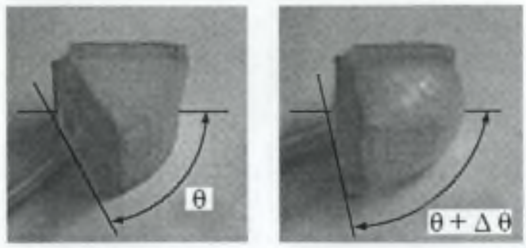

Figure 2.22: Actuation of the Pneumatic Rotary Soft Actuator: when the device is pressurized, the thickness of the side plates prevents them from deforming while the radial deformation of the sector circular arc is hindered by the fibres. Consequently the device expands only in the circumferential direction, its opening angle θ is increased and a rotation is achieved. Figure from [61].

B) First example of rotational motion achieved thanks to an articulated structure in which one or several flexible fluidic actuators are inserted: an antagonistic architecture in which "Pneumatic Artificial Muscles" (PAMs) are inserted

"Pneumatic Artificial Muscles" (PAMs) are made of a flexible closed membrane that is reinforced and fixed to fittings at both ends. When pressurized gas is introduced in such a device (when gas is sucked out), the membrane bulges out (squeezes) and contracts axially (see Fig. 2.23) [31]. A PAM is then able to pull a load attached to one of its ends.

Figure 2.23: Deflated and inflated states of a Pneumatic Artificial Muscle (PAM) presenting a pleated structure. When pressurized gas is introduced in this PAM, the membrane bulges out and contracts axially. Figure from [84].

Although they can only contract, perform linear motion and develop pulling force, PAMs can generate a rotation when used in an antagonistic set-up, as shown in Fig. 2.24. Antagonistic architectures are composed of two muscles but they can be used with other types of contracting actuators. Some architectures allow to obtain a bidirectional rotation but others allow a bidirectional linear motion [31].

A detailed description of the different kinds of PAMs can be found in [29], [31], [49], etc. According to [31], the PAM's behaviour rules are the following:

- *"A PAM shortens by increasing its enclosed volume."*
- *"It will contract against a constant load if the pneumatic pressure is increased."*
- *"A PAM will shorten at a constant pressure if its load is decreased."*
- *"Its contraction has an upper limit at which it develops no force and its enclosed volume is maximal."*

- *"For each pair of pressure and load a PAM has an equilibrium length"*.

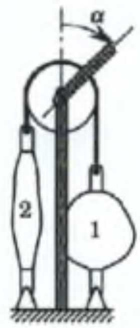

Figure 2.24: Antagonistic set-up generating a bidirectional rotational motion. It is composed of two Pneumatic Artificial Muscles (PAMs) and of an articulated structure. When one of the PAMs is pressurized, it contracts and actuates the structure which generates a rotational motion. Figure from [31].

The PAM's behaviour contrasts with that of bellows which stretch when pressurized. It also differs from the behaviour of a pneumatic cylinder which develops the same force for a constant pressure, whatever the piston displacement (while, at constant pressure, a PAM develops a different pulling force according to its length).
PAMs are mostly used in robotic applications where two important features are the compliance and a high power to weight ratio [31]. For example, they actuate the anthropomorphic robot LUCY [84] and [31] relates applications such as prosthesis/orthotics and an underwater manipulator (for which the driving fluid was water without causing weight problems because the surrounding fluid was also water). At present, the company Festo Ag. & Co. [38] sells fluidic muscles which can be used in a wide range of applications such as positioning systems, machining, etc.
Remark: According to [31], the McKibben PAM *"is the most frequently used and published about at present"*.

C) Second and third examples of rotational motions achieved thanks to an articulated structure in which one or several flexible fluidic actuators are inserted: the "Expansion Behaviour Based Actuators" (EBBAs) and the "Pneumatically Driven Microcage"

In [70], small size flexible fluidic actuators, based on an "expansion behaviour", are presented. They will hereafter be referred to as "EBBAs" (="Expansion Behaviour Based Actuators"). These actuators consist of a chamber connected to two movable parts. When pressurized fluid (air or liquid) is introduced in the chamber through a feeding channel, the volume and height of the chamber increase, involving the movable parts to move relatively to each other. This is what is called the "expansion behaviour". Different kinds of joints can be obtained by using EBBAs. For example, to design a linear joint, two parallel plates can be linked by a chamber in such a way that a pressure rise increases the gap between the plates while keeping them parallel. On the other hand, a rotation joint can be achieved with a chamber placed between two movable parts linked by a joint; a pressure increase then involves a rotation of the movable parts, as shown in Fig. 2.25.

Figure 2.25: Rotation joint composed of a chamber placed between two movable parts linked by a joint. When the pressure in the chamber is increased, a rotation of the movable parts is involved. Figure from [70].

EBBAs are said to present high flexibility (due to their mechanical construction), are lightweight and have a very low manufacturing cost. Besides, using several EBBAs enables to achieve very complex motions.
An artificial hand, based on these actuators, has been developed. It is equipped with miniaturized rotation joints based on EBBAs and integrated into the fingers and the wrist. Many different objects can be grasped by the hand which adapts itself to their shape, thanks to the EBBAs' flexibility. Moreover, it performs movements that appear very natural.

In [63], a "Pneumatically Driven Microcage" is presented. This device aims at capturing microscale objects in biological liquid. It works on the same principle as the EBBAs; the deformation of an elastic membrane is used to achieve the displacement of rigid parts. The cage consists of curved beams or fingers placed in a circular manner and resting on a rubber membrane. When the pressure under the membrane is increased, the latter inflates and involves the rotation of the beams and thus the opening of the cage (see Fig. 2.26).

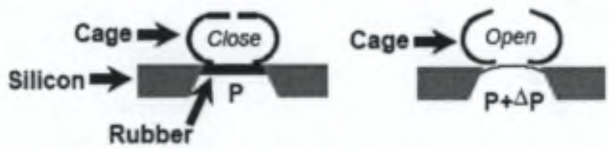

Figure 2.26: Actuation of the Pneumatically Driven Microcage: the cage consists of curved beams or fingers placed in a circular manner and resting on a rubber membrane. When the pressure under the membrane is increased, the latter inflates and involves the rotation of the beams and thus the opening of the cage. Figure adapted from [63].

D) Fourth example of rotational motion achieved thanks to an articulated structure in which one or several flexible fluidic actuators are inserted: the Torsion joint based on Flexible Pneumatic Actuators (FPAs)

A "Flexible Pneumatic Actuator" (FPA) is presented in [85]. It is a hollow cylinder made of elastic rubber (see no. 3 in Fig. 2.27) and containing a spiral steel wire (see no. 2 in Fig. 2.27). This wire reinforces the cylinder and prevents its deformation in the radial direction. Covers (see no. 4 in Fig. 2.27) close both ends of the device and an air feeding tube (see no. 1 in Fig. 2.27) is connected to one of them. When the FPA is pressurized, the cylinder expands in the axial direction without any other deformation. When the pressure is decreased, it goes back to its initial state thanks to the elasticity of the rubber.

A torsion joint based on FPAs has been developed (see Fig. 2.28); it is composed of a steady plate (see no. 3 in Fig. 2.28), a moving plate (see no. 1 in Fig. 2.28) and two FPAs (see no. 2 in Fig. 2.28). The moving plate is connected to the steady plate through a bearing and the FPAs' ends are fixed to each plate. When the air pressure is increased in the FPAs, they expand, push on the moving plate and force it to turn around its axis.

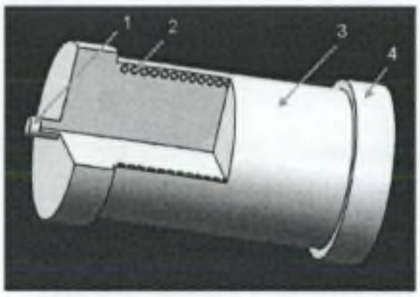

Figure 2.27: Structure of a Flexible Pneumatic Actuator (FPA): 1) Air feeding tube 2) Spiral steel wire 3) Elastic rubber cylinder 4) Cover. An FPA is a hollow cylinder made of elastic rubber and containing a spiral steel wire. This wire reinforces the cylinder and prevents its deformation in the radial direction. When the FPA is pressurized, the cylinder expands in the axial direction without any other deformation. Figure redrawn and adapted from [85].

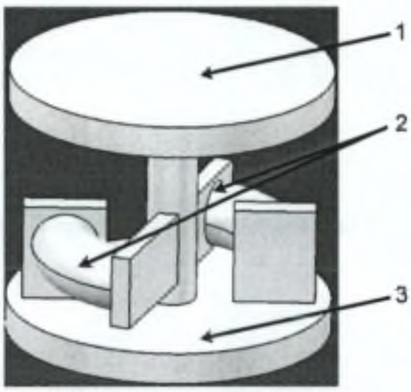

Figure 2.28: Torsion joint based on Flexible Pneumatic Actuators (FPAs): 1) Moving plate 2) Two FPAs 3) Steady plate. The moving plate is connected to the steady plate through a bearing and the FPAs' ends are fixed to each plate. When the air pressure is increased in the FPAs, they expand, push on the moving plate and force it to turn around its axis. Figure redrawn and adapted from [85].

2.4.5 Stretching or shortening

Some flexible fluidic actuators are able to stretch themselves or to shorten when they are pressurized. They are listed below:

- Stretching ability:
  - bellows (see no. 1 in Fig. 2.3)
  - the "Flexible Pneumatic Actuator" (FPA) presented in Fig. 2.27
- Shortening ability:
  - the "Pneumatic Artificial Muscles" (PAMs) (see Fig. 2.23)

– an elastic tube with fibres fixed to it in the axial direction (see no. 3 in Fig. 2.3)

Besides, all the actuators that bend thanks to internal chambers differently pressurized (see Section 2.4.2) can stretch themselves or shorten when all their chambers are equally pressurized.

2.5 Conclusions

Flexible fluidic actuators present interesting characteristics regarding an application in the field of robotics or inside the human body. According to the application targeted, it might be necessary to miniaturize the actuators but also their peripherics and some solutions have been presented in this respect.

At the light of the literature review, it has been established that the flexible fluidic actuators can bend themselves, stretch themselves, shorten or develop a rotational motion and some of them present several DOFs. Two different methods to achieve bending have been identified. The first technique is based on "internal chambers differently pressurized" and the other one on "anisotropic rigidity". Besides, two methods to generate a rotational motion have also been identified. The actuators based on the first technique present a structure reinforced in places (with fibres or by increasing the material thickness) in such a way that when the actuators are pressurized, their structure involves a rotation. The second method to generate a rotational motion consists in an articulated structure in which one or several flexible fluidic actuators are inserted. When the actuators are pressurized, they actuate the structure which involves a rotation.
There exists a multitude of flexible fluidic devices and additional actuators can be obtained by combining different principles, in order to achieve more or less DOFs. Hence, this review can helps to develop medical flexible instruments based on flexible fluidic actuators. Besides, tools to be placed at the tips of the instruments could also be designed and based on flexible fluidic actuators such as, for example, the Hydraulic Forceps, the FMA Gripper or the Pneumatically Driven Microcage.

According to the bulkiness that is allowed for the instrument in the targeted application, it will be necessary to assess the miniaturization potential of the actuators presented in the review. In this respect, actuators presenting a simple structure with a small number of parts will be better candidates to design miniature instruments. Hence, the actuators that seem to have the best miniaturization potential in each category are the following:

- Bending thanks to internal chambers differently pressurized: the "Flexible Microactuator" (FMA) (see Fig. 2.6)
- Bending thanks to anisotropic rigidity: the four ways presented in Fig. 2.13 and 2.14 can lead to actuators quite easy to miniaturize. In the actuators presented in details, the "Pneumatic Balloon Actuator" (PBA, see Fig. 2.15) and the FMA gripper (see Fig. 2.17) are good candidates.
- Rotational motion: the actuators based on a structure reinforced in places and designed to develop a rotational motion are better candidates to be miniaturized than those based on an articulated structure.
- Stretching ability: bellows (see no. 1 in Fig. 2.3) and the "Flexible Pneumatic Actuator" (FPA) presented in Fig. 2.27
- Shortening ability: an elastic tube with fibres fixed to it in the axial direction (see no. 3 in Fig. 2.3)

Finally, it is worth noting that preventing unwanted deformations of the membranes, thanks to fibres or a larger thickness at strategic places, is a rule of design that permeates this review.

Tables 2.1 and 2.2 summary the characteristics of most of the actuators described in this review. These characteristics are the DOFs, the materials, the manufacturing process, the actuator dimensions, the actuation mode (pneumatic or hydraulic), the pressure range and the performances in terms of developed force and displacement.
Remark: Complementary information about some of the actuators mentioned in the review can be found in [40] as well as a series of patented flexible fluidic actuators sorted into the different categories.

Among the interesting features linked to the use of flexible fluidic actuators, one has caught our eye. Indeed, in [79], the "Flexible Microactuator" (FMA) is presented and it is suggested that the measurements of the fluid pressure and of the volume of supplied fluid allow to determine and control the position of the actuator and the force it develops. This property has been called the "Pressure-Volume-Force-Position principle" or "PVFP principle" and it means being able to determine the displacement of a flexible fluidic actuator and the force it develops without using a displacement sensor or a force sensor [79].
To study and implement this principle, that could have applications in the medical field, a flexible fluidic actuator having a simple design, one DOF and which is easily manufactured has been looked for in the review presented above and the "Pneumatic Balloon Actuator" (PBA) has been selected. The implementation of the PVFP principle on this actuator is detailed in Chapter 5.

A miniaturization work has been performed on a special type of Pneumatic Artificial Muscle called the "Pleated Pneumatic Artificial Muscle" (PPAM). Although it is not one of the better candidates to be miniaturized, this actuator has been selected because it can generate large forces and theoretical models predict that miniaturized PPAMs, whose dimensions are small enough to be inserted into MIS medical instruments, could be able to develop the forces required to allow the instruments to perform most surgical actions (see Section 3.2.2 and Table 3.1). Therefore, the PPAMs have been studied in order to assess their miniaturization potential; this is detailed in Chapter 7.

Device	Actuation mode	Pressure range	Dimensions	DOFs	Materials
FMA reinforced with fibres [73]-[72]	P or H	some bar	D: 1 to 20 mm	3 $S, 2B_1$	silicone rubber and nylon fibres
FMA with restraint beams [76]	P or H	some bar	reported values of D: 1.8 mm and 4.8 mm	3 $S, 2B_1$	rubber-like material reacting to UV light
Optimized fibreless FMA [78]	P or H	some bar	initial D: 1 to 100 mm initial L: 2 to 100 times D	3 $S, 2B_1$	rubber-like material
Positioning system for catheter tips [68]	P	0.1 to 0.2 bar	1 balloon : maximum $D = 3$ mm $L = 4$ mm	2 $2B_1$	balloon: polyurethane
Fluidic Bellows Manipulator [25]	P	up to 4 bar	$D = 25$ mm / $L = 365$ mm	2 S, B_1	vulcanized balloons, elastomer tube, ABS parts, steel wire, spine (polycarbonate + high-strength steel sheet)
Suction Active Catheter [60]	H	up to 0.8 bar	$L = 5.5$ mm $D = 0.94$ mm	1 B_2	Ni-Ti tube, silicone rubber tube
Balloon Jointed Micro-Finger [56]	P	0 to ≈ 8 bar	1 finger = 2 blocks (900 µm X 300 µm, $t = 200$ µm) + 2 balloons (540 µm X 640 µm, $t = 6$ µm)	1 B_2	blocks: silicon balloons: parylene
PBA [50]	P	up to 0.6 bar	$L = 16$ mm $l = 16$ mm $t = 775$ µm	1 B_2	polyimide film, silicone rubber membrane, (silicone rubber glue)
Micro PBA [52] [51]	P	0 to 2.1 bar	1 PBA : $W = 300$ to 700 µm $L = 700$ to 1500 µm	1 B_2	2 PDMS with different stiffnesses
FMA Gripper [74]	P or H	some bar	$L = 18$ mm / $l = 8$ mm	1 B_2	rubber-like material and nylon fibres
Hydraulic Forceps [54]	H	not specified	not specified	1 B_2	flexible material
Pneumatic Rotary Soft Actuator [61]	P	up to 0.4 bar	side plate: 17 mm × 17 mm, $t = 3$ mm sector circular arc: $t = 0.5$ mm max opening angle: 85°	1 R	silicone rubber, fibres
FPA [85]	P	up to 3.5 bar	not specified	1 S	elastic rubber, steel wire
EBBA rotation joint [70]	P or H	up to 0.5 bar	not specified	1 R	flexible material
PAM [31]	P or H	up to max 5 - 8 bar	see [31]	1 Sh	see [31]

Table 2.1: Characteristics of the flexible fluidic actuators presented in Section 2.4. "P", "H", "D", "L", "l" and "t" mean "pneumatic", "hydraulic", "diameter", "length", "width" and "thickness", respectively. "S", "Sh", "B_1", "$2B_1$", "B_2" and "R" mean "stretching ability", "shortening ability", "bending thanks to chambers differently pressurized", "two bending motions thanks to chambers differently pressurized", "bending thanks to anisotropic rigidity" and "rotation ability", respectively. Concerning the positioning system for catheter tips, two bending DOFs are mentioned in [68] but a third DOF (a stretching DOF) is probably available.

Device	Manufacturing Process	Results
FMA reinforced with fibres [73]-[72]	Moulding	$D = 12$ mm / $L = 50$ mm $p = 4$ bar in one chamber / $\lambda = 100°$
FMA with restraint beams [76]	Stereolithography	$restr = 2$ / $D = 4.8$ mm / $L = 15$ mm $p = 3$ bar in one chamber / $\lambda \approx 60°$
Optimized fibreless FMA [78]	Extrusion moulding process	$p = 4$ bar $\lambda = 90°$
Positioning system for catheter tips [68]	balloons: polyurethane tubes locally widened other parts : moulding	into a glass tube with 4 mm inner diameter $p = 0.15$ bar / maximum deflection $= 5°$ maximum lateral displacement $= 0.5$ mm
Fluidic Bellows Manipulator [25]	Not specified	$W \approx 0.13$ kg / $p = 4$ bar in one balloon $F_v = 9$ N (2 N) / $\alpha = 30°$ (115°)
Suction Active Catheter [60]	Ni-Ti tube: laser ablation	curvature radius $= 1.4$ mm $\lambda = 160°$
Balloon Jointed Micro-Finger [56]	RIE etching + vapor phase deposition of parylene	$p \approx 4$ bar / $F_v = 1.225$ mN (0 N) $\Delta z \approx 300$ µm (760 µm)
PBA [50]	Gluing	$p = 0.2$ bar $F_v = 0.05$ N (0 N) / $\Delta z = 0$ mm (4.5 mm)
Micro PBA [52] [51]	coating, spin-coating and curing processes	-
FMA Gripper [74]	Moulding	able to generate a 2 N gripping force
Hydr. Forceps [54]	Not specified	the prototype succeeded in producing a force of 1 N
Pneumatic Rotary Soft Actuator [61]	Moulding	$p = 0.4$ bar / variation of the opening angle $= 25°$ (0° and opening angle constrained at 65°) / $torque = 0$ Nm (0.15 Nm)
FPA [85]	Not specified	$p = 3.5$ bar / $\Delta L = 10$ mm
EBBA rotation joint [70]	Low cost but not specified	finger equipped with EBBA rotation joints: $W = 20$ g / max force at the finger tip > 3 N for $p = 0.5$ bar / $\Delta t = 100$ ms
PAM [31]	Not specified	Pleated PAM: $p = 3$ bar / $D = 25$ mm / $L = 100$ mm $W = 60$ g / pulling force of 3500 N

Table 2.2: Characteristics of the flexible fluidic actuators presented in Section 2.4. For a given device, all the data presented in column "Results" are part of the same result (data given in brackets constitute a second result). The notations are the following: D=diameter, L=length, W=weight of the device, p=pressure, λ=bending angle (defined as shown in Fig. 2.6), ΔL=lengthening, $restr$=number of FMA restraint beams per chamber, F_v=developed vertical force (the device being initially placed horizontally), α=bending angle of the Fluidic Bellows Manipulator (defined as shown in Fig. 2.10), Δz=vertical out-of-plane displacement of the actuator tip (the device being initially placed horizontally), Δt=duration taken by a finger equipped with EBBA rotation joints to flex completely and to extend.

Chapter 3

Test bench

3.1 Introduction

To characterize flexible fluidic actuators, a test bench has been developed. Section 3.2 establishes the requirements of the test bench and Section 3.3 presents the design solution chosen for the test bench. This solution consists in a syringe-pump composed of a linear motor linked to a cylinder and Section 3.4 describes the methodology followed to select the linear motor and the cylinder. Afterwards, Section 3.5 describes the whole test bench and Section 3.6 finally concludes about the fulfilment of the requirements listed for the test bench.

Among all the actuators listed in the literature review (see Section 2.4), it has been decided to study PBAs ("Pneumatic Balloon Actuators", see Section 2.4.3) and miniaturized PPAMs ("Pleated Pneumatic Artificial Muscles", see Section 2.4.4 for the PAMs and Chapter 7 for the PPAMs). Miniaturized PPAMs will be developed and characterized in order to assess the miniaturization potential of the PPAMs while PBAs will be used to implement and study the PVFP principle. They have been chosen since they present one DOF, a simple design and are easily manufactured.

According to the PVFP principle, it is possible to determine the position of a flexible fluidic actuator and the force it develops thanks to the measurements of the pressure and of the volume of the fluid having been supplied to the actuator. Fig. 3.1 presents a PBA linked to a syringe-pump; the actuation fluid is air. The volume of fluid supplied to the actuator is considered to be the volume swept by the piston during its displacement; this swept volume is proportional to the piston displacement u and equals Su, where S is the syringe-pump cross-section. Therefore, the piston displacement u will be used for the PVFP principle instead of the swept volume.

When a displacement u is imposed to the piston, the inner pressure p_{in} increases and the PBA inflates and its free end A moves upwards. The vertical and horizontal displacements of this point are Δy_0 and Δx_0, respectively. Afterwards, keeping the piston position constant, if a weight w is hung from the PBA free end, the inner pressure p_{in} increases and the displacements Δy and Δx of the PBA free end decrease. According to the PVFP principle, knowing the values of p_{in} and u allows to determine the displacements of point A and the value of the weight w.

In conclusion, the test bench will be used to characterize the miniaturized PPAMs and to study the PVFP principle implemented on a PBA.

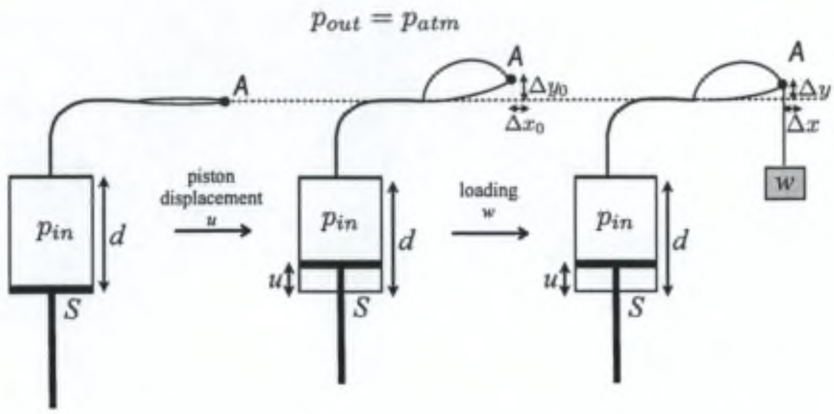

Figure 3.1: Pneumatic Balloon Actuator (PBA) linked to a syringe-pump.

3.2 Requirements

3.2.1 List of requirements

The features the test bench has to present to allow the characterization of flexible fluidic actuators and the study of the PVFP principle are the following:

- measurement of the **pressure** inside the studied flexible fluidic actuator,
- measurement of the volume of fluid supplied to the actuator: in practice, this volume will be considered to be the **volume swept** by the piston of a syringe-pump connected to the actuator,
- measurement of the **force developed** by the actuator,
- measurement of the **displacement** of the actuator,
- the test bench should be able to **maintain the pressurization states of the actuator**,
- the test bench should be able to **dynamically pressurize the actuator at a given frequency**.
- the test bench is also meant to **control the displacement and the developed force** of the studied actuators.

Also,

- the test bench should allow the characterization of a **large range of flexible fluidic actuators** and **in particular of the PBAs and miniaturized PPAMs**,
- the test bench should allow the study of flexible fluidic **actuators driven by gas or by liquid**.

3.2.2 Quantitative requirements

A) Maximum required pressurization frequency

The test bench should be able to pressurize the studied flexible fluidic actuator in 0.05 s. Indeed, a human reflex action can reach a frequency up to 10 Hz [65]. As a consequence, an actuated surgical instrument should have a bandwidth of at least 10 Hz to be able to properly follow the surgeon's movements. To test the bandwidth of the flexible fluidic actuators, the test bench should thus be able to actuate them at a rate up to 10 Hz. Hence, if the studied actuator has a bandwidth of 10 Hz, it means that it is able to go from its lower position to its upper position and back again in 0.1 *s*; its displacement between its extreme positions lasts 0.05 s and its pressurization should be performed in 0.05 s.

B) Ranges of the pressure, the volume of fluid supplied to the actuator, the developed force and the displacement of the studied actuator

Concerning the other requirements listed before, different application cases related to PBAs and PPAMs have been considered in order to get an idea of the pressure, volume of supplied fluid, developed force and displacement ranges of these actuators. All these cases consider that the actuation fluid is air.

- PBAs

  - The first two application cases (cases no. 0.1 and 0.2, see Table 3.1) concern a home-made PBA. It is made of two Thermoplastic Polyurethane (TPU) sheets of different thicknesses (100 µm and 200 µm). The sheets have been welded to each other with a soldering iron in order to create a square-shaped pocket presenting a cavity of 30 mm × 30 mm. The actuator is pressurized with air thanks to a syringe. When it is pressurized to the maximum, its inner volume V_{max} equals 10 ml while the syringe is completely empty. On the other hand, when the actuator is completely deflated, the volume at atmospheric pressure p_{atm} of the syringe equals $V_{atm} = 15$ ml (the volume of the actuator is assumed to equal zero). The absolute pressure p_{max} corresponding to the volume V_{max} of the pressurized actuator is then computed as follows, using the gas law for a system whose gas quantity is constant and assuming that the temperature is constant:

$$p_{max} = \frac{p_{atm} \cdot V_{atm}}{V_{max}} \tag{3.1}$$

    The gauge pressure p_{r_max} corresponding to the absolute pressure p_{max} is computed as follows:

$$p_{r\_max} = p_{max} - p_{atm} \tag{3.2}$$

    Besides, when pressurized and fixed as a cantilever, the home-made PBA has been able to generate at its free end a vertical force F of 0.07 N while the produced vertical displacement Δy equals 0 mm.
    All these results are summarized in the cases no. 0.1 and 0.2 in Table 3.1.

  - The three application cases no. 1.1, 1.2 and 1.3 (see Table 3.1) are based on some data found in [50]. The PBA described in [50] is a square-shaped pocket whose side length is 16 mm, while the cavity is a 10 mm × 10 mm square. The PBA is fixed as a cantilever. The maximum gauge pressure p_{r_max} reached by the actuator equals about 60 kPa (the actuation fluid is air). For this pressure, the PBA generates at its free end a vertical displacement $\Delta y = 6$ mm and a vertical force $F = 0$ N. The corresponding inner volume V_{max} of the PBA is not specified in [50] but it has been overestimated to 10 ml. Indeed, this is the volume of ten cubes of 10 mm side.
    When the PBA is pressurized at $p_{r\_max} = 20$ kPa, it can generate a vertical force $F = 0.05$ N for a vertical displacement $\Delta y = 0$ mm but it can also generate a

vertical force $F = 0$ N for a vertical displacement $\Delta y \approx 4.5$ mm.
All these results are summarized in the cases no. 1.1, 1.2 and 1.3 in Table 3.1.

- Miniature PPAMs
The PPAMs are described in details in Section 7.2.2. As the miniature PPAMs will be developed after the building of the test bench, theoretical models have been used to design the application cases related to these actuators. These theoretical models (see equations 3.3, 3.4 and 3.5) come from [30] and are presented in details in Section 7.2.2. These models assume an ideal PPAM having an inelastic membrane (see Section 7.2.2 for a definition of an ideal PPAM). They allow to estimate the equatorial diameter D and the enclosed volume V of the pressurized PPAM, as well as the pulling force F it generates:

$$D = l\ d(\epsilon, \frac{l}{R}) \tag{3.3}$$

$$V = l^3\ \nu(\epsilon, \frac{l}{R}) \tag{3.4}$$

$$F = pl^2\ f(\epsilon, \frac{l}{R}) \tag{3.5}$$

where
l = initial length of the PPAM (i.e. length of the PPAM when it is not pressurized)
l_c = contracted length of the PPAM (i.e. length of the PPAM when it is pressurized)
$\epsilon = 1 - \frac{l_c}{l}$, ϵ is the contraction of the PPAM
R = initial radius of the PPAM (i.e. radius of the PPAM when it is not pressurized)
p = gauge pressure inside the pressurized PPAM
$d(\epsilon, \frac{l}{R})$, $\nu(\epsilon, \frac{l}{R})$ and $f(\epsilon, \frac{l}{R})$ are dimensionless functions. Figures 7.5, 7.6 and 7.8 in Section 7.2.2 show the evolution of these functions with respect to the contraction ϵ and for different $\frac{l}{R}$ ratios.

For each application case, a particular muscle of initial length l and initial radius R is considered and a given contraction ϵ is assumed. The $\frac{l}{R}$ ratio and the contraction ϵ are then used to determine the values of $\nu(\epsilon, \frac{l}{R})$ and $f(\epsilon, \frac{l}{R})$. Afterwards, the enclosed volume V_{max} of the pressurized muscle is calculated using equation (3.4) while the corresponding gauge pressure p_{r_max} necessary for the muscle to reach a pulling force F of 200 N is computed thanks to equation (3.5). As explained before in Section 1.3, the miniaturized PPAMs should be able to develop a force of this order of magnitude so that once they would be integrated into a more complex medical instrument, the latter would be able to generate a force of about 13 N at its tip (see Fig. 1.5), which would allow it to perform most surgical gestures. Hence, the dimensions l and R have also been chosen so that the corresponding PPAMs would be small enough to be inserted in MIS medical instruments whose diameter must no exceed 10 mm.
The displacement Δy of the PPAM end corresponds to its contraction ϵ and is calculated as follows:

$$\Delta y = l.\epsilon \tag{3.6}$$

The quantity of gas located in the pressurized PPAM has a volume V_{max} at pressure p_{r_max} and a volume V_{atm} at atmospheric pressure p_{atm}. Hence, V_{atm} is computed as follows, using the gas law for a system whose gas quantity is constant and assuming that the temperature is constant:

$$V_{atm} = \frac{V_{max} \cdot (p_{r\_max} + p_{atm})}{p_{atm}}, \tag{3.7}$$

The application cases related to miniature PPAMs are summarized in Table 3.1. The application cases no. 2 to 5 and no. 2' to 5' assume a contraction ϵ of 10%, while cases 2" to 5" assume a contraction ϵ of 20%. For cases no. 2' to 5', the enclosed volume V_{max} is overestimated and computed as follows:

$$V_{overestimated} = \pi(\frac{D}{2})^2(l - l\epsilon) \tag{3.8}$$

with D that is calculated thanks to equation (3.3). $V_{overestimated}$ is the volume of the cylinder whose cross-section is the central cross-section of the inflated PPAM.

The last four cases of Table 3.1 (no. 6.1, 6.2, 7.1 and 7.2) concern miniature McKibben PAMs and have been found in the literature. As can be seen, the forces developed by these muscles are far lower than the forces the miniature PPAMs are expected to produce.

3.2.3 Conclusions

As explained before in Section 3.2.1, the test bench will allow to measure the pressure, the volume of supplied fluid, the developed force and the displacement of the studied flexible fluidic actuator.
As can be seen in Table 3.1, the ranges of these parameters are the following:

- pressure range (see column entitled "p_{r_max}", in Table 3.1): up to 60 kPa for the PBAs and up to 667 kPa for the PAMs. Since these ranges are very different, it will not be possible to study these two kinds of actuators with the same pressure sensor. Indeed, if the accuracy of a sensor is good enough to study the PAMs, it will not be suitable for the PBAs. Two different pressure sensors will thus be used.

- range of the volume of supplied fluid (see column entitled "V_{atm}", in Table 3.1): up to 65.75 ml.

- force range (see column entitled "F", in Table 3.1): up to 0.07 N for the PBAs and up to 200 N for the PAMs. Again, this large difference between the ranges will require a solution adapted to each of the two actuator types considered here.

- displacement range (see column entitled "Δy", in Table 3.1): up to 10 mm. The displacement $\Delta y = 37.8$ mm of the miniaturized McKibben muscle from [55] is not taken into account. Indeed, this large displacement is linked to the length ($l = 180$ mm) of this actuator and this length is far bigger than the one expected for the miniaturized PPAMs that will be developed.

These ranges will be used to design the test bench. However, even if these ranges are particular to PBAs and miniaturized PAMs, the test bench will allow to study other flexible fluidic actuators, as can be seen from Table 2.2.

Application case	l (mm)	R (mm)	ϵ (%)	V_{max} (ml)	p_{r_max} (kPa)	V_{atm} (ml)	F (N)	Δy (mm)
0.1 (home-made PBA)	/	/	/	10	50.65	15	0	*NS*
0.2				NS	NS	NS	0.07	0
1.1 (PBA, [50])	/	/	/	NS, but 10	60	14.92	0	6
1.2				NS	20	NC	0.05	0
1.3				NS	20	NC	0	≈ 4.5
2 (PPAM, $\epsilon = 10\%$)	50	5	10	18.75	106.7	38.76	200	5
3 (PPAM, $\epsilon = 10\%$)	30	2	10	4.05	404	20.41	200	3
4 (PPAM, $\epsilon = 10\%$)	20	2	10	1.2	667	9.2	200	2
5 (PPAM, $\epsilon = 10\%$)	20	4	10	2.4	526	15.02	200	2
2' (PPAM, $\epsilon = 10\%$ and $V_{overestimated}$)	50	5	10	31.81	106.7	65.75	200	5
3' (PPAM, $\epsilon = 10\%$ and $V_{overestimated}$)	30	2	10	6.87	404	34.62	200	3
4' (PPAM, $\epsilon = 10\%$ and $V_{overestimated}$)	20	2	10	2.04	667	15.65	200	2
5' (PPAM, $\epsilon = 10\%$ and $V_{overestimated}$)	20	4	10	3.62	526	22.66	200	2
2" (PPAM, $\epsilon = 20\%$)	50	5	20	25	106.7	51.68	200	10
3" (PPAM, $\epsilon = 20\%$)	30	2	20	5.4	404	27.22	200	6
4" (PPAM, $\epsilon = 20\%$)	20	2	20	1.6	667	12.27	200	4
5" (PPAM, $\epsilon = 20\%$)	20	4	20	3.2	526	20.03	200	4
6.1 (McKibben, [55])	180	0.5	21	NS	600	NC	0	37.8
6.2			0	NS	600	NC	3.8	0
7.1 (McKibben, [86])	50	3	0	NS	100	NC	10	0
7.2			0.6	NS	100	NC	0	0.3

Table 3.1: Application cases related to PBAs, miniature PPAMs and miniature McKibben PAMs. l and R are the initial length and radius of the considered miniature PAM. ϵ is the contraction presented by the muscle. V_{max} is the enclosed volume of the pressurized actuator and p_{r_max} is the corresponding gauge pressure of the actuator. The quantity of gas located in the pressurized actuator has a volume V_{max} at pressure p_{r_max} and a volume V_{atm} at atmospheric pressure p_{atm}. For the PBAs, Δy and F are the vertical displacement and force generated by the end of the actuator when the latter is fixed as a cantilever. For the PAMs, Δy is the displacement corresponding to the contraction ϵ of the muscle and F is the pulling force generated by the muscle. "NS" indicates that the data was not specified in the cited source or that the data has not been measured. "NC" indicates that V_{atm} has not been computed because V_{max} was not specified in the cited source.

3.3 Design of the test bench

A syringe-pump design is chosen for the test bench. The flexible fluidic actuator will be connected to the output of the syringe-pump and this will create a fluidic circuit composed of the chamber of the syringe-pump, the connection tubes and the flexible fluidic actuator. When the piston of the syringe-pump will be actuated, the pressure in the fluidic circuit will increase or decrease according to the actuation direction and the actuator will be actuated. In practice, a cylinder will be used as the syringe (see no. 5 in Fig. 3.2). Besides, although a syringe-pump design can be used with gas or liquid, air will be used as fluid. Indeed, this will ease the use of the test bench because air is a readily available source, it can be freely evacuated in the ambient air [71] and possible leakages will not risk damaging the test bench (e.g. the electrical connections).

The volume of fluid supplied to the actuator is considered to be the volume swept by the piston of the syringe-pump. Hence, this volume is proportional to the displacement of the cylinder piston and in practice, the piston displacement is the variable that will be used instead of the swept volume.

The solution chosen to implement the syringe-pump is presented in Fig. 3.2 and consists in the actuation of the cylinder piston (no. 4 in Fig. 3.2) by a linear motor (no. 1 in Fig. 3.2). This motor will be equipped with a position sensor to measure the displacement of the cylinder piston. To set up this solution, the linear motor only needs to be aligned with the cylinder and a part linking the cylinder piston and the slider of the linear motor (no. 3 in Fig. 3.2) needs to be manufactured.
This solution has been chosen after studying different ones. The chosen solution has been selected because most of its parts are already integrated which will ease the setting up of the test bench and because it should offer a better positioning accuracy than the other considered solutions. Section A.1 presents these other solutions and compares them to the chosen one.

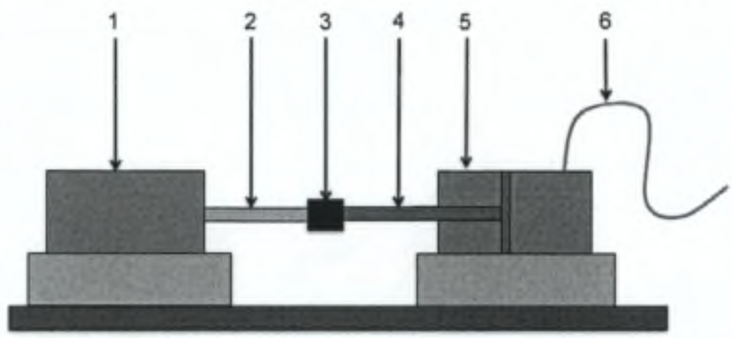

Figure 3.2: Scheme of the syringe-pump test bench: 1) linear motor + position sensor 2) slider of the linear motor 3) linking part 4) pneumatic cylinder piston 5) pneumatic cylinder 6) pneumatic tube

3.4 Pneumatic cylinder and linear motor selection

This section presents the methodology followed to select the pneumatic cylinder and the linear motor.

3.4.1 Selection of the cylinder type

As explained before, the volume of fluid supplied to the flexible fluidic actuator is considered to be the volume swept by the piston of the syringe-pump. However, considering this swept volume does make sense only if the test bench does not present any leakage. In this case, a given displacement of the cylinder piston will always lead to the same pressurization of the fluidic circuit and of the flexible fluidic actuator, when no external force is applied to the latter. Hence, a mandatory requirement for the test bench in general and for the pneumatic cylinder in particular is that there must be no leakages.
Another requirement for the test bench and the cylinder is to present as little friction as possible, because friction adds a non-linear characteristic to the system that will be difficult to model if the PVFP principle is implemented in a control loop.
Following these two requirements, the DNC cylinder with option "low friction" has been chosen among the different pneumatic cylinder types proposed by the Festo company. This cylinder presents 0.1 bar of friction. This means that at least 0.1 bar of pressure must be applied to the cylinder piston to be able to displace it. This friction is due to the sealing whose function is to insure the air-tightness of the cylinder. As long as the pressure inside the cylinder chamber remains lower than the maximum recommended pressure (12 bar), the

cylinder should not present any leakage.
The chosen cylinder has the following characteristics:

- It is a DNC cylinder with "low friction" option (= option S11), sold by the Festo company.
- It is a double-acting cylinder with a diameter of 32 mm (it is the smallest diameter available in the DNC series).
- It presents flexible cushioning rings/pads at both ends.
- Its maximum recommended speed is 0.9 m/s.

The stroke still needs to be defined and this will be done in the next section.

Remark: The Airpot Company [9] proposes pneumatic cylinders presenting less friction than those proposed by the Festo company but they have leakages.

3.4.2 Design of the "cylinder-linear motor" combination

To select a linear motor, the maximum stroke and continuous force required by the application need to be known. Besides, once the motor is chosen, a dynamic study has to be made to assess if the motor is able to perform the required movements when it is connected to its load.
To determine the maximum stroke and continuous force required for the test bench, the application cases of Table 3.1 have been considered. The goal is to use the syringe-pump test bench to inject gas in the PBAs or the miniature PPAMs of the application cases in order to actuate them.
As explained before, each application case specifies the gauge pressure p_{r_max} of the pressurized actuator as well as its enclosed volume V_{max}. To achieve this state of pressurization, the cylinder and the linear motor need a given stroke L and to maintain this state of pressurization, the linear motor must be able to develop a given continuous force $F_{max\_statics}$. These parameters have been computed for each application case with the method described below. The maximum values of these parameters have then been used to select a linear motor among the products of the Linmot company [14] and to finalize the selection of the cylinder. However, there is another requirement to take into account: as explained in Section 3.2.2, the test bench should be able to pressurize the studied actuator in 0.05 s. To assess whether the combination "cylinder-linear motor" is able to fulfil this dynamic requirement, a dynamic study has been made, as explained below.

A) Computation of the parameters L and $F_{max\_statics}$

Let us consider an inflated flexible fluidic actuator connected to a cylinder, as presented in Fig. 3.3. The enclosed volume, inner absolute pressure and inner gauge pressure of the pressurized actuator are V_{max}, p_{max} and p_{r_max}, respectively. The cylinder chamber is assumed to be empty.
To maintain the state of pressurization, the linear motor needs to develop a continuous force $F_{max\_statics}$. This force is computed as follows, by multiplying the inner gauge pressure p_{r_max} of the actuator by the cross-section S of the cylinder piston:

$$F_{max\_statics} = S \cdot p_{r\_max}, \tag{3.9}$$

$$S = \pi(\frac{0.032\ m}{2})^2. \tag{3.10}$$

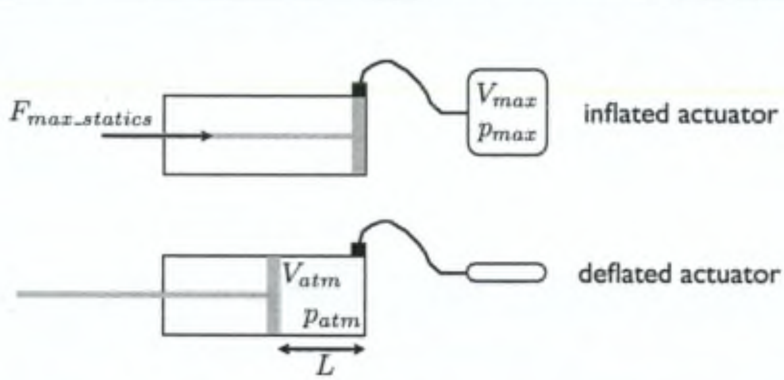

Figure 3.3: Flexible fluidic actuator connected to the output of the test bench cylinder. When inflated, the flexible fluidic actuator has an enclosed volume V_{max} and an inner absolute pressure p_{max}. To maintain the state of pressurization, the linear motor must apply a continuous force $F_{max\_statics}$ to the cylinder piston. When the actuator is completely deflated, all the gas is assumed to be located in the cylinder chamber at the atmospheric pressure p_{atm} and with a volume V_{atm}. The stroke required for the cylinder and the linear motor to pressurize the actuator is L.

In fact, equation 3.9 overestimates the force $F_{max\_statics}$ a little bit because the cylinder presents a friction of 0.1 bar. This friction contributes to maintain the piston in place but it is not taken into account in equation 3.9.
The relationship between p_{r_max} and p_{max} is the following:

$$p_{r\_max} = p_{max} - p_{atm}, \tag{3.11}$$

where p_{atm} is the atmospheric pressure.
To compute the stroke L necessary to reach such a state of pressurization, it is assumed that when the actuator is completely deflated all the gas is located in the cylinder chamber at the atmospheric pressure p_{atm} and the volume of the actuator equals zero (see Fig. 3.3). The volume of the gas at atmospheric pressure is V_{atm} and it is computed as follows, using the gas law for a system whose gas quantity is constant and assuming that the temperature is constant:

$$V_{atm} = \frac{V_{max} \cdot p_{max}}{p_{atm}} \tag{3.12}$$

V_{atm} has already been computed in Section 3.2.2 and is listed in Table 3.1.
The stroke L required to pressurize the actuator is thus:

$$L = \frac{V_{atm}}{S}, \tag{3.13}$$

Equation 3.12 assumes that the pneumatic tubes connecting the cylinder to the actuator are completely empty.

As can be seen, these simple maths allow to determine:

- the stroke L necessary to reach the pressurization state of a given flexible fluidic actuator
- the continuous force $F_{max\_statics}$ required to maintain the pressurization state.

The parameters V_{atm}, p_{atm}, V_{max} and p_{r_max} of the application cases are summarized in Table 3.2, as well as the stroke L and the continuous force $F_{max\_statics}$ required to perform each application case.

Remark: Application cases no. 0.1 and 0.2 have been removed since being able to pressurize case no. 1.1 automatically allows to pressurize both cases. Cases no. 1.2 and 1.3 have been removed for the same reason while case no. 1.1 has been kept under the number 1. Finally, cases no. 6.1, 6.2, 7.1 and 7.2 have been removed since they concern miniature McKibben muscles and because their V_{atm} parameter is not specified.

Application case	V_{atm} (ml)	p_{atm} (kPa)	V_{max} (ml)	p_{r_max} (kPa)	L (mm)	$F_{max\_statics}$ (N)
1 (PBA, [50])	15.92	101.3	10	60	19.79	48.25
2 (PPAM, $\epsilon = 10\%$)	38.76	101.3	18.75	106.7	48.19	85.81
3 (PPAM, $\epsilon = 10\%$)	20.41	101.3	4.05	404	25.38	324.92
4 (PPAM, $\epsilon = 10\%$)	9.2	101.3	1.2	667	11.44	536.43
5 (PPAM, $\epsilon = 10\%$)	15.02	101.3	2.4	526	18.68	423.04
2' (PPAM, $\epsilon = 10\%$ and $V_{overestimated}$)	65.75	101.3	31.81	106.7	81.75	85.81
3' (PPAM, $\epsilon = 10\%$ and $V_{overestimated}$)	34.62	101.3	6.87	404	43.05	324.92
4' (PPAM, $\epsilon = 10\%$ and $V_{overestimated}$)	15.65	101.3	2.04	667	19.46	536.43
5' (PPAM, $\epsilon = 10\%$ and $V_{overestimated}$)	22.66	101.3	3.62	526	28.18	423.04
2" (PPAM, $\epsilon = 20\%$)	51.68	101.3	25	106.7	64.26	85.81
3" (PPAM, $\epsilon = 20\%$)	27.22	101.3	5.4	404	33.85	324.92
4" (PPAM, $\epsilon = 20\%$)	12.27	101.3	1.6	667	15.26	536.43
5" (PPAM, $\epsilon = 20\%$)	20.03	101.3	3.2	526	24.91	423.04

Table 3.2: Parameters V_{atm}, p_{atm}, V_{max}, p_{r_max}, L and $F_{max\_statics}$ of the different application cases of Table 3.1. V_{max} is the enclosed volume of the pressurized actuator and p_{r_max} is its corresponding gauge pressure. The quantity of gas located in the pressurized actuator has a volume V_{max} at pressure p_{r_max} and a volume V_{atm} at atmospheric pressure p_{atm}. L is the necessary stroke for the cylinder and the linear motor to reach the considered state of pressurization of the actuator. $F_{max\_statics}$ is the continuous force necessary for the linear motor to maintain the considered state of pressurization of the actuator.

B) Selection of the cylinder and of the linear motor

As can be seen in Table 3.2, the longest stroke and highest continuous force necessary to perform the application cases are 81.75 mm and 536.43 N, respectively. These values have been used to select a motor among the products proposed by the Linmot company [14] and to select a DNC cylinder.
Among the proposed Linmot motors, the PO1-48X240 series is the one that can develop the highest continuous force. The value of this force is 257 N and to reach such a force, the motor needs to be installed in a flange (see Fig. A.12) and to be cooled by a fan. Although this force is approximately half of the maximum continuous force required, it will nevertheless be sufficient for the experiments to be performed.
Indeed, the application cases related to miniature PPAMs (cases no. 2 to 5, 2′ to 5′ and 2″ to 5″) consider that the actuator develops a pulling force of 200 N. However, to get interesting conclusions from the experiments, it is not necessary that the actuators reach such a force and it will be sufficient to have a test bench able to pressurize miniature PPAMs so that they develop a pulling force of 100 N. A linear motor developing a maximum continuous force of 257 N will thus be suitable.
The motor the PO1-48X240/90X240 has been finally chosen. It is able to develop its maxi-

mum peak force all over a 90 mm stroke but it has a total stroke of 240 mm. A 90 mm stroke has also been chosen for the pneumatic cylinder.
More details about the chosen motor are available in Section A.2.3.

C) Dynamic study of the "cylinder-linear motor" combination

Now that the cylinder and the linear motor have been selected, the dynamic study can be performed in order to answer the following question: is the "cylinder-linear motor" combination able to pressurize the studied actuator in 0.05 s?
To perform this study, a motor sizing software called "Linmot Designer" is used (this software is available for download on the LinMot website [14]).
To study an application case with this design software, some data must be provided such as the motor type, the servo controller type (a B1100VF controller has been chosen, see Section A.2.4 for more details about this choice), the mass the motor has to displace when it is actuated, the external force and friction applied to the motor, the motion cycle (the curve type for the displacement, the velocity and the acceleration, the displacement, the maximum recommended velocity, etc.), etc. The details of all the parameters encoded in the software are available in Section A.2.4.
If the linear motor combined with the controller and the cylinder, is not able to perform the proposed motion cycle, warnings are indicated by the Linmot Designer program. These warnings notify, for example, that the dynamic force the motor has to produce exceeds the peak force limits of the "motor - servo controller" combination.

For each application case of Table 3.2, a start position is chosen for the motor (see Section A.2.4 for more details on the start position choice) and the following motion cycle is studied:

1. a forward motion of stroke L with an external force $F_{ext} = -F_{max\_statics}$ and a maximum velocity $v_{max} = 0.9$ m/s
2. a backward motion of stroke L with an external force $F_{ext} = -F_{max\_statics}$ and a maximum velocity $v_{max} = 0.9$ m/s

The external force F_{ext} is the force applied by the pressurized gas to the cylinder piston. According to the sign convention of the software, if this force has a negative value, it means that it tends to push the slider inside the stator.
The constraint on the velocity is due to the pneumatic cylinder. Indeed, according to the Festo support, a velocity larger than 0.9 m/s could damage the flexible cushioning rings/pads placed at both ends of the chosen cylinder.

The goal of the dynamic study is to approach a duration time of 0.05 s for the forward motion and the backward motion, respectively. With this target in mind, a search is done for each application case in order to find a curve type and the values of the corresponding parameters so that the motor, combined with the controller and the cylinder, would be able to perform the motion cycle.

Remark 1: The available curve types for the travel through the stroke are: sine, standstill, point to point, limited jerk or minimal jerk.
Remark 2: In the software, the external force $F_{ext} = -F_{max\_statics}$ is applied continuously to the cylinder piston during the motion. However, in practice, when the cylinder piston is displaced and the actuator is pressurized (depressurized), the external force increases (decreases) and its intensity finally becomes equal to $F_{max\_statics}$ (0 N), at the end of the displacement. Hence, considering that $F_{ext} = -F_{max\_statics}$ during all the motion overestimates the real external force.

Table 3.3 summarizes the results of the dynamic study of the application cases of Table 3.2. For each case, the following data are listed: the parameters L and $F_{max\_statics}$ previously computed (see Table 3.2), the start position of the motor, the motion cycle (forward motion and backward motion) the motor, combined with the servo controller and cylinder, is able to perform according to the Linmot Designer program (i.e. no warnings). The curve type and its parameters are specified as well as the duration T of the motion and the external force F_{ext} applied during the motion.

As can be seen in Table 3.3, for a majority of the application cases related to miniature PPAMs, the motor is not able to pressurize the actuators when a constant external force $F_{ext} = -F_{max\_statics}$ is applied to the motor. However, for a constant external force $F_{ext} \approx -\frac{F_{max\_statics}}{2}$, the motor can perform these application cases and this is sufficient for the test bench. Indeed, as explained before, this means that the motor can pressurize the miniature PPAMs so that they can develop a pulling force of about 100 N and besides, the constant external force F_{ext} overestimates the real external force applied to the motor.
Concerning the velocity of pressurization, the pressurization times of cases no. $2, 2', 3', 2''$ and $3''$ are too long. Nevertheless, the chosen "cylinder - linear motor - controller" combination will be kept because:

- cases no. $2'$ and $3'$ consider an overestimated volume of the inflated PPAMs, this involves an overestimated stroke L and increases the time necessary to cover this distance
- the duration time of case no. $3''$ is very close to the required time
- all the application cases are overestimated since the external force F_{ext} is applied constantly during the motion whereas in reality, this force increases or decreases while the motor slider is displaced. For the motor, counterbalancing this constant external force F_{ext} consumes energy that could otherwise be used to accelerate more and decrease the duration time.

Conclusion

At the light of this dynamic study, the chosen "cylinder - linear motor - controller" combination is kept.
Table 3.4 summarizes its main properties. The datasheets of the chosen linear motor and controller are available in Section A.2.3, in Fig. A.11, A.16, A.17 and A.18.

Application case	L (mm)	$F_{max\_statics}$ (N)	start position (mm)	curve type	acc. (m/s^2)	dec. (m/s^2)	T (ms)	F_{ext} (N)
1 (PBA, [50])	19.79	48.25	25.21					
forward motion				pt 2 pt	35	35	47.6	−48.2
backward motion				pt 2 pt	35	35	47.6	−48.2
2 (PPAM, $\epsilon = 10\%$)	48.19	85.81	−3.19					
forward motion				pt 2 pt	100	100	62.5	−85.8
backward motion				pt 2 pt	100	100	62.5	−85.8
3 (PPAM, $\epsilon = 10\%$)	25.38	324.92	19.62					
forward motion				pt 2 pt	40	40	50.7	−220
backward motion				pt 2 pt	40	40	50.7	−220
4 (PPAM, $\epsilon = 10\%$)	11.44	536.43	33.56					
forward motion				pt 2 pt	20	20	47.8	−250
backward motion				pt 2 pt	20	20	47.8	−250
5 (PPAM, $\epsilon = 10\%$)	18.68	423.04	26.32					
forward motion				pt 2 pt	30	30	49.9	−240
backward motion				pt 2 pt	30	30	49.9	−240
2' (PPAM, $\epsilon = 10\%$ and $V_{overestimated}$)	81.75	85.81	−36.75					
forward motion				pt 2 pt	110	110	99	−85.8
backward motion				pt 2 pt	110	110	99	−85.8
3' (PPAM, $\epsilon = 10\%$ and $V_{overestimated}$)	43.05	324.92	1.95					
forward motion				pt 2 pt	50	50	65.8	−200
backward motion				pt 2 pt	50	50	65.8	−200
4' (PPAM, $\epsilon = 10\%$ and $V_{overestimated}$)	19.46	536.43	25.54					
forward motion				pt 2 pt	30	30	50.9	−240
backward motion				pt 2 pt	30	30	50.9	−240
5' (PPAM, $\epsilon = 10\%$ and $V_{overestimated}$)	28.18	423.04	16.82					
forward motion				pt 2 pt	50	50	49.3	−200
backward motion				pt 2 pt	50	50	49.3	−200
2" (PPAM, $\epsilon = 20\%$)	64.26	85.81	−19.26					
forward motion				pt 2 pt	110	110	79.6	−85.8
backward motion				pt 2 pt	110	110	79.6	−85.8
3" (PPAM, $\epsilon = 20\%$)	33.85	324.92	11.15					
forward motion				pt 2 pt	50	50	55.6	−200
backward motion				pt 2 pt	50	50	55.6	−200
4" (PPAM, $\epsilon = 20\%$)	15.26	536.43	29.74					
forward motion				pt 2 pt	25	25	49.4	−250
backward motion				pt 2 pt	25	25	49.4	−250
5" (PPAM, $\epsilon = 20\%$)	24.91	423.04	20.09					
forward motion				pt 2 pt	40	40	50.2	−220
backward motion				pt 2 pt	40	40	50.2	−220

Table 3.3: Dynamic study of the application cases: the table lists the motion cycles (forward motion and backward motion) that the motor, combined with the servo controller and the cylinder, is able to perform according to the Linmot Designer software. During a cycle, an external force F_{ext} is applied to the motor slider and the motor makes a forward motion and a backward motion of stroke L without exceeding the maximum velocity $v_{max} = 0.9$ m/s. The start position of the motor is specified as well as the curve type of the motion ("pt 2 pt" means "point to point") and its parameters (the acceleration ("acc."), the deceleration ("dec.")). T is the duration of the motion. L and $F_{max\_statics}$ are the parameters computed previously in Table 3.2.

Pneumatic cylinder	
brand	Festo
type	DNC-32-90-p-S11 (double-acting cylinder)
diameter	32 mm
stroke	90 mm
maximum recommended speed	0.9 m/s
friction	10 kPa
damping	flexible cushioning rings/pads placed at both ends of the cylinder
piston mass	243 g
pneumatic connexion	G1/8 female
Linear motor	
brand	Linmot
type	PO1-48X240/90X240
maximum stroke	240 mm
stroke SS	90 mm
maximum continuous force with fan cooling	257 N
force constant	39 N/A
maximum peak force (with a B1100VF controller: i.e. maximum current 8 A)	39 N/A . 8 A = 312 N
position repeatability	±0.05 mm
linearity	±0.2 %
position repeatability with external sensor	±0.01 mm
linearity with external sensor	±0.01 mm
Controller	
brand	Linmot
type	B1100-VF
maximum peak current delivered to the motor	8 A
command types	current command or slider position command

Table 3.4: Main properties of the pneumatic cylinder, the linear motor and the controller chosen for the test bench.

3.5 Description of the test bench

3.5.1 Test bench board

Most parts of the test bench are installed on a board (see Fig. 3.4). This is a M-TD-22 Breadboard proposed by Newport. Its dimensions are 600 mm × 600 mm × 28 mm. It presents threaded M6 holes distributed every 25 mm in two perpendicular directions, over the surface of the board.

Figure 3.4: Newport board on which most components of the test bench are installed. Figure from [19].

3.5.2 Platform for measurement and control

As explained in Section 3.2.1, the test bench will allow to characterize flexible fluidic actuators and to investigate the PVFP principle. To do so, it will be equipped with different sensors whose measurements will need to be acquired. Besides, the test bench is also meant to control the displacement and the developed force of the studied actuators. Hence, to acquire the sensors measurements and to offer control possibilities to the test bench, an integrated platform for measurement and control has been chosen.
National Instruments [18] and dSPACE [12] propose such platforms that have already been used by colleagues. The products proposed by these companies offer quite similar services however:

- If two similar solutions, National Instruments and dSPACE, are compared, it can be noted that the National Instruments solution will be half as expensive as the other one.
- The products proposed by National Instruments are developed for the industry. Hence, National Instruments provides follow up for its products (e.g. it proposes software updates and ensures compatibility for the components) for several tens of years. Concerning dSPACE, the products are especially developed for the automobile industry where the projects last approximately four years.
  NB: Answering questions about the lasting of a given product, a dSPACE employee said he couldn't guarantee how long the product would be proposed and would receive a follow up.

These two arguments have led to choose the National Instruments products and among the proposed platforms, the NI PXI system has been selected (see (a) in Fig. 3.5).

It uses the Labview software and is composed of a chassis, a controller and different modules that can be chosen according to the needs of the application. This makes this solution very polyvalent. The main properties of the chosen NI PXI configuration are summarized in

Main components of the chosen NI PXI configuration
Chassis with 8 slots and universal AC power supply
NI PXI-8106 controller: core 2 duo, 2.16 GHz, Windows Vista
Extra memory: 1 GB DDR2 RAM
Module with 32 analog output channels
Data acquisition module: 32 analog inputs, 48 digital inputs/outputs
Connector blocks for the analog output module and the data acquisition module

Table 3.5: Main components of the chosen NI PXI configuration

Table 3.5. A detailed list of the platform components is available in Section A.4. As can be seen in Table 3.5, "connector blocks" (see (b) in Fig. 3.5) are used. They are connected to the modules of the NI PXI platform and offer screw terminals for easy connections between the modules and the points where signals need to be sent or collected.

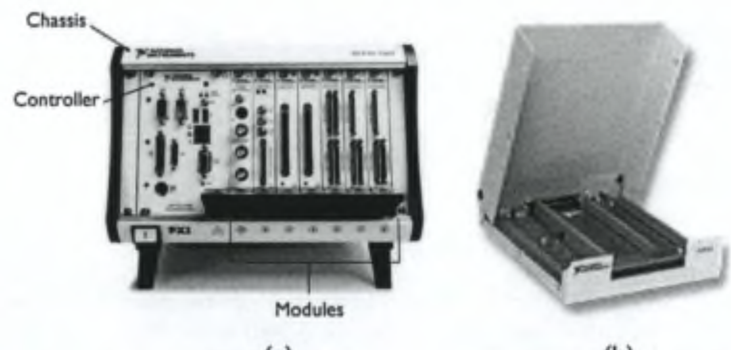

Figure 3.5: (a) NI PXI solution proposed by National Instruments (b) Connector block. Figures from [18].

3.5.3 Pneumatic cylinder and linear motor

As explained before, the test bench is composed of a linear motor combined with a pneumatic cylinder (see Fig. 3.7). This constitutes a syringe-pump that is connected to the flexible fluidic actuator to be studied. When the motor (no. 1 in Fig. 3.7) is actuated, its slider (no. 2 in Fig. 3.7) is displaced. This slider drives the piston of the cylinder (no. 4 in Fig. 3.7) and this involves a pressure variation in the pneumatic circuit (i.e. the cylinder chamber, the flexible fluidic actuator and the pneumatic tubes linking the cylinder and the actuator (no. 6 in Fig. 3.7), from which results the actuation of the actuator.

Figure 3.8 presents the practical implementation of the test bench. As can be seen in this figure,

- the linear motor (no. 1 in Fig. 3.8) is fixed on two aluminium plates A and A' which are screwed to the test bench board (no. 5 in Fig. 3.8).
- the aluminum part B ensures the linking between the slider (no. 2 in Fig. 3.8) and the piston (no. 3 in Fig. 3.8). The slider and the piston are screwed to this part.

- the cylinder (no. 4 in Fig. 3.8) is fixed on two aluminium parts C and C' which are screwed to the test bench board.

- the linear motor is equipped with a flange and a fan (no. 1 in Fig. 3.8).

- the linear motor is equipped with an external position sensor (no. 6 in Fig. 3.8). The motor has an internal position sensor that allows to position the slider with a repeatability of ± 0.05 mm and a linearity of ± 0.2 % (see Table 3.4). However, to have the best possible accuracy, an external sensor available in the LinMot catalog has been added to the test bench. Indeed, with such a sensor, a repeatability of ± 0.01 mm is achieved as well as a linearity of ± 0.01 mm (see Table 3.4).
  The external sensor has to displace above a magnetic strip (no. $6'$ in Fig. 3.8) and the sensor implementation has to fulfill some requirements presented in Fig. 3.6. The connection between the sensor and part B has thus been designed with this in mind and is ensured via the rods D and D'. Hence, when these rods are horizontal, the requirements are fulfilled.
  More information about the external position sensor is available in Section A.2.3, in Fig. A.14 and A.15.

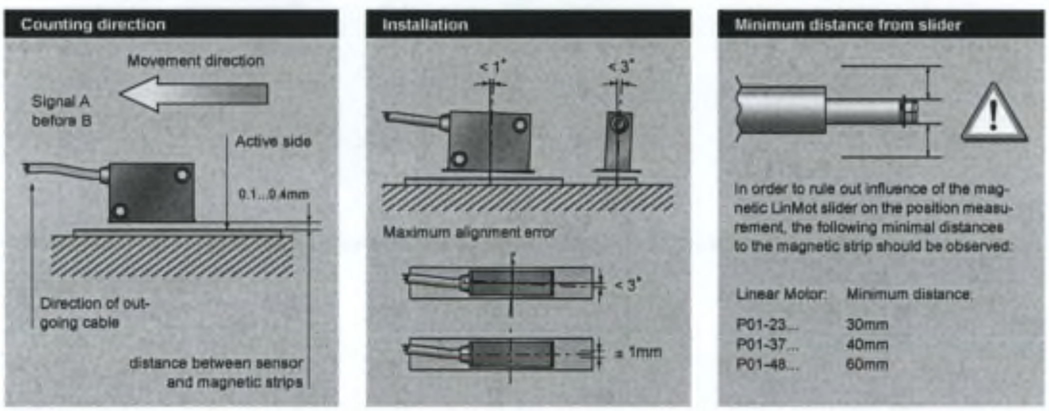

Figure 3.6: Requirements to fulfill when installing the external position sensor of the linear motor. Figure from [1].

- to ensure the horizontality of rods D and D', the rotation of the slider must be avoided. To do so, part B presents a flat surface which slides on the Teflon part E. Teflon has been chosen to limit the friction.

<u>Remark 1</u>: Linear guides (see Fig. A.21, in Appendix A.2.3) are available in the Linmot catalog [1]. Such guides should be used if the slider is subjected to radial loads, if the rotation of the slider or the 0.5 mm gap between the slider and the stator causes inconvenience. Hence, the Teflon part E could be replaced by a linear guide.

<u>Remark 2</u>: When the external position sensor is plugged to the motor controller, the latter uses the measurement of the external sensor to control the slider position, instead of using the measurement of the internal sensor of the linear motor.

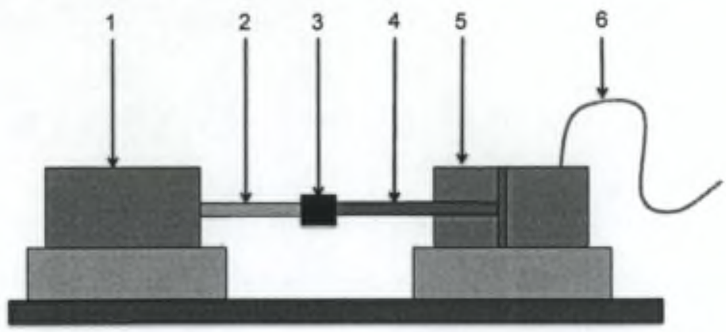

Figure 3.7: The syringe-pump test bench: 1) linear motor 2) slider of the linear motor 3) linking part 4) piston of the pneumatic cylinder 5) pneumatic cylinder 6) pneumatic tubes connecting the cylinder and the actuator (which is not represented in this figure)

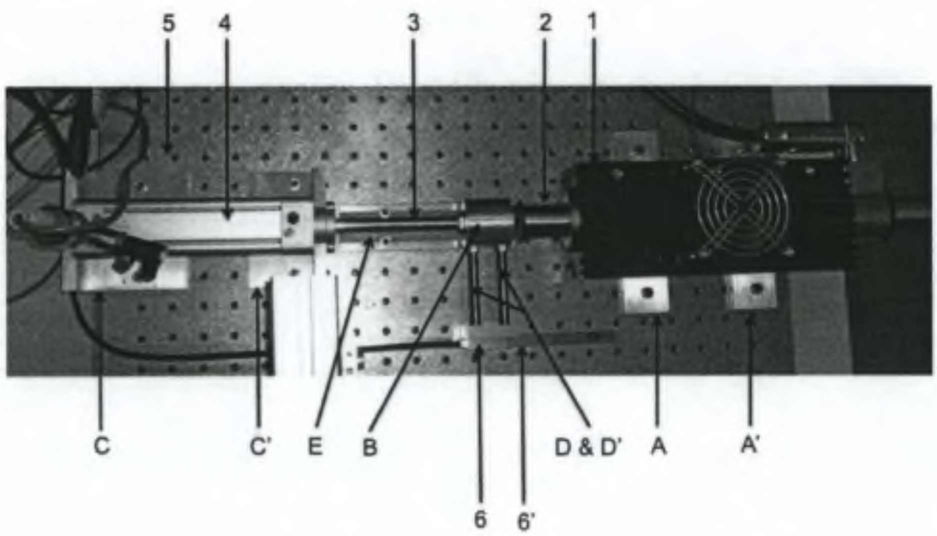

Figure 3.8: Top view of the test bench: 1) linear motor + flange + fan 2) slider of the linear motor 3) piston of the pneumatic cylinder 4) pneumatic cylinder 5) test bench board 6) external position sensor 6') magnetic strip A&A') mounting parts of the linear motor B) linking part between the slider and the piston C&C') mounting parts of the cylinder D&D') linking parts between the external position sensor and part B. E) Teflon part on which part B slides to avoid the rotation of the slider.

3.5.4 Connections between the motor controller, the motor fan and the different power supplies

Fig. A.32 in Appendix A.5 explains how the controller of the linear motor has to be connected; it is connected to two power supplies: the linear motor supply (72 VDC) and the logic supply (24 VDC). The 24 VDC logic supply was not provided with the linear motor. Hence, a 24 VDC power supply has been bought and its main characteristics are summarized in Table A.1, in Section A.5. Following the explanations of Fig. A.32, the connections between the controller, the 72 VDC motor supply, the 24 VDC logic supply, the fan and its supply have been made as shown in Fig. 3.9. The main characteristics of the fan supply (this supply was neither provided with the linear motor and has been bought separately) are summarized in Table A.2, in Section A.5.

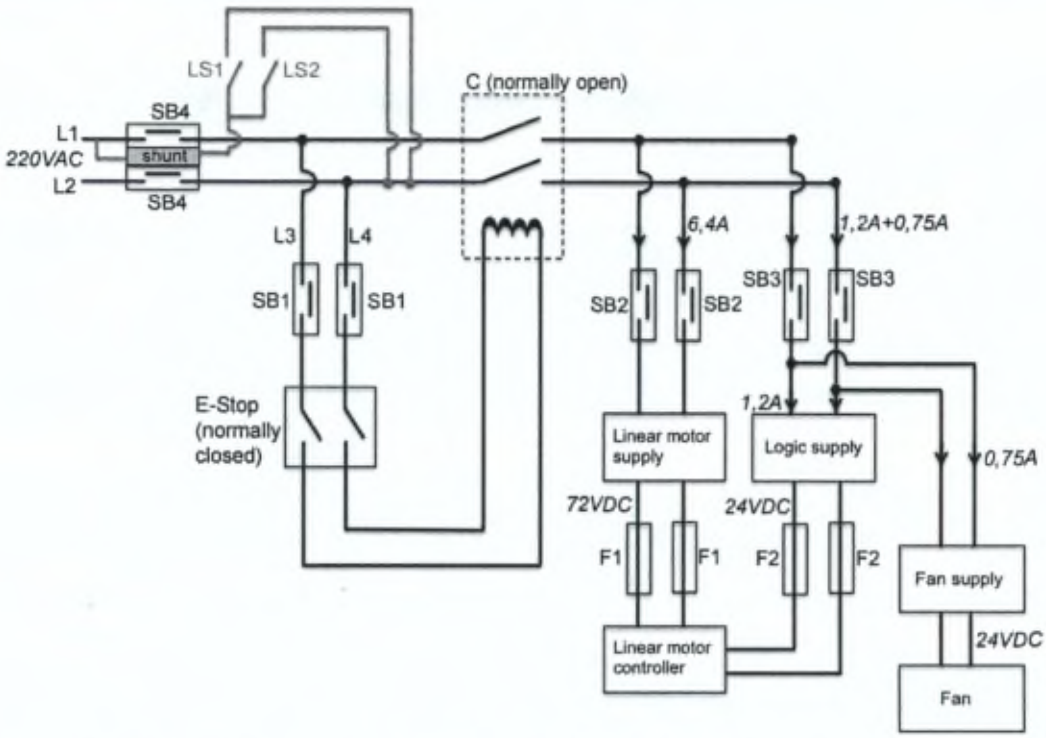

Figure 3.9: Connections between the controller, the 72 VDC motor supply, the 24 VDC logic supply, the fan and its supply. "F", "SB", "L", "C" and "LS" stand for "fuse", "switching break", "line", "contactor" and "limit switch", respectively.

As can be seen, the circuit of Fig. 3.9 presents fuses ("F" in Fig. 3.9), switching breaks ("SB" in Fig. 3.9), limit switches ("LS" in Fig. 3.9), a contactor ("C" in Fig. 3.9), a shunt and an E-stop button.
The E-Stop button allows to shut down the circuit when it is pressed (i.e. the current is switched off). As for the limit switches, they have been installed on the test bench because they can help to increase the safety of operation of the linear motor. Indeed, as the motor has a much larger stroke than the pneumatic cylinder, the limit switches can be used to shut down the motor supply when the displacement of the motor slider risks exceeding the cylinder stroke.
Fig. 3.10 presents the practical implementation of the circuit of Fig. 3.9. As can be observed, except the E-Stop button and the limit switches, all the components presented in this section are installed on two DIN rails, which are fixed to a gantry made of MiniTec parts (see Section A.3 for a short description of the MiniTec parts). Concerning the fuses, they are inserted in fuse holders that are fixed to the DIN rails.

More information about the circuit, its design and its components is available in Section A.5, as well as two summarizing tables (see Tables A.3 and A.4) presenting the main characteristics of the circuit components.

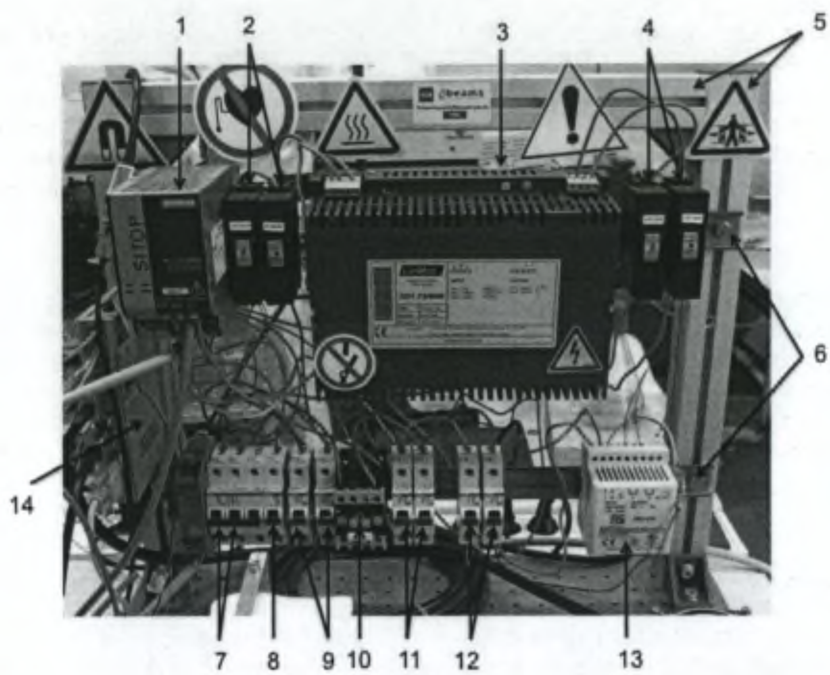

Figure 3.10: Picture of the test bench: the linear motor supply, the logic supply and the fan supply, the linear motor controller, the fuses, the switching breaks, the shunt and the contactor are installed on two DIN rails. The DIN rails are fixed to a gantry made of MiniTec parts. 1) logic supply 2) fuses F + fuse holders 3) motor supply 4) fuses F + fuse holders 5) MiniTec parts 6) two DIN rails 7) switching breaks SB4 8) shunt (bond to the SB4 switching breaks) 9) switching breaks SB 10) contactor C 11) switching breaks SB 12) switching breaks SB 13) fan supply 14) linear motor controller

Remark: In practice, the limit switches have not been used a lot. Indeed, the user-friendly program "Linmot-Talk", that enables to control the motor, allows to program the slider motion in different ways. For example, it is possible to specify a start position and an end position for the slider and to specify the velocity and acceleration of the slider when it moves between both positions. If the start and end positions are chosen so that the slider displacement does not exceed the cylinder stroke, the limit switches become superfluous.

3.5.5 Sensors

To characterize a flexible fluidic actuator, four parameters are measured for each measurement point:

1. The volume of fluid supplied to the actuator. As explained before, this volume will be considered to be the volume swept by the piston of a syringe-pump connected to the actuator. Hence, this volume is proportional to the displacement of the cylinder piston u (it is equal to the displacement of the motor slider) and in practice, the piston displacement is the variable that will be used instead of the swept volume. It is imposed by the linear motor which is equipped with a position controller and it is measured by the external position sensor of the linear motor.
   Remark: The piston displacement u is equal to the piston position with respect to the

position for which the volume of the cylinder chamber is maximum.

2. The vertical force F developed by the flexible fluidic actuator. It is measured by hanging given weights from the tip of the flexible fluidic actuator. The gravitational force of the weight corresponds to the vertical force developed upwards by the actuator.

3. The vertical displacement Δy of the actuator tip. It is measured by a camera or a laser sensor.

4. The relative pressure p inside the flexible fluidic actuator. It is measured by pressure sensors. For static measurements (i.e. all parameters are stabilized before a measurement is taken), it is assumed that the pressure is uniform in the fluidic circuit.

The measurements are made as follows:

1. The motor imposes a given displacement u_1 to the cylinder piston.

2. No external load is applied to the actuator. The pressure p and the displacement Δy are measured: their values are p_1 and Δy_1, respectively.

3. The piston position is kept constant and a given weight w is attached to the actuator tip (the corresponding force is F_2). Consequently, the pressure increases and the vertical displacement decreases. Their values are measured and are p_2 (with $p_2 > p_1$) and Δy_2 (with $\Delta y_2 < \Delta y_1$), respectively.

These three steps are then repeated for each measurement point.

A) Measurement of the piston displacement u

The piston displacement u is measured by the external position sensor of the linear motor. This sensor has a resolution of 0.001 mm and an accuracy of $\pm$ 0.01 mm/m (see Fig. A.14 and A.15, in Section A.2.3). The measurement of the sensor can be read on the control panel of the user-friendly software "Linmot-talk", which allows to control the motion of the motor. With this sensor, the motor is able to position its slider (and thus the cylinder piston) with a repeatability of $\pm$ 0.01 mm and a linearity of $\pm$ 0.01 mm (see Table 3.4, in Section 3.5.3). The volume swept by the piston is computed by multiplying the displacement of the cylinder piston by its cross-section (diameter of the cross-section = 32 mm). Hence, the accuracy of $\pm$ 0.01 mm/m on the measurement of the piston displacement involves an accuracy of $\pm$ 0.01 ml/l on the measurement of the swept volume. Besides, since the displacement of the cylinder piston can be imposed with an accuracy of $\pm$ 0.02 mm (repeatability + linearity), the swept volume can be imposed with an accuracy of $\pm$ 0.0161 ml.

B) Measurement of the actuator tip displacement Δy

The tip displacement Δy of the PBAs is measured with a Keyence camera (CV-551 controller + CV-050 camera). The controller screen presents 512 $\times$ 480 pixels (i.e. more than 240000 pixels).
The tip displacement Δy of the miniaturized PPAMs is measured with a laser sensor Keyence LC-2440. This sensor has a measurement range of $\pm$ 3 mm, a resolution of 0.2 µm and a linearity of $\pm$ 0.05%.

C) Measurement of the force F developed by the actuator

The force F developed by the flexible fluidic actuator is measured by hanging given weights at the tip of the actuator. The gravitational force of the weight corresponds to the vertical force developed upwards by the actuator.

To load the flexible fluidic actuators, KERN [13] precision weights of class M1 have been used. Some of these weights present a slot (see Fig. 3.11) and can be placed on a 10 g hook (see Fig. 3.12). The other weights (see Fig. 3.13) are already equipped with a hook. Table 3.6 presents the KERN weights and the tolerance on their values.
Dumbbell weights have also been used when heavier weights than the available KERN weights were necessary.

Figure 3.11: Picture of the KERN 10 g hook and of the KERN weights presenting a slot. These weights have been used to load the flexible fluidic actuators.

Figure 3.12: Picture of the KERN 10 g hook loaded with KERN weights presenting a slot. These weights have been used to load the flexible fluidic actuators.

Figure 3.13: Picture of the KERN weights equipped with a hook. These weights have been used to load the flexible fluidic actuators.

KERN Weight	Tolerance on the weight value
Slot weights	
1 g	± 1 mg
2 g	± 1.2 mg
5 g	± 1.6 mg
10 g	± 2 mg
20 g	± 2.5 mg
50 g	± 3 mg
100 g	± 5 mg
Hook weights	
1 g	± 1 mg
2 g	± 1.2 mg
5 g	± 1.6 mg
10 g hook	± 1.33 mg

Table 3.6: KERN weights (and the tolerance on their values) used to load the flexible fluidic actuators.

D) Measurement of the relative pressure p inside the flexible fluidic actuator

To measure the pressure inside the PBAs and the miniaturized PPAMs, different pressure sensors are used. Indeed, as explained in Section 3.2.3, these two kinds of actuators present different pressure ranges: up to 60 kPa for the PBAs and up to 667 kPa for the miniaturized PAMs, according to Table 3.1.
Hence, two relative pressure sensors presenting ranges of $0-1$ bar and of $0-6$ bar have been used for the PBAs and for the miniaturized PPAMs, respectively.
The $0-1$ bar relative pressure sensor presents the features summarized in Table 3.7. The cumulated error of this sensor has been computed on the basis of the sensor certificate of calibration. This cumulated error takes into account the accuracy, the span tolerance, the supply voltage sensitivity and equals maximum ± 0.6 % of the measured pressure value.

$0-1$ *bar* relative pressure sensor	
brand	GEMS
type	2200 R G A10 01 D 3 D B
pressure range	$0-1$ bar
zero tolerance	1 % FS[1]
pressure port	G1/4 male
response time	0.5 ms
cumulated error	max ± 0.6 % of the measured pressure value

Table 3.7: Characteristics of the $0-1$ bar relative pressure sensor

The $0-6$ bar relative pressure sensor presents the features summarized in Table 3.9. Its accuracy equals maximum ± 0.25% FS, i.e. ± 0.015 bar.
To measure the pressure inside the PBAs, a differential pressure sensor is used in addition to the $0-1$ bar relative pressure sensor. While the relative pressure sensor is used to measure the actuator pressure corresponding to a given piston position, the differential pressure sensor is used to measure the pressure variation involved when a weight is hung to the actuator tip, for a given piston position. Indeed, it has been experimentally noticed that these pressure variations are to small to be measured by the relative pressure sensor.
The differential pressure sensor has a measurement range of 1000 Pa and presents the characteristics summarized in Table 3.8. Because the fluidic circuit presents small air leakages, the pressure variation involved when attaching a weight at the PBA free end, is measured by measuring the jump that the signal of the differential pressure sensor makes when the

weight is hung. The pressure variation is thus a difference between two measurements made by the differential pressure sensor. The non-linearity and the hysteresis of the sensor both are $\leq \pm 0.10$ % FS, i.e. $\leq \pm 1$ Pa. The cumulated error on one measurement is thus $\leq \pm 0.20$ % FS, i.e. $\leq \pm 2$ Pa. Since the pressure variation will be determined by doing the difference between two measurements, the cumulated error on the pressure variation is $\leq \pm 0.40$ % FS, i.e. $\leq \pm 4$ Pa.

1000 Pa differential pressure sensor	
brand	IMPRESS sensors and systems
type	DPS 100 differential pressure transmitter 200-0100-2-3-B -Y00-1
pressure range	$0 - 1000$ Pa
non-linearity (BFSL)	$\leq \pm 0.10$ % FS
hysteresis	$\leq \pm 0.10$ % FS
pressure ports	11 mm × 6.6 mm OD for flex. tube with an $ID = 6$ mm OD=outer diameter ID=inner diameter
response time	T_{90} approx 0.02 s
cumulated error	$\leq \pm 0.40$ % FS

Table 3.8: Characteristics of the 1000 Pa differential pressure sensor

$0 - 6$ bar relative pressure sensor	
brand	Druck
type	PMP 1400
pressure range	$0 - 6$ bar
accuracy (combined non-linearity, hysteresis and repeatability) Best straight line definition	max ± 0.25% FS
zero tolerance	± 0.5% FS
pressure port	G1/4 female
response time	/ (not specified)

Table 3.9: Characteristics of the $0 - 6$ bar relative pressure sensor

The measurements of the relative and differential pressure sensors are acquired by the NI PXI platform at a sampling rate $f_{sampling}$. Hence, anti-aliasing filters have been designed to avoid the aliasing of the acquired signals due to the sampling of the data. Indeed, according to the Shannon theorem, if a sampling rate $f_{sampling}$ is used, all the acquired signals having a frequency larger than $f_{sampling}/2$ will be aliased. To avoid this phenomenon, the sampling rate $f_{sampling}$ must verify the following condition:

$$f_{sampling} > 2f_{max} \tag{3.14}$$

where f_{max} is the maximum frequency of the acquired signal. In practice, the following condition is applied:

$$f_{sampling} \geq 10 f_{max} \tag{3.15}$$

Since, it has been chosen to acquire the measurements with a sampling rate of 10 kHz, the maximum frequency of the acquired signal must verify the following condition:

$$1\ kHz \geq f_{max} \tag{3.16}$$

To fulfill this condition, anti-aliasing filters presenting a cutoff frequency of 1 kHz have been designed and the measurements of the pressure sensors pass through these filters before being acquired by the NI PXI platform. The electronic circuit of these filters is presented in Fig. 3.14:

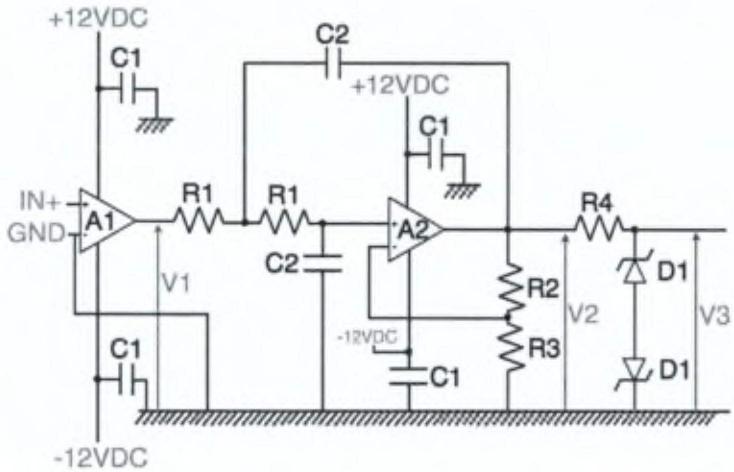

Figure 3.14: Electronic circuit of the anti-aliasing filters

This circuit is composed of:

- an instrumentation amplifier (component A1 in Fig. 3.14): it computes the difference between the two input signals. The gain of this amplifier equals 1. This amplifier has been added to the circuit in order to have an anti-aliasing filter that could be used for floating sensors as well as for referenced sensors. Indeed, this amplifier offers a differential input to the circuit.
  In practice, all the sensors of the test bench are referenced sensors whose reference is the same as the reference of the rest of the circuit. "IN+" and "GND" are the measurement signal of the sensor and the reference of the circuit, respectively.
- a second order Butterworth low-pass filter (= components located between voltages V1 and V2, A2 is an operational amplifier). Strictly speaking, this filter is the anti-aliasing filter. It has been designed so that its cutoff frequency equals 1 kHz. Its gain equals 1.586.
- two Zener diodes (components D1 in Fig. 3.14): they insure that the voltage V3, which is acquired by the NI PXI platform, stays in the range allowed by this platform, i.e. between -10 V and $+10$ V.
- decoupling capacitors (components C1 in Fig. 3.14): they help to stabilize the supply voltages. Indeed, by providing their discharge current, they avoid that an inrush current involves a voltage drop on the supply voltage lines.

More details about the following points are given in Section A.6.

- the components of these anti-aliasing circuits (see Table A.5)
- the manufacturing of the electronic cards
- the connections between the pressure sensors, the NI PXI platform, the supplies, the anti-aliasing filters and other components

3.6 Conclusions

A test bench has been developed to characterize flexible fluidic actuators and to study the PVFP principle. This test bench presents the following features:

- it allows **to characterize two specific kinds of actuators: the PBAs and the miniaturized PPAMs**. However, this test bench can be used to study **other flexible fluidic actuators**, as can be deduced from the comparison of the summarizing tables of the literature review (see Tables 2.1 and 2.2) and of the table presenting the application cases used to design the test bench (see Table 3.1).
- it is able **to maintain the pressurization states of the studied actuator**.
- it is able **to dynamically pressurize the studied actuator at a frequency up to** 10 Hz.
- it is equipped with a measurement and control platform that can be used **to control the displacement and the developed force of the studied actuator**.
- it allows **to measure the pressure inside the studied actuator**. The study of the application cases (see Table 3.1) foresees pressure ranges of $0 - 60$ kPa and $0 - 667$ kPa for the PBAs and the miniaturized PPAMs, respectively. Pressure sensors have been chosen accordingly and Table 3.10 presents the measurement ranges and accuracies of these sensors.

Sensor range and type	Accuracy
$0-1$ bar relative pressure sensor	$\pm$ 0.6 % of the measured pressure value
$0-6$ bar relative pressure sensor	$\pm$ 0.015 bar
1000 Pa differential pressure sensor	$\leq \pm 4$ Pa

Table 3.10: Measurement ranges and accuracies of the test bench pressure sensors

- it allows **to measure the cylinder piston displacement and the volume swept by the cylinder piston**. The test bench is able to measure the piston displacement u with an accuracy of $\pm$ 0.01 mm/m. Besides, it allows to impose the piston displacement u with an accuracy of $\pm$ 0.02 mm (repeatability + linearity). The test bench is able to measure the swept volume with an accuracy of $\pm$ 0.01 ml/l. Besides, it allows to impose the swept volume with an accuracy of $\pm$ 0.0161 ml.
- it allows **to measure the force developed by the studied actuator**. To do so, calibrated weights are hung at the tip of the actuator.
- it allows **to measure the displacement of the studied actuator**. To do so, a camera or a laser sensor is used.

The test bench is built as a syringe-pump whose fluidic circuit (i.e. the chamber of the cylinder, the fluidic tubes and the flexible fluidic actuator) is closed. This actuation principle can be used to pressurize pneumatic actuators with gas but also hydraulic actuators with liquid. In practice, the linear motor can be used for all the fluids while the cylinder and the pressure sensors have to be compatible with the used fluid. If they are not, it will be necessary to replace them by compatible components.

Chapter 4

Study of the PVFP principle and of the Pneumatic Balloon Actuators: Test bench particularities

4.1 Introduction

As explained before, a simple flexible fluidic actuator was necessary to investigate the PVFP principle. Therefore, an actuator having one DOF, a simple design and which is easily manufactured was looked for among the actuators listed in the review of the literature (see Section 2.4). The actuator that has finally been chosen is the "Pneumatic Balloon Actuator" (PBA, see Section 2.4.3 and [50]).

Section 4.2.1 briefly describes the original PBA developed by [50], while Section 4.2.2 presents the PBAs manufactured for the test bench. Afterwards, the particularities of the test bench linked to the study of the PBAs are presented in Section 4.3.

4.2 The Pneumatic Balloon Actuators

4.2.1 Short description of the original Pneumatic Balloon Actuator

Fig. 4.1 presents the "Pneumatic Balloon Actuator" (PBA) invented by S. Konishi et al. [50]. This device is fixed as a cantilever and comprises two square-shaped flexible films. The upper one acts as a membrane and is a silicone rubber film while the lower one plays the role of a substrate and is a polyimide film. These films are glued to one another along their surrounding edge with a silicone rubber glue and this configuration forms a cavity. When pressurized air is introduced in this cavity, the silicone rubber film inflates without supporting any bending load (like a membrane). On the other hand, the polyimide film bends due to the moment produced by the tensile forces in the membrane. This behaviour results in a large out-of-plane vertical displacement (i.e. in the y-direction) and in a horizontal displacement (i.e. in the x-direction) of the free end of the actuator. In Fig. 4.1, one can notice the presence of silicon ribs glued below the polyimide film. They aim at preventing an unwanted swelling of the substrate and at forcing the device to bend around the ribs z-axis, in order to avoid an unwanted corner folding.

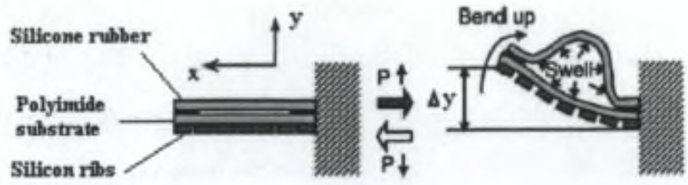

Figure 4.1: Working principle of a Pneumatic Balloon Actuator (PBA): PBA at rest and pressurized PBA on the left hand side and the right hand side, respectively. When the PBA is pressurized (i.e. the pressure P is increased), its free end moves upwards. Figure adapted from [50].

In conclusion, a PBA is an actuator presenting a cavity formed by two square-shaped flexible films of different rigidities and fastened to each other along their surrounding edge.

4.2.2 Manufacturing of Pneumatic Balloon Actuators for the test bench

As explained in Section 4.2.1, a PBA can be obtained by simply gluing two plastic squares of different rigidities along their surrounding edges, in order to form a cavity. Since this manufacturing process seemed very easy, it was decided to try developing home-made PBAs. Three methods, presented in Section B.1, have been tested: gluing the films, welding the films and moulding a PBA in latex. However, as each of these methods presented disadvantages, it has been eventually decided to look for a company to produce the PBAs. The chosen company is PRONAL [20], which is specialized in the design and manufacturing of flexible structures.

PBAs with a 40 mm × 40 mm cavity have been ordered (see Fig. 4.2).

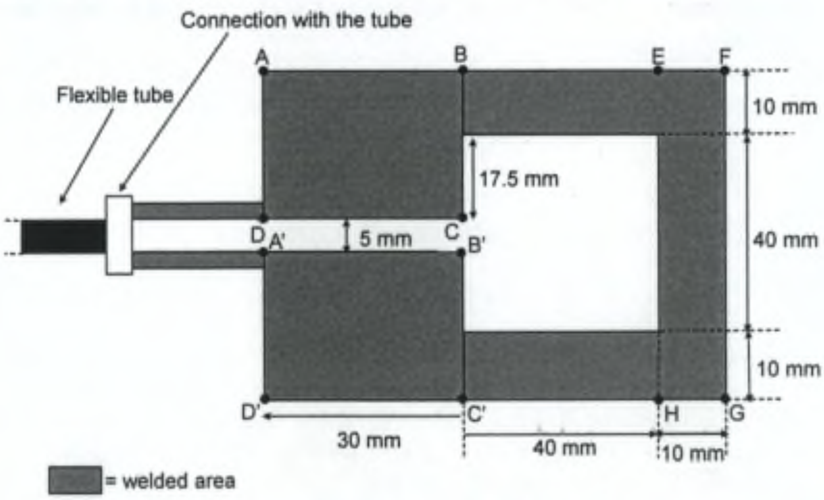

Figure 4.2: Drawing of the PBA to be manufactured by the PRONAL company. The dimensions of the cavity are 40 mm × 40 mm.

The PBAs manufactured by PRONAL are made of Polyurethane (PU), which is an elastomer. An elastomer is necessary for its elasticity, so that the films deform elastically when the PBA is pressurized and they regain their initial shape when the pressure decreases. The PBAs are obtained by fastening two layers of PU to each other by a high frequency welding

method. To have different rigidities for the two PU layers, different thicknesses have been used. Hence, the lower layer has a thickness of 1 mm and is more rigid than the upper one, which has a thickness of 0.5 mm.
The PBA should not be pressurized above $0.2 - 0.3$ bar to avoid leakages but also to avoid the plastic deformation of the polyurethane.
A flexible tube is welded to the PBA and the end of the tube is equipped with a standard pneumatic connection. The rectangles $ABCD$ and $A'B'C'D'$ (see Fig. 4.2) are aimed at being clamped to fix the PBA as a cantilever. The rectangle $EFGH$ (see Fig. 4.2) foresees room at the extremity of the PBA to hang weights for the characterization tests.
The PBAs developed by PRONAL are shown in Fig. B.7, in Appendix B.2.

Remark 1: A PBA made of two layers of the same material has a different behaviour than a PBA whose layers are of two different materials [51]. For PBAs made of only one material, when the pressure increases, their free end lifts until some pressure is reached, it then goes down when the pressure is increased further. The PBAs developed by PRONAL are entirely made of the same material and risk presenting this behaviour. However, only the lifting stage will be studied here.
Remark 2: If the PBA is placed between two plates instead of being fixed as a cantilever, it can be pressurized at pressures up to 0.5 bar, according to PRONAL.
Remark 3: PU is non-porous to air.

Fig. 4.3 presents the mounting parts used to fix the PBAs as cantilevers.

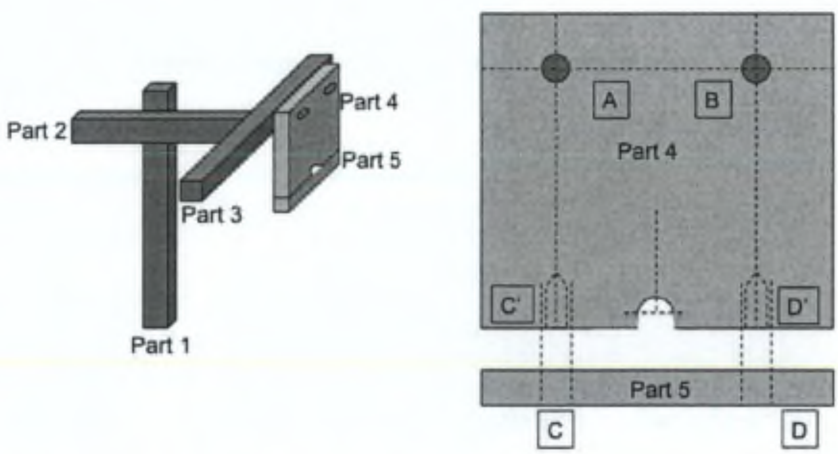

Figure 4.3: Drawings of the mounting parts used to fix the PBAs as cantilevers: the rectangles $ABCD$ and $A'B'C'D'$ of the PBA (see Fig. 4.2) are clamped between parts 4 and 5 so that the PBA is fixed as a cantilever.

Parts 1, 2 and 3 are MiniTec profiles (see Section A.3). They are assembled together with screws, nuts and squares. Part 4 is fixed to part 3 with screws, placed in the holes A and B, and with nuts. The rectangles $ABCD$ and $A'B'C'D'$ of the PBA (see Fig. 4.2) are clamped between parts 4 and 5 so that the PBA is fixed as a cantilever. Parts 4 and 5 are assembled together with screws placed in the holes C and D and in the threads C' and D'. The mounting parts allow to modify the position of the PBA in the x-, y- and z-directions.

4.3 Sensors and measurements

A PBA having a cavity of 40 mm × 40 mm is fixed as a cantilever between the parts 4 and 5 described in Section 4.2.2. The PBA is placed so that its upper layer is the thinner one. Fig. 4.4 presents a schematic view of the pressurized PBA and shows the convention chosen for the x- and y-axes. Δy and Δx are the vertical and horizontal displacements of the free end A of the PBA.

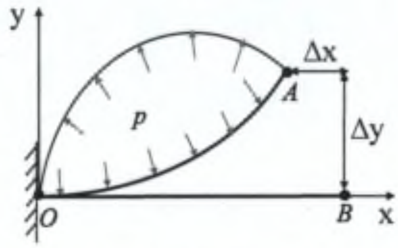

Figure 4.4: Cross-section of a pressurized PBA. The PBA is fixed as a cantilever so that its upper layer is the thinner one of its two layers. This figure shows the convention chosen for the x- and y-axes. Δy and Δx are the vertical and horizontal displacements of the free end A of the PBA.

As explained in Section 3.5.5, two different pressure sensors are used to measure the pressure inside the PBAs:

- a $0-1$ bar relative pressure sensor, whose characteristics are summarized in Table 3.7. This sensor is used to measure the actuator pressure corresponding to a given piston position.
- a $0-10$ mbar differential pressure sensor, whose characteristics are summarized in Table 3.8. This sensor is used to measure the pressure variation involved when a weight is hung to the actuator tip, for a given piston position. Indeed, it has been experimentally noticed that these pressure variations are to small to be measured by the $0-1$ bar relative pressure sensor.

The relative and differential pressure sensors are integrated into the fluidic circuit presented in Fig. 4.5. This circuit is composed of the pneumatic cylinder chamber, the flexible fluidic actuator to be studied, the pressure sensors, a solenoid valve and the fittings and tubes connecting all these components. More details about the fluidic circuit components are available in Appendix B.3.

The solenoid valve is a 2/2-way valve presenting two pressure ports; when it is open/closed, the ports are/are not connected. The solenoid valve is normally closed. This means that when it is not powered, it is closed. On the other hand, as soon as power is supplied, it commutes and opens itself. To control the closing/opening of the valve with the NI PXI platform (see Section 3.5.2), an electronic circuit has been built and it is presented in Appendix B.3.

It is assumed that the pressure is uniform in the fluidic circuit and the pressure sensors and the solenoid valve are used as follows to measure the pressure inside the PBA:

1. The solenoid valve is open and the motor moves the cylinder piston to a given position u.

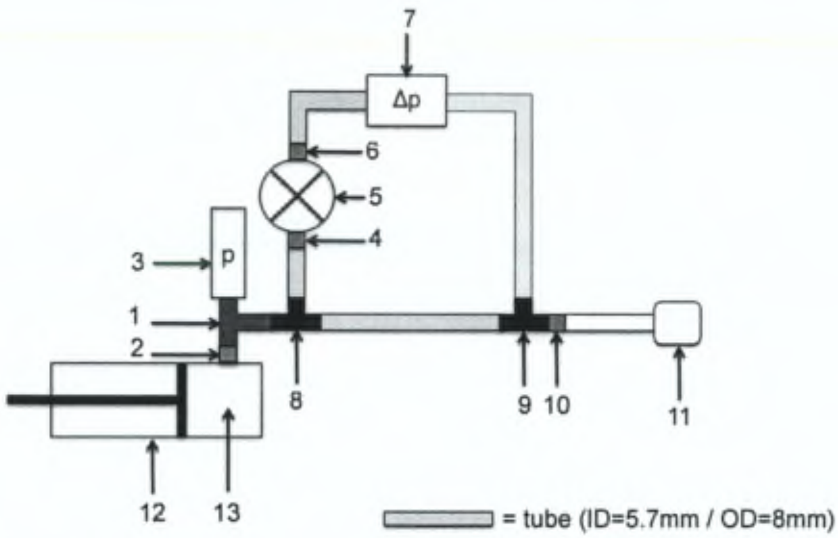

Figure 4.5: Fluidic circuit implemented to study the PBAs: 1), 2), 4), 6), 8), 9) and 10) are different kinds of fittings. 3) relative pressure sensor 5) solenoid valve 7) differential pressure sensor 11) PBA 12) pneumatic cylinder 13) pneumatic cylinder chamber. The light grey areas represent the tubes used to link the circuit components: ID=inner diameter and OD=outer diameter. All the fittings are equipped with seals.

2. No external load is applied to the PBA. The pressure p of the fluidic circuit is measured, once it is stabilized, with the relative pressure sensor. Indeed, as will be explained later, the pressure p needs some time to establish itself and to become constant.

3. The piston position u is kept constant and the solenoid valve is closed. A quantity of air at pressure p is thus trapped in the tube placed between the solenoid valve and the differential pressure sensor. A given weight is then hung to the actuator tip. Consequently, the pressure increases in the fluidic circuit (apart from the tube between the solenoid valve and the differential pressure sensor which stays at pressure p) and takes the value $p + \Delta p$. The pressure ports of the differential pressure sensor are thus at pressures p and $p + \Delta p$ and the pressure variation Δp is measured by this pressure sensor.

Hence, for a given piston position and a given weight attached to the actuator, the pressure $p + \Delta p$ of the fluidic circuit is obtained by adding the measurements of the relative and differential pressure sensors.

The X- and Y-displacements of the actuator tip Δx and Δy are measured thanks to the Keyence camera (see Section 3.5.5). A small black ball (diameter = 3 mm) is fixed at the actuator tip at 5 mm of the cavity and the position of the ball center is measured by the camera. Indeed, the camera can be programmed in order to find a given pattern in the window frame and to measure its position. Prior to making measurements with the camera, the latter needs to be calibrated in order to establish the pixels-millimeters relationship. This is done by visualizing a rectangle of graph paper in the plane where the ball placed at the actuator tip moves.

The measurements are thus made as follows:

1. The solenoid valve is open and the motor moves the cylinder piston to a given position

u.

2. No external load is applied to the PBA; the pressure p of the fluidic circuit is measured, once it is stabilized, with the relative pressure sensor and the displacements Δx_0 and Δy_0 of the actuator tip are measured with the camera.

3. The piston position u is kept constant and the solenoid valve is closed. A given weight w is then hung to the actuator tip. Consequently, the pressure increases in the fluidic circuit (apart from the tube between the solenoid valve and the differential pressure sensor which stays at pressure p) and takes the value $p + \Delta p$. The pressure variation Δp is measured by the differential pressure sensor. On the other hand, the actuator tip moves downwards and its displacements Δx and Δy are measured with the camera. The weight is then removed.

These three steps are then repeated for all the measurement points.

Remark: In practice, if the linear motor is asked to perform a given piston displacement u^*, it will perform a displacement u' close to u^* but not equal to u^*. The difference between u^* and u' can be as large as 1 mm; this differs from the positioning accuracy foreseen by the datasheets of the motor (see Section 3.5.5). Hence, in the measurements taken during the experiments, u is the piston displacement u' performed in practice and not the asked value u^*. u' is measured with the external position sensor of the motor and its measurement can be read on the control panel of the user-friendly software "Linmot-talk" (which allows to control the motion of the motor) with an accuracy of $\pm$ 0.01 mm.

The errors on the measurements are summarized in Table 4.1.

Variable	Error on the measurement of the variable
piston displacement u	$\pm$ 0.01 mm
weight w	$\leq \pm$ 0.1 % of the weight (see Table 3.6, the larger error ($\pm$ 0.1 % of the weight) corresponds to the tolerance on the 1 g weight)
pressure p	$\leq \pm 0.6$ % of the measured value
pressure variation Δp	$\leq \pm 4$ Pa
X- and Y- displacements Δx_0, Δy_0, Δx, and Δy	± 0.13 mm

Table 4.1: Errors on the measurements

Although the test bench has been set up with a lot of care, it presents some air leakages. Between the beginning and the end of a set of experiments, the maximum drop that has noticed on the pressure p for a given piston displacement is 0.55 kPa. Hence, before performing a new set of experiments with the test bench, it is refilled with air at atmospheric pressure.

Chapter 5

The PVFP principle

5.1 Introduction

5.1.1 Understanding the PVFP principle with a simple flexible fluidic actuator

As explained before, a flexible fluidic actuator called "the Flexible Microactuator" is presented in [79] and it is suggested that the measurements of the fluid pressure and of the volume of supplied fluid allow to determine and control the position of the actuator and the force it develops. This property, that is referred to as the "Pressure-Volume-Force-Position principle" or "PVFP principle", means being able to determine the displacement of a flexible fluidic actuator and the force it develops without using a displacement sensor or a force sensor [79].

To better understand this principle, let us consider the simple flexible fluidic actuator presented in the left hand side of Fig. 5.1. It is composed of a cylinder whose top is closed by a flexible membrane. The cylinder has a length d and a circular section S of radius R; $S = \pi R^2$. The atmospheric pressure is assumed to be constant and known and the pressure is assumed to be constant.
The outside absolute pressure p_{out} equals the atmospheric pressure p_{atm} and initially, the inner absolute pressure p_{in} is such that $p_{in} = p_{out} = p_{atm}$. When a displacement u is imposed to the piston, the inner pressure p_{in} increases and the membrane deforms and takes the shape of a spherical cap of radius r (see the right hand side of Fig. 5.1). The volume of the spherical cap V_{cap} is completely determined by its radius r and is computed as follows:

$$V_{cap}(r) = \frac{2\pi r^3}{3}\left[1 - \frac{3}{2}(1 - \frac{R^2}{r^2})^{\frac{1}{2}} + \frac{1}{2}(1 - \frac{R^2}{r^2})^{\frac{3}{2}}\right] \tag{5.1}$$

If Poisson's effect is neglected, the membrane surface tension γ is also completely determined by the membrane radius r and is calculated with the following equations:

$$\gamma = \sigma e \tag{5.2}$$

$$\sigma = E_m \frac{\Delta L}{L} \tag{5.3}$$

$$\Delta L = 2r \ \arcsin(\frac{R}{r}) - 2R \tag{5.4}$$

where σ are the stresses in the membrane, e is the membrane thickness, E_m is the membrane Young's modulus, ΔL is the lengthening of the initial membrane length $L = 2R$.

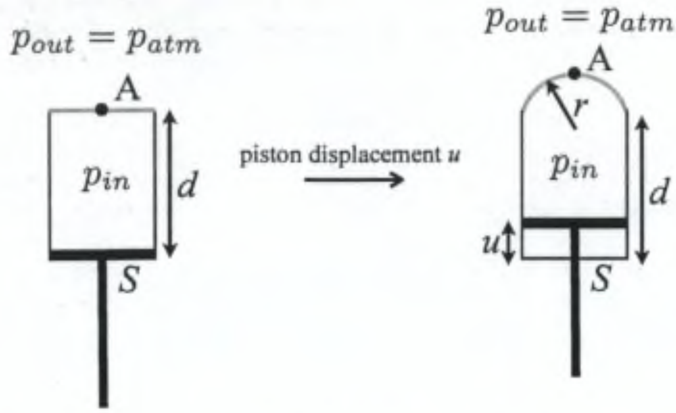

Figure 5.1: Flexible fluidic actuator composed of a cylinder whose top is closed by a flexible membrane. When a displacement u is imposed to the piston, the inner pressure p_{in} increases and the membrane deforms and takes the shape of a spherical cap of radius r. According to the PVFP principle, knowing the values of p_{in} and u allows to determine the vertical displacement of point A and the external pressure p_{ext} applied to the membrane in addition to the atmospheric pressure p_{atm} (see Fig. 5.2).

The volume of fluid supplied to the actuator is considered to be the volume swept by the piston during its displacement; this swept volume is proportional to the piston displacement u and equals Su. Therefore, the piston displacement u will be the variable used for the PVFP principle rather than the swept volume.
According to the PVFP principle, knowing the values of p_{in} and u allows to determine the displacement of the flexible fluidic actuator and the force it develops. For the actuator considered here, the vertical displacement of point A (see Fig 5.1) will be determined and instead of the force developed by the actuator it is the external pressure p_{ext} applied to the membrane (in addition to the atmospheric pressure p_{atm} (see Fig. 5.2)) that will be determined.

First, no external pressure is applied to the membrane and the configuration is that of the right hand side of Fig. 5.1; two cases can be considered:

1. The actuation fluid is incompressible. In this case, the cylinder is initially filled with a volume $V = Sd$ of fluid. When a displacement u is imposed to the piston, the volume of fluid in the cylinder becomes $V' = S(d-u)$ and the volume of the spherical cap equals $V_{cap}(r) = V - V'$. Knowing V_{cap}, equation (5.1) allows to determine the corresponding radius r and knowing r, the vertical displacement of point A can be determined.
   Since r is known, $\gamma(r)$ can be computed with equations (5.2) to (5.4). Concerning the inner pressure p_{in}, it is linked to the outside pressure p_{out}, the membrane radius r and the membrane surface tension γ by the Laplace's equation:
   $$p_{in} - p_{out} = \frac{2\gamma}{r} \tag{5.5}$$
   Since the values of r and γ are known, if the inner pressure p_{in} is measured, the Laplace's equation allows to determine the outside pressure p_{out}. It is thus discovered that $p_{out} = p_{atm}$ and it is deduced that there is no external pressure applied to the membrane.

2. The actuation fluid is compressible. In this case, the cylinder is initially filled with a volume $V = Sd$ of fluid at atmospheric pressure p_{atm}. When a displacement u is

imposed to the piston, the volume of fluid in the cylinder becomes $V' = S(d-u)$. If the pressure p_{in} is measured, r and p_{out} can be determined by the following two equations:

$$p_{atm} S d = p_{in}(V_{cap}(r) + S(d-u)) \tag{5.6}$$

$$p_{out} = p_{in} - \frac{2\gamma(r)}{r} \tag{5.7}$$

Equation (5.7) is the Laplace's equation while equation (5.6) is the gas law applied to the system whose fluid quantity is constant and assuming that the temperature is constant.
Knowing the value of r, the vertical displacement of point A can be determined and from the value of p_{out}, it can be deduced that there is no external pressure applied to the membrane.

As can be seen, when the membrane is not loaded by an external pressure p_{ext}, the knowledge of the piston displacement u and of the pressure p_{in} allows to determine the displacement of the actuator and to establish that the actuator is not loaded.

Keeping the piston position constant, if an external load is applied to the membrane in the form of an external pressure p_{ext}, the inner pressure p_{in} increases and the radius r of the spherical cap decreases, as represented in Fig. 5.2.

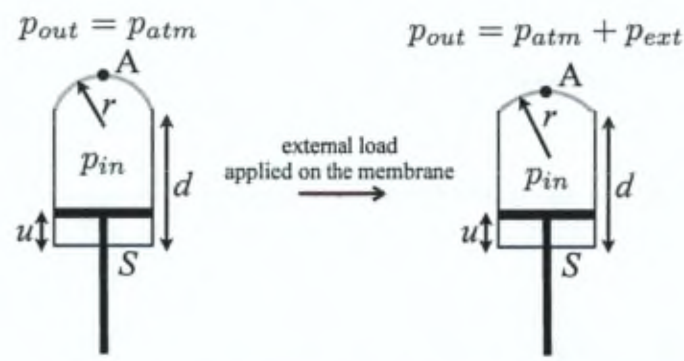

Figure 5.2: Flexible fluidic actuator composed of a cylinder whose top is closed by a flexible membrane. When a displacement u is imposed to the piston, the inner pressure p_{in} increases and the membrane deforms and takes the shape of a spherical cap of radius r. Afterwards, keeping the piston position constant, if an external pressure p_{ext} is applied to the membrane in addition to the atmospheric pressure p_{atm}, the inner pressure p_{in} increases and the radius r of the spherical cap decreases. According to the PVFP principle, knowing the values of p_{in} and u allows to determine the vertical displacement of point A and the external pressure p_{ext}.

Again, two cases can be considered:

1. The actuation fluid is incompressible. In this case, the volume of the cap V_{cap} does not change since the fluid volume V' in the cylinder remains the same. As a consequence, the membrane radius r also remains the same as well as $\gamma(r)$ and as the vertical displacement of point A. If p_{in} is measured, the external pressure p_{ext} can be determined

with the following two equations (the first one being the Laplace's equation):

$$p_{out} = p_{in} - \frac{2\gamma(r)}{r} \tag{5.8}$$

and

$$p_{ext} = p_{out} - p_{atm} \tag{5.9}$$

In fact, since p_{out} increases by an amount p_{ext} while the shape of the membrane does not change, p_{in} increases by the same amount.

2. The actuation fluid is compressible. Since the value of u is known, if p_{in} is measured, the following three equations allow to determine p_{ext} and r (the second equation is the Laplace's equation and the first one is the gas law applied to the system whose fluid quantity is constant and assuming that the temperature is constant) :

$$p_{atm}Sd = p_{in}(V_{cap}(r) + S(d-u)) \tag{5.10}$$

$$p_{out} = p_{in} - \frac{2\gamma(r)}{r} \tag{5.11}$$

$$p_{ext} = p_{out} - p_{atm} \tag{5.12}$$

The vertical displacement of point A can then be determined from the value of r.

As can be seen, when the membrane is loaded, the knowledge of the piston displacement u and of the inner pressure p_{in} allows to determine the displacement of the actuator and the external pressure applied to it.

For the simple actuator discussed in this section, the implementation of the PVFP principle consists thus in the equations that model the behaviour of the actuator and that allow to determine the displacement of the actuator and the external pressure applied to it, on the basis of the values of u and p_{in}.

In the mathematical developments presented in this section, the temperature is considered to be constant as well as the atmospheric pressure. However, in practice, it can happen that the ambient temperature or the atmospheric pressure changes. Let us now consider the effect of those changes on the predictions provided by PVFP principle, in the cases of an incompressible and of a compressible fluid.

1. The actuation fluid is incompressible:
   - If the atmospheric pressure increases by an amount p^*, the absolute outside and inside pressures p_{out} and p_{in} increase by the same amount and the PVFP principle implemented on the actuator perceives this as the application of an external pressure $p_{ext} = p^*$. To get rid of the influence of an atmospheric pressure change, a gauge pressure sensor could be used to measure p_{in} or the atmospheric pressure could be measured and updated, if necessary, in the implementation of the PVFP principle (i.e. in equation (5.9)).
   - If the ambient temperature increases by a small amount such that the volume of fluid does not change (no expansion), it will have no influence on the results provided by the PVFP principle, i.e. the predictions of the actuator displacement and of the external pressure applied to the membrane will not be distorted.

2. The actuation fluid is compressible.

   - If the atmospheric pressure increases by an amount p^*, the absolute outside pressure p_{out} increases by the same amount, the radius r of the spherical cap decreases as well as the vertical displacement of point A and p_{in} increases but not by the same amount as p_{out}. Indeed, if p_{out} and p_{in} increased by the same amount, equation (5.7) would lead to an unchanged radius r while in practice r decreases. The PVFP principle implemented on the actuator perceives the change of the atmospheric pressure as the application of an external pressure $p_{ext} = p^*$. As already said, the change of the atmospheric pressure has lead to a change of the vertical displacement of point A but the prediction of the PVFP principle, according to which $p_{ext} = p^*$, can be used to compensate this change and to restore the displacement of point A. The PVFP principle does not allow to distinguish a change of the atmospheric pressure from the application of a real external pressure p_{ext}; to be able to do so, it is necessary to measure the atmospheric pressure.
     The atmospheric pressure needs thus to be measured and updated in the implementation of the PVFP principle (i.e. in equation (5.12)) and its effect on the displacement of point A needs to be compensated if it is non-negligible.
   - If the ambient temperature increases, the volume of fluid expands in the actuator. Since the volume V' in the cylinder does not change because the piston position is imposed, the volume V_{cap} of the spherical cap increases as well as the vertical displacement of point A. The inner pressure p_{in} increases and the PVFP principle implemented on the actuator perceives this change as the application of an external pressure $p_{ext} = p^*$ that would have decreased the displacement of point A. Hence, the prediction of the PVFP principle, according to which $p_{ext} = p^*$, can not be used to compensate the change in the displacement of point A due to the temperature increase; indeed, doing so would lead to a further increase of the displacement of this point! The temperature needs thus to be measured and taken into account in the implementation of the PVFP principle and its effect on the displacement of point A needs to be compensated.

In conclusion, for the simple actuator considered here, the PVFP principle is applicable with an incompressible or a compressible actuation fluid. Besides, if an incompressible actuation fluid and a gauge pressure sensor (to measure p_{in}) are used, the predictions provided by the PVFP principle implemented on the actuator will not be influenced by the changes of the atmospheric pressure and of the temperature.

5.1.2 Implementing the PVFP principle on the Pneumatic Balloon Actuator

The Pneumatic Balloon Actuator (PBA) has been chosen to study the PVFP principle. This actuator is described in Section 4.2 and is installed on the test bench described in Sections 3.5 and 4.3.
Fig. 5.3 is a schematic representation of the PBA linked to the cylinder of the test bench. The actuation fluid is air. When a displacement u is imposed to the piston, the inner pressure p_{in} increases and the PBA inflates and its free end A moves upwards. The vertical and horizontal displacements of this point are Δy_0 and Δx_0, respectively. Afterwards, keeping the piston position constant, if a weight w is hung from the PBA free end, the inner pressure p_{in} increases by an amount Δp and the displacements Δy and Δx of the PBA free end decrease. According to the PVFP principle, knowing the values of p_{in} and u allows to determine the displacements of point A and the value of the weight w.

As explained before, the pressure variation Δp due to the loading of the PBA with a weight is measured with another sensor than the inner pressure p due to the piston displacement (p is the gauge pressure corresponding to the absolute pressure p_{in}).

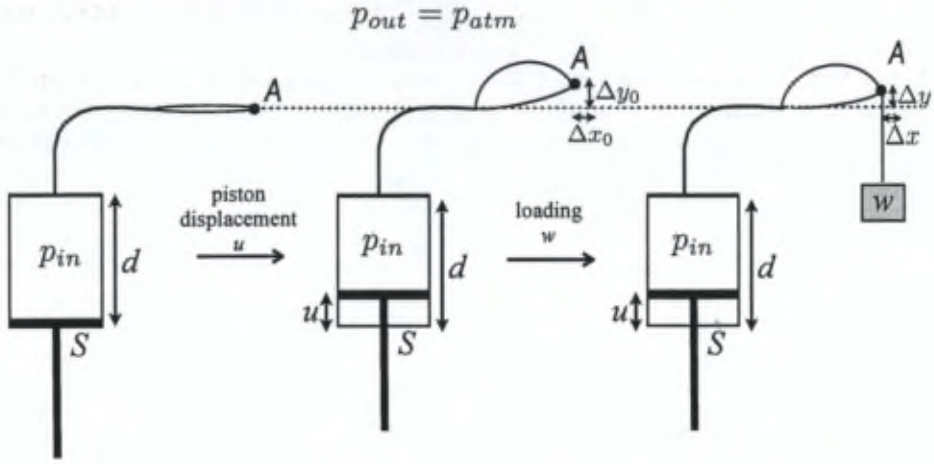

Figure 5.3: Pneumatic Balloon Actuator (PBA) linked to the cylinder of the test bench. The actuation fluid is air. When a displacement u is imposed to the piston, the inner pressure p_{in} increases and the PBA inflates and its free end A moves upwards. The vertical and horizontal displacements of this point are Δy_0 and Δx_0, respectively. Afterwards, keeping the piston position constant, if a weight w is hung from the PBA free end, the inner pressure p_{in} increases and the displacements Δy and Δx of the PBA free end decrease. According to the PVFP principle, knowing the values of p_{in} and u allows to determine the displacements of point A and the value of the weight w.

To implement the PVFP principle on the PBA, experiments are performed in order to establish experimental models of the PBA; this is done is Section 5.2.1 and the following experimental models are established:

- $p = p(u)$
- $\Delta x_0 = \Delta x_0(u)$
- $\Delta y_0 = \Delta y_0(u)$
- $\Delta p = \Delta p(u, w)$
- $\Delta x = \Delta x(u, w)$
- $\Delta y = \Delta y(u, w)$

Afterwards, in Section 5.2.2, the PVFP principle is used to predict the PBA displacements Δx and Δy and the load w attached from its free end, on the basis of the measurements of u and p. In summary, this is done as follows:

- If it is known that the PBA is not loaded (i.e. no pressure variation Δp is measured while the piston position is kept constant), the measurement of the piston displacement u allows to determine the inner pressure p and the PBA displacements Δx_0 and Δy_0, thanks to the first three experimental models.

- If it is known that the PBA is loaded (i.e. a pressure variation Δp is measured while the piston position is kept constant), the measurements of the piston displacement u and of the pressure variation Δp allow to determine the PBA displacements Δx and Δy as well as the load w, thanks to the last three experimental models.

Finally, Section 5.2.3 studies the hysteresis of the PBA and Section 5.3 discusses the relevance of the PVFP principle and its practical implementation.

5.2 Experimental study of the PVFP principle

5.2.1 Establishing experimental models of the PBA's behaviour

The aim of the experiments is to establish the following relationships:

- $p = p(u)$
- $\Delta x_0 = \Delta x_0(u)$
- $\Delta y_0 = \Delta y_0(u)$
- $\Delta p = \Delta p(u, w)$
- $\Delta x = \Delta x(u, w)$
- $\Delta y = \Delta y(u, w)$

To do so, a design of experiments (DOE) has been established with the help of the Design-Expert 8 software [11]. Since there are two factors, u and w, a response surface design has been chosen and more precisely a central composite design (CCD). A CCD has been selected because quadratic models can be established with it and because previous experiments revealed that the relationships listed above can be approached by polynomials not higher than quadratic ones. A CCD will lead to models giving very good predictions in the middle of the experimental space $u - w$; it is a factorial design to which center and axial points are added to estimate the quadratic terms. The DOE proposed by the software counts thirteen experiments, i.e. combinations (u, w) of the factors u and w, that have to be performed in a random order. These experiments are represented in the experimental space $u - w$, in Fig. 5.4.

As can be seen,

- five experiments repeat the same combination (u, w) which is placed at the center of the experimental space; these replicated center points are used to estimate pure error for the lack of fit test. Lack of fit indicates how well the chosen model fits the data. Moreover, these center points are used to estimate the quadratic terms.
- four experiments are combinations (u, w) placed on the horizontal or vertical axis passing through the center point of the experimental space; these axial points are also used to estimate the quadratic terms.
- four experiments are combinations (u, w) which are not placed on the horizontal nor the vertical axis passing through the center point of the experimental space; these experiments correspond to the factorial design associated with the two factors u and w.

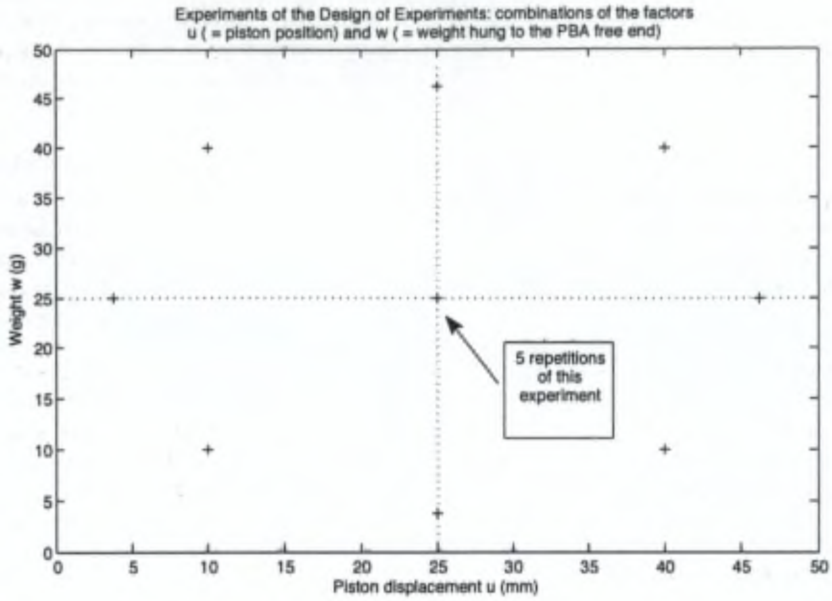

Figure 5.4: Experiments of the Design of Experiments (DOE) performed to establish the following relationships for the studied PBA: $p = p(u)$, $\Delta x_0 = \Delta x_0(u)$, $\Delta y_0 = \Delta y_0(u)$, $\Delta p = \Delta p(u, w)$, $\Delta x = \Delta x(u, w)$, $\Delta y = \Delta y(u, w)$. The chosen DOE is a central composite design of thirteen experiments: five central points, four axial points and four other points corresponding to the factorial design associated to the two factors u (= piston displacement) and w (= weight hung to the PBA free end).

- the DOE requires to perform specific experiments. However, in practice, if the linear motor is asked to perform a given piston displacement u^*, it will perform a displacement u' close to u^* but not equal to u^*; the difference between u^* and u' can be as large as 1 mm. Besides, some weights were not feasible, such as 3.79 g or 46.21 g, and were replaced by 4 g and 46 g, respectively. Hence, the DOE has been updated to take these differences into account.

- the practical range of u is [4 mm, 46 mm]. The lower value has been chosen because the corresponding position of the PBA is quite well repeatable. Indeed, the PBA needs to be a little bit pressurized to have a repeatable position. The upper value allows to pressurize the PBA without exceeding its maximum admitted pressure of 0.3 bar. The position of the PBA has been measured for $u = 4.46$ mm and it has been considered to be the PBA rest position, i.e. no X- or Y-displacements, since then.

For each experiment, the required piston displacement u has been reached. Then the pressure p and the X- and Y-displacements Δx_0 and Δy_0 have been measured. Afterwards, the specified weight w has been hung from the PBA free end and the pressure variation Δp, the X- and Y-displacements Δx and Δy have been measured. The weight has then been removed before performing the next experiment.
Fig. 5.5 to 5.11 present the results of this DOE. The crosses and circles indicate the experiments (some points may be superimposed) while the lines and surfaces represent the experimental models established on the basis of these experiments.

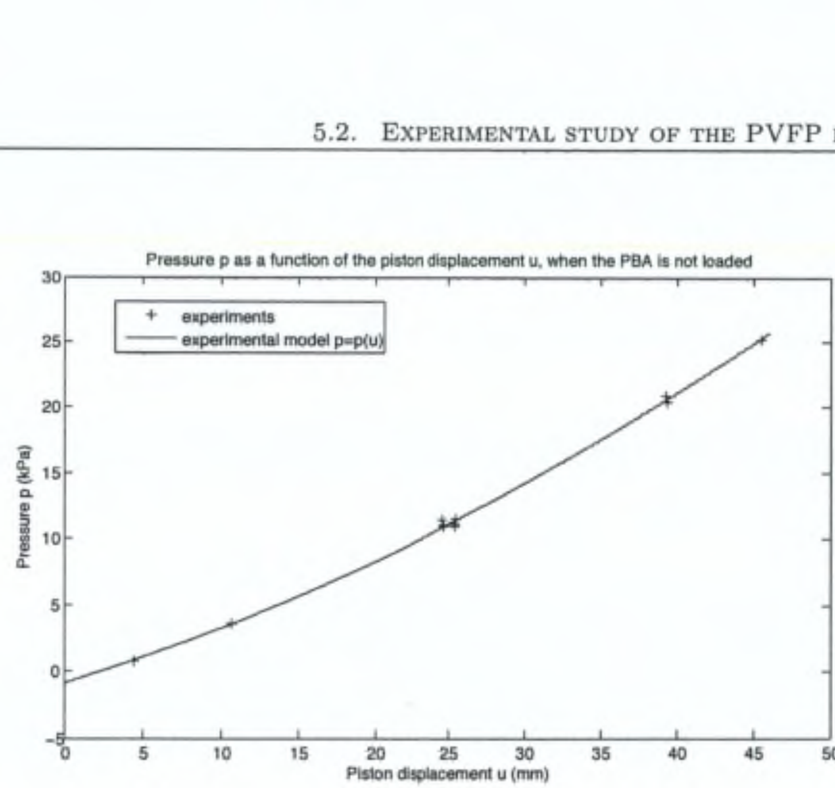

Figure 5.5: Pressure p as a function of the piston displacement u, when the PBA is not loaded. The crosses represent the thirteen performed experiments (some points may be superimposed) and the line is the experimental model $p = p(u)$ established on the basis of these experiments.

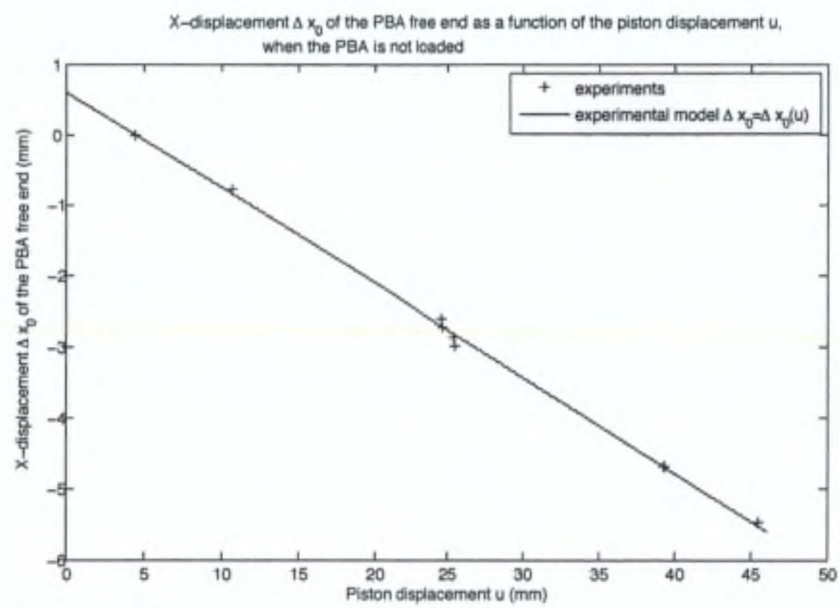

Figure 5.6: X-displacement Δx_0 of the PBA free end as a function of the piston displacement u, when the PBA is not loaded. The crosses represent the thirteen performed experiments (some points may be superimposed) and the line is the experimental model $\Delta x_0 = \Delta x_0(u)$ established on the basis of these experiments.

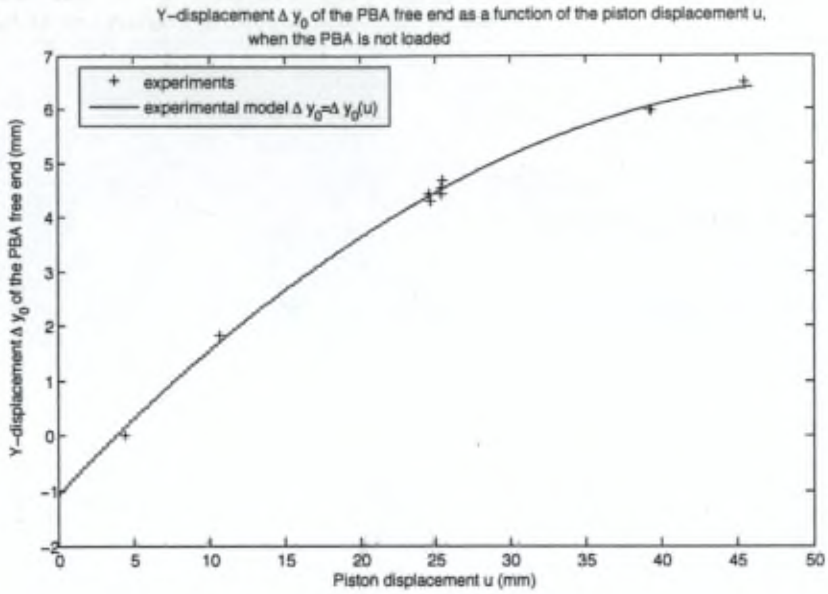

Figure 5.7: Y-displacement Δy_0 of the PBA free end as a function of the piston displacement u, when the PBA is not loaded. The crosses represent the thirteen performed experiments (some points may be superimposed) and the line is the experimental model $\Delta y_0 = \Delta y_0(u)$ established on the basis of these experiments.

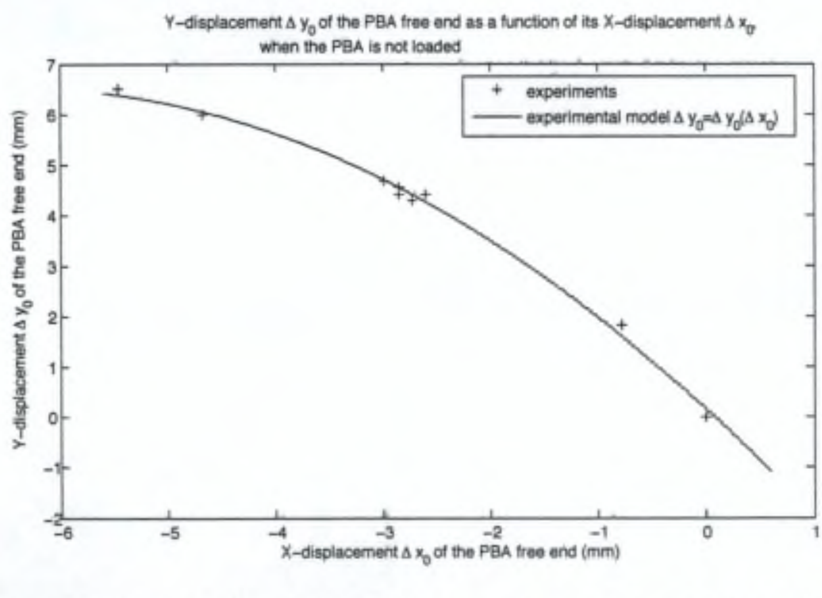

Figure 5.8: Y-displacement Δy_0 of the PBA free end as a function of its X-displacement Δx_0, when the PBA is not loaded. The crosses represent the thirteen performed experiments (some points may be superimposed) and the line is the experimental model $\Delta y_0 = \Delta y_0(\Delta x_0)$ established on the basis of these experiments.

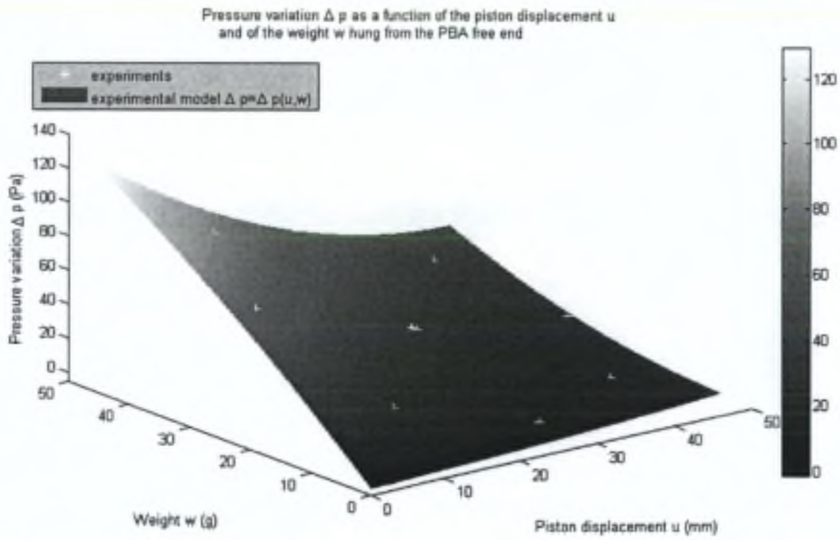

Figure 5.9: Pressure variation Δp as a function of the piston displacement u and of the weight w hung from the PBA free end. The crosses represent the thirteen performed experiments (some points may be superimposed) and the surface is the experimental model $\Delta p = \Delta p(u, w)$ established on the basis of these experiments.

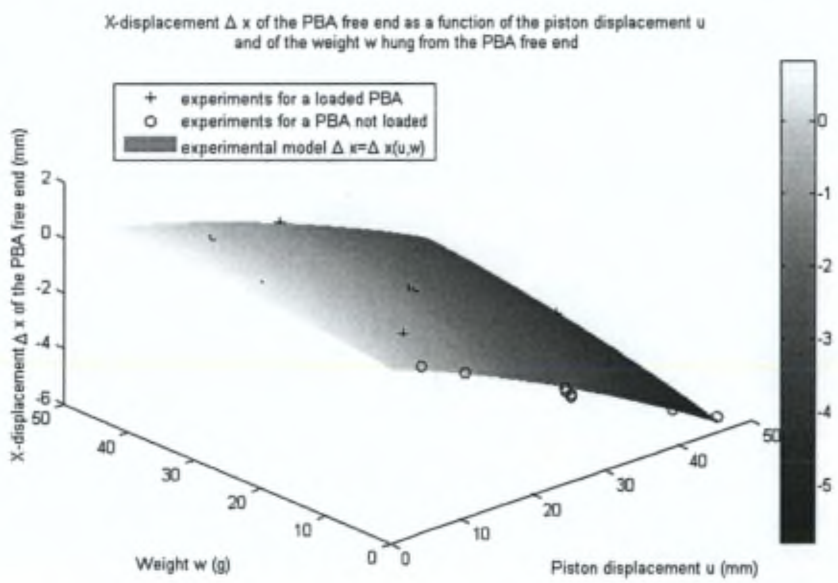

Figure 5.10: X-displacement Δx of the PBA free end as a function of the piston displacement u and of the weight w hung from the PBA free end. The crosses represent the thirteen performed experiments (some points may be superimposed) and the surface is the experimental model $\Delta x = \Delta x(u, w)$ established on the basis of these experiments. The circles represent the experiments performed for a PBA not loaded (these are the experiments presented in Fig. 5.6).

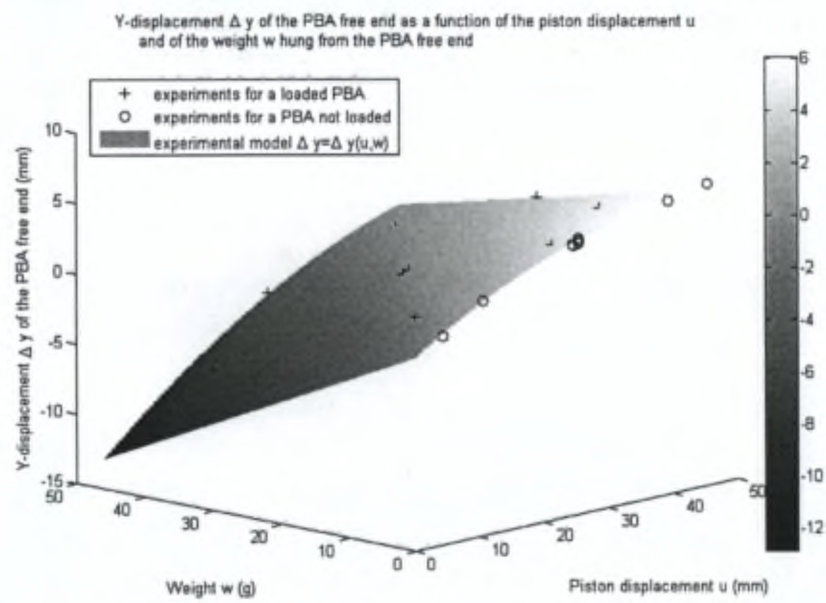

Figure 5.11: Y-displacement Δy of the PBA free end as a function of the piston displacement u and of the weight w hung from the PBA free end. The crosses represent the thirteen performed experiments (some points may be superimposed) and the surface is the experimental model $\Delta y = \Delta y(u, w)$ established on the basis of these experiments. The circles represent the experiments performed for a PBA not loaded (these are the experiments presented in Fig. 5.7).

The equations of the experimental models are the following (the values of the coefficients are given in Table 5.1):

$$p = c_1 + c_2u + c_3u^2 \tag{5.13}$$

$$\Delta x_0 = d_1 + d_2u \tag{5.14}$$

$$\Delta y_0 = f_1 + f_2u + f_3u^2 \tag{5.15}$$

$$\Delta p = b_1 + b_2u + b_3w + b_4u\ w + b_5u^2 + b_6w^2 + b_7u^2w + b_8u\ w^2 \tag{5.16}$$

$$\Delta x = g_1 + g_2u + g_3w + g_4u\ w + g_5u^2 + g_6w^2 \tag{5.17}$$

$$\Delta y = a_1 + a_2u + a_3w + a_4u\ w + a_5u^2 \tag{5.18}$$

Coefficients	Coefficients
$a_1 = -1.155$	$c_1 = -0.8826$
$a_2 = 0.3100$	$c_2 = 0.3656$
$a_3 = -0.2545$	$c_3 = 4.606\ 10^{-3}$
$a_4 = 2.887\ 10^{-3}$	$d_1 = 0.6049$
$a_5 = -3.327\ 10^{-3}$	$d_2 = -0.1348$
$b_1 = -1.135$	$f_1 = -1.089$
$b_2 = 5.067\ 10^{-2}$	$f_2 = 0.2913$
$b_3 = 3.313$	$f_3 = -2.787\ 10^{-3}$
$b_4 = -0.1048$	$g_1 = 0.2557$
$b_5 = 3.146\ 10^{-3}$	$g_2 = -9.785\ 10^{-2}$
$b_6 = -1.016\ 10^{-2}$	$g_3 = 3.598\ 10^{-2}$
$b_7 = 7.688\ 10^{-4}$	$g_4 = 7.567\ 10^{-4}$
$b_8 = 5.469\ 10^{-4}$	$g_5 = -7.232\ 10^{-4}$
	$g_6 = -5.561\ 10^{-4}$

Table 5.1: Values of the coefficients of the experimental models

As can be seen,

- the pressure p has a quadratic evolution with respect to the piston displacement u and if u is increased, p increases.
- the X-displacement Δx_0 has a linear evolution with respect to the piston displacement u. If u is increased, the PBA free end moves upwards, Δx_0 increases in absolute value (Δx_0 is negative and decreases).
- the Y-displacement Δy_0 has a quadratic evolution with respect to the piston displacement u. If u is increased, the PBA free end moves upwards and Δy_0 increases.
- the pressure variation Δp has a cubic evolution with respect to the piston displacement u and to the weight w hung from the PBA free end. For a given piston displacement u, if the weight w is increased, the pressure variation Δp increases. On the other hand, for a given weight w, if the piston displacement u is increased, the pressure variation Δp decreases.
  In practice, when the PBA is not loaded ($w = 0$), the pressure variation Δp equals zero but the experimental model forecasts a pressure variation Δp up to 8 Pa, as can be

seen in Fig. 5.9 and 5.12. On the other hand, in practice, when there is no pressure variation ($\Delta p = 0$), it means that the PBA is not loaded ($w = 0$) but the experimental model forecasts a non-zero weight, apart from one value of u, as can be seen in Fig. 5.9 and 5.13.

To correct these wrong predictions, the coefficients b_1, b_2 and b_5 could be put to zero. However, this has not be done since, as will be explained later, when no pressure variation is measured ($\Delta p = 0$), it is directly deduced, without using the model (5.16), that the PBA has not been loaded and that $w = 0$.

- the X- and Y-displacements Δx and Δy have both a quadratic evolution with respect to the piston displacement u and to the weight w hung from the PBA free end. For a given piston displacement u, if the weight w is increased, the PBA free end moves downwards and Δy decreases. On the other hand, for a given weight w, if the piston displacement u is increased, the PBA free end moves upwards and Δy increases.

In Fig. 5.14 and 5.15, it is interesting to notice that the experimental models $\Delta x_0 = \Delta x_0(u)$ and $\Delta y_0 = \Delta y_0(u)$ are quite similar to the experimental models $\Delta x = \Delta x(u, w)$ and $\Delta y = \Delta y(u, w)$, respectively, when there is no load ($w = 0$). As a consequence, the models of Δx and Δy can be rewritten as follows:

$$\Delta x(u, w) \approx \Delta x_0(u) + \Delta x_w(u, w) \tag{5.19}$$

with

$$\Delta x_w(u, w) = (g_3 + g_4 u)w + g_6 w^2 \tag{5.20}$$

$$\Delta y(u, w) \approx \Delta y_0(u) + \Delta y_w(u, w) \tag{5.21}$$

with

$$\Delta y_w(u, w) = (a_3 + a_4 u)w \tag{5.22}$$

With these expressions, one can clearly see that Δx and Δy are the results of two contributions:

1. $\Delta x_0(u)$ and $\Delta y_0(u)$: these first contributions are linked to the piston displacement u when the PBA is not loaded; $\Delta x|_{u,w=0} = \Delta x_0(u)$ and $\Delta y|_{u,w=0} = \Delta y_0(u)$.

2. $\Delta x_w(u, w)$ and $\Delta y_w(u, w)$: this contribution is linked to the weight w hung from the PBA free end but also to the piston displacement u. Hence, if a given weight is hung at the PBA free end, the corresponding X- and Y-displacements Δx_w and Δy_w will be different for two different piston displacements. The expression 5.22 of $\Delta y_w(u, w)$ indicates that $\Delta y_w(u, w)$ has a linear evolution with respect to the weight w, whose slope depends on the piston displacement u. In other words, $\Delta y_w(u, w)$ evolves as a spring with respect to the weight, whose stiffness depends on the piston displacement: the higher the piston displacement, the stiffer the spring.

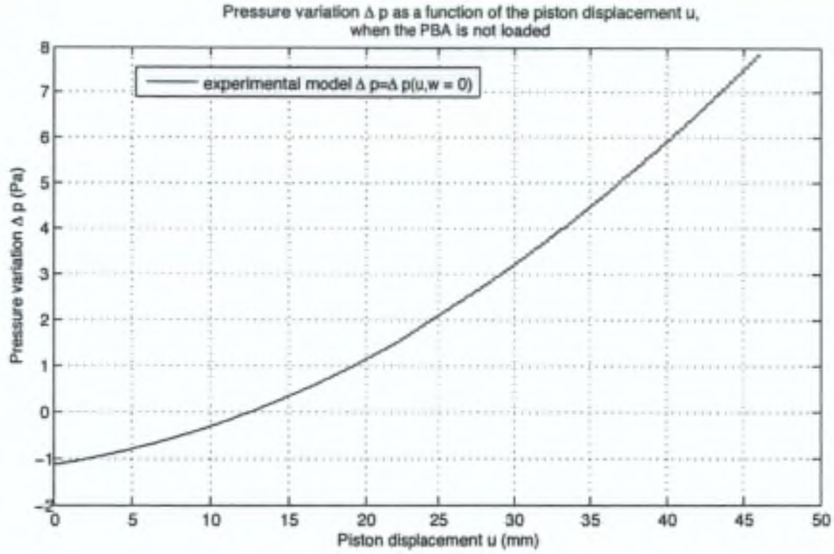

Figure 5.12: Pressure variation Δp as a function of the piston displacement u, when the PBA is not loaded. The solid line is the experimental model $\Delta p = \Delta p(u, w)$, when there is no load ($w = 0$). In practice, Δp equals zero when the PBA is not loaded but the experimental model forecasts a value up to 8 Pa.

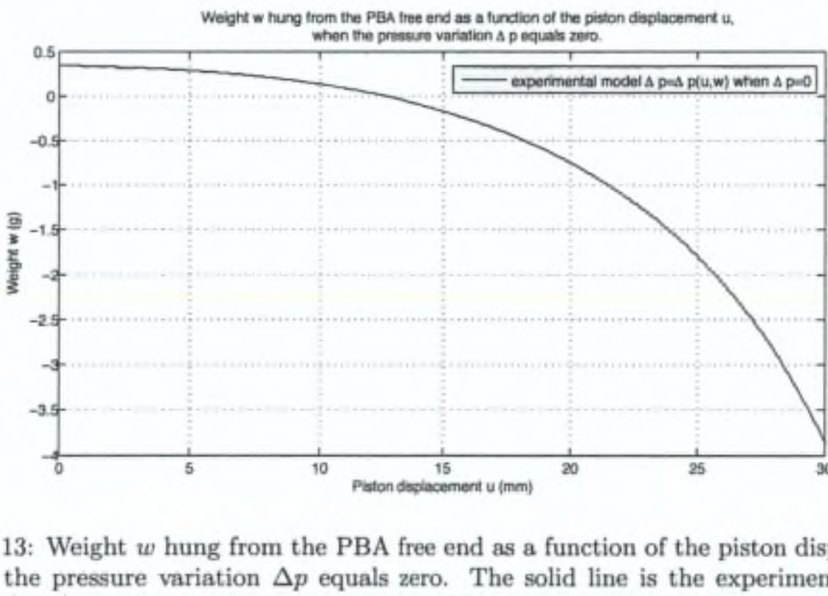

Figure 5.13: Weight w hung from the PBA free end as a function of the piston displacement u, when the pressure variation Δp equals zero. The solid line is the experimental model $\Delta p = \Delta p(u, w)$ for $\Delta p = 0$. In practice, when there is no pressure variation, it means that the PBA is not loaded but the experimental model forecasts a non-zero weight, apart from one value of u. u does not range above 30 mm because above this value the experimental model keeps on forecasting negative weights and even weights having an imaginary part.

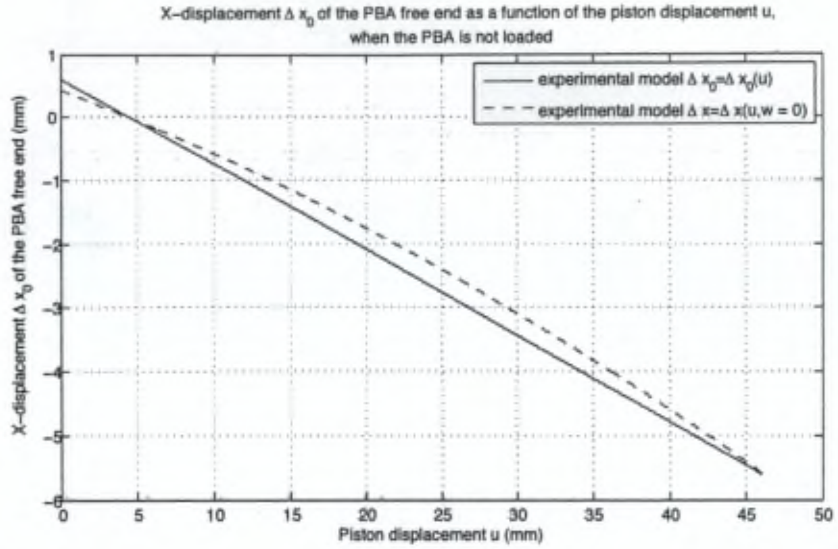

Figure 5.14: X-displacement Δx_0 of the PBA free end as a function of the piston displacement u. The solid line is the experimental model $\Delta x_0 = \Delta x_0(u)$ while the dashed line is the experimental model $\Delta x = \Delta x(u, w)$ when the PBA is not loaded ($w = 0$). As can be seen, both models are quite similar.

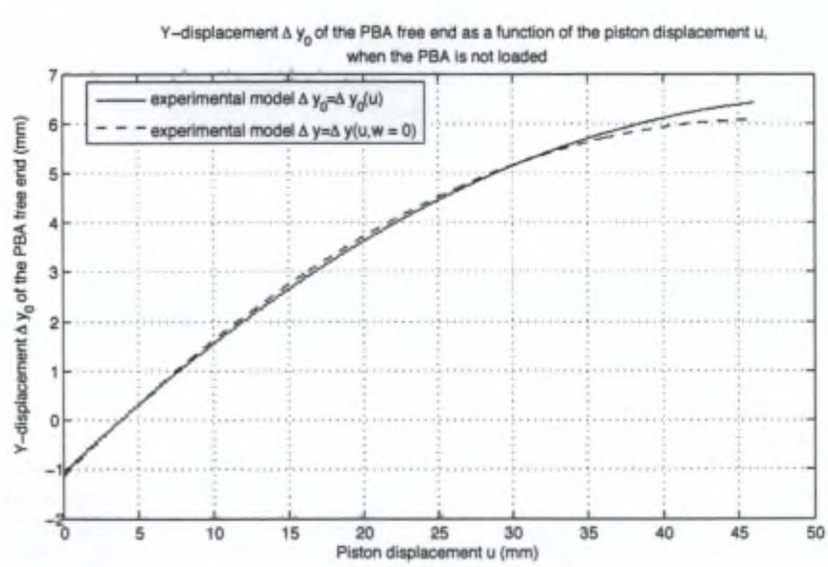

Figure 5.15: Y-displacement Δy_0 of the PBA free end as a function of the piston displacement u. The solid line is the experimental model $\Delta y_0 = \Delta y_0(u)$ while the dashed line is the experimental model $\Delta y = \Delta y(u, w)$ when the PBA is not loaded ($w = 0$). As can be seen, both models are quite similar.

5.2.2 Application of the PVFP principle: using the PBA as a sensor

Now that the experimental models of the PBA's behaviour have been established, they can be used to implement the PVFP principle. As presented in Fig. 5.16, the goal is to use the measurements of the piston displacement u and of the pressure variation Δp together with the experimental models to predict the values of the actuator displacements and of the weight attached from its end.

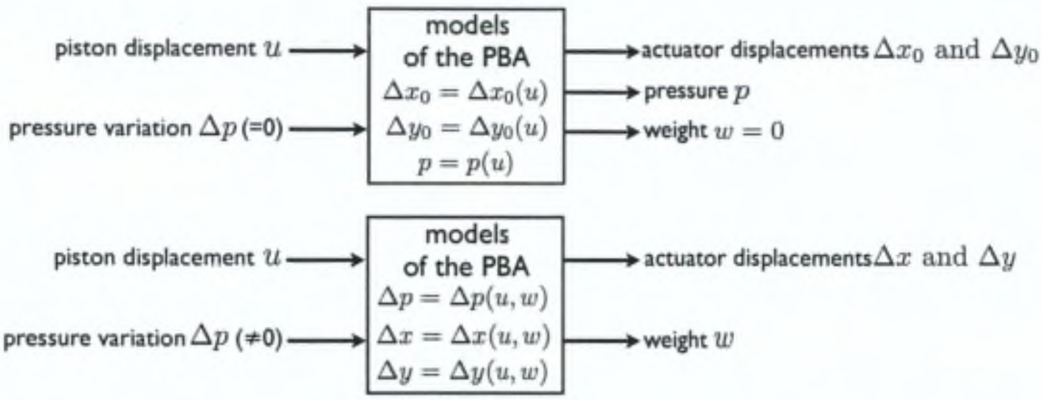

Figure 5.16: Representation of the implementation of the PVFP principle: on the basis of the measurements of the the piston displacement u and of the pressure variation Δp, the experimental models of the PBA are used to predict the values of the actuator displacements and of the weight attached to it.

1. If there is no pressure variation while the piston position is kept constant, i.e. $\Delta p = 0$, it means that the actuator has not been loaded with a weight. Hence, it can be predicted that $w = 0$; it is better to say directly that $w = 0$ than to use the experimental model $\Delta p = \Delta p(u, w)$ to predict the weight w because, as explained before, this model will not predict a zero value for the weight if $\Delta p = 0$ (see Fig. 5.13). The experimental models $p = p(u)$, $\Delta x_0 = \Delta x_0(u)$ and $\Delta y_0 = \Delta y_0(u)$ (see expressions 5.13, 5.14 and 5.15 and Fig. 5.5, 5.6 and 5.7) can then been used to predict the values p^*, Δx_0^* and Δy_0^* of p, Δx_0 and Δy_0 on the basis of the piston displacement measurement u

2. If there is a pressure variation while the piston position is kept constant, i.e. $\Delta p \neq 0$, it means that the actuator has been loaded with a weight w. The experimental models $\Delta p = \Delta p(u, w)$, $\Delta x = \Delta x(u, w)$ and $\Delta y = \Delta y(u, w)$ can then been used to predict the values w^*, Δx^* and Δy^* of w, Δx and Δy on the basis of the piston displacement and pressure variation measurements u and Δp.
   This is presented in Fig. 5.17, 5.18 and 5.19. First, both measurements u and Δp are used together with the experimental model $\Delta p = \Delta p(u, w)$ to predict the value w^* of the weight w that loads the PBA. Indeed, as can be seen in Fig. 5.17, for a given piston displacement u and a given pressure variation Δp, there is only one possible prediction for the weight. Afterwards, the piston displacement measurement u and the predicted value of the weight w^* are used together with the experimental models $\Delta x = \Delta x(u, w)$ and $\Delta y = \Delta y(u, w)$ to predict the values Δx^* and Δy^* of Δx and Δy. As can be seen in Fig. 5.18 and 5.19, there is only one possible prediction for Δx or Δy, for a given piston displacement u and a given weight w^*.

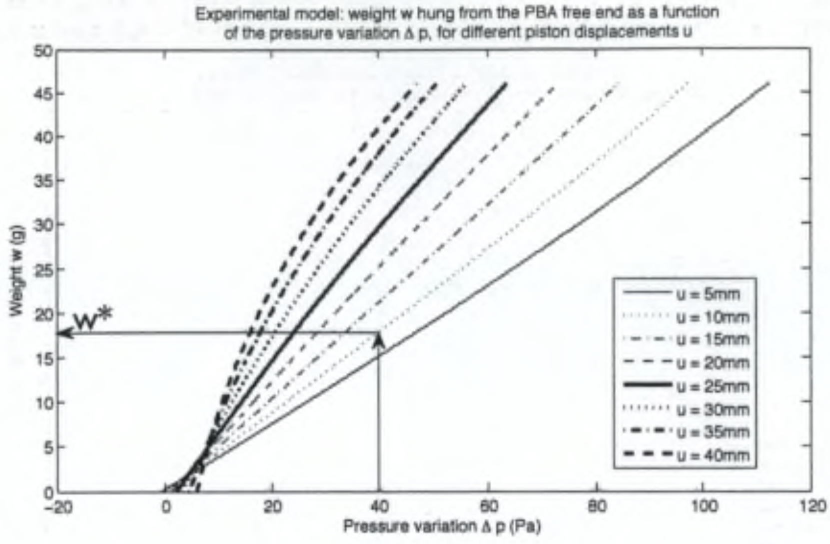

Figure 5.17: Experimental model $\Delta p = \Delta p(u, w)$, for a loaded PBA: the weight w hung from the PBA free end is presented with respect to the pressure variation Δp, for different values of the piston displacement u. On the basis of the measurements u and Δp, this model can predict the value w^* of the weight that loads the PBA. Indeed, as can be seen in the figure, for a given u and a given Δp, there is only one possible prediction w^* for the weight. For example, if $u = 10$ mm and $\Delta p = 40$ Pa, the experimental model predicts that $w^* = 17.8522$ g.

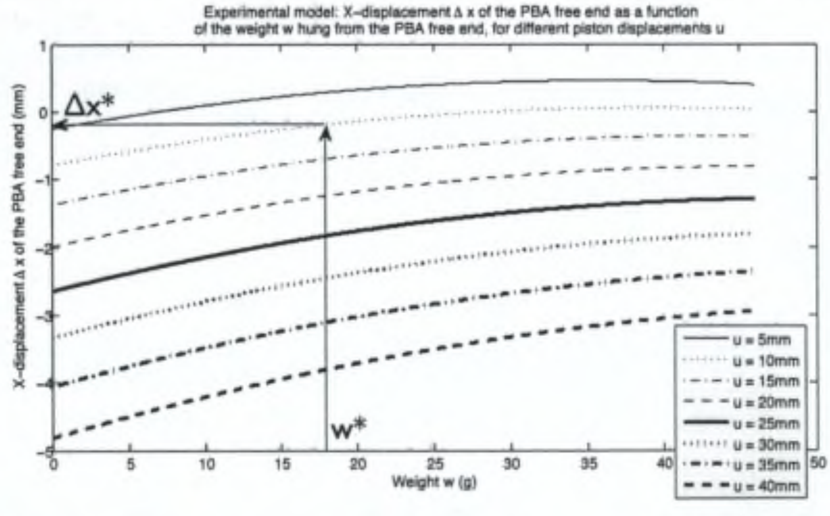

Figure 5.18: Experimental model $\Delta x = \Delta x(u, w)$, for a loaded PBA: the X-displacement Δx of the PBA free end is presented with respect to the weight w, for different values of the piston displacement u. On the basis of the measurement u and the prediction w^*, this model can predict the value Δx^* of the X-displacement of the PBA. Indeed, as can be seen in the figure, for a given u and a given w^*, there is only one possible prediction Δx^* for the X-displacement. For example, if $u = 10$ mm and $w^* = 17.8522$ g, the experimental model predicts that $\Delta x^* = -0.1949$ mm.

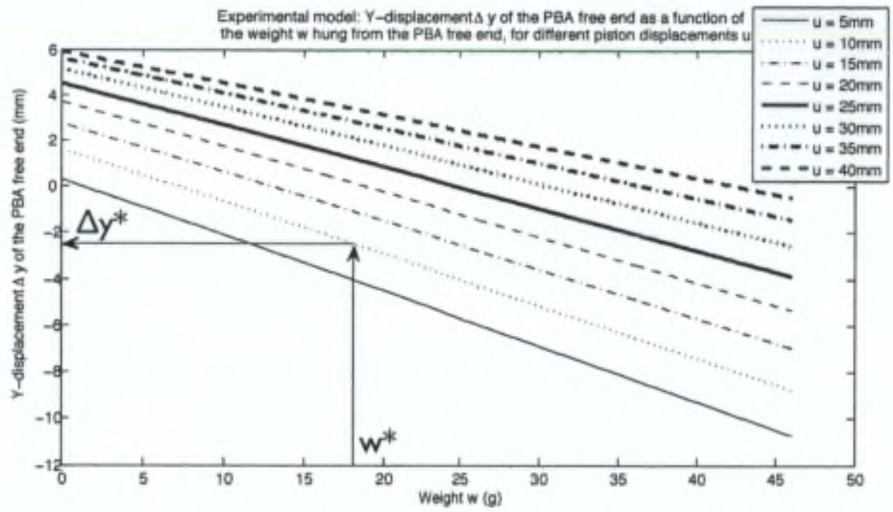

Figure 5.19: Experimental model $\Delta y = \Delta y(u, w)$, for a loaded PBA: the Y-displacement Δy of the PBA free end is presented with respect to the weight w, for different values of the piston displacement u. On the basis of the measurement u and the prediction w^*, this model can predict the value Δy^* of the Y-displacement of the PBA. Indeed, as can be seen in the figure, for a given u and a given w^*, there is only one possible prediction Δy^* for the Y-displacement. For example, if $u = 10$ mm and $w^* = 17.8522$ g, the experimental model predicts that $\Delta y^* = -2.4154$ mm.

To test the implementation of the PVFP principle on the studied PBA, the experiments summarized in Table 5.2 have been performed:

Experiment number	Piston displacement (mm)	Weight (g)	Measurements
1	15.61	0	p, Δx_0, Δy_0
2	15.61	35	Δp, Δx, Δy
3	15.61	15	Δp, Δx, Δy
4	15.61	20	Δp, Δx, Δy
5	19.71	0	p, Δx_0, Δy_0
6	19.71	35	Δp, Δx, Δy
7	19.71	15	Δp, Δx, Δy
8	19.71	20	Δp, Δx, Δy
9	34.36	0	p, Δx_0, Δy_0
10	34.36	35	Δp, Δx, Δy
11	34.36	15	Δp, Δx, Δy
12	34.36	20	Δp, Δx, Δy

Table 5.2: Experiments performed to test the implementation of the PVFP principle on the studied PBA. For each experiment, the table indicates for the chosen piston displacement u and weight w as well as the made measurements.

It has to be underlined that for each experiment, the specified weight w has been hung from the PBA free end and then removed before the next experiment is performed. For each experiment, the predictions have been made as explained above.

The experiments no. 1, 5 and 9 and corresponding predictions are presented in Fig. 5.20, 5.21 and 5.22; the PBA is not loaded for these experiments.
As can be seen,

- in Fig. 5.20, the measured pressures p are very close to the predicted ones p^*.
- in Fig. 5.21, the measured X-displacements Δx_0 are larger in absolute value than the predicted ones Δx_0^*.
- in Fig. 5.22, the measured Y-displacements Δy_0 are larger than the predicted ones Δy_0^*.

Fig. 5.23 and 5.24 present the absolute and relative errors, respectively, on the predictions of p, Δx_0 and Δy_0. These errors are summarized in Table 5.3. The absolute and relative errors on a given prediction are computed as follows:

$$absolute\ error = measured\ value - prediction \tag{5.23}$$

$$relative\ error = 100(measured\ value - prediction)/measured\ value \tag{5.24}$$

Parameter	Absolute error	Relative error
p	max 0.24 kPa	max 3.30% of the measured value
Δx_0	max 0.26 mm in absolute value	max 11.26% of the measured value
Δy_0	max 0.73 mm	max 20.83% of the measured value

Table 5.3: Absolute and relative errors on the predictions of p, Δx_0 and Δy_0.

For the other experiments (i.e. experiments no. 2, 3, 4, 6, 7, 8, 10, 11 and 12), the PBA is loaded; they are presented, together with the corresponding predictions, in Fig. 5.25, 5.26, 5.27 and 5.28. As can be seen in Fig. 5.26, the measured X-displacements Δx are larger in absolute value than the predicted ones Δx^*.
Fig. 5.29 and 5.30 present the absolute and relative errors, respectively, on the predictions of w, Δx and Δy. These errors are summarized in Table 5.4.

Parameter	Absolute error	Relative error
w	max 1.85 g in absolute value	max 10.68% of the measured value, in absolute value
Δx	max 0.38 mm in absolute value	max 28.81% of the measured value
Δy	max 0.55 mm in absolute value	experiment no. 3: 61.70% of the measured value experiment no. 10: 139.40% of the measured value other experiments: max 20.28% of the measured value, in absolute value

Table 5.4: Absolute and relative errors on the predictions of w, Δx and Δy.

As can be seen in Fig. 5.30 and Table 5.4, experiments no. 3 and 10 have a relative error on the prediction of Δy that equals to 61.70% and 139.40% of the measured value, respectively; on the other hand, the other experiments have a relative error on the prediction of Δy of maximum 20.28% of the measured value. To understand these two outliers, one has to look at the corresponding absolute errors (see Table 5.5). As can be seen, these absolute errors have reasonable values compared to the rest of the experiments but they are of the same order of magnitude than the corresponding Δy measurements and this explains the high values of the relative errors. The relative error on the prediction of Δy of experiment

no. 8 is not represented in Fig. 5.30 because it is infinite; indeed, the Δy measurement of this experiment equals zero (see Table 5.5).
Remark: In Fig. 5.28, it is interesting to notice that the curve $\Delta y = \Delta y(\Delta x)$ travelled by the PBA free end when it is loaded is different according to the piston displacement u.

Experiment number	Δy measurement	Δy^* prediction	Absolute error	Relative error
3	-0.39 mm	-0.1494 mm	-0.2406 mm	61.70% of the measured value
8	0 mm	-0.13 mm	0.13 mm	∞
10	0.26 mm	-0.1024 mm	0.3624 mm	139.40% of the measured value

Table 5.5: Table summarizing the Δy measurement, the Δy^* prediction, the absolute and relative errors on the prediction of Δy, for the experiments no. 3, 8 and 10. Experiments no. 3 and 10 have very large relative errors on the prediction of Δy (in comparison with the other experiments) because their absolute errors are of the same order of magnitude than their Δy measurements. Experiment no. 8 has an infinite relative error on the prediction of Δy because its Δy measurement equals zero.

In conclusion, this section has proved experimentally that the PVFP principle can be applied to the PBA. The quality of the predictions provided by the PVFP principle implemented on the PBA has to be evaluated with respect to an application. Hence, the predictions presented here can be sufficient for an application where qualitative results are needed, such as being able to compare loads applied to the PBA and having a coarse idea of the resulting position of the PBA free end. For an application requiring more accurate results, the predictions presented here may be insufficient.
The errors on the measurements (see Table 4.1) have not been taken into account while computing the absolute and relative errors of Tables 5.3 and 5.4, but if they were, they would increase the maximum errors that can be obtained.
The errors between the predictions and the corresponding measurements may be due to the fact that the fluidic circuit presents some leakages, that the experimental models are not perfect, that the PBA presents some hysteresis as will be shown in the Section 5.2.3 and that there are errors on the measurements due to the sensors.

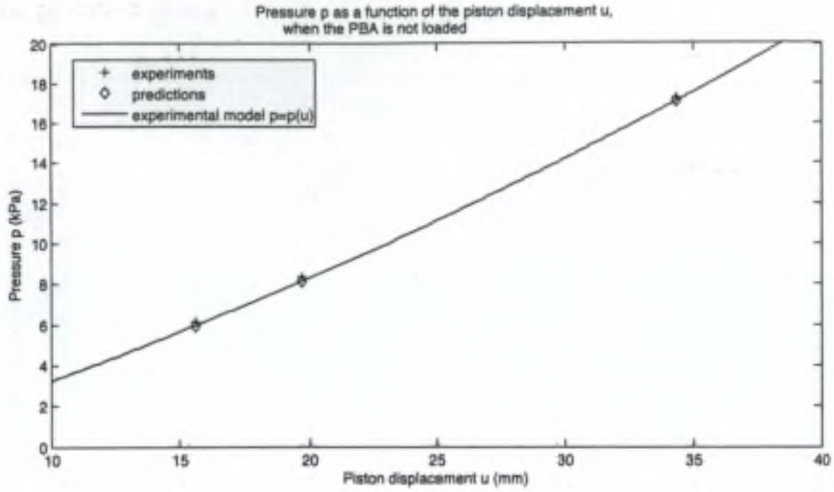

Figure 5.20: Pressure p as a function of the piston displacement u, when the PBA is not loaded: The crosses represent the experiments no. 1, 5 and 9 of Table 5.2 while the diamonds represent the corresponding predictions. Indeed, for the given piston displacements u, the PVFP principle implemented on the studied PBA predicts pressures p^* thanks to the experimental model $p = p(u)$. The predictions are represented by the diamonds. The solid line is the experimental model $p = p(u)$. As can be seen, the measured pressures p are very close to the predicted ones p^*.

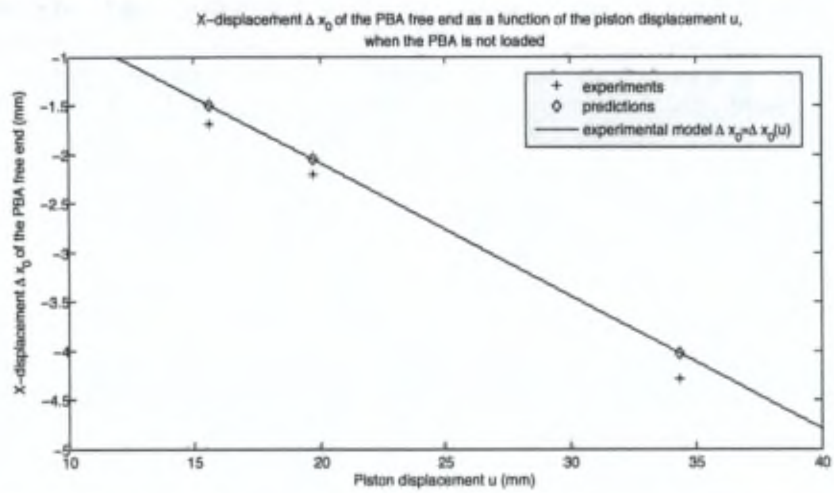

Figure 5.21: X-displacement Δx_0 of the PBA free end as a function of the piston displacement u, when the PBA is not loaded: The crosses represent the experiments no. 1, 5 and 9 of Table 5.2 while the diamonds represent the corresponding predictions. Indeed, for the given piston displacements u, the PVFP principle implemented on the studied PBA predicts X-displacements Δx_0^* thanks to the experimental model $\Delta x_0 = \Delta x_0(u)$. The predictions are represented by the diamonds. The solid line is the experimental model $\Delta x_0 = \Delta x_0(u)$. As can be seen, the measured X-displacements Δx_0 are larger in absolute value than the predicted ones Δx_0^*.

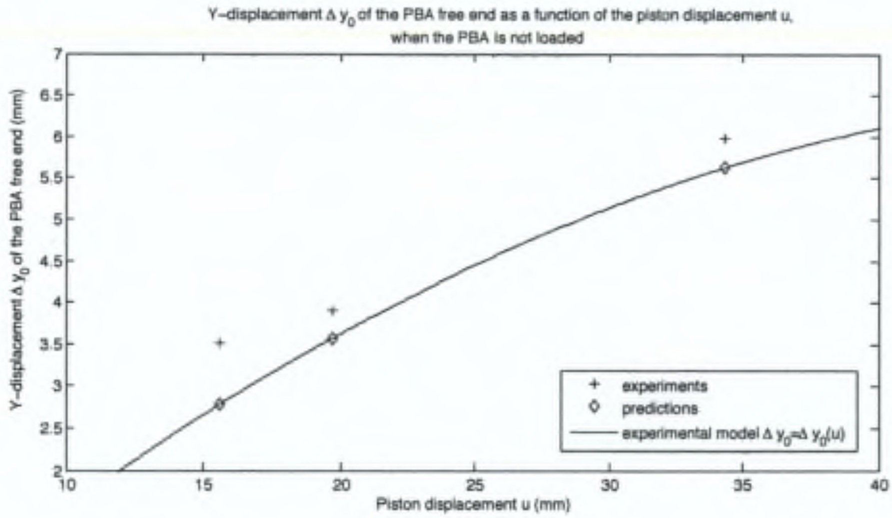

Figure 5.22: Y-displacement Δy_0 of the PBA free end as a function of the piston displacement u, when the PBA is not loaded: The crosses represent the experiments no. 1, 5 and 9 of Table 5.2 while the diamonds represent the corresponding predictions. Indeed, for the given piston displacements u, the PVFP principle implemented on the studied PBA predicts Y-displacements Δy_0^* thanks to the experimental model $\Delta y_0 = \Delta y_0(u)$. The predictions are represented by the diamonds. The solid line is the experimental model $\Delta y_0 = \Delta y_0(u)$. As can be seen, the measured Y-displacements Δy_0 are larger than the predicted ones Δy_0^*.

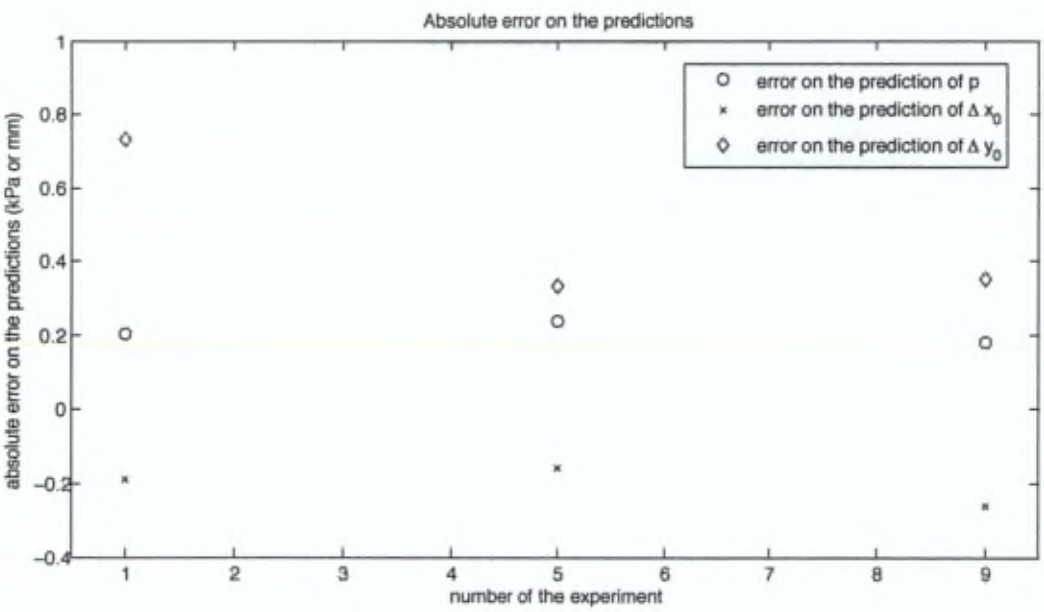

Figure 5.23: Absolute errors on the predictions of p, Δx_0 and Δy_0 for the experiments no. 1, 5 and 9 of Table 5.2. For the given piston displacements u, the PVFP principle implemented on the studied PBA predicts pressures p^*, X-displacements Δx_0^* and Y-displacements Δy_0^* thanks to the experimental models $p = p(u)$, $\Delta x_0 = \Delta x_0(u)$ and $\Delta y_0 = \Delta y_0(u)$. According to the parameter (p, Δx_0 or Δy_0), the error is expressed in kPa or mm.

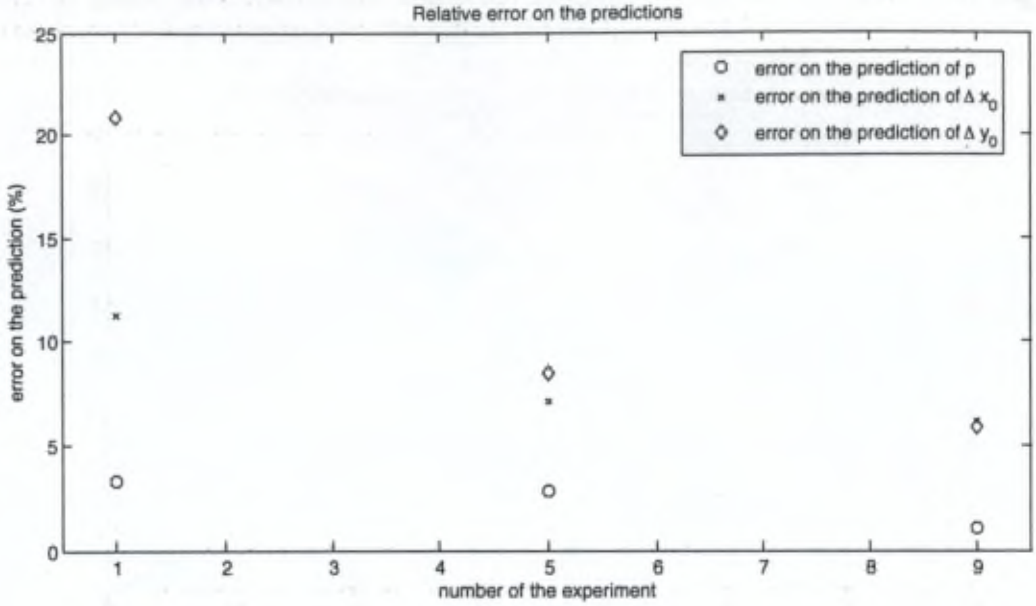

Figure 5.24: Relative errors on the predictions of p, Δx_0 and Δy_0 for the experiments no. 1, 5 and 9 of Table 5.2. For the given piston displacements u, the PVFP principle implemented on the studied PBA predicts pressures p^*, X-displacements Δx_0^* and Y-displacements Δy_0^* thanks to the experimental models $p = p(u)$, $\Delta x_0 = \Delta x_0(u)$ and $\Delta y_0 = \Delta y_0(u)$.

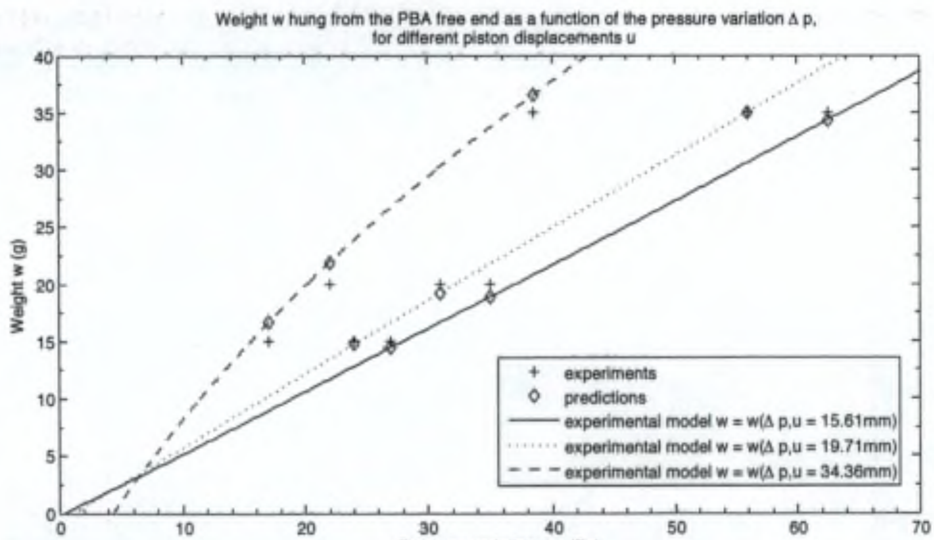

Figure 5.25: Weight w attached to the PBA free end as a function of the pressure variation Δp, for different piston displacements u: The crosses represent the experiments no. 2, 3, 4, 6, 7, 8, 10, 11 and 12 of Table 5.2 while the diamonds represent the corresponding predictions. Indeed, for the given piston displacements u and the given pressure variations Δp, the PVFP principle implemented on the studied PBA predicts weights w^* thanks to the experimental model $\Delta p = \Delta p(u, w)$.

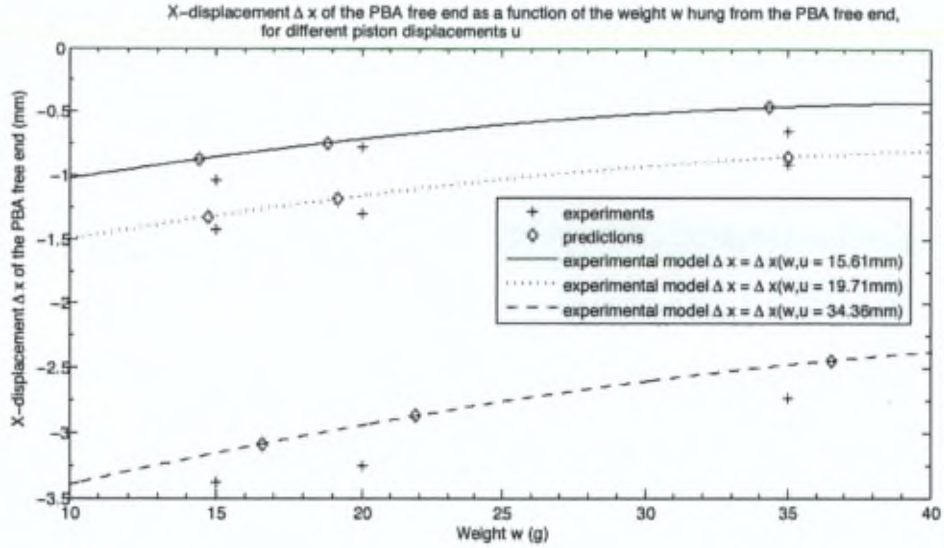

Figure 5.26: X-displacement Δx of the PBA free end as a function of the weight w hung from the PBA free end, for different piston displacements u: The crosses represent the experiments no. 2, 3, 4, 6, 7, 8, 10, 11 and 12 of Table 5.2 while the diamonds represent the corresponding predictions. Indeed, for the given piston displacements u and the predicted weights w^*, the PVFP principle implemented on the studied PBA predicts X-displacements Δx^* thanks to the experimental model $\Delta x = \Delta x(u, w)$. As can be seen, the measured X-displacements Δx are larger in absolute value than the predicted ones Δx^*.

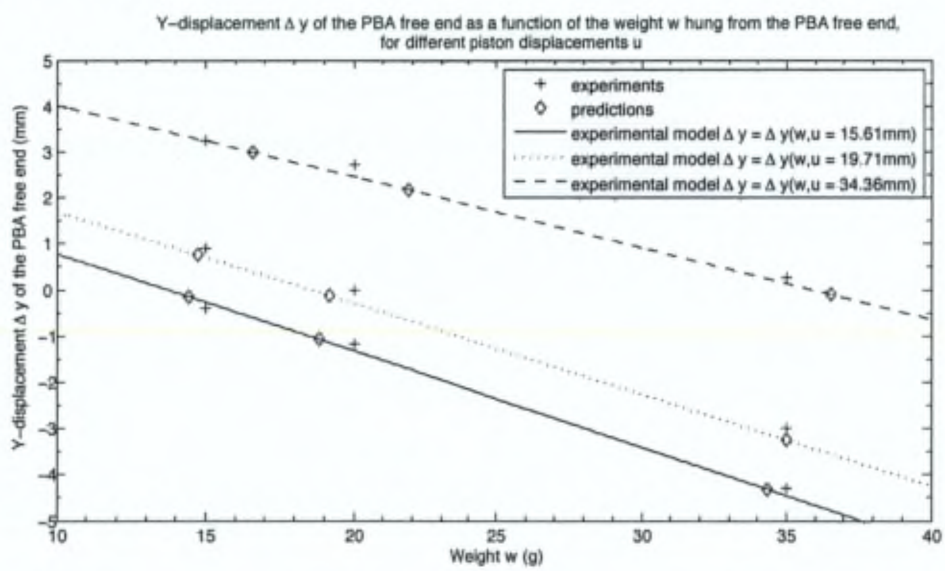

Figure 5.27: Y-displacement Δy of the PBA free end as a function of the weight w hung from the PBA free end, for different piston displacements u: The crosses represent the experiments no. 2, 3, 4, 6, 7, 8, 10, 11 and 12 of Table 5.2 while the diamonds represent the corresponding predictions. Indeed, for the given piston displacements u and the predicted weights w^*, the PVFP principle implemented on the studied PBA predicts Y-displacements Δy^* thanks to the experimental model $\Delta y = \Delta y(u, w)$.

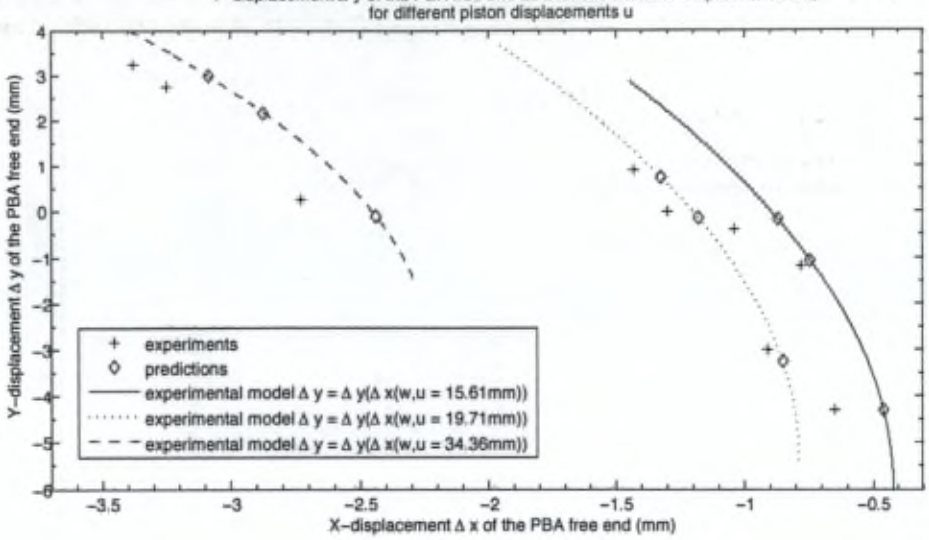

Figure 5.28: Y-displacement Δy of the PBA free end as a function of its X-displacement Δx, for different piston displacements u: The crosses represent the experiments no. 2, 3, 4, 6, 7, 8, 10, 11 and 12 of Table 5.2 while the diamonds represent the corresponding predictions. Indeed, for the given piston displacements u and the predicted weights w^*, the PVFP principle implemented on the studied PBA predicts X-displacements Δx^* and Y-displacements Δy^* thanks to the experimental models $\Delta x = \Delta x(u, w)$ and $\Delta y = \Delta y(u, w)$.

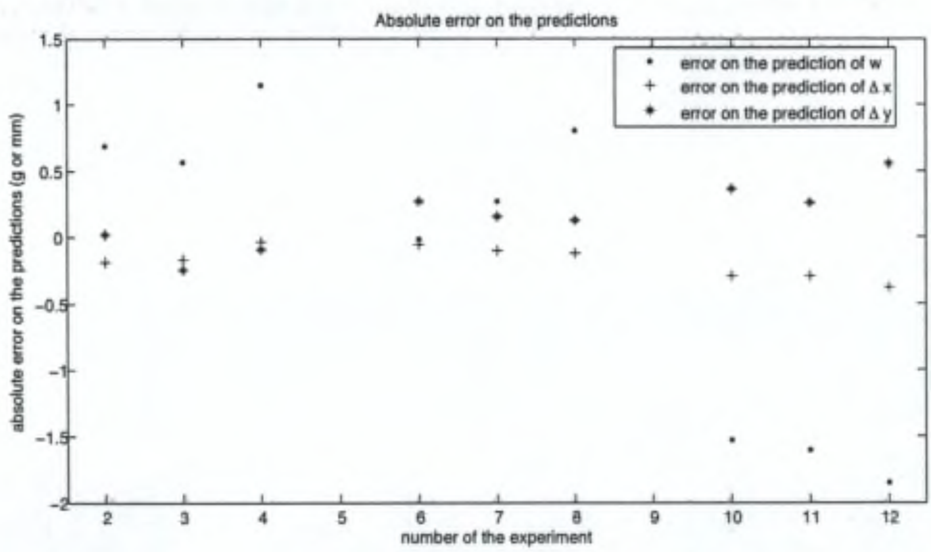

Figure 5.29: Absolute errors on the predictions of Δp, Δx and Δy for the experiments no. 2, 3, 4, 6, 7, 8, 10, 11 and 12 of Table 5.2. For the given piston displacements u and the given pressure variations Δp, the PVFP principle implemented on the studied PBA predicts weights w^*, X-displacements Δx^* and Y-displacements Δy^* thanks to the experimental models $\Delta p = \Delta p(u, w)$, $\Delta x = \Delta x(u, w)$ and $\Delta y = \Delta y(u, w)$. According to the parameter (w, Δx or Δy), the error is expressed in g or mm.

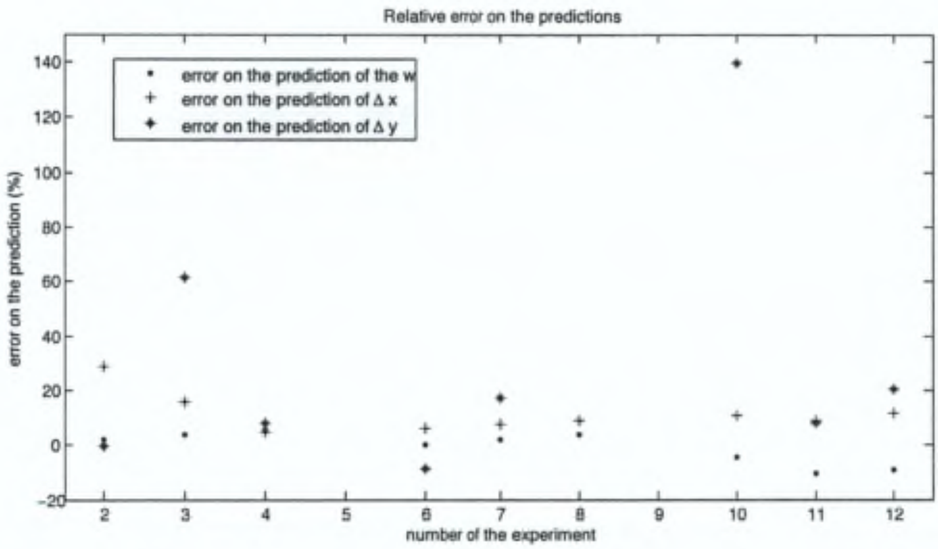

Figure 5.30: Relative errors on the predictions of Δp, Δx and Δy for the experiments no. 2, 3, 4, 6, 7, 8, 10, 11 and 12 of Table 5.2. For the given piston displacements u and the given pressure variations Δp, the PVFP principle implemented on the studied PBA predicts weights w^*, X-displacements Δx^* and Y-displacements Δy^* thanks to the experimental models $\Delta p = \Delta p(u, w)$, $\Delta x = \Delta x(u, w)$ and $\Delta y = \Delta y(u, w)$.

5.2.3 Study of the hysteresis of the PBA

Models have been established in order to implement the PVFP principle on the studied PBA. These models have been built on the basis of a DOE counting thirteen experiments performed in a random order. This means that if PBA variables (i.e. p, Δx_0, Δy_0, Δp, Δx or Δy) present hysteresis with respect to the piston displacement u or with respect to the weights w attached to the PBA, this hysteresis is not properly modeled by the experimental models. A study has thus been made to determine whether some of the PBA variables show hysteresis with respect to u and/or w. First, the hysteresis with respect to the piston displacement u has been investigated. Three hysteresis loops have been performed as follows:

1. first hysteresis loop: 1) $u = 5$ mm, 2) $u = 15$ mm, 3) $u = 5$ mm
2. second hysteresis loop: 1) $u = 5$ mm, 2) $u = 15$ mm, 3) $u = 25$ mm, 4) $u = 15$ mm, 5) $u = 5$ mm
3. third hysteresis loop: 1) $u = 5$ mm, 2) $u = 15$ mm, 3) $u = 25$ mm, 4) $u = 35$ mm, 5) $u = 25$ mm, 6) $u = 15$ mm, 7) $u = 5$ mm

For each piston displacement, the pressure p and the X- and Y-displacements Δx_0 and Δy_0 have been measured and the PBA has not been loaded. The results of this hysteresis study are presented in Fig. 5.31 to 5.38.

Remark: Let us consider that the error on two measurements equals $\pm$ s. If both measurements are spaced out by a difference smaller than $2s$, there is a probability that the exact measurements corresponding to them are equal. On the other hand, if both measurements are spaced out by a difference larger than $2s$, it is sure that the exact measurements corresponding to them are different. Table 4.1 summarizes the errors on the measurements.

Concerning the results of the hysteresis study:

- As can be seen in Fig. 5.31 and 5.32, the pressure p presents nearly no hysteresis with respect to the piston displacement u.
- As can be seen in Fig. 5.33 and 5.34, it can be concluded that the X-displacement Δx_0 presents a hysteresis with respect to the piston displacement u: when comparing the increasing and decreasing phases of u, the maximum difference in X-displacement that has been measured is about 0.26 mm (the accuracy on the measurement of Δx_0 equals ± 0.13 mm)
- As can be seen in Fig. 5.35 and 5.36, it can be concluded that the Y-displacement Δy_0 presents a hysteresis with respect to the piston displacement u: when comparing the increasing and decreasing phases of u, the maximum difference in Y-displacement that has been measured is larger than 0.26 mm (the accuracy on the measurement of Δy_0 equals ± 0.13 mm).

The experimental models $p = p(u)$, $\Delta x_0 = \Delta x_0(u)$ and $\Delta y_0 = \Delta y_0(u)$ have been established with a DOE whose experiments are performed in a random order. As a consequence, the hysteresis of Δx_0 and Δy_0 with respect to the piston displacement u is not properly modeled by these experimental models. On the contrary, it is drowned into these models.

Afterwards, the hysteresis with respect to the weight w attached from the PBA free end has been investigated. Again, three hysteresis loops have been performed, but not the same day as the previous hysteresis study:

1. first hysteresis loop: 1) $w = 0$ g, 2) $w = 10$ g, 3) $w = 0$ g

2. second hysteresis loop: 1) $w = 0$ g, 2) $w = 10$ g, 3) $w = 20$ g, 4) $w = 10$ g, 5) $w = 0$ g
3. third hysteresis loop: 1) $w = 0$ g, 2) $w = 10$ g, 3) $w = 20$ g, 4) $w = 40$ g, 5) $w = 20$ g, 6) $w = 10$ g, 7) $w = 0$ g

During these three loops, the piston displacement has been kept constant and equal to $u =$ 24.61 mm. Contrary to the experiments performed before (see Sections 5.2.1 and 5.2.2), for these hysteresis loops, the weight w is progressively increased or decreased from an experiment to the next one. For example, the second hysteresis loop is performed as follows:

- first experiment: no weight is attached to the PBA free end. $\Delta p = 0$ and the X- and Y-displacements Δx and Δy are measured. Since the PBA is not loaded, $\Delta x = \Delta x_0$ and $\Delta y = \Delta y_0$.
- second experiment: a weight of 10 g is attached to the PBA free end and Δp, Δx and Δy are measured.
- third experiment: a second weight of 10 g is added to reach a total weight of 20 g and Δp, Δx and Δy are measured.
- fourth experiment: 10 g are removed to leave a 10 g weight hanging at the PBA free end. Δp, Δx and Δy are measured.
- fifth experiment: finally, the last 10 g are removed. Δp, Δx and Δy are measured. Since the PBA is no more loaded, $\Delta x = \Delta x_0$ and $\Delta y = \Delta y_0$.

The results of this hysteresis study are presented in Fig. 5.39 to 5.46:

- As can be seen in Fig. 5.39 and 5.40, it can be concluded that Δp presents nearly no hysteresis with respect to the weight w. Indeed, 0.5 Pa is the maximum difference in pressure variation measured during the hysteresis loops, when comparing the increasing and decreasing phases of w (the accuracy on a pressure variation measurement is $\leq \pm 4$ Pa).
- As can be seen in Fig. 5.41 and 5.42, it can be concluded that Δx presents a hysteresis with respect to the weight w: when comparing the increasing and decreasing phases of w, the maximum difference in X-displacement that has been measured is smaller than 0.26 mm (the accuracy on the measurement of Δx equals ± 0.13 mm).
- As can be seen in Fig. 5.44, it can be concluded that Δy presents a hysteresis with respect to the weight w: when comparing the increasing and decreasing phases of w during the third hysteresis loop, the maximum difference in Y-displacement that has been measured is larger than 0.26 mm. In Fig. 5.43, the maximum difference in Y-displacement that has measured during the first and second hysteresis loops is smaller than 0.26 mm (the accuracy on the measurement of Δy equals ± 0.13 mm).

The hysteresis of Δx and Δy with respect to the weight w is not taken into account in the experimental models $\Delta x = \Delta x(u, w)$ and $\Delta y = \Delta y(u, w)$ established previously.

In conclusion, to properly model the hysteresis of Δx_0 and Δy_0 with respect to the piston displacement u and the hysteresis of Δx and Δy with respect to the weight w, new experimental models should be established. To do so, more hysteresis loops as the ones presented above should be performed to better understand the hysteresis behaviour of the variables. Besides, complementary hysteresis tests have to be performed because the variables Δp, Δx and Δy depend on w but also on u; however, only their hysteresis with respect to w has been studied. To study the hysteresis of these variables with respect to u, the following tests can be performed:

- a given weight w is attached at the PBA free and Δx and Δy are measured while u performs cycles (one cycle = increasing phase + decreasing phase). This allows to study the hysteresis of Δx and Δy with respect to u.

- while u performs cycles, the same weight is hung and then removed from the PBA free end and Δp is measured. This allows to study the hysteresis of Δp with respect to u.

Before modeling the hysteresis, it has to be assessed whether this hysteresis is problematic or not with respect to the targeted application. Indeed, for a given application, the hysteresis of the variables may be small enough to be negligible; in this case, there is no need to model the hysteresis. On the other hand, for another application, the hysteresis of the variables may be too large to be ignored; in this case, it has to be modeled properly.

As can be seen in Fig. 5.31 and Fig. 5.32, the difference between the pressure p measured during the hysteresis study and the experimental model $p = p(u)$ equals about 1 kPa. This difference can be explained by a change of the ambient atmospheric pressure between the day when the experimental models were established and the day when the hysteresis loops were performed. This will be discussed later in more details.

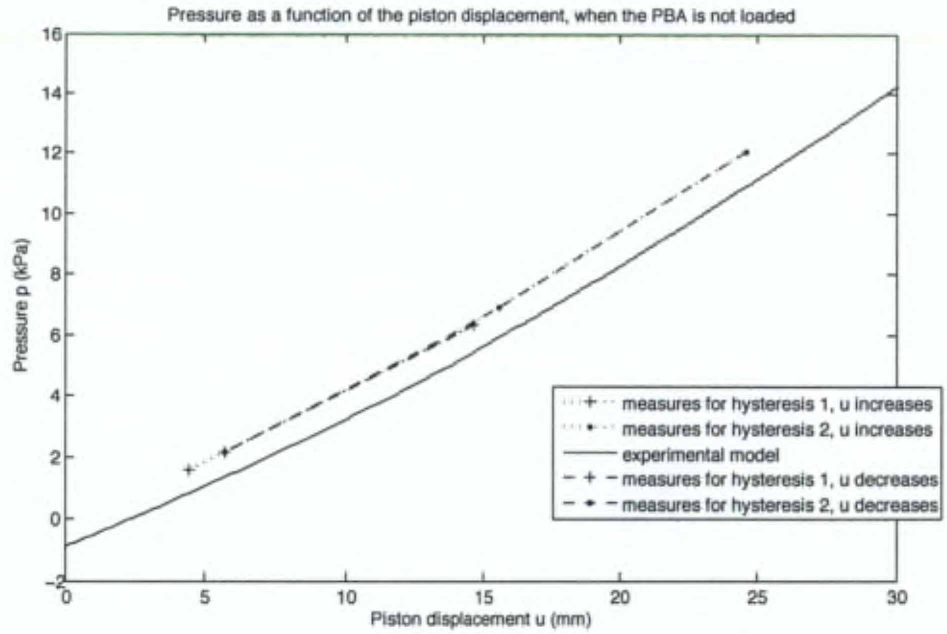

Figure 5.31: Hysteresis study of the pressure p with respect to the piston displacement u, when the PBA is not loaded: the test bench piston describes two cycles (one cycle = increasing phase of u + decreasing phase of u) during which p is measured. As can be seen, the pressure p presents nearly no hysteresis with respect to the piston displacement u.

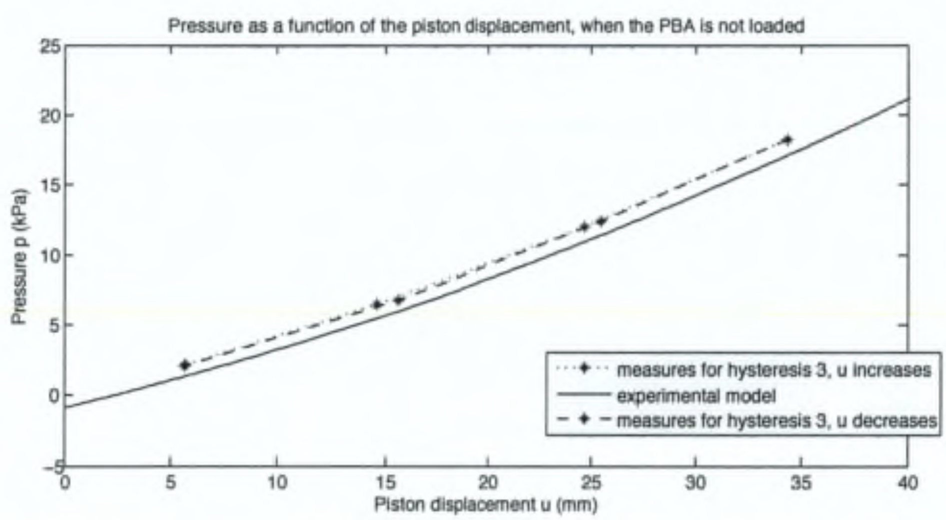

Figure 5.32: Hysteresis study of the pressure p with respect to the piston displacement u, when the PBA is not loaded: the test bench piston describes one cycle (one cycle = increasing phase of u + decreasing phase of u) during which p is measured. As can be seen, the pressure p presents nearly no hysteresis with respect to the piston displacement u.

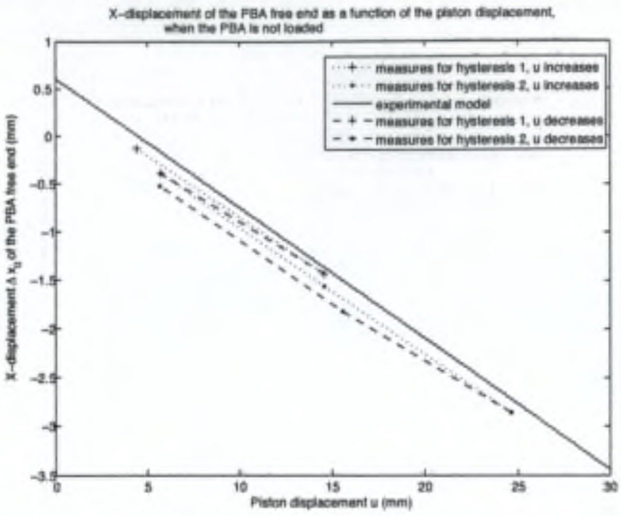

Figure 5.33: Hysteresis study of the X-displacement Δx_0 of the PBA free end with respect to the piston displacement u, when the PBA is not loaded: the test bench piston describes two cycles (one cycle = increasing phase of u + decreasing phase of u) during which Δx_0 is measured. As can be seen in the figure, it can be concluded that the X-displacement Δx_0 presents a hysteresis with respect to the piston displacement u: the maximum difference in X-displacement measured during the hysteresis loops is about 0.26 mm (the accuracy on the measurement of Δx_0 equals ± 0.13 mm).

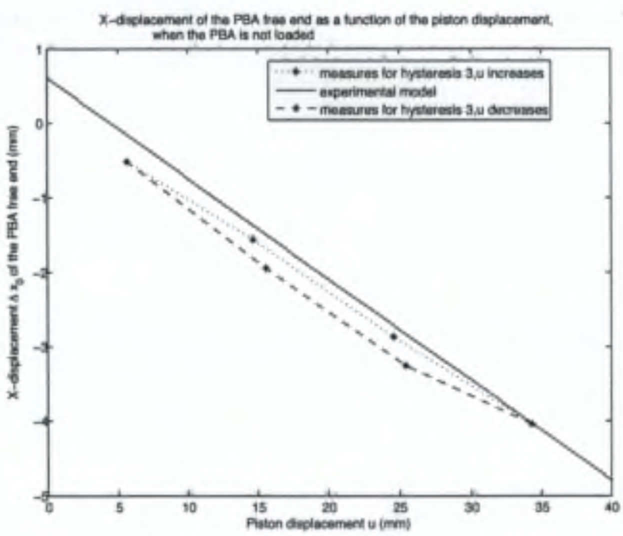

Figure 5.34: Hysteresis study of the X-displacement Δx_0 of the PBA free end with respect to the piston displacement u, when the PBA is not loaded: the test bench piston describes one cycle (one cycle = increasing phase of u + decreasing phase of u) during which Δx_0 is measured. As can be seen in the figure, it can be concluded that the X-displacement Δx_0 presents a hysteresis with respect to the piston displacement u: the maximum difference in X-displacement measured during the hysteresis loops is about 0.26 mm (the accuracy on the measurement of Δx_0 equals ± 0.13 mm).

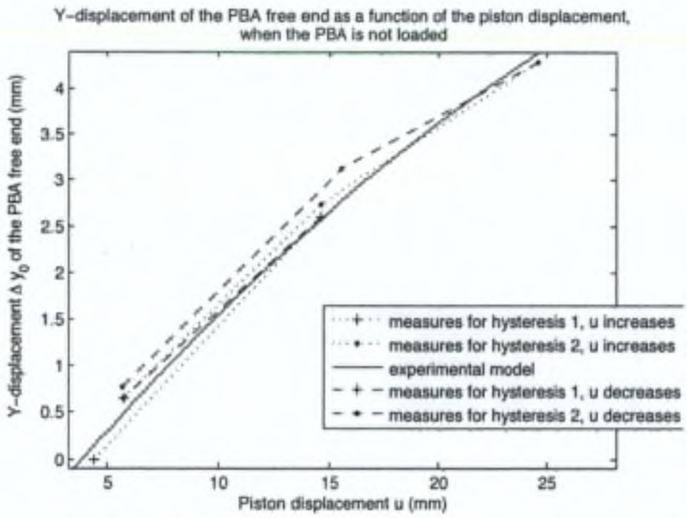

Figure 5.35: Hysteresis study of the Y-displacement Δy_0 of the PBA free end with respect to the piston displacement u, when the PBA is not loaded: the test bench piston describes two cycles (one cycle = increasing phase of u + decreasing phase of u) during which Δy_0 is measured. As can be seen in the figure, it can be concluded that the Y-displacement Δy_0 presents a hysteresis with respect to the piston displacement u: the maximum difference in Y-displacement measured during the hysteresis loops is larger than 0.26 mm (the accuracy on the measurement of Δy_0 equals ± 0.13 mm).

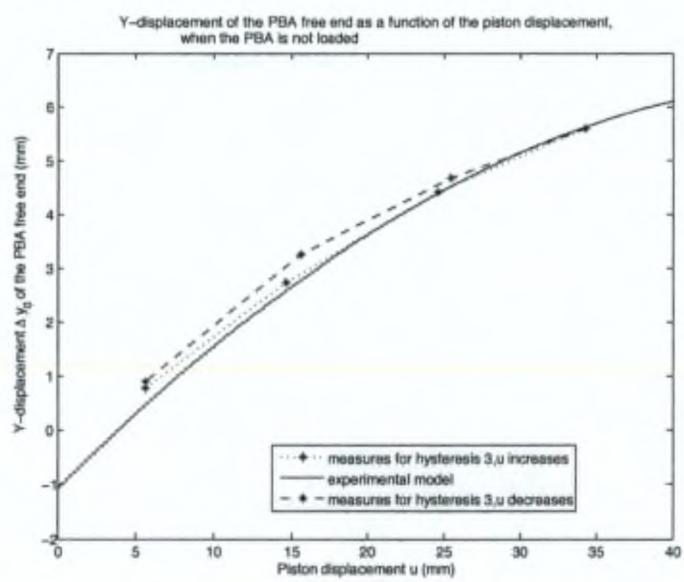

Figure 5.36: Hysteresis study of the Y-displacement Δy_0 of the PBA free end with respect to the piston displacement u, when the PBA is not loaded: the test bench piston describes one cycle (one cycle = increasing phase of u + decreasing phase of u) during which Δy_0 is measured. As can be seen in the figure, it can be concluded that the Y-displacement Δy_0 presents a hysteresis with respect to the piston displacement u: the maximum difference in Y-displacement measured during the hysteresis loops is larger than 0.26 mm (the accuracy on the measurement of Δy_0 equals ± 0.13 mm).

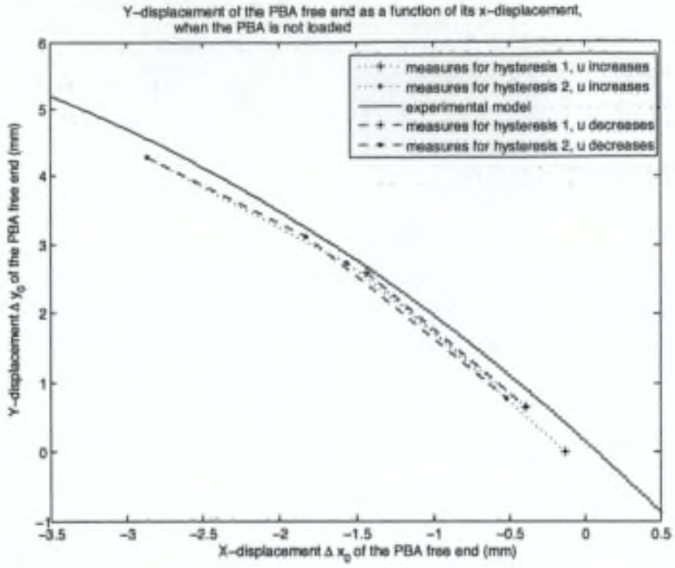

Figure 5.37: Hysteresis study of the X- and Y-displacements Δx_0 and Δy_0 of the PBA free end with respect to the piston displacement u, when the PBA is not loaded: the test bench piston describes two cycles (one cycle = increasing phase of u + decreasing phase of u) during which Δx_0 and Δy_0 are measured.

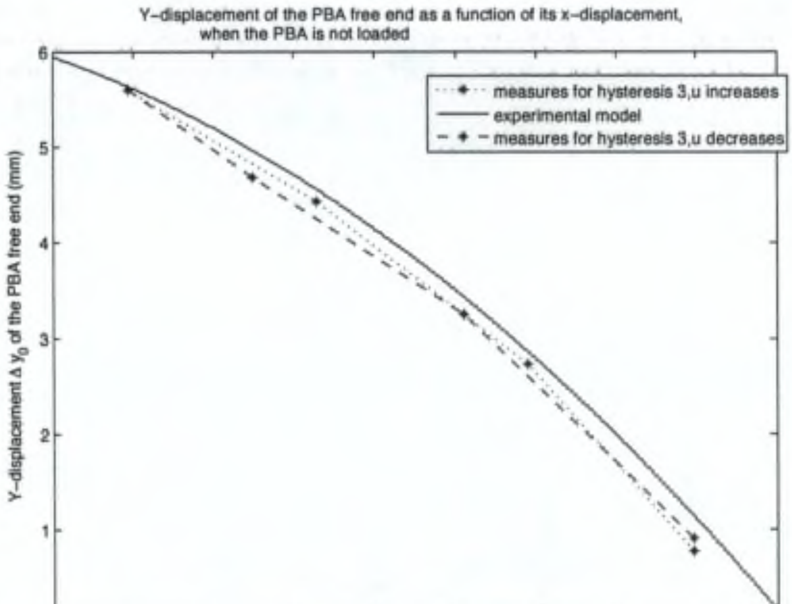

Figure 5.38: Hysteresis study of the X- and Y-displacements Δx_0 and Δy_0 of the PBA free end with respect to the piston displacement u, when the PBA is not loaded: the test bench piston describes one cycle (one cycle = increasing phase of u + decreasing phase of u) during which Δx_0 and Δy_0 are measured.

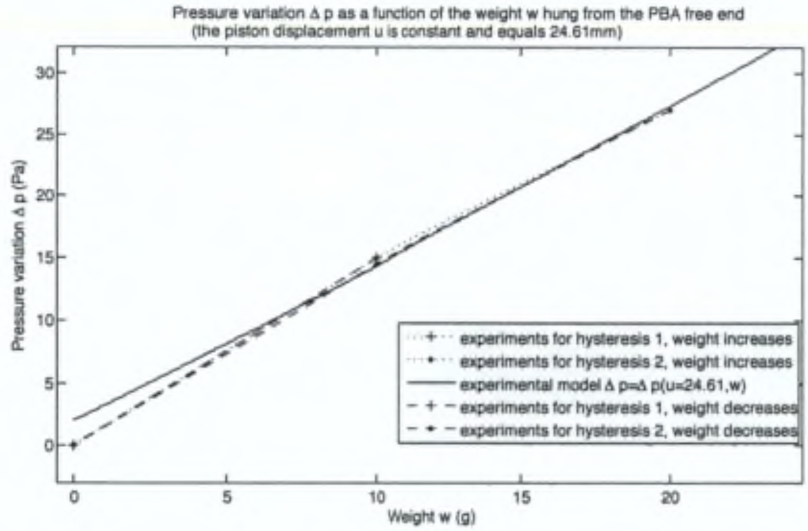

Figure 5.39: Hysteresis study of the pressure variation Δp with respect to the weight w hung from the PBA free end: the test bench piston is fixed at a given position $u = 24.61$ mm and two loading cycles of the PBA are performed (one cycle = increasing phase of w + decreasing phase of w) during which Δp is measured. As can be seen in the figure, it can be concluded that Δp presents nearly no hysteresis with respect to the weight w. Indeed, 0.5 Pa is the maximum difference in pressure variation measured during the hysteresis loops (the accuracy on a pressure variation measurement is $\leq \pm 4$ Pa).

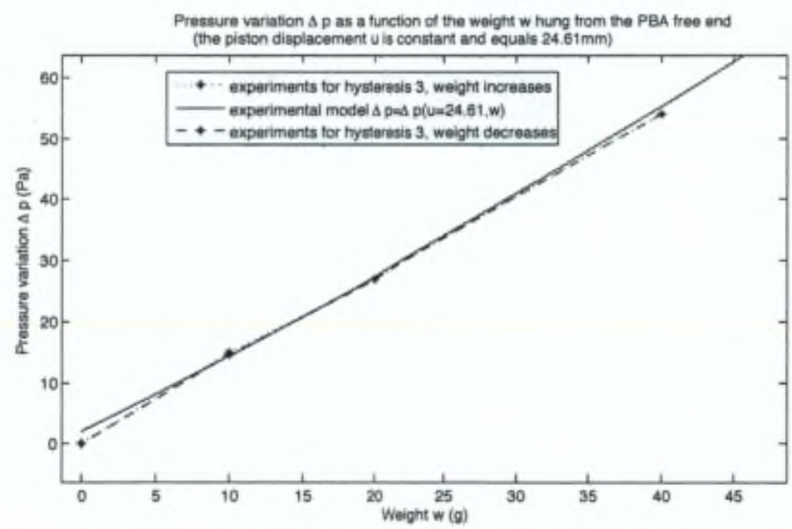

Figure 5.40: Hysteresis study of the pressure variation Δp with respect to the weight w hung from the PBA free end: the test bench piston is fixed at a given position $u = 24.61$ mm and one loading cycle of the PBA is performed (one cycle = increasing phase of w + decreasing phase of w) during which Δp is measured. As can be seen in the figure, it can be concluded that Δp presents nearly no hysteresis with respect to the weight w. Indeed, 0.5 Pa is the maximum difference in pressure variation measured during the hysteresis loops (the accuracy on a pressure variation measurement is $\leq \pm 4$ Pa).

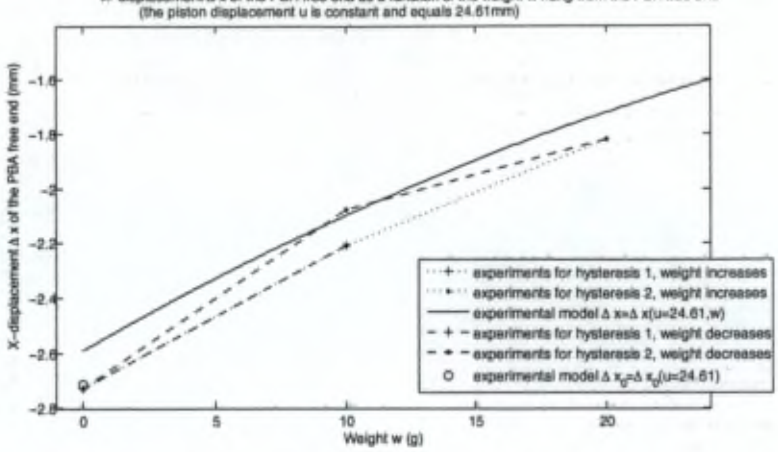

Figure 5.41: Hysteresis study of the X-displacement Δx of the PBA free end with respect to the weight w hung from the PBA free end: the test bench piston is fixed at a given position $u = 24.61$ mm and two loading cycles of the PBA are performed (one cycle = increasing phase of w + decreasing phase of w) during which Δx is measured. As can be seen in the figure, it can be concluded that Δx presents a hysteresis with respect to the weight w: the maximum difference in X-displacement measured during the hysteresis loops is smaller than 0.26 mm (the accuracy on the measurement of Δx equals ± 0.13 mm).

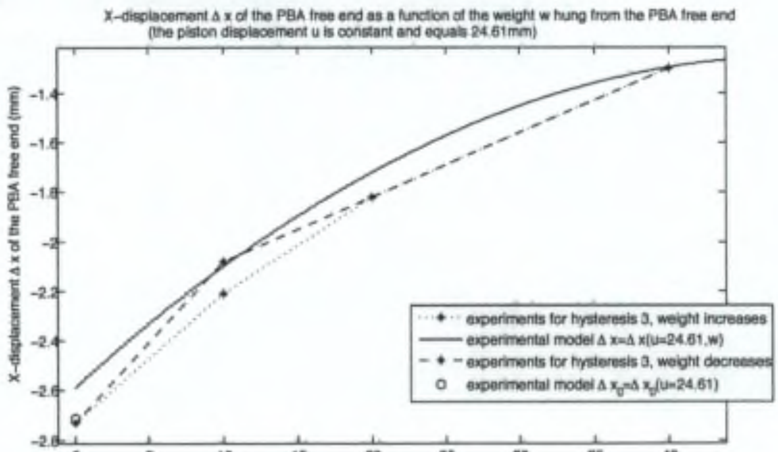

Figure 5.42: Hysteresis study of the X-displacement Δx of the PBA free end with respect to the weight w hung from the PBA free end: the test bench piston is fixed at a given position $u = 24.61$ mm and one loading cycle of the PBA is performed (one cycle = increasing phase of w + decreasing phase of w) during which Δx is measured. As can be seen in the figure, it can be concluded that Δx presents a hysteresis with respect to the weight w: the maximum difference in X-displacement measured during the hysteresis loops is smaller than 0.26 mm (the accuracy on the measurement of Δx equals ± 0.13 mm).

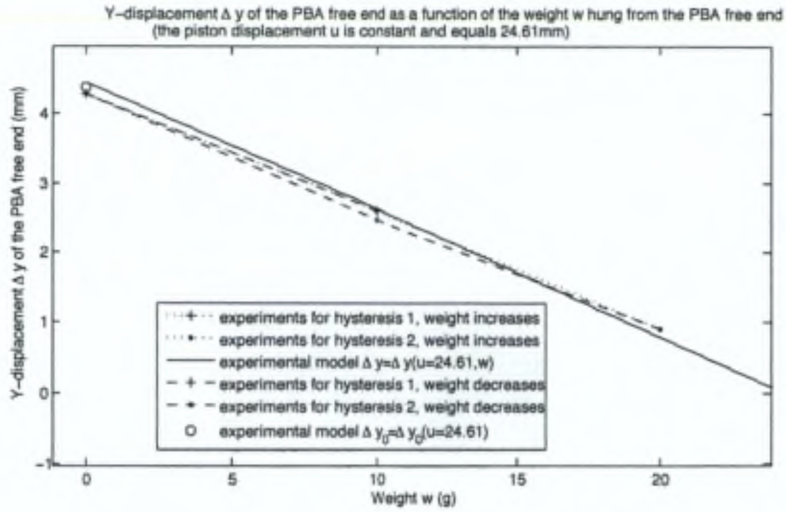

Figure 5.43: Hysteresis study of the Y-displacement Δy of the PBA free end with respect to the weight w hung from the PBA free end: the test bench piston is fixed at a given position $u = 24.61$ mm and two loading cycles of the PBA are performed (one cycle = increasing phase of w + decreasing phase of w) during which Δy is measured. As can be seen in the figure, it can be concluded that Δy presents a hysteresis with respect to the weight w: the maximum difference in Y-displacement measured during the hysteresis loops is smaller than 0.26 mm (the accuracy on the measurement of Δy equals ± 0.13 mm).

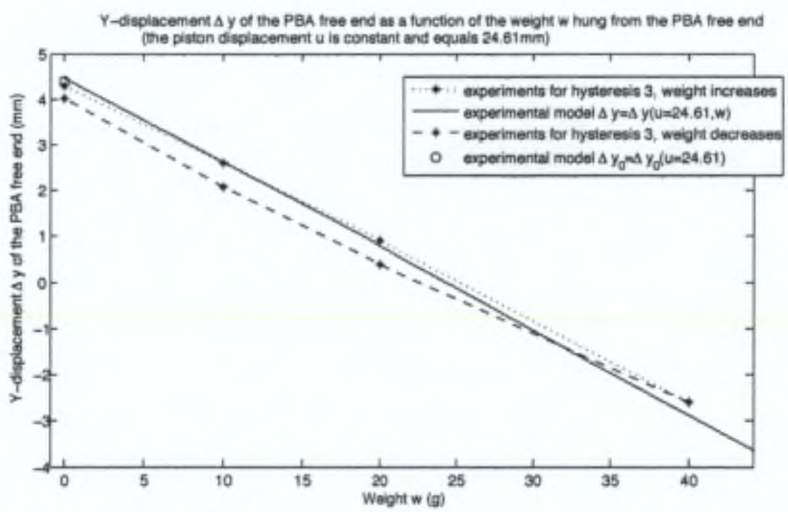

Figure 5.44: Hysteresis study of the Y-displacement Δy of the PBA free end with respect to the weight w hung from the PBA free end: the test bench piston is fixed at a given position $u = 24.61$ mm and one loading cycle of the PBA is performed (one cycle = increasing phase of w + decreasing phase of w) during which Δy is measured. As can be seen in the figure, it can be concluded that Δy presents a hysteresis with respect to the weight w: the maximum difference in Y-displacement measured during the third hysteresis loop is larger than 0.26 mm (the accuracy on the measurement of Δy equals ± 0.13 mm).

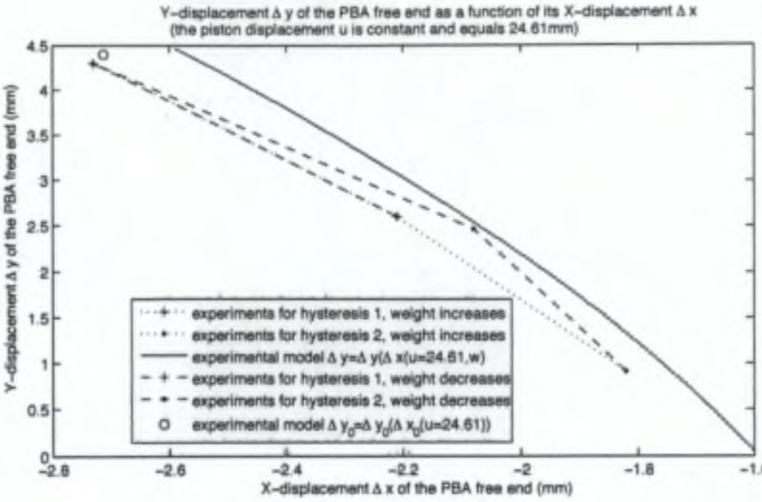

Figure 5.45: Hysteresis study of the X- and Y-displacements Δx and Δy of the PBA free end with respect to the weight w hung from the PBA free end: the test bench piston is fixed at a given position $u = 24.61$ mm and two loading cycles of the PBA are performed (one cycle = increasing phase of w + decreasing phase of w) during which Δx and Δy are measured.

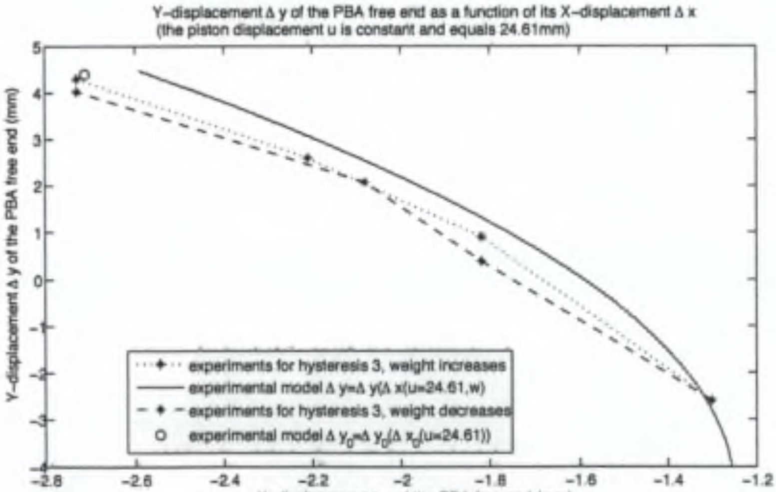

Figure 5.46: Hysteresis study of the X- and Y-displacements Δx and Δy of the PBA free end with respect to the weight w hung from the PBA free end: the test bench piston is fixed at a given position $u = 24.61$ mm and one loading cycle of the PBA is performed (one cycle = increasing phase of w + decreasing phase of w) during which Δx and Δy are measured.

5.3 Discussion

5.3.1 Relevance of the PVFP principle

Being able to determine the displacement of a flexible fluidic actuator and the force it develops thanks to the measurements of the fluid pressure and of the volume of the supplied fluid, means being able to determine the displacement and the force without a displacement sensor or a force sensor placed on the actuator [79].

This is an interesting measuring concept for applications where the space is limited and where a miniaturization effort is required. This is for example the case in Teleoperated Minimally Invasive Surgery (MIS), where it is necessary to measure the force applied by the tools to the organs to ensure a force feedback of good quality. However, this measurement is not straightforward. Indeed, if the force sensor is placed outside the body of the patient, the measurement will be polluted by the friction of the trocar. To solve this problem, some researchers propose to place the sensor at the end of the tool but this raises the challenge to develop a small and sterilizable force sensor [64]. Using flexible fluidic actuators to actuate the surgical tools would allow to measure the force applied to the organs without the need of a force sensor. Besides, flexible fluidic actuators could also answer the need for flexible instruments, i.e. instruments presenting a large number of DOFs and able to perform snake-like movements when avoiding obstacles. This need has been expressed by the medical field in applications such as the MIS [33], the endoluminal surgery [4] or the active catheters [46].

In [53], a flexible sensor to be placed under the PBA is proposed. It is a flexible plate presenting a pneumatic channel. Airflow is supplied to the channel and the bending of the PBA is detected by measuring the airflow changes in the channel. Besides, measuring the airflow changes in the channel and the pressure inside the PBA allows to determine the stiffness of an object in contact with the PBA. If the PVFP principle was implemented on this PBA, it would allow doing the same measurements without such an additional sensor. Indeed, a piston displacement u could be performed so that the PBA bends and comes in contact with the object to palpate. The PVFP principle allows then to determine the contact force F between the PBA and the object and the displacement Δz the PBA has performed while pushing on the object. These two informations can then be used to determine the stiffness $F/\Delta z$ of the object.

The PVFP principle has been experimentally validated with the PBA, i.e. an actuator presenting only one DOF. With such an actuator, the applied force can be predicted at only one precise point and along only one precise direction. However, the principle could be applied to more complex structures. For example, let us consider the "Flexible Microactuator" described in [79] (see Fig. 5.47). It is a cylinder whose end is closed and which presents three internal chambers. It is composed of silicone rubber reinforced with nylon fibres disposed in a circular direction. The function of these fibres is to prevent radial deformations. When one chamber is pressurized, the cylinder bends in the direction opposite this chamber. This actuator presents three DOFs (one stretching and two bending motions). Measuring the pressure in the three chambers and the fluid volume supplied to the chambers would allow to determine the posture of the actuator and the three components of any force applied to a precise given point, for example, to the end point of the actuator.

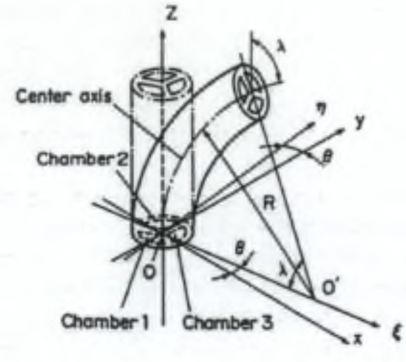

Figure 5.47: Bending Flexible Microactuator (FMA): when a chamber is pressurized, its length increases while the other chambers keep their initial length and consequently the cylinder bends in the direction opposite the pressurized chamber. The figure presents a bending FMA whose chambers no. 1 and 2 are pressurized. Figure from [73].

5.3.2 Practical implementation of the PVFP principle in a targeted application

As can be seen in Fig. 5.26 and 5.27, for a given piston displacement u, there exists a duality between the force developed by the PBA free end (or in other words, the weight attached to its end) and the displacements Δx and Δy of its tip: if the load of the PBA increases, the PBA free end moves downwards and the displacements Δx and Δy decrease in absolute value. It is thus not possible to impose the displacements of the PBA tip and the force it develops at the same time. In practical applications, a choice will have to be made between imposing the force and imposing the displacements, according to the task to be performed.

The PVFP principle could be implemented in a control loop in order to control the displacement of a flexible fluidic actuator tip or the force it develops, without using displacement or force sensor. If the dynamics of the system are quite slow, static models such as those established for the PBA in this chapter can be used in the control loop. Hence, the control loop makes a quasi-static approximation of the system dynamics. For example, to control the actuator displacement, the control loop presented in Fig. 5.48 can be build. It works as follows:

1. The actuator is required to perform a displacement Δy^*.
2. Δy^* is compared to the predicted displacement Δy.
3. The difference $\Delta y^* - \Delta y$ is the input of the model of the flexible fluidic actuator. Knowing the value of the predicted external force F_{ext} applied to the actuator, the model determines the piston displacement u^* that needs to be performed in order to reach Δy^*.
4. u^* is compared to the actual measured piston displacement u and the difference $u^* - u$ is the input of a controller. It acts on the physical system so that the required piston displacement is achieved. The physical system comprises the flexible fluidic actuator and the syringe-pump pressurization system.
5. The piston displacement u and the pressure p are measured on the physical system.

6. On the basis of the measurements u and p, the model of the flexible fluidic actuator predicts the displacement Δy performed by the actuator and the external force F_{ext} applied to the actuator. These predictions are then used as if they were measurements.

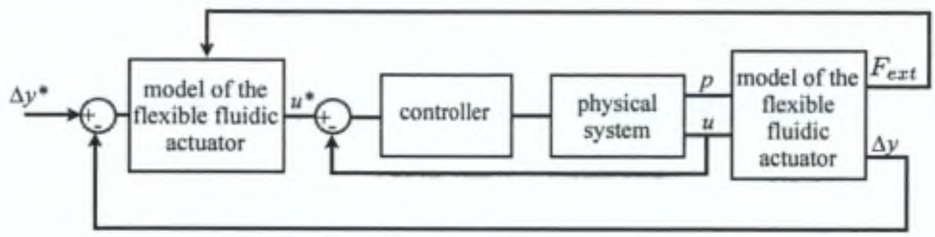

Figure 5.48: Control loop in which the PVFP principle is implemented in order to control the displacement Δy of the flexible fluidic actuator, without using force or displacement sensors.

The quality of the predictions provided by the PVFP principle implemented on the flexible fluidic actuator has to be evaluated with respect to the targeted application. Indeed, the predictions can be accurate enough for a given application but not for another one.
The same remark can be made if the actuator presents hysteresis. Before modeling the hysteresis, it has to be assessed whether this hysteresis is problematic or not with respect to the targeted application. Indeed, for a given application, the hysteresis may be small enough to be negligible; in this case, there is no need to model the hysteresis. On the other hand, for another application, the same hysteresis may be too large to be ignored; in this case, it has to be modeled properly.

The practical implementation of the PVFP principle raises some questions such as the effect that a variation of the ambient atmospheric pressure or temperature would have on the predictions provided by the PVFP principle. This question has already been discussed in Section 5.1.1 in the case of a simple flexible fluidic actuator but it would be interesting to try answering this question in the case of the PBA studied here. Fig. 5.49 presents a schematic view of the PBA linked to the cylinder of the test bench. The actuation fluid is air but the PVFP principle should also work with an incompressible fluid. Maybe a difference happens when a weight is hung from the PBA free end: since the volume in the cylinder will not change because the piston position is fixed, the volume of the PBA will not change and the position of the PBA free end will remain the same. On the other hand, it is also possible, thanks to the elasticity of the PBA rubber that the PBA free end moves downwards while the PBA keeps the same volume.

First, let us consider a change of the atmospheric pressure or ambient temperature happening when using the PBA and the PVFP principle implemented on it:

1. The actuation fluid is incompressible:
   - If the atmospheric pressure increases by an amount p^*, the absolute outside pressure p_{out} increases by the same amount. The volume of the PBA does not change because the volume of fluid inside the cylinder does not change and since the atmospheric pressure is applied to the top of the PBA as well as on its underside, the atmospheric pressure increase will not modify the displacements of point A. Since the shape of the PBA does not change, the inner absolute pressure p_{in} will probably increase by the same amount as p_{out} and the PVFP principle implemented on the actuator perceives this as the application of a load w^* that would have decreased the displacement of the PBA free end. The predictions of the PVFP

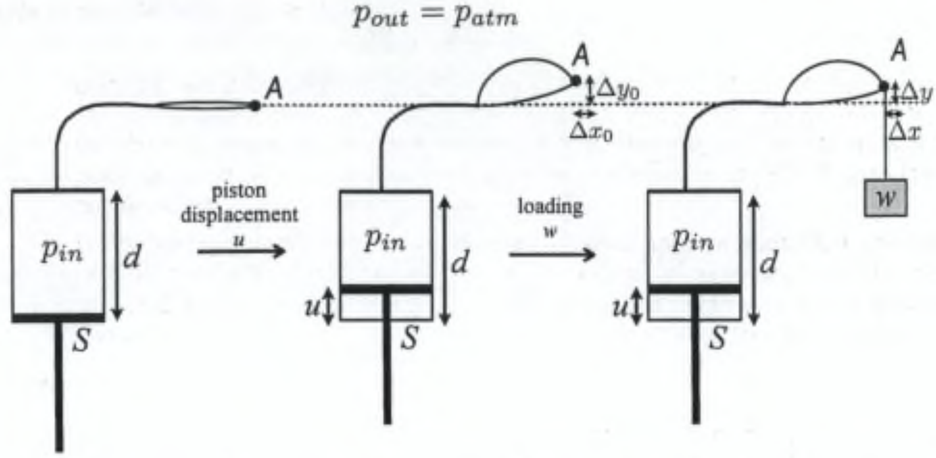

Figure 5.49: Pneumatic Balloon Actuator (PBA) linked to the cylinder of the test bench. The actuation fluid is air. When a displacement u is imposed to the piston, the inner pressure p_{in} increases and the PBA inflates and its free end A moves upwards. The vertical and horizontal displacements of this point are Δy_0 and Δx_0, respectively. Afterwards, keeping the piston position constant, if a weight w is hung from the PBA free end, the inner pressure p_{in} increases and the displacements Δy and Δx of the PBA free end decrease. According to the PVFP principle, knowing the values of p_{in} and u allows to determine the displacements of point A and the value of the weight w.

principle are distorted but to get rid of the influence of an atmospheric pressure change, a gauge pressure sensor could be used to measure p_{in} (it was the case for the experiments performed on the PBA in this chapter) or the atmospheric pressure could be measured so that the false prediction of the PVFP principle can be corrected.

- If the ambient temperature increases by a small amount such that the volume of fluid does not change (no expansion), it will have no influence on the results provided by the PVFP principle, i.e. the predictions of the actuator displacement and of the external pressure applied to the membrane will not be distorted.

2. The actuation fluid is compressible.

   - If the atmospheric pressure increases by an amount p^*, the absolute outside pressure p_{out} increases by the same amount, the volume of the PBA decreases and point A moves downwards. p_{in} increases but probably not by the same amount as p_{out}. The PVFP principle implemented on the actuator perceives the change of the atmospheric pressure as the application of a load w^* that would have decreased the vertical displacement of point A. However, it is not sure that using this prediction would allow to compensate correctly the change of the displacements of point A. The PVFP principle does not allow to distinguish a change of the atmospheric pressure from the application of a load to the PBA free end; to be able to do so, it is necessary to measure the atmospheric pressure.
   - If the ambient temperature increases, the volume of fluid expands in the actuator. Since the volume V' in the cylinder does not change because the piston position is imposed, the volume of the PBA increases and point A moves upwards. The inner pressure p_{in} increases and the PVFP principle implemented on the actuator perceives this change as the application of a load $w*$ that would have decreased

the vertical displacement of point A. Hence, the prediction of the PVFP principle can not be used to compensate the change of displacements of point A due to the temperature increase; indeed, doing so would lead to a further increase of the displacement of this point! The temperature needs thus to be measured and taken into account in the implementation of the PVFP principle and its effect on the PBA free end displacement needs to be compensated.

In conclusion, the PVFP principle seems applicable to the PBA with an incompressible or a compressible actuation fluid. Besides, if the PVFP principle is implemented on the PBA with an incompressible fluid and a gauge pressure to measure p_{in}, it seems that the predictions provided by the PVFP principle implemented on the actuator will not be influenced by the changes of the atmospheric pressure and of the temperature, occuring during the use of the actuator.

During the experiments described in this chapter, the actuation fluid that has been used is air. Since the fluidic circuit presents some leakages, it is refilled with air at atmospheric pressure before each use of the test bench. A change of atmospheric pressure or ambient temperature can then happen between the day when the models were established and the day when the test bench is used again and refilled with air, whose initial pressure or temperature has thus changed.
During the use of the PBA, the quantity of gas is constant and if the temperature is constant, the gas law leads to the following equation:

$$\frac{p_{atm}Sd}{T} = \frac{p_{in}(V_{PBA} + S(d-u))}{T} \tag{5.25}$$

As can be seen, if the temperature is constant during the use of the actuator, it has no effect on the equation. Hence, if the ambient temperature was $T = T_1$ the day when the experimental models have been established and $T = T_2$ the day when the test bench has been refilled with air, the difference between T_1 and T_2 will have no influence on equation (5.25) and the experimental models on which the PVFP rests will still be valid.
If the atmospheric pressure was $p_{atm} = p_{atm\_1}$ the day when the experimental models have been established and $p_{atm} = p_{atm\_2}$ the day when the test bench has been refilled with air, the experimental models on which the PVFP rests will no more be valid due to the difference between p_{atm_1} and p_{atm_2} and its influence on equation (5.25). This is what happened with the hysteresis studies presented in Section 5.2.3. Since equation (5.25) had changed, the relationship between p_{in} and u changed also, as can be seen in Fig. 5.31 and 5.32 when the PBA was not loaded.
Again, with an incompressible fluid, such a change of the atmospheric pressure seems to have no influence on the PVFP principle, if a gauge pressure is used or if the atmospheric pressure is monitored.

As explained in Section 5.1 and above for the PBA, the PVFP principle seems to work for those flexible fluidic actuators whatever the actuation fluid (compressible or incompressible). Hence, for medical applications where gas leakages are forbidden, the PVFP principle can be implemented on these flexible fluidic actuators actuated by an incompressible physiological saline solution.

Replacing gas by liquid brings also the advantage that the system gets rid of the compressibility of the actuation fluid. During the experiments presented in this chapter, it has been noticed that the gas pressure takes several minutes to stabilize after a piston displacement. This can be seen in Fig. 5.50 when the piston displacement decreases from $u = 34.35$ mm to $u = 5.7$ mm. As can be noticed, the pressure decreases until a minimum value and then

slightly increases to reach a stabilized value after approximately 3 minutes (the stabilization of the pressure can not be seen in the figure).
Fig. 5.51 presents what happens if the piston displacement increases from $u = 5.7$ mm to $u = 34.36$ mm. As can be seen, the pressure increases until a maximum value and then decreases slightly to reach a stabilized value after approximately 4.3 minutes (the stabilization of the pressure can not be seen in the figure).
The fact that the pressure needs a long time to stabilize can be accredited to the gas compressibility, to the elasticity of the pneumatic tubes and to the elasticity of the flexible fluidic actuator. Studying the quantitative effect of each of these three causes would help to determine which action to take in order to reduce the establishment time of the pressure in the fluidic circuit and to increase the bandwidth of the system.
However, before performing this study, it would be interesting to study the sensibility of the actuator displacements with regard to the pressure establishment. Indeed, as can be seen in Fig. 5.50 and 5.51, in the case of the test bench used in this chapter, when the pressure establishes itself, its variation is of maximum 1 kPa. If this variation has a small effect on the actuator displacements, it may be superfluous to make a thorough study of the pressure dynamics.
Remark: In the experiments described in this chapter, the measurements have been made once the pressure had stabilized.

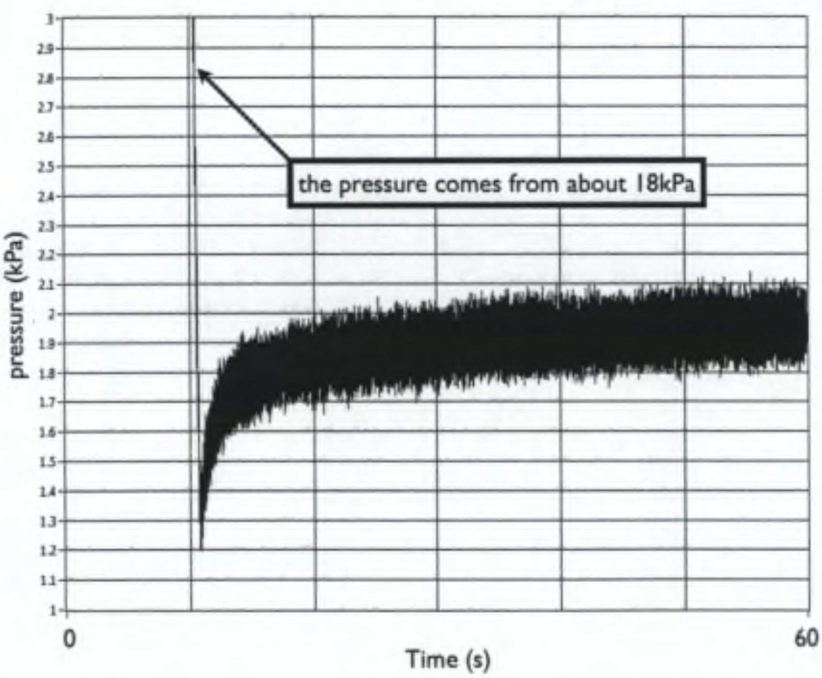

Figure 5.50: Evolution of the pressure in the test bench fluidic circuit when the piston displacements decreases from $u = 34.35$ mm to $u = 5.7$ mm.

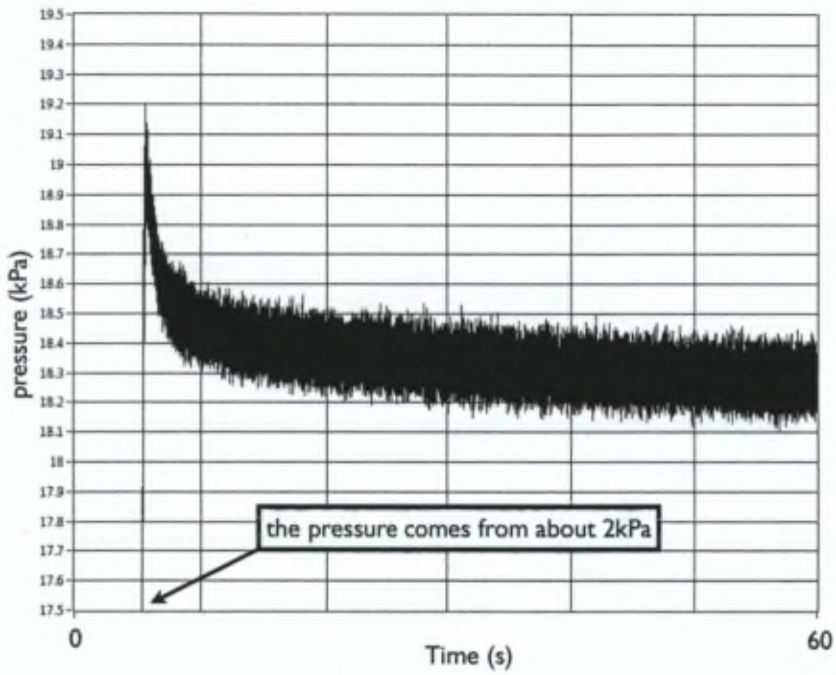

Figure 5.51: Evolution of the pressure in the test bench fluidic circuit when the piston displacement increases from $u = 5.7$ mm to $u = 34.36$ mm.

However, replacing gas by liquid implies larger pressure losses whose effect has to be studied. Besides, a flexible fluidic actuator filled with liquid will be heavier and as a consequence it will develop smaller displacements, for a given pressure level, than the same actuator filled with gas. Hence, the actuator will probably present a pressure threshold because a minimum pressure level will be required to compensate the weight of the liquid. An actuator filled with liquid will also be less compliant.

Chapter 6

Model of the Pneumatic Balloon Actuator

6.1 Introduction

This chapter presents a 2D-model of the Pneumatic Balloon Actuator (PBA); it has been established by modeling the physics that seem to underly the behaviour of this actuator. Section 6.2 presents the assumptions and equations on which the model rests and it describes the numerical method developed to solve these equations. Afterwards, Section 6.3 compares the results provided by the numerical model with the experiments performed on two prototypes of PBA. Finally, Section 6.4 discusses and concludes about the developed model.

Remark: The equations of the model have been established by the BEAMS department of the ULB while the solving method of these equations has been developed and implemented in a software by Benjamin Gorissen of the PMA department of the KUL, during its Master's thesis under the supervision of Michäel De Volder.

6.2 Model

The aim of the model is to predict the evolutions, with respect to the pressure, of the vertical and the horizontal displacements (Δy and Δx respectively in Fig. 6.1) of the free end of a PBA (point A in Fig. 6.1).
The assumptions on which the model rests are the following:

1. When pressurized, the PBA deforms in such a way that its cross-section is identical along its width; this cross-section is presented in Fig. 6.1. What happens in the surroundings of the PBA outline is thus assumed to be negligible and this first hypothesis allows an analysis in two dimensions (in the plane xy) of the PBA.

2. The PBA is fixed as a cantilever so that its upper layer is the thinner one of its two layers.

3. The lower layer is modelled as a beam and will hereafter be referred to as "beam".

4. The upper layer is modelled as a membrane and will hereafter be referred to as "membrane".

5. The shear stresses are negligible in the membrane.

6. The normal stresses σ are uniform in the membrane.

7. The membrane thickness e is uniform and remains unchanged when the PBA is pressurized (Poisson's effect is thus assumed to be negligible).

8. The membrane material is homogeneous and follows Hooke's law. The Young's modulus of the membrane E_m is thus assumed to remain unchanged when the membrane deforms.

9. Bernoulli's law is verified for the beam: in the deformed configuration, the straight sections remain plane and perpendicular to the axis of the beam and to all fibres of the beam [39], no warping occurs.

10. The beam material is homogeneous and follows Hooke's law. The Young's modulus of the beam E_b is thus assumed to remain unchanged when the beam deforms.

11. The beam displacements due to shear and normal forces are negligible in comparison to those due to the bending moment.

12. The weights of the beam, the membrane and of the gas inside the PBA are negligible.

13. The pressure p is homogeneous inside the PBA.

14. The beam thickness h (and thus the beam inertia I_b) is uniform and remains unchanged when the PBA is pressurized (Poisson's effect is thus assumed to be negligible).

15. The neutral axis of the beam keeps a constant length L even when the PBA is pressurized.

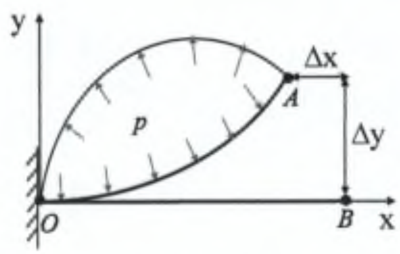

Figure 6.1: Cross-section of a pressurized PBA. The PBA is fixed as a cantilever so that its upper layer is the thinner one of its two layers. The upper layer is modelled as a membrane while the lower one is modelled as a beam. Δy and Δx are the vertical and horizontal displacements of the free end A of the PBA. At rest, OB is the position of the lower layer of the PBA.

Under hypotheses 4 and 5, the behaviour of the membrane is ruled by the Laplace's equation [22]:

$$\gamma(\frac{1}{r_1} + \frac{1}{r_2}) = p_{in} - p_{out} \tag{6.1}$$

where γ is the surface tension in the membrane, r_1 and r_2 are the principal curvature radii of the membrane and $p_{in} - p_{out}$ is the pressure difference between the inside and the outside of the membrane. p_{out} will here assumed to be zero and the pressure inside the membrane will be noted as p. Due to hypothesis 1, one curvature of the membrane is zero and (6.1) becomes

$$\frac{\gamma}{r} = p, \tag{6.2}$$

where r is the radius of curvature of the membrane. Due to hypothesis 6, the surface tension is uniform in the membrane. As a consequence, r is constant along the membrane which thus takes the shape of an arc of circle.
Under hypotheses 3, 9, 10 and 11, the deformation of the beam is ruled by the Euler-Bernoulli's equation [39]:

$$\frac{1}{R(s)} = \frac{M(s)}{E_b I_b}, \tag{6.3}$$

where R is the curvature radius of the beam, M is the bending moment due to the loads applied to the beam and $I_b = \frac{bh^3}{12}$, with b the width of the PBA (along axis z). As shown in Fig. 6.2, the beam is subjected to a concentrated load $\overline{F}$ applied by the pressurized membrane and to pressure p (i.e. a distributed load), or more precisely to $q = pb$. P is the

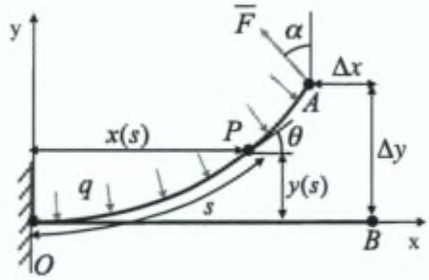

Figure 6.2: Loads applied to the PBA lower layer, which is modelled as a beam. The beam is subjected to a concentrated load $\overline{F}$ applied by the pressurized membrane and to pressure p (i.e. a distributed load), or more precisely to $q = pb$. P is the point of the beam where bending moment $M(s)$ is evaluated. Its coordinates are $x(s)$ and $y(s)$. s is the distance along the beam between points O and P. θ is the angle between the horizontal direction and the tangential direction of the beam at point P. α is the angle of inclination of force $\overline{F}$, with reference to the vertical direction. Δy and Δx are the vertical and horizontal displacements of the free end A of the PBA. When the PBA is not pressurized, OB is the position of the beam.

point of the beam where bending moment $M(s)$ is evaluated. Its coordinates are $x(s)$ and $y(s)$. s is the distance along the beam between points O and P and θ is the angle between the horizontal direction and the tangential direction of the beam at point P. Since

$$\frac{1}{R(s)} = \frac{d\theta(s)}{ds} \quad [39], \tag{6.4}$$

(6.3) becomes:

$$\frac{d\theta(s)}{ds} = \frac{M(s)}{E_b I_b}. \tag{6.5}$$

Solving (6.5) gives a function $\theta = \theta(s)$ from which the coordinates of the points of the deformed beam can be computed using the following expressions:

$$x(s) = \int_0^s \cos(\theta(u))du \tag{6.6}$$

$$y(s) = \int_0^s \sin(\theta(u))du. \tag{6.7}$$

The X- and Y-displacements of the PBA free end are given by

$$\Delta x = L - x(L) \tag{6.8}$$

and

$$\Delta y = y(L) \tag{6.9}$$

and the coordinates of end point A are given by

$$x_A = x(L) \tag{6.10}$$

and

$$y_A = y(L). \tag{6.11}$$

For the configuration presented in Fig. 6.2, the expression of bending moment $M(s)$ is:

$$\begin{aligned} M(s) = F\left[\cos(\alpha)(L - \Delta x - x(s)) + \sin(\alpha)(\Delta y - y(s))\right] \\ - \textstyle\int_s^L q\cos(\theta(u))(x(u) - x(s))du \\ - \textstyle\int_s^L q\sin(\theta(u))(y(u) - y(s))du, \end{aligned} \tag{6.12}$$

where F is the norm of force $\overline{F}$ and α is the angle of inclination of force $\overline{F}$, with reference to the vertical direction (see Fig. 6.2). To get rid of the integrals, an equation based on the shearing force dM/ds instead of the bending moment M can be used [24]. To obtain this equation, (6.5) is differentiated with respect to s and, with assumptions 10 and 14, this gives:

$$\frac{d^2\theta(s)}{ds^2} = \frac{1}{E_b I_b}\frac{dM(s)}{ds}. \tag{6.13}$$

To compute the expression of dM/ds, the following formula is used

$$\begin{aligned} \tfrac{d}{ds}\textstyle\int_{w(s)}^{v(s)} f(s,u)du = \tfrac{dv(s)}{ds} f(s, v(s)) - \tfrac{dw(s)}{ds} f(s, w(s)) \\ + \textstyle\int_{w(s)}^{v(s)} \tfrac{\partial f(s,u)}{\partial s} du, \end{aligned} \tag{6.14}$$

and it leads to:

$$\begin{aligned} \tfrac{dM(s)}{ds} = -F\left[\cos(\alpha)\cos(\theta(s)) + \sin(\alpha)\sin(\theta(s))\right] \\ +q\left[\cos(\theta(s))(L - \Delta x - x(s)) + \sin(\theta(s))(\Delta y - y(s))\right]. \end{aligned} \tag{6.15}$$

Equation (6.13) becomes then:

$$\begin{aligned} \tfrac{d^2\theta(s)}{ds^2} = \tfrac{-F}{E_b I_b}\left[\cos(\alpha)\cos(\theta(s)) + \sin(\alpha)\sin(\theta(s))\right] \\ +\tfrac{q}{E_b I_b}\left[\cos(\theta(s))(L - \Delta x - x(s)) + \sin(\theta(s))(\Delta y - y(s))\right], \end{aligned} \tag{6.16}$$

with the boundary conditions

$$\theta|_{s=0} = 0 \tag{6.17}$$

and

$$\tfrac{d\theta}{ds}|_{s=L} = 0. \tag{6.18}$$

Equation (6.16) can be used to compute the X- and Y-displacements Δx and Δy but firstly F and α need to be evaluated. The following equations allow to determine F and α since p is given and since the coordinates (x_A,y_A) of end point A are assumed:

$$\|\overline{OA}\| = \sqrt{(x_A)^2 + (y_A)^2} \tag{6.19}$$

$$\tan(\epsilon) = \frac{y_A}{x_A} \tag{6.20}$$

$$2\beta r = L + \Delta L \tag{6.21}$$

$$\sigma = E_m \frac{\Delta L}{L} \tag{6.22}$$

$$\frac{\gamma}{r} = p \tag{6.23}$$

$$r = \frac{\|\overline{OA}\|}{2\sin(\beta)} \tag{6.24}$$

$$\gamma = \sigma e \tag{6.25}$$

$$F = \gamma b \tag{6.26}$$

$$\alpha = \frac{\pi}{2} - \beta + \epsilon \tag{6.27}$$

where ΔL and $\frac{\Delta L}{L}$ are the lengthening and the strain of the deformed membrane, respectively. Angles ϵ and β are defined as shown in Fig. 6.3.
Equations (6.19), (6.20), (6.21), (6.24) and (6.27) are geometrically deduced from Fig. 6.3. Equation (6.22) is the relation between the stress σ and the strain $\frac{\Delta L}{L}$ of the membrane. Equation (6.23) is the Laplace's equation (6.2). Equation (6.25) is the relation between the surface tension γ and the stress σ of the membrane. Equation (6.26) is the relation between the surface tension γ of the membrane and the norm F of the force $\overline{F}$ developed by the pressurized membrane.

Remark: As can be seen from the previous equations, the model is suitable for compressible as well as for incompressible fluids.

Equation (6.16) has the following shape:

$$\tfrac{d^2\theta(s)}{ds^2} = f(\theta(s)) \tag{6.28}$$

and it can be approximated by the following expression:

$$\tfrac{\theta_{i+1}-2\theta_i+\theta_{i-1}}{(\Delta s)^2} = f(\theta_i), \tag{6.29}$$

with $\theta_i = \theta(s)|_{s=i\Delta s}$, $i = 0, \ldots, N$ and $\Delta s = \frac{L}{N}$ (see Fig. 6.4).

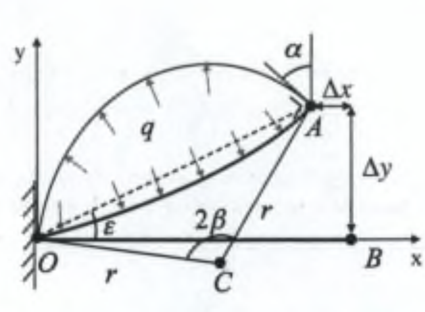

Figure 6.3: Cross-section of a pressurized PBA. The PBA upper layer is modelled as a membrane while the lower one is modelled as a beam. The beam is subjected to a concentrated load $\overline{F}$ applied by the pressurized membrane and to pressure p (i.e. a distributed load), or more precisely to $q = pb$. α is the angle of inclination of force $\overline{F}$, with reference to the vertical direction. C and r are the curvature centre and radius of the deformed membrane, respectively. Angles ϵ and β are defined as shown in the figure. Δy and Δx are the vertical and horizontal displacements of the free end A of the PBA. When the PBA is not pressurized, OB is the position of the beam.

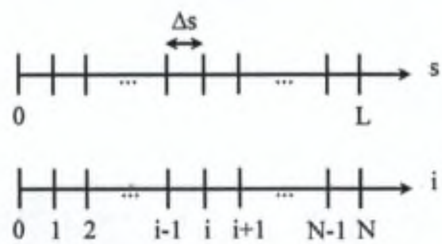

Figure 6.4: s is the distance along the beam. s ranges from 0 to L. The length L of the PBA is divided into segments of length Δs. The parameter i is used in the approximation of the equation $\frac{d^2\theta}{ds^2} = f(\theta(s))$. The length along the beam corresponding to i is $s = i\Delta s$.

The two following equations are the boundary conditions of equation (6.29); they correspond to the boundary conditions (6.17) and (6.18), respectively:

$$\theta_0 = 0 \tag{6.30}$$

and

$$\theta_{N-1} = \theta_N \tag{6.31}$$

Equation (6.29) is then used iteratively to compute the solution θ_i with $i = 0, \ldots, N$; this is done as follows:

$$\frac{\theta_{i+1}^{n+1} - 2\theta_i^{n+1} + \theta_{i-1}^{n+1}}{(\Delta s)^2} = f(\theta_i^n) \tag{6.32}$$

1. The initial solution $n = 0$ ($\theta_i^{n=0}$ with $i = 0, \ldots, N$) is used to compute $f(\theta_i^n)$ (including the calculations of F and α) and equation (6.32) allows then to compute the solution $n = 1$ ($\theta_i^{n=1}$ with $i = 0, \ldots, N$).

2. If the solutions $n = 1$ and $n = 0$ are too far from each other, the solution $n = 1$ ($\theta_i^{n=1}$ with $i = 0, \ldots, N$) is used to compute $f(\theta_i^n)$ and equation (6.32) allows then to compute the solution $n = 2$ ($\theta_i^{n=2}$ with $i = 0, \ldots, N$).

3. If the solutions $n = 2$ and $n = 1$ are too far from each other, etc.

The iterations are repeated until the method converges to a solution $n = j$ ($\theta_i^{n=j}$ with $i = 0, \ldots, N$); this solution is such that the solutions $n = j$ and $n = j - 1$ are close enough to each other, i.e.:

$$\frac{\sum_{i=0}^{N}(\theta_i^j - \theta_i^{j-1})^2}{\sum_{i=0}^{N}(\theta_i^j)^2} < 1\% \tag{6.33}$$

A database comprising hundred initial solutions has been established. These initial solutions are beams whose free end has displaced upwards or downwards. For a given initial solution, if after fifty iterations the method has not converged, the next initial solution of the database is tried.

The model and its solving method have been implemented in a software. The characteristics of the PBA (L, b, e, h, E_m and E_b) and the pressure p have to be provided to the software which computes the corresponding deformed configuration of the PBA and in particular the displacements Δx and Δy of the PBA free end (see Fig. 6.5).

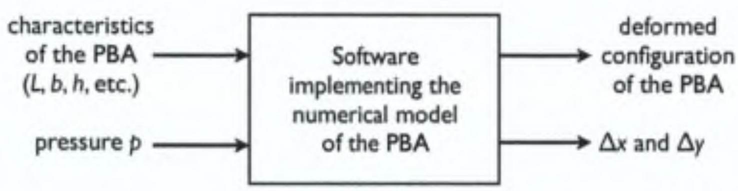

Figure 6.5: Inputs and outputs of the software implementing the numerical model of the PBA.

In practice, when performing experiments with the test bench as described in Chapter 5, it is not the pressure p that is imposed but the displacement u of the cylinder piston (see Fig. 6.6). It could then be interesting to establish the relationship existing between p and u. This relationship could then be added to the software so that its inputs would be the characteristics of the PBA and u, rather than p (see Fig. 6.7).
For a given pressure p, the software provides the complete deformed configuration of the PBA. The inner volume V_{PBA} of the PBA can be computed from this deformed configuration and assuming $V_{PBA} = 0$ when $u = 0$, V_{PBA} can be related to u as follows:

- in the case of an incompressible fluid: the total volume of fluid V equals Sd (S is the cross-section of the cylinder and d is its length (see Fig. 6.6)) and

$$V_{PBA} = Su \tag{6.34}$$

- in the case of a compressible fluid: the total volume V_{atm} at the atmospheric pressure p_{atm} equals Sd. The temperature is assumed to be constant and since the fluidic circuit is closed, the quantity of fluid is also constant. After a piston displacement u, the PBA has a volume V_{PBA} and the total volume is $V_1 = V_{PBA} + S(d - u)$ at the absolute pressure $p_1 = p_{atm} + p$. The gas law leads thus to:

$$p_{atm}V_{atm} = p_1V_1 \tag{6.35}$$

and more precisely to

$$p_{atm}Sd = (p_{atm} + p)(V_{PBA} + S(d - u)) \tag{6.36}$$

Establishing the relationship between u and p for a given PBA can thus be done as follows:

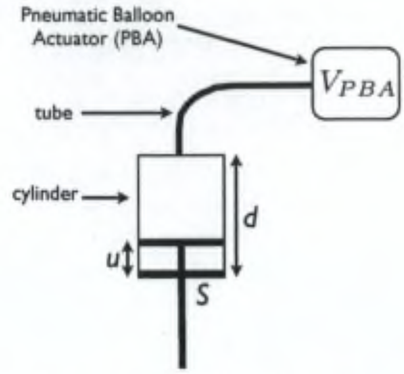

Figure 6.6: PBA connected to a cylinder with a tube. When the cylinder piston performs a displacement u, the PBA inflates and its volume is V_{PBA}. When $u = 0$, it is assumed that $V_{PBA} = 0$. S is the cross-section of the cylinder.

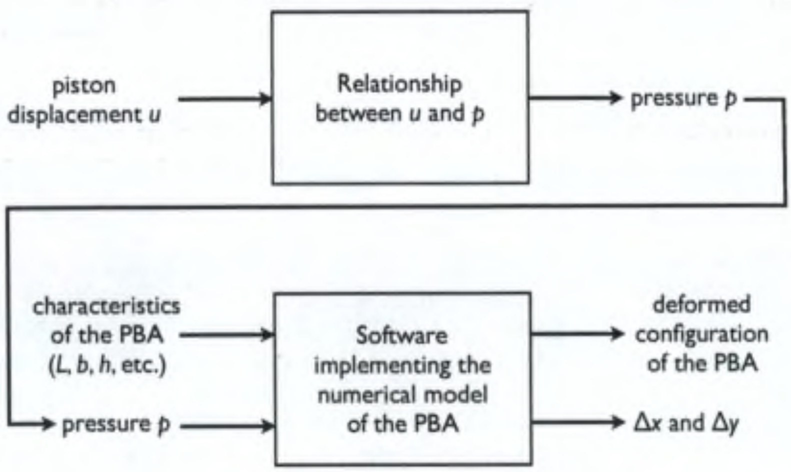

Figure 6.7: The relationship existing between the piston displacement u and the pressure p can be added to software implementing the numerical model of the PBA. Hence, the inputs of the software would be the characteristics of the PBA and u, rather than p.

1. For different pressures p^*, the deformed configuration of the PBA is calculated with the software and the corresponding inner volume V^*_{PBA} of the PBA is computed from this deformed configuration.

2. Equation (6.34) or (6.36) is then used to calculate the piston displacements u^* corresponding to the different PBA volumes V^*_{PBA}.

3. The pressure values p^* are plotted with respect to the corresponding piston displacements u^*; this graph represents the relationship existing between u and p for the studied PBA.

6.3 Results of the model

6.3.1 Modeling of the original PBA

The original PBA described in [50] has been modeled with the numerical model described in the previous section. The original PBA will hereafter be referred to as "Konishi's PBA" to distinguish it from its modeled counterpart.
The size of Konishi's PBA is 16 mm × 16 mm while the size of its cavity is 10 mm × 10 mm; the cavity is located at the centre of the actuator. Only this cavity can be modeled by the numerical model and the parameters of Konishi's PBA are summarized in Table 6.1. The values of the Young's moduli of the silicone rubber and the polyimide, given in Table 6.1, have been looked for with the Cambridge Engineering Selector (CES) software. Indeed, these values were not specified in the description of Konishi's PBA in [50].

Parameter	Value
length of the cavity L	$10\ 10^{-3}$ m
width of the cavity b	$10\ 10^{-3}$ m
length of the actuator L'	$16\ 10^{-3}$ m
width of the actuator b'	$16\ 10^{-3}$ m
membrane thickness e	$200\ 10^{-6}$ m
beam thickness h	$50\ 10^{-6}$ m
membrane Young's modulus E_m	silicone rubber: 0.005 to 0.05 10^9 Pa
beam Young's modulus E_b	polyimide: 2.07 to 2.76 10^9 Pa
pressure p	$p_{max} = 65.1$ kPa
beam inertia I_b	$I_b = \frac{b'h^3}{12} + 2\frac{E_m}{E_b}\left[\frac{\frac{b'-b}{2}e^3}{12} + e\frac{b'-b}{2}(\frac{e+h}{2})^2\right]$

Table 6.1: Parameters of Konishi's PBA described in [50].

The total width b' of Konishi's PBA is 16 mm while the width b of the cavity equals 10 mm and the surrounding edges of the cavity, where the membrane and the beam are glued to each other, contribute to the inertia of the beam. Fig. 6.8 presents the cross-section of the actuator; the areas contributing to the inertia of the beam are colored in grey. As can be seen a part of the membrane (areas no. 1 and 2) contributes to it. To take the contributions of areas no. 1, 2 and 3 into account, the inertia of the beam is computed as follows:

$$I_b = \frac{b'h^3}{12} + 2\frac{E_m}{E_b}\left[\frac{\frac{b'-b}{2}e^3}{12} + e\frac{b'-b}{2}\left(\frac{e+h}{2}\right)^2\right] \tag{6.37}$$

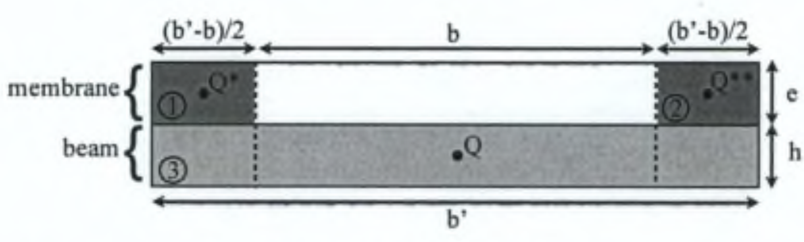

Figure 6.8: Cross-section of Konishi's PBA described in [50]. The grey area contributes to the inertia of the beam.

Fig. 6.10, 6.12 and 6.13 present the results provided by the numerical model for $p = 2$ kPa, $E_m = 0.0275\ 10^9$ Pa and $E_b = 2.415\ 10^9$ Pa (the values chosen for E_m and E_b are the mid values of the ranges given in Table 6.1):

- As can be seen in Fig. 6.10, when the pressure increases up to 0.76 kPa, the free end of the modeled PBA moves upwards; this behaviour corresponds to that of Konishi's PBA and is thus physically correct. Above 0.76 kPa, the free end of the modeled PBA moves downwards. Hence, according to the numerical model, the PBA presents a bidirectional motion: when pressurized, the PBA moves its end upwards, until a given pressure level is reached and above this level, the PBA tip is moved downwards. This behaviour has been experimentally noticed by [51] and by Benjamin Gorissen and Michael De Volder of the KUL, for PBAs made of two layers of the same material (the same PDMS) and of different thicknesses (see Fig. 6.11). However, Konishi's PBA is made of two different materials and no bidirectional motion has been reported for it in [50].
As can be noticed in Fig. 6.12 and 6.13, the numerical model predicts that the change in actuation direction happens instantaneously for a given pressure level. However, in practice, this happens continuously.
As can be seen in Fig. 6.10, the representation of the membrane is not correct when the PBA tip moves downwards.

- As can be seen in Fig. 6.12, for the upwards motion phase, the Y-displacements Δy_0 predicted by the numerical model:

  - are of the same order of magnitude than those measured on Konishi's PBA.
  The numerical model predicts the tip displacements of the PBA cavity, as presented in Fig. 6.1. However, the measurements performed on Konishi's PBA are the tip displacements of the 16 mm × 16 mm actuator and not the tip displacements of its 10 mm × 10 mm cavity (see Fig. 6.9). The tip displacements measured on Konishi's PBA are thus larger than the tip displacements of its cavity.

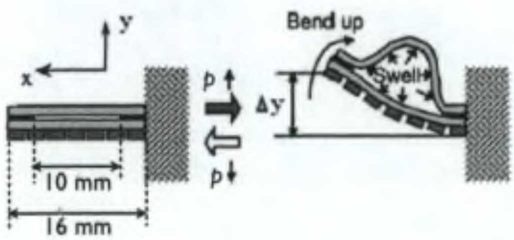

Figure 6.9: Schematic cross-section views of Konishi's PBA (described in [50]): PBA at rest and pressurized PBA (p = pressure) on the left hand side and the right hand side, respectively. The PBA is fixed as a cantilever and the displacements are measured at its tip. Figure adapted from [50].

  - have an evolution with the pressure p similar to that of the measurements performed on Konishi's PBA. However, the maximum pressure $p^* = 0.76$ kPa, for which upwards displacements are predicted by the numerical model, is nearly ninety times smaller than for Konishi's PBA ($p^* = 65.1$ kPa).

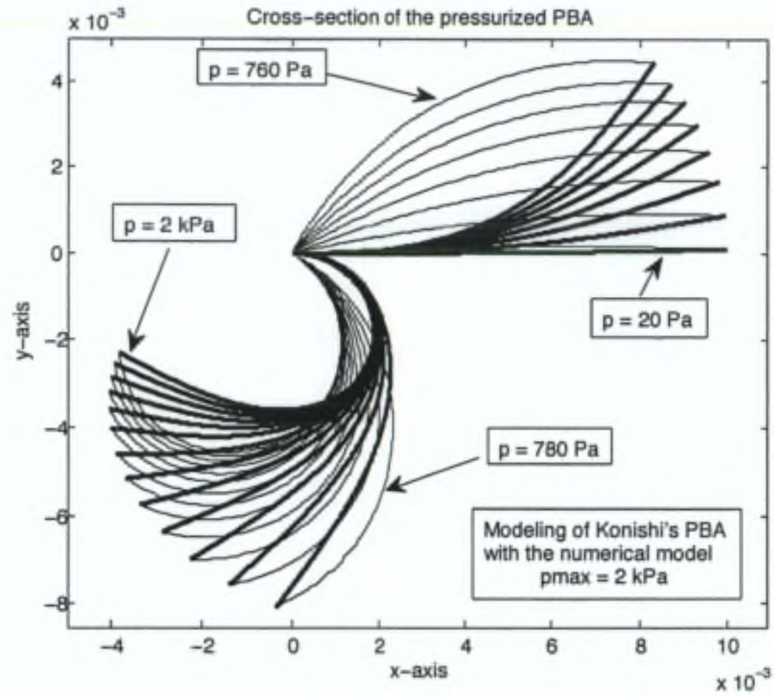

Figure 6.10: Modeling of Konishi's PBA (described in [50]) with the numerical model: cross-section of the PBA for a pressure p up to 2 kPa (the different representations of the cross-section correspond to pressures spaced out by about 100 Pa). The thin and thick lines represent the membrane and the beam, respectively. As can be seen, the numerical model predicts a bidirectional motion of the PBA.

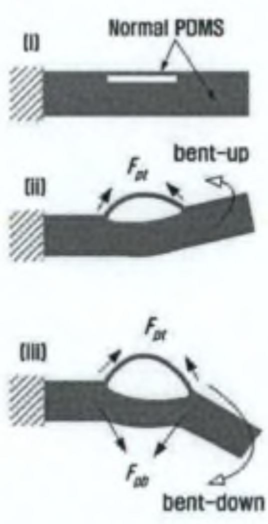

Figure 6.11: Bidirectional motion of a PBA made of two layers of the same material (the same PDMS) and of different thicknesses (see (i) for the PBA at rest). When pressurized, the PBA moves its end upwards (see (ii)) until a given pressure level is reached; above this level, the PBA tip is moved downwards (see (iii)). Figure from [51].

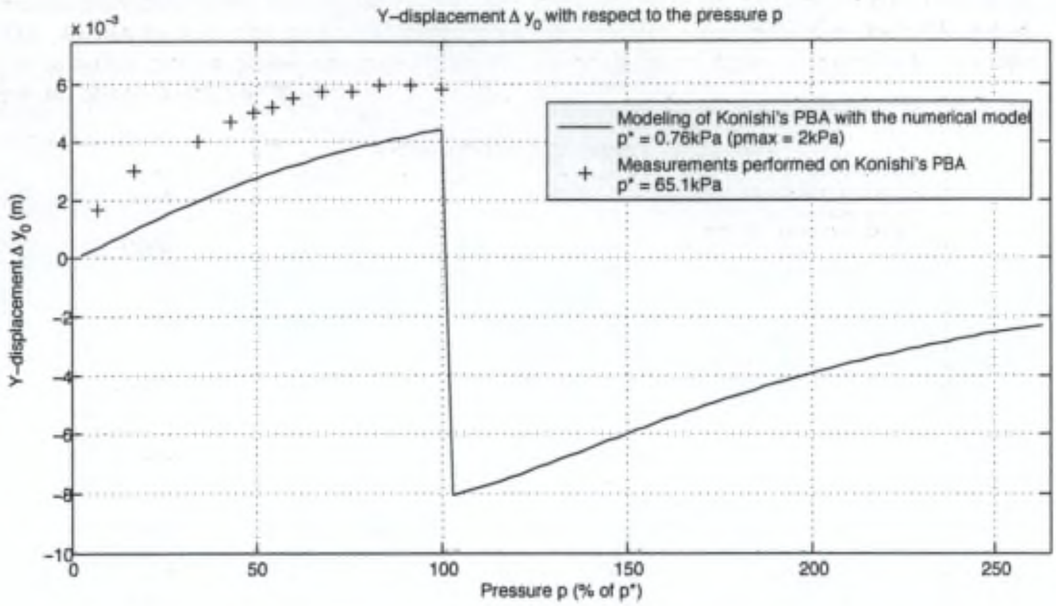

Figure 6.12: Y-displacement Δy_0 of the PBA free end with respect to the pressure p. Comparison between the measurements performed on Konishi's PBA (described in [50]) and the results provided by the numerical model. The measurements on Konishi's PBA come from [50]. As can be seen, the numerical model predicts a bidirectional motion of the PBA and in the upwards motion phase, the measurements are of the same order of magnitude than the results of the numerical model.

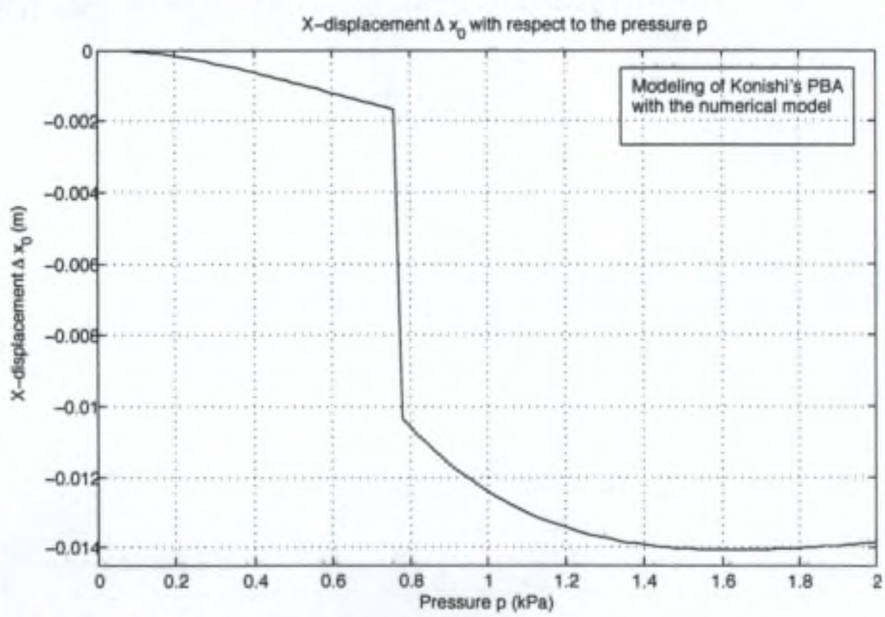

Figure 6.13: Modeling of Konishi's PBA (described in [50]) with the numerical model: X-displacement Δx_0 of the PBA free end with respect to the pressure p. As can be seen, the numerical model predicts a bidirectional motion of the PBA.

6.3.2 Modeling of the test bench PBA

The PBA used on the test bench and described in Section 4.2.2 has been modeled with the numerical model. This prototype will hereafter be referred to as "test bench PBA" to distinguish it from its modeled counterpart.
The size of the test bench PBA is 50 mm×60 mm while the size of its cavity is 40 mm×40 mm. Only this cavity can be modeled by the numerical model and the parameters of the test bench PBA are summarized in Table 6.2. The values of the polyurethane Young's modulus, given in Table 6.2, have been looked for with the Cambridge Engineering Selector (CES) software. Indeed, the PRONAL company which has manufactured the actuators could not specify these values.

Parameter	Value
length of the cavity L	$40\ 10^{-3}$ m
width of the cavity b	$40\ 10^{-3}$ m
length of the actuator L'	$50\ 10^{-3}$ m
width of the actuator b'	$60\ 10^{-3}$ m
membrane thickness e	$0.5\ 10^{-3}$ m
beam thickness h	$1\ 10^{-3}$ m
membrane and beam Young's moduli E_m and E_b	polyurethane: minimum found value = $0.0025\ 10^9$ Pa maximum found value = $2.07\ 10^9$ Pa
pressure p	max $20-30$ kPa (see Section 4.2.2)
beam inertia I_b	$I_b = \frac{b'h^3}{12} + 2\frac{E_m}{E_b}\left[\frac{\frac{b'-b}{2}e^3}{12} + e\frac{b'-b}{2}(\frac{e+h}{2})^2\right]$

Table 6.2: Parameters of the test bench PBA.

The total width b' of the test bench PBA is 60 mm while the width b of the cavity equals 40 mm and the surrounding edges of the cavity, where the membrane and the beam are fixed to each other, contribute to the inertia of the beam. Hence, exactly as for Konishi's PBA, Fig. 6.8 presents the cross-section of the actuator and the areas contributing to the inertia of the beam are colored in grey. To take the contributions of areas no. 1, 2 and 3 into account, the inertia of the beam is computed with the formula (6.37).
Fig. 6.15 to 6.18 present the results provided by the numerical model for $p = 25$ kPa and $E_m = E_b = 1.03625\ 10^9$ Pa (the value chosen for E_m and E_b is the mid value of the range given in Table 6.2):

- As can be seen in Fig. 6.15, when the pressure p increases up to 25 kPa, the free end of the modeled PBA moves upwards. This behaviour corresponds to that of the test bench PBA and is thus physically correct.
- As can be seen in Fig. 6.16, 6.17 and 6.18, when the pressure p increases, the PBA free end moves upwards and Δx_0 and Δy_0 increase in absolute value. Besides, it can be noticed that:
  - the displacements Δx_0 and Δy_0 predicted by the numerical model are of the same order of magnitude than those measured on the test bench PBA.
  - the displacements Δy_0 predicted by the numerical model are larger than those measured on the test bench PBA, all the more that the numerical model predicts the displacements of the cavity tip (see point A' in Fig. 6.14) and that, as explained in Section 4.3, the measurements Δx_0 and Δy_0 made on the test bench PBA are the displacements of a point located 5 mm far from the cavity tip (see point B' in Fig. 6.14). This implies than the tip displacements measured on the test bench PBA are larger, in absolute value, than the tip displacements of its cavity.

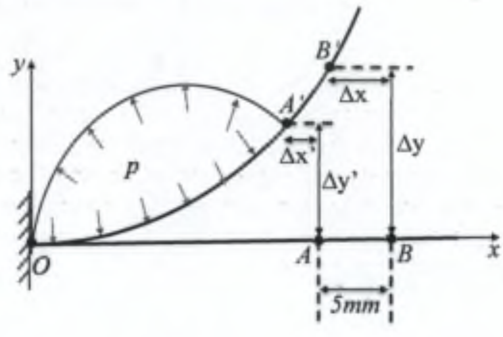

Figure 6.14: Schematic cross-section of the test bench PBA. The numerical model predicts the X- and Y- displacements of point A' ($\Delta x'_0$ and $\Delta y'_0$) while the measurements performed on the test bench PBA are the X- and Y- displacements of point B' (Δx_0 and Δy_0).

- the displacements Δx_0 of the cavity tip predicted by the numerical model are smaller, in absolute value, than the measurements performed on the test bench PBA but, as explained before, these measurements are larger, in absolute value, than the tip displacements of the cavity (see Fig. 6.14).
- the displacements Δy_0 predicted by the numerical model present an evolution with the pressure p similar to that of the measurements performed on the test bench PBA. This is not the case for the displacements Δx_0 predicted by the numerical model.

As already said, the displacements Δy_0 predicted by the numerical model are larger than those measured on the test bench PBA for the same pressure. The predictions of the numerical model have been achieved for large Young's moduli E_m and E_b. If the Young's moduli and the pressure keep the same ratio, the same displacements Δx_0 and Δy_0 are predicted by the model. This means that if the Young's moduli of the test bench PBA are in reality ten times smaller than those used to establish the curves of Fig. 6.15 to 6.18, the same displacements Δx_0 and Δy_0 will be predicted by the numerical model but for a maximum pressure that is ten times smaller than $p = 25$ kPa. However, since the actual Young's moduli are not known, it is difficult to conclude about the results provided by the numerical model.

If the pressure is increased above 25 kPa, the numerical model predicts that the test bench PBA has a bidirectional motion and that the change in actuation direction happens for $p = 32$ kPa.

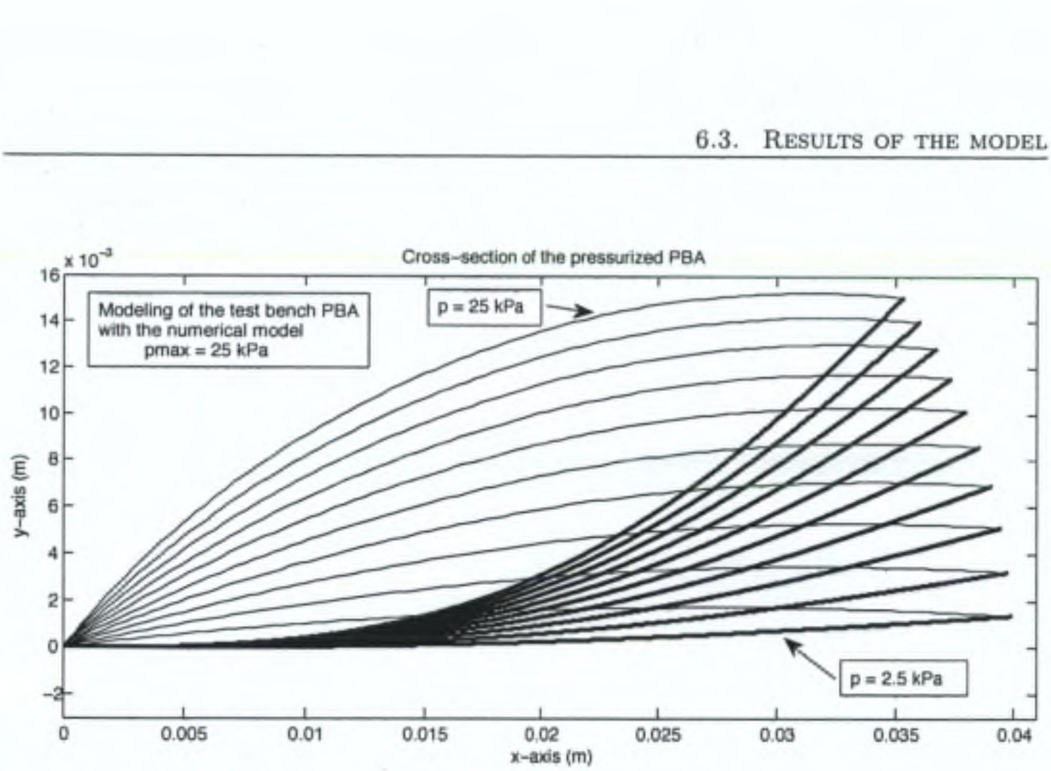

Figure 6.15: Modeling of the test bench PBA with the numerical model: evolution of the PBA cross-section with the pressure p. When the pressure p increases, the PBA free end moves upwards. The thin and thick lines represent the membrane and the beam, respectively. The different representations of the cross-section correspond to pressures spaced out by 2.5 kPa.

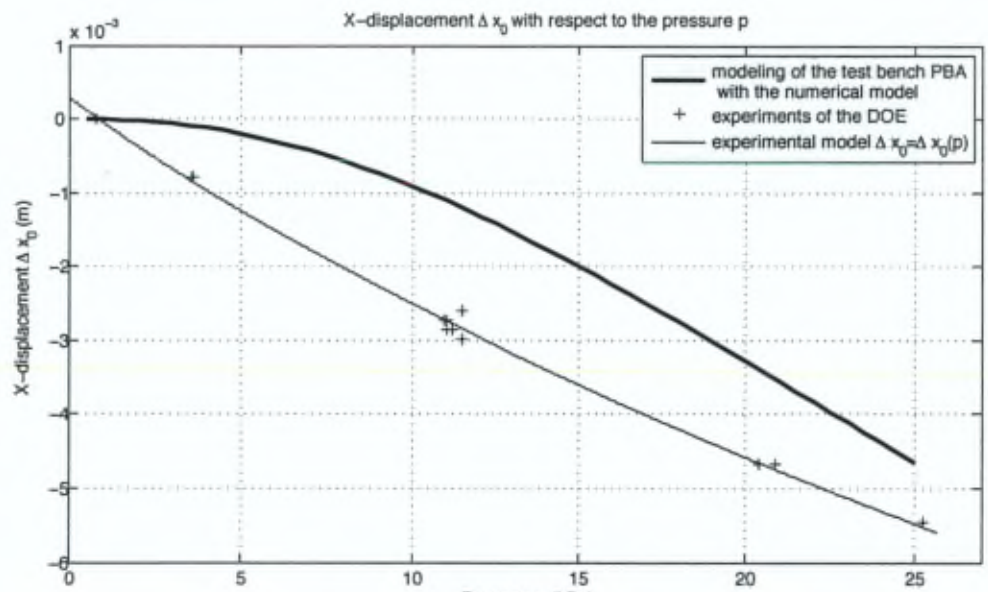

Figure 6.16: X-displacement Δx_0 of the PBA free end with respect to the pressure p. When the pressure p increases, the PBA free end moves upwards and Δx_0 increases in absolute value. The thick line is computed by the numerical model. The crosses are the experiments of the DOE (described in Section 5.2.1) that has been applied to the test bench PBA; the thin line is the experimental model $\Delta x_0 = \Delta x_0(p)$ deduced from these experiments.

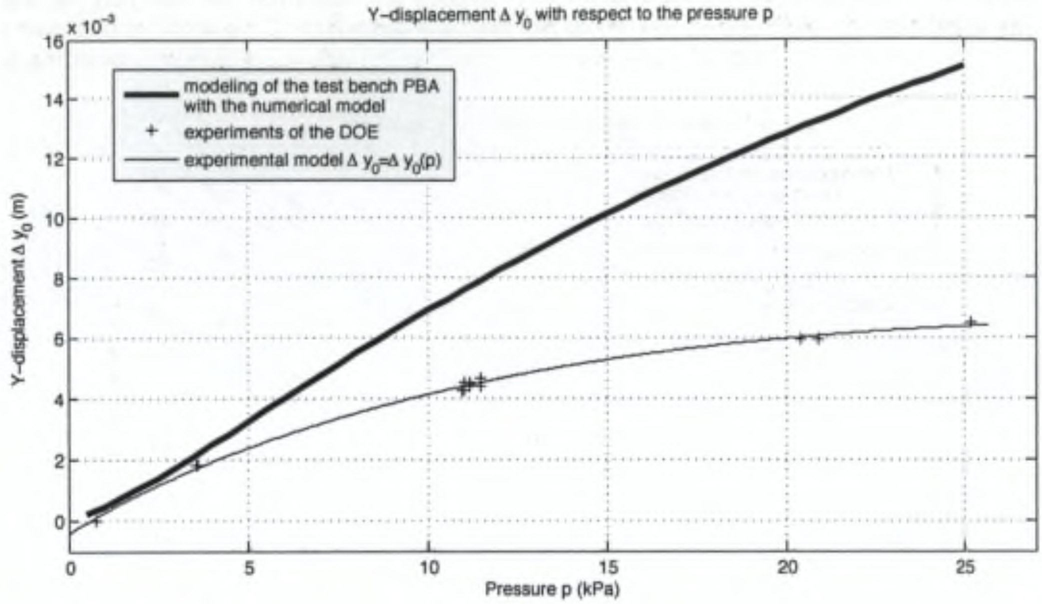

Figure 6.17: Y-displacement Δy_0 of the PBA free end with respect to the pressure p. When the pressure p increases, the PBA free end moves upwards and Δy_0 increases. The thick line is computed by the numerical model. The crosses are the experiments of the DOE (described in Section 5.2.1) that has been applied to the test bench PBA; the thin line is the experimental model $\Delta y_0 = \Delta y_0(p)$ deduced from these experiments.

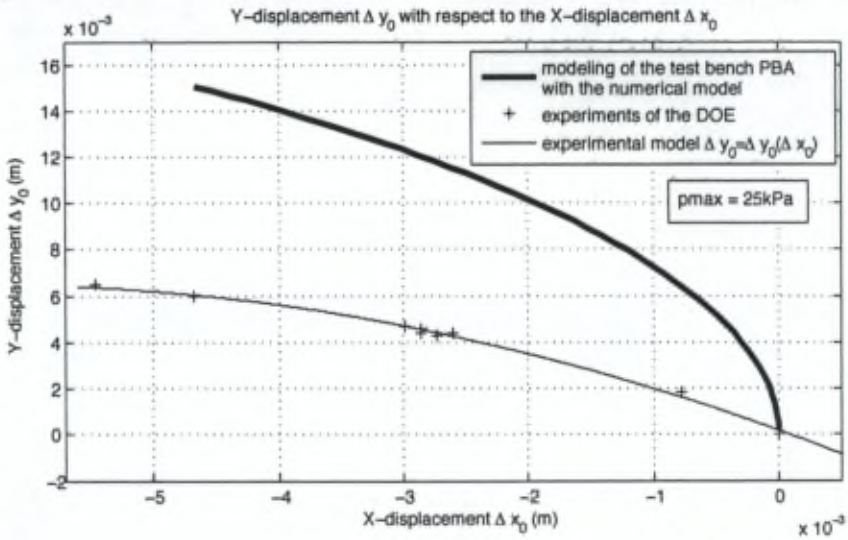

Figure 6.18: Y-displacement Δy_0 of the PBA free end with respect to its X-displacement Δx_0. When the pressure p increases, the PBA free end moves upwards and Δx_0 and Δy_0 increase in absolute value. The thick line is computed by the numerical model. The crosses are the experiments of the DOE (described in Section 5.2.1) that has been applied to the test bench PBA; the thin line is the experimental model $\Delta y_0 = \Delta y_0(\Delta x_0)$ deduced from these experiments.

6.4 Discussion and conclusions

As already said,

- the upwards Y-displacements Δy_0 predicted by the numerical model are of the same order of magnitude than the measurements made on Konishi's PBA but they are achieved for a pressure that is much lower than the actual pressure.

- the Y-displacements Δy_0 predicted by the numerical model are larger than those measured on the test bench PBA for the same pressure. Besides, these predictions have been achieved for Young's moduli E_m and E_b that are maybe too large compared to the actual Young's moduli of the test bench PBA.

This means that the PBA of the numerical model is less stiff than its real counterpart. This can be explained by the fact that some of the assumptions on which the model rests are too far from the reality.
Indeed, according to hypothesis 1: "*When pressurized, the PBA deforms in such a way that its cross-section is identical along its width; this cross-section is presented in Fig. 6.1. What happens in the surroundings of the PBA outline is thus assumed to be negligible and this first hypothesis allows an analysis in two dimensions (in the plane xy) of the PBA*".
Hence, the model assumes that the membrane is fixed to the beam only by the two sides placed in the width direction. In practice however, both layers of the PBA are fixed to one another along their four sides. The model neglects thus the forces applied to the membrane along the sides placed in the length direction and the cross-section of the PBA is not identical along the width. Hence, in practice, the shear stresses are probably not negligible in the membrane (assumption 5) and the stresses σ not uniform in the membrane (assumption 6). By neglecting all these phenomena, the model leads to a PBA less rigid than the real prototype.

Besides, in the case of Konishi's PBA and of the test bench PBA, hypothesis 3 is not valid. Indeed, according to this assumption, the lower PBA layer is modeled as a beam. However, Konishi's PBA and the test bench PBA have dimensions such that $L = b$ while by definition, a beam has a length which is larger than its two other dimensions. Hence, the bottom layer of Konishi's PBA and of the test bench PBA should better be modeled by a plate.
In addition to this, in the case of Konishi's PBA, since the cavity is placed at the centre of the actuator, the membrane applies a pulling force F at two places to the beam: at its beginning and at its end. However, the numerical model only takes into account the pulling force applied to the end of the beam.

In conclusion, a PBA modeled with the numerical model will be less stiff than its real counterpart and some of the assumptions on which the model rests are not verified in reality; this leads to large differences between the predictions provided by the model and the measurements performed on the prototypes (e.g. too large displacements, too low pressures, incorrect shape of the evolution of the X-displacements Δx_0 with respect to the pressure). However, the numerical model is able to predict the bidirectional behaviour of a PBA and allows to better understand the physics underlying. The bidirectional behaviour is due to the pressure applied to the beam and to the force applied by the pressurized membrane to the beam. If the force applied by the membrane is predominant, the PBA free end moves upwards while if the pressure is predominant, it moves downwards.
It has to be mentioned that the numerical model seems to predict that all PBAs show this bidirectional behaviour while in practice, this behaviour has been reported for PBAs completely made of the same material and it is not established whether this behaviour happens

for PBAs whose layers are made of different materials.

Looking at the equations of the model, it can be noticed that the bending stiffness of the beam equals $E_b I_b = E_b \frac{b' h^3}{12} + 2E_m \left[\frac{\frac{b'-b}{2} e^3}{12} + e\frac{b'-b}{2}(\frac{e+h}{2})^2 \right]$. Hence, according to the numerical model, since the thicknesses h and e of the beam and the membrane are to the power three, they will have more influence on the PBA displacements than the widths b and b' of the cavity and the actuator, and than the Young's moduli E_b and E_m of the beam and the membrane.
If a dimensional analysis is performed on the model parameters (b' is not considered here) L, b, E_m, E_b, e, h, p, Δx and Δy, the corresponding dimensionless numbers are $\pi_1 = \frac{e}{h}$, $\pi_2 = \frac{b}{h}$, $\pi_3 = \frac{L}{h}$, $\pi_4 = \frac{\Delta x}{h}$, $\pi_4' = \frac{\Delta y}{h}$, $\pi_5 = \frac{E_m}{E_b}$ and $\pi_6 = \frac{p}{E_b}$, which are linked by the following two relationships:

$$\pi_4 = \frac{\Delta x}{h} = f(\pi_1, \pi_2, \pi_3, \pi_5, \pi_6) \tag{6.38}$$

$$\pi_4' = \frac{\Delta y}{h} = g(\pi_1, \pi_2, \pi_3, \pi_5, \pi_6) \tag{6.39}$$

Hence, if the dimensionless numbers $\pi_1, \pi_2, \pi_3, \pi_5$ and π_6 keep the same values, $\pi_4 = \frac{\Delta x}{h}$ and $\pi_4' = \frac{\Delta y}{h}$ also keep the same values. This means that if the dimensions of the PBA L, b, e and h are multiplied by a given factor, the displacements Δx and Δy will increase by the same factor. Besides, if the Young's moduli E_m and E_b and the pressure p are multiplied by a given factor, the displacements Δx and Δy will not change.

The numerical model could be modified in order to predict the displacements of the actuator tip rather than the displacements of the cavity tip. This would allow a better comparison between the predictions of the numerical model and the measurements performed on Konishi's PBA and the test bench PBA.

However, at this stage, it is not possible to conclude whether the numerical model could be used to predict the qualitative effects, on the tip displacements, of the change of a PBA parameter. To answer this question, more experimental validations are required with prototypes whose parameters are perfectly known.

Chapter 7

Miniaturization of Pleated Pneumatic Artificial Muscles

7.1 Introduction

As explained before in Section 1.3, a literature review has established that a force of about 13 N is required at the end of a surgical instrument to allow the execution of all the surgical gestures (see Table 1.1). Fig. 7.1 presents schematically a surgical instrument having a length L and a width l. F is the force applied by the organs to the tip of the surgical instrument. An actuator applies a vertical force F' to the basis of the instrument and α is the angle of inclination of the instrument. For $L = 2l$, if α equals $\pi/2$, the actuator has to develop a force $F' = 104$ N so that the instrument can develop a force $F = 13$ N at its tip. On the other hand, if α equals $\pi/6$, the actuator has to develop a force $F' = 208$ N so that the instrument can develop a force $F = 13$ N at its tip.

As explained in Section 3.2.2 (see Table 3.1), according to theoretical models, miniaturized Pleated Pneumatic Artificial Muscles (PPAMs), whose dimensions are small enough to be inserted into MIS medical instruments, could be able to develop the required force of $104 - 208$ N. In this chapter, the PPAMs have therefore been studied in order to assess their miniaturization potential and miniaturized PPAMs have been manufactured.

There exist other types of Pneumatic Artificial Muscles (PAMs) also able to generate large forces and the most frequently used PAM is the McKibben one. However, the PPAM has been chosen because its design has been thought about in order to improve the drawbacks presented by the McKibben PAM. Hence, the PPAM presents a low hysteresis, a low pressure threshold and a larger force. In addition to this, the design of the PPAM is relatively simple compared to some other muscles and the proximity of the ULB and the Vrije Universiteit Brussel (VUB), whose Department of Mechanical Engineering has developed the PPAM, eases the contacts and collaborations.

This miniaturization work has been performed by Nhat-Quang CAO as a Master's thesis [27], under the supervision of Prof. Pierre Lambert and myself, in collaboration with the VUB.

Section 7.2 describes the PAMs in general and the PPAMs in particular. Afterwards, Section 7.3 presents the miniaturization work performed on the PPAMs and Section 7.4 concludes about it and presents perspectives of future works.

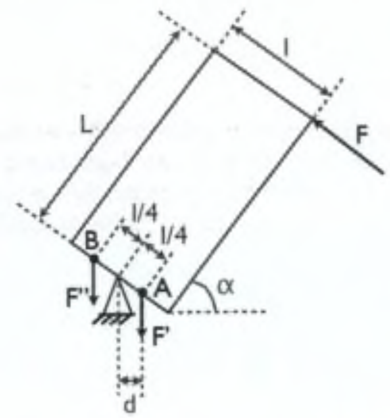

$F' > 0$ and $F'' = 0$
$F'.d = F.L$
with $d = \frac{l}{4} sin(\alpha)$

$$\boxed{F' = F \frac{4L}{l.sin(\alpha)}}$$

For $L = 2.l$ and $F = 13\ N$
1) $\alpha = \pi/2$
$\boxed{F' = 104\ N}$
2) $\alpha = \pi/6$
$\boxed{F' = 208\ N}$

Figure 7.1: The surgical instrument has a length L and a width l. F is the force applied by the organs to the tip of the surgical instrument. An actuator applies a vertical force F' to the basis of the instrument. α is the angle of inclination of the instrument. For $L = 2l$, if α equals $\pi/2$, the actuator has to develop a force $F' = 104$ N so that the instrument can develop a force $F = 13$ N at its tip. On the other hand, if α equals $\pi/6$, the actuator has to develop a force $F' = 208$ N so that the instrument can develop a force $F = 13$ N at its tip.

7.2 PAMs and PPAMs

7.2.1 General description of the PAMs and description of the McKibben PAMs

PAMs are made of a flexible closed membrane that is reinforced and fixed to fittings at both ends. When pressurized gas is introduced in such a device (when gas is sucked out), the membrane bulges out (squeezes) and contracts axially (see Fig. 7.2) [31]. A PAM is then able to lift a load attached to one of its ends.

Figure 7.2: Deflated and inflated states of a Pneumatic Artificial Muscle (PAM) presenting a pleated membrane. When pressurized gas is introduced in this PAM, the membrane bulges out and contracts axially. Figure from [84].

Under quasi-static conditions and neglecting energy losses and especially the energy required to deform the membrane, the force F generated by a PAM can be expressed as follows [30]:

$$F = -p\frac{dV}{dl_c} \tag{7.1}$$

with
V = enclosed membrane volume

l_c = PAM's contracted length
$p = p_{in} - p_{out}$, p_{in} and p_{out} being the PAM's inner and outer pressures; p is a gauge pressure.

Equation (7.1) indicates the maximum theoretical force a given PAM can develop. As can be seen, this force depends on the pressure p and on the evolution of the membrane volume V with respect to the muscle length l_c. This evolution is characteristic of the type of membrane used and thus of the studied muscle. The state of a given muscle is thus completely determined by its length l_c and the pressure p. In practice, a PAM will develop a lower force because some energy is required to deform the membrane and because energy is dissipated by friction [30]. In addition to energy losses, friction also involves hysteresis.

The most frequently used PAM is the McKibben one (see Fig. 7.3). It is composed of a rubber tube and a braided sleeve surrounding the tube (the braid angle is θ). The tube and the sleeve are connected at both ends to fittings which transfer fiber tension and enclose the gas. When the tube is pressurized, it is pressed against the sleeve. The braid angle changes and the sleeve expands and contracts. The gas pressure is balanced by the fiber tension which is transferred to the fittings. The muscle is then able to lift a load attached to one of its ends [31] [32].

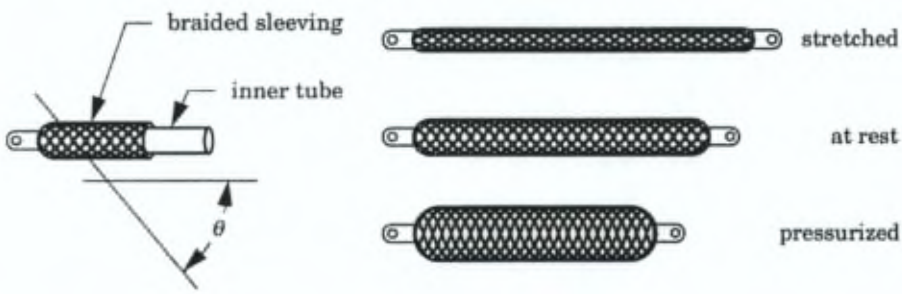

Figure 7.3: Different states of a McKibben Pneumatic Artificial Muscle. It is composed of a rubber tube and a braided sleeve surrounding the tube (the braid angle is θ). The tube and the sleeve are connected at both ends to fittings which transfer fiber tension and enclose the gas. When the tube is pressurized, it is pressed against the sleeve. The braid angle changes and the sleeve expands and contracts. The gas pressure is balanced by the fiber tension which is transferred to the fittings. The muscle is then able to lift a load attached to one of its ends. Figure from [31].

The McKibben PAM is easy to manufacture but it presents some important drawbacks: a limited contraction (about 20 % to 30 %), a substantial hysteresis (due to the friction between the tube and the sleeve), a high pressure threshold under which the muscle does not contract (this threshold is due to the tough rubber used to avoid the bursting of the tube; pressure threshold typically about 90 kPa) and a limited output force (due to the energy losses implied by the rubber deformation) [32].

7.2.2 Description and models of the PPAMs

To solve the drawbacks of the McKibben PAM, a new type of PAM has been developed at the Department of Mechanical Engineering of the VUB. This muscle is made of a membrane having a high tensile stiffness to avoid membrane deformation. The membrane is fold so that

its pleats are arranged along its long axis and it is connected to fittings at both ends (see Fig. 7.2). These fittings carry the gas inlet and outlet and transfer the membrane stresses. When the membrane is pressurized, it bulges by unfolding the pleats and the muscle contracts itself. In the middle of the membrane, the unfolding is the highest and it decreases from the middle of the membrane towards both ends; at the ends, the pleats are not unfold at all.
No friction occurs during the unfolding of the pleats and consequently the muscle shows practically no hysteresis. Besides, the pleats unfolding requires a very low amount of energy. Indeed, the parallel stresses (i.e. membrane stresses along the parallels (see Fig. 7.4)) are very low during the expansion of the membrane. As a consequence, the output force will be close to its maximum theoretical value. In addition to this, since only a very small amount of energy is necessary to expand the membrane, the pressure threshold of this muscle is generally low [31] [32].

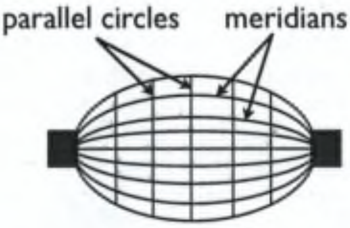

Figure 7.4: Side view of a closed axisymmetrical membrane. The parallel circles are the sections of the membrane with planes perpendicular to its axis of symmetry. The meridians are the sections of the membrane with planes containing its axis of symmetry.

An ideal PPAM is a PPAM that would have "*an infinite amount of infinitely narrow pleats, leading to an axisymmetrical membrane surface that would thus only be loaded by meridional stresses (i.e. along fold lines) and not by parallel stresses (i.e. along parallels, which are sections of the surface and any plane perpendicular to the axis of symmetry). This can be seen as follows. If any parallel stress would exist in such a membrane at some equilibrium contraction, it would unfold the membrane further, since folds cannot withstand tensile stress. As a result of this, the membrane diameter would have to increase, which, at a fixed contraction, can only happen by stretching in the meridional direction. The high tensile stiffness of the material makes it nearly unstretchable though and, therefore, unfolding can only happen if the membrane contracts further. An ideal PPAM, consequently, cannot have parallel stress components. Its lateral expansion can happen unhampered and at no energy cost.*" ... "*The ideal pleated PAM can mathematically be described by an orthotropic membrane that is closed, flexible, axisymmetrical and subjected to an axial force F at both ends and to a uniform orthogonal surface load p, which is the pressure difference across the surface. This orthotropic membrane has a zero modulus of Young in the parallel direction but not in the meridional direction. This amounts to a zero parallel stress condition and actually states that the external loads are balanced by meridional membrane stress only.*" [30].

Assuming an ideal PPAM having an inelastic membrane (i.e. a membrane having a Young Modulus $E = \infty$ in the meridional direction), [30] has established theoretical models for the PPAM (see equations (7.2), (7.3), (7.5) and (7.4)). However, these models are also used for high tensile stiffness membranes as the influence of elasticity is very small for these membranes at contractions of more than 5%.
These theoretical models allow to estimate the equatorial diameter D, the enclosed volume V and the membrane meridional tensile stress σ of the pressurized PPAM, as well as the

pulling force F it generates:

$$D = l\ d(\epsilon, \frac{l}{R}) \tag{7.2}$$

$$V = l^3\ \nu(\epsilon, \frac{l}{R}) \tag{7.3}$$

$$\sigma = p\frac{l^2}{A}\ \zeta(\epsilon, \frac{l}{R}) \tag{7.4}$$

$$F = pl^2\ f(\epsilon, \frac{l}{R}) \tag{7.5}$$

where
l = initial length of the PPAM (i.e. length of the PPAM when it is not pressurized)
l_c = contracted length of the PPAM (i.e. length of the PPAM when it is pressurized)
l and l_c do not take the fittings into account but only measure the length of the PPAM membrane.
$\epsilon = 1 - \frac{l_c}{l}$, ϵ is the contraction of the PPAM
R = initial radius of the PPAM (i.e. radius of the PPAM when it is not pressurized)
p = gauge pressure inside the pressurized PPAM
A = area of the membrane cross-section
$d(\epsilon, \frac{l}{R})$, $\nu(\epsilon, \frac{l}{R})$, $\zeta(\epsilon, \frac{l}{R})$ and $f(\epsilon, \frac{l}{R})$ are dimensionless functions. Fig. 7.5, 7.6, 7.7 and 7.8 show the evolution of these functions with respect to the contraction ϵ and for different $\frac{l}{R}$ ratios (the ratio $\frac{l}{R}$ is also called "slenderness").

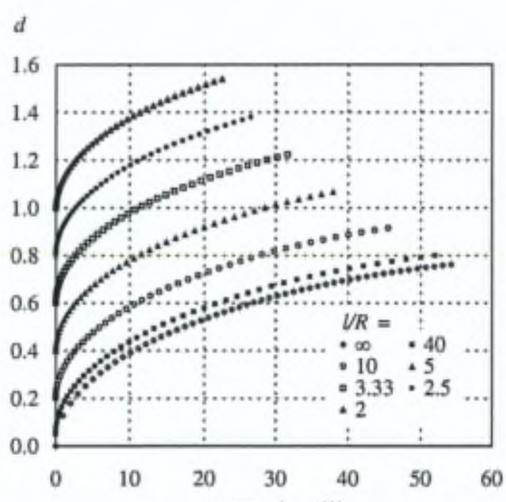

Figure 7.5: Dimensionless diameter function $d(\epsilon, \frac{l}{R})$ with respect to the contraction ϵ and for different $\frac{l}{R}$ ratios, $d(\epsilon, \frac{l}{R}) = \frac{D}{l}$. l and R are the initial length and radius of the PPAM and D is the equatorial diameter of the pressurized PPAM. Figure from [30].

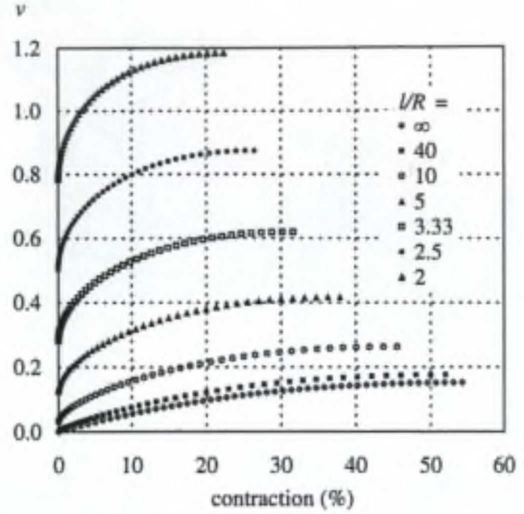

Figure 7.6: Dimensionless volume function $\nu(\epsilon, \frac{l}{R})$ with respect to the contraction ϵ and for different $\frac{l}{R}$ ratios, $\nu(\epsilon, \frac{l}{R}) = \frac{V}{l^3}$. l and R are the initial length and radius of the PPAM and V is the enclosed volume of the pressurized PPAM. Figure from [30].

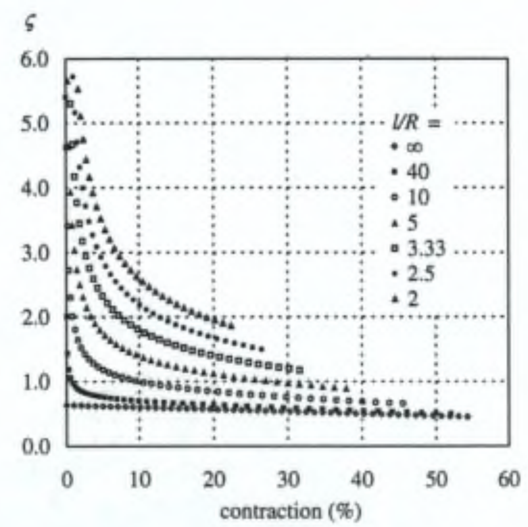

Figure 7.7: Dimensionless stress function $\zeta(\epsilon, \frac{l}{R})$ with respect to the contraction ϵ and for different $\frac{l}{R}$ ratios, $\zeta(\epsilon, \frac{l}{R}) = \frac{\sigma A}{pl^2}$. l and R are the initial length and radius of the PPAM, p is the inner gauge pressure of the pressurized PPAM, A is the area of the membrane cross-section and σ is the membrane meridional stress of the pressurized PPAM (the meridional direction is along the long axis of the PPAM). Figure from [30].

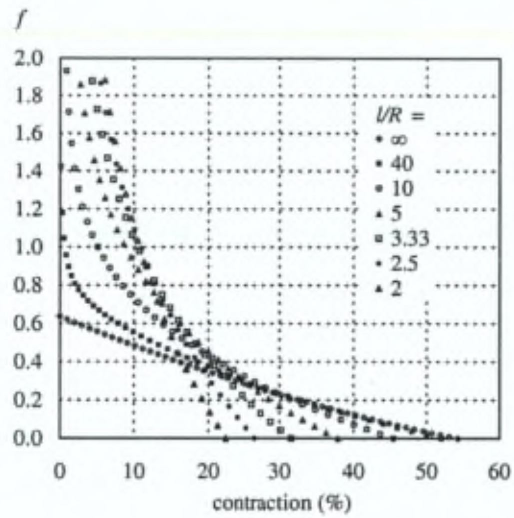

Figure 7.8: Dimensionless force function $f(\epsilon, \frac{l}{R})$ with respect to the contraction ϵ and for different $\frac{l}{R}$ ratios, $f(\epsilon, \frac{l}{R}) = \frac{F}{pl^2}$. l and R are the initial length and radius of the PPAM, p is the inner gauge pressure of the pressurized PPAM and F is the pulling force it develops. Figure from [30].

As can be seen in Fig. 7.8, the developed force F has a non-linear evolution with respect to the contraction ϵ. Apart from the case for which $\frac{l}{R} = \infty$, the force tends to infinity for zero contraction. In practice, the developed force will be lower at small contractions because of the elasticity of the membrane. As shown in the figure, as the contraction increases, the developed force decreases until it becomes null at the PPAM's maximum contraction. Stubbier membranes, i.e. membranes having a low value of slenderness $\frac{l}{R}$, develop a higher force at small contractions but it decreases faster and the maximum contraction is smaller. This is due to the fact that stubbier membranes offer a larger surface for the gas pressure to act on it but on the other hand they present end closures whose surface is also larger. If the pressure acting on the membrane contributes positively to the force F developed by the muscle, the pressure acting on the surface of the end closures makes this force decreases since it acts in the direction opposite to the pulling force direction [30].
The highest maximum contraction equals about 54.3 % and is obtained for an infinitely slim membrane, i.e. a membrane for which $\frac{l}{R} = \infty$; however, this case is not feasible in practice. $\frac{l}{R} = 10$ is a more practical slenderness for which the maximum achieved contraction equals about 45.5 %.

Fig. 7.7 shows that the meridional stress σ decreases when the contraction ϵ increases but it never becomes null. Indeed, a fully inflated muscle is tense although it does not generate a pulling force [30].

From Fig. 7.5, it can be seen that the equatorial diameter of stubbier membranes presents a relative increase smaller than for slimmer membranes. This means that stubbier PPAMs require less pleats to be able to fully expand and are consequently more easy to manufacture [30].

Fig. 7.6 shows that stubbier membranes present a higher increase in volume with contraction. This means that stubbier PPAMs have a higher possible transfer of work (see equation

7.1). Although stubbier membranes show this interesting characteristic and are easier to manufacture, they present a large dead volume (i.e. at $\epsilon = 0$) that does not contribute to the pulling force developed by the muscle. However, this volume needs to be pressurized or depressurized whenever the inner pressure of the muscle is changed [30].

As explained before, stubbier membranes develop higher forces and present smaller maximum contractions. This involves that these PPAMs act with more force on the structure they are connected to in comparison with slimmer PPAMs developing the same work.

[30] also shows that slimmer membranes apply higher stresses to the end fittings although their developed forces are generally lower. The manufacturing of slimmer PPAMs will thus be limited by this characteristic and by the fact that slimmer PPAMs require more pleats to be able to fully expand.

The theoretical models have been experimentally validated and agree very well with the experiments. For example, a muscle of 60 g, $l = 10$ cm, $R = 1.25$ cm and having 44 folds, whose depth equals 2.5 mm, has been used to perform experiments. [32] reports that:

- "*Noticeable deviations were only found in the lower and upper regions of contraction and for low values of pressure.*"
- "*For contractions ranging from* 5 % *to about* 30 %, *the measured values of force and diameter were seen to be within* 1−2 *percents of the values predicted by the mathematical model.*"
- "*Stroke was predicted to be* 43.5 % *and experimentally found to be* 41.5 %."

Three generations of PPAMs, each one improving the drawbacks of the previous one, have been developed at the Department of Mechanical Engineering of the VUB. The first generation PPAMs are made of a high tensile stiffness membrane while the muscles of the second and third generations present a more flexible membrane, used in combination with high tensile stiffness fibres placed in the pleats.
To model the PPAMs of the second and third generations, another theoretical model has been established by [84]. While the previous model considered a continuous axisymmetrical circular membrane, the new model focuses on the high tensile stiffness fibres and assumes that longitudinal tension is only transferred by these fibres. According to this model, the force F developed by the PPAM equals:

$$F = p\frac{n}{2\pi}sin(\frac{2\pi}{n})l^2 \; f(\epsilon, \frac{l}{R}) \tag{7.6}$$

with
p, l, R and ϵ as defined before
n = the number of fibres (or pleats)
$f(\epsilon, \frac{l}{R})$ = the dimensionless force function presented in Fig. 7.8.

In comparison with equation (7.5) given by the previous model, equation 7.6 presents an extra term: $\frac{n}{2\pi}sin(\frac{2\pi}{n})$. If the number of fibres decreases, equation 7.6 predicts, because of this term, a developed force F smaller than the one predicted by equation (7.5). But as the number of fibres increases, both traction models get closer to each other and for a number of fibres larger than 15, the difference between both models is less than 3 % [84].
Experiments on a second generation PPAM have been performed to validate this new traction model. These experiments showed that the theoretical model gives a good approximation of the real force function.

Because of the design differences between the second and the third generations, the initial radius R of the second generation PPAMs is the muscle radius taken at the top of the folds when the muscle in not pressurized while for the third generation PPAMs, this radius is the radius at which the fibres are placed.

7.3 Miniaturization of the PPAMs

This section summarizes the miniaturization work performed by Nhat-Quang CAO during his Master's thesis [27].

7.3.1 Introduction and requirements

As explained in Section 7.1, a miniaturization work is performed on the PPAMs in order to reach a size that would allow to use them in flexible medical instruments. For example, for applications in Minimally Invasive Surgery, instruments must have a diameter less than 10 mm [66] in order to pass through the trocars, while the diameter of catheters can be as low as 1 mm or less [60].
For this first miniaturization work, the target is to develop a miniaturized muscle able to develop a force of about 100 N (see Fig. 7.1) and having a diameter at rest of about 1 cm. No specific objective is set concerning the stroke of the muscle.

7.3.2 Design of the miniaturized PPAM

The design of the third generation PPAMs developed at the VUB has been studied and applied to the miniaturized PPAMs.
Fig. 7.9 presents a view of a miniaturized PPAM. It is composed of two end fittings and of a pleated membrane. Each end fitting comprises three parts: an inner ribbed part, an outer ribbed part and a fastening. The folds of the membrane are placed between both ribbed parts. Both fastenings have an external thread: that of the lower fastening allows to attach a weight to the muscle end while that of the upper fastening allows the fixation of the muscle to an external support and the fixation of the air inlet. Besides, the upper fastening presents a hole along its length to allow the air feeding of the muscle. The membrane is made of two layers of PVC adhesive tape (tesa 4120) and two layers of a 100 % polyester fabric. Besides, the fabric is covered by glue (permanent glue 3M) to better stick to the adhesive tape. The thickness of the membrane is about 0.3 mm.
One single string is used to pass in all the folds. This is done as follows: the string is attached to a fastening, travels through a fold, is wound round the second fastening, travels back through the next fold, is wound round the first fastening, etc. and the string is finally attached to the first fastening.

There are some differences between the designs of the miniaturized PPAM and the third generation PPAM of the VUB:

- The membrane of the third generation PPAM presents three layers of adhesive tape. The membrane of the miniaturized PPAM presents only two layers of adhesive tape in order to ease the realization of small folds.

- An Aluminum ring (see Fig. 7.15) is fixed to each external ribbed part of the third generation PPAM, in order to improve their resistance. These rings have not been reproduced for the miniaturized PPAM in order to decrease the number of the muscle parts. In practice, the external ribbed parts have revealed to be resistant enough without such rings.

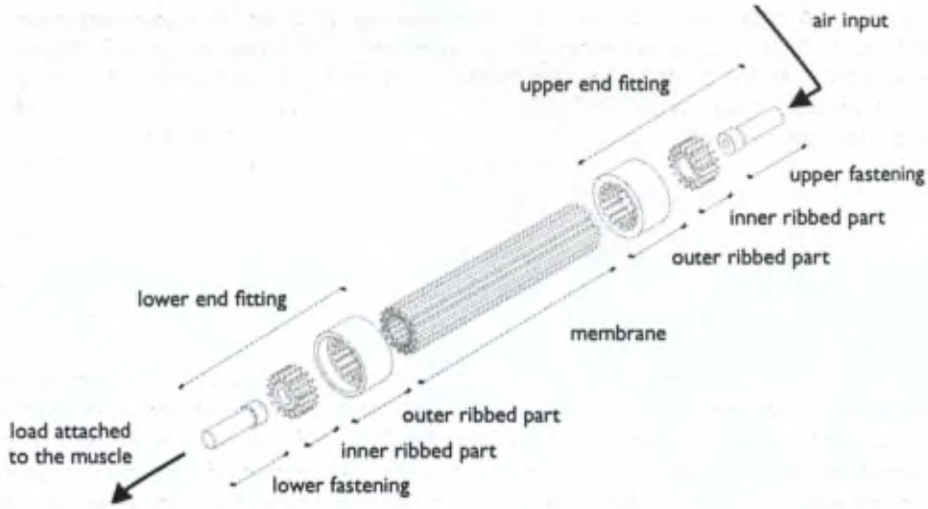

Figure 7.9: View of the design of the miniaturized PPAM. This miniaturized PPAM has the same design as the third generation PPAMs developed at the Department of Mechanical Engineering of the VUB. Figure adapted from [27].

- Both fastenings of the third generation PPAM present a threaded hole along their length. During the assembly of the muscle, a threaded bar is inserted in these threaded holes and it goes through all the muscle from one end to the other one. This allows to fix the muscle along an axis during the assembly. This has not been reproduced for the miniaturized PPAM because its small size would require a threaded bar having a very small diameter and thus difficult to manufacture.

A) The membrane

As shown before by the theoretical model developed by [30], an ideal PPAM having an infinite number of infinitely shallow pleats does not present parallel stresses and as a consequence develop the highest possible pulling force. To get close to this ideal case, a PPAM should present as much folds as possible with the smallest depth possible.
Folds have been made manually with the membrane in order to determine the minimum depth that could be achieved. Fig. 7.10 represents three teeth of the inner ribbed part. X is the distance between the tops of two adjacent teeth. Since the pleats of the membrane are inserted between the teeth of the inner ribbed part, X is also the distance between the tops of two adjacent folds. The folds obtained during the experiments have revealed that under a distance X= 5 mm, it was not possible to insure some regularity of the folds.

The number of folds is linked to the design of the inner ribbed parts whose diameter has be about maximum 1 cm. Taking this requirement into account and knowing that the membrane (whose thickness is about 0.3 mm), the string and a tooth of the outer ribbed part are inserted between two teeth of the inner ribbed part, it has been decided to make 16 folds in the membrane leading to an outer diameter of 10.4 mm for the inner ribbed part and to an outer diameter of 11 mm for the unpressurized folded membrane. The useful membrane length (i.e. the length of the membrane measured between the end fittings) is fixed at l = 50 mm while the total length is 60 mm due to the insertion of the membrane ends between the inner and outer ribbed parts. Fig. 7.11 presents the dimensions of the membrane.

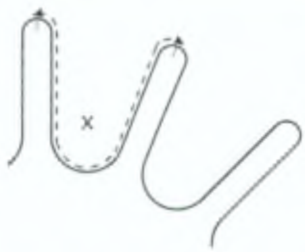

Figure 7.10: View of three teeth of the inner ribbed part. X is the distance between the tops of two adjacent teeth. Since the pleats of the membrane are inserted between the teeth of the inner ribbed part, X is also the distance between the tops of two adjacent folds. Figure from [27].

Figure 7.11: Design of the membrane of the miniaturized PPAM. The membrane counts 16 folds of 2.5 mm depth. When folded and unpressurized, its outer diameter equals 11 mm. The useful membrane length is fixed to $l = 50$ mm while the total length is 60 mm due to the insertion of the membrane ends between the inner and outer ribbed parts. Figure adapted from [27].

B) The end fittings and the string

Fig. 7.12 presents the design of the inner ribbed parts. As explained before, these parts count 16 teeth and have an outer diameter of 10.4 mm. They are inserted in the membrane at its both ends and are glued to it with epoxy resin. To ease the manipulation of these parts and to have a surface to glue that is not too small, a thickness of 5 mm has been chosen for these parts.

The inner and outer ribbed parts have been manufactured by Selective Laser Melting (SLM) and are made of titanium. Concerning the fastenings, they have been achieved from M4 screws that have been machined: the head of these screws has been machined in order to reduce its diameter to 5 mm and a hole of 2 mm diameter has been performed along the screw axis in the screw used as upper fastening to allow the air feeding of the muscle. The dimensions of the screws and of the upper fastening hole have been chosen in order to reduce as less as possible the mechanical resistance of the inner ribbed parts and of the screws while allowing the better possible circulation of air. The screws are inserted in the inner ribbed parts (and glued to them) and are supported by the circular edge shown in Fig. 7.12 (see (b) and (c)). When the muscle is loaded, all the force is applied to the circular edge of both inner ribbed parts and a material resistant enough to support this has been chosen for these parts. Fig. 7.13 presents the design of the outer ribbed parts. These parts are placed around the membrane at its both ends and are fixed to it with epoxy resin. The edge (see (b) in Fig. 7.13) is foreseen to be filled with epoxy resin in order to make the end fittings airtight.

The string is a fishing nylon thread (geologic x-stress) whose diameter equals 0.35 mm.

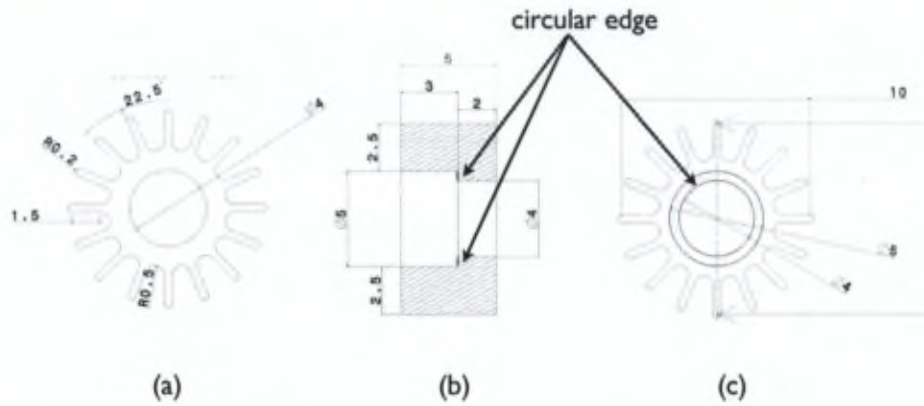

Figure 7.12: Design of the inner ribbed parts of the miniaturized PPAM. (a) front view (b) transversal view (c) back view. These parts count 16 teeth and have an outer diameter of 10.4 mm. They are inserted in the membrane at its both ends and are glued to it with epoxy resin. Figure adapted from [27].

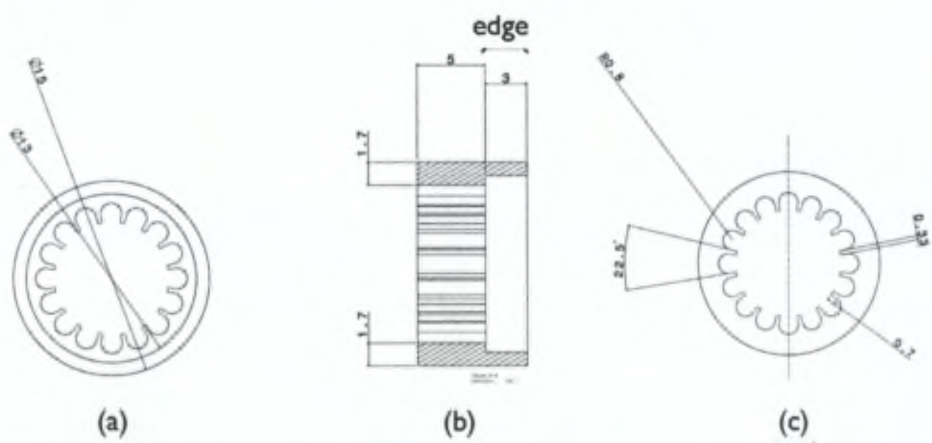

Figure 7.13: Design of the outer ribbed parts of the miniaturized PPAM. (a) front view (b) transversal view (c) back view. These parts are placed around the membrane at its both ends and are fixed to it with epoxy resin. The edge (see (b) in the figure) is foreseen to be filled with epoxy resin in order to make the end fittings airtight. Figure adapted from [27].

C) Comparison of the miniaturized PPAM with the third generation PPAM developed at the VUB

Fig. 7.14 and 7.15 are pictures of the miniaturized PPAM and of the third generation PPAM developed at the VUB, respectively. Table 7.1 compares the geometric characteristics of both muscles and highlights the miniaturization work that has been performed. As can be seen, the length of the PPAM developed at the VUB has been divided by two while its outer diameter has been nearly divided by three.

Figure 7.14: Picture of the miniaturized PPAM. Figure from [27].

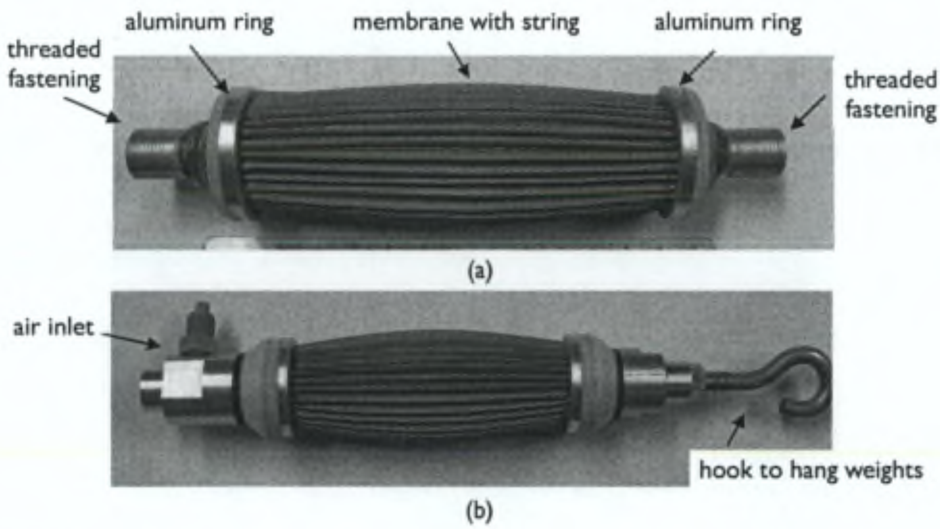

Figure 7.15: Picture of the third generation PPAM developed at the VUB. (a) and (b): without and with the air inlet and the hook to hang weights. Figure adapted from [27].

D) Prediction of the traction model

As explained in Section 7.2.2, the initial radius R of a third generation PPAM is the radius at which the fibres are placed. In the case of the miniaturized PPAM described here, this radius equals about 3.5 mm. Indeed, as presented in Fig. 7.16, the hollows between the teeth of the inner ribbed part are located at a radius of 3 mm and since the membrane has a thickness of about 0.3 mm and the nylon thread a diameter of 0.35 mm, the centres of the

	Miniaturized PPAM	Third generation PPAM of the VUB
total length (from the end of a fastening to the end of the other fastening)	± 90 mm	± 180 mm
total length of the membrane	60 mm	± 140 mm
outer diameter of the outer ribbed part	15 mm	40 mm
number of folds	16	32
distance X between the tops of two adjacent folds (see Fig. 7.10)	5 mm	10 mm
weight	17 g	not known

Table 7.1: Comparison of the geometric characteristics of the miniaturized PPAM with the third generation PPAM developed at the VUB

fibres are located at a radius R of about 3.5 mm.

Since the useful length of the membrane equals l = 50 mm, the slenderness $\frac{l}{R}$ of the miniaturized muscle equals about 14 and according to equation (7.6), the muscle should be pressurized at a pressure $p = 0.6$ bar in order to develop a force $F = 100$ N while producing a contraction $\epsilon = 10$ %.

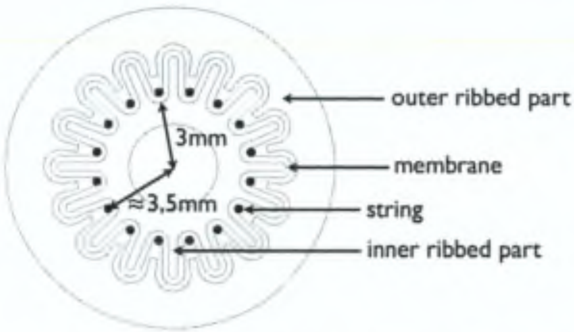

Figure 7.16: Side view of the miniaturized PPAM. The initial radius R of the miniaturized PPAM equals about 3.5 mm. It is the radius at which the fibres are placed. Figure adapted from [27].

7.3.3 Test bench particularities

To characterize the miniaturized muscle, experiments have been performed on the test bench described in Section 3.5. Fig. 7.17 presents this test bench; its particularities are the following:

- The $0-6$ bar pressure sensor described in Section 3.5.5 is screwed to the T-fitting (see Table B.1) placed at the output of the pneumatic cylinder. It measures the pressure inside the pneumatic circuit (= chamber of the pneumatic cylinder + pneumatic tube + miniaturized PPAM) and thus the inner pressure of the muscle, since the pressure is assumed to be uniform in the pneumatic circuit.
- The Festo pneumatic fittings used to connect the muscle to the T-fitting are the following: 1) QS - 1/4 - 6: to connect the pneumatic tube (whose outer diameter equals 6 mm) to the T-fitting, 2) QSF - 1/8 - 6 - B and NPFB - R - G18 - M5 - MF to connect the tube to the upper fastening of the muscle.
- The miniaturized PPAM is fixed to a support thanks to its upper fastening while a thin metallic plate is fixed horizontally at the lower muscle fastening. The laser sensor, described in Section 3.5.5, is placed as close as possible to the muscle and measures the vertical displacement of the plate which is the same as the vertical displacement of the muscle end. The contraction of the muscle is then computed by dividing this displacement by the initial length of the muscle membrane.
- The muscle is loaded by dumbbell weights attached to the lower fastening.

The measurements are made as follows:

1. The motor moves the cylinder piston to a given position.
2. A weight is attached to the muscle. The inner pressure p of the muscle is measured as well as its contraction ϵ.
3. The piston position is kept constant. Another weight is hung to the muscle and the inner pressure and contraction of the muscle are measured.
4. etc.

and these steps are repeated for different piston positions.
The errors on the measurements are summarized in Table 7.2.

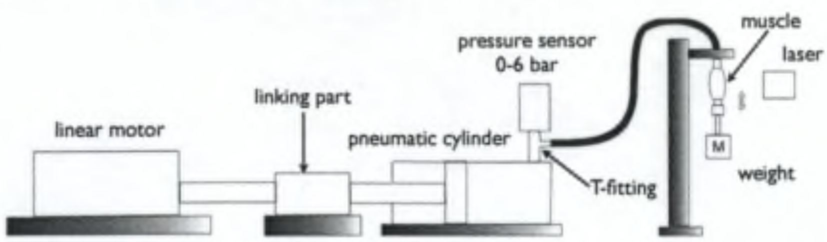

Figure 7.17: Test bench used to perform the experiments in order to characterize the miniaturized PPAM. Figure adapted from [27].

Variable	Error on the measurement of the variable
weight	not known
inner pressure p of the muscle	$\pm$ 0.015 bar
muscle contraction ϵ	linearity of the laser sensor = $\pm$ 0.003 mm

Table 7.2: Errors on the measurements

7.3.4 Experiments: observations and measurements

Two miniaturized PPAMs have been tested. For both muscles, the membrane is folded manually using a tool looking like an iron to press the folds. A second folding step is then performed for the second muscle but not for the first one. This second step consists in using a model part to improve the regularity of the folds. This model part is presented in Fig. 7.18. It has been manufactured in resin by stereolithography; its cross-section is the same as that of the inner ribbed parts and its length equals 60 mm. The folded membrane is placed around this model part and the string is inserted in the hollows of the pleats. The membrane is then heated with an hairdryer while pressing the folds hollows. The string and the model part are then removed. This second folding step has led to a better regularity of the folds and to a muscle presenting better characteristics as will be shown later.
Remark: For the third generation PPAMs developed at the VUB, these two folding steps are also performed but the model part is different. It has a flat side while the other side presents a pattern corresponding to the folds that have to be made in the membrane.

A) Observations

During the first pressurization-depressurization cycles, the membrane of the first muscle presented a torsion leading to a rotation of the lower end fitting. Besides, the unfolding of the pleats was irregular: some pleats unfolded faster than others leading to a radial displacement of the lower end fitting. This displacement has not been measured. This irregular unfolding is due to the manual folding of the membrane which involves that the tension of the string is not the same in every hollow and that the pleats are not regular and do not present the same depth. However, after some cycles, the membrane torsion has strongly decreased and the folds have become more regular as well as the unfolding, involving a decreasing of the radial displacement.
When the muscle is pressurized, two areas, each one located near one of the end fittings,

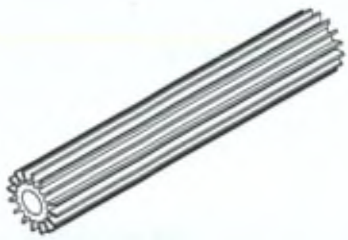

Figure 7.18: Model part used to improve the regularity of the membrane folds. First the folds are made manually. Afterwards, the folded membrane is placed around this model part and the string is inserted in the hollows of the pleats. The membrane is then heated with an hairdryer while pressing the folds hollows. The string and the model part are then removed. Compared to the miniaturized PPAM whose folds have been made in one step, this second folding step has led to a better regularity of the folds and to a muscle presenting better characteristics. Figure adapted from [27].

are not unfolded at all and as a consequence do not contribute to the contraction of the muscle. When the inner pressure of the muscle increases, the pleats unfold more in these areas which thus decrease and consequently the maximum contraction of the muscle increases. Fig. 7.19 shows these areas when the muscle folds are completely unfolded in the middle of the membrane.

After a pressurization-depressurization cycle, the muscle does not come back to its initial cylindrical shape. Its membrane keeps a rounded shape (more pronounced if the pressure was larger) whose length is smaller than the initial length $l = 50$ mm that the muscle showed after its building.

Finally, it has been noticed that the pneumatic circuit presents leakages.

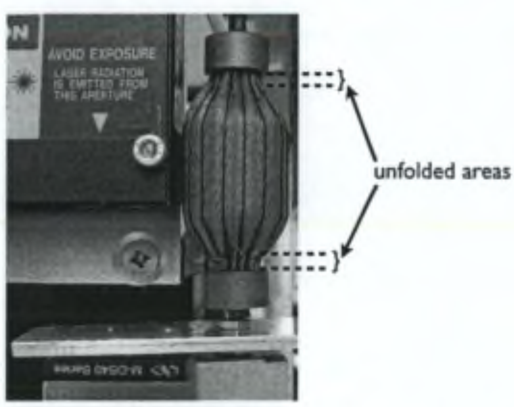

Figure 7.19: First miniaturized PPAM. The areas shown in the figure are located near the end fittings and are not unfolded at all. As a consequence they do not contribute to the contraction of the muscle. Figure adapted from [27].

Concerning the second miniaturized PPAM, it better comes back to its initial cylindrical shape when it is depressurized. Like the first one, this second muscle presents an irregular unfolding and a radial displacement but these behaviours diminish after some pressurization-depressurization cycles. This muscle also presents areas located near the end fittings and which do not unfold. Its maximum contraction also increases with the pressure.

B) Static load tests

Static load tests have been performed on the miniaturized muscles; more precisely, they have been subjected to loading-unloading cycles with weights up to 64 N.
The membrane length of the muscle at rest has been used to compute the contractions. As explained before, since the muscle does not regain its initial cylindrical shape when it is depressurized, its membrane length at rest is smaller than the length $l = 50$ mm that the muscle showed after its building. This explains why the miniaturized PPAMs present negative contractions at high loads, for some pressure levels.
As already said in Section 7.3.3, a thin metallic plate is fixed horizontally at the lower muscle fastening and a laser sensor measures its vertical displacement which is normally equal to the muscle displacement. However, during the experiments, this plate does not stay perfectly horizontal. To minimize the effect that this has on the measurements, the laser sensor has been placed so that its axis is located as close as possible to the axis of the muscle.
As explained before in Section 7.3.3, the loading-unloading cycles have been performed for constant positions of the cylinder piston. Hence, the pressure is not constant during a cycle but increases and decreases when the weight attached to the muscle is increased or decreased, respectively. Once the experiments were done, the measured data have been combined in order to establish isotonic curves (i.e. at constant muscle load) of the pressure with respect to the contraction. These curves have then been used to establish the isobaric curves presented in Fig. 7.20 to 7.23.

Fig. 7.20 presents the developed force F of the first miniaturized PPAM, with respect to its contraction ϵ and for different pressure levels p. As can be seen:

- The muscle presents some hysteresis.
- A phenomenon occurs at forces larger than about 41 N: the loading curve passes under the unloading curve.
- For pressure levels ranging between 0.3 bar and 0.6 bar, the maximum contractions range between 5.7 % and 8 %. As the pressure increases, the maximum contraction increases. This is due to the fact that the areas located near the end fittings slightly unfold when the pressure is increased and this contributes to increase the enclosed volume of the muscle and the contraction.

The first miniaturized PPAM has also been pressurized at $p = 1$ bar and it was able to develop a pulling force $F = 100$ N while producing a contraction $\epsilon = 4$ %.
After all these tests, the muscle has not recovered its initial cylindrical shape but has a rounded shape. However, its membrane and string do not present any damages.
The tests have revealed that the first muscle presents a pressure threshold. It has not been determined since it was difficult to measure it because of its low value.

Fig. 7.21 presents the developed force F of the second miniaturized PPAM, with respect to its contraction ϵ and for different pressure levels p. As can be seen:

- The muscle presents some hysteresis but the loading curves always stay above the unloading curves. Since the folds of the second muscle present a better regularity, the phenomenon that has been noticed for the first muscle is probably due to the irregularity of its pleats.

- For the same pressure levels as for the first muscle, the maximum contractions produced by the second muscle seem to be larger. This is probably due to the better regularity of the muscle folds.

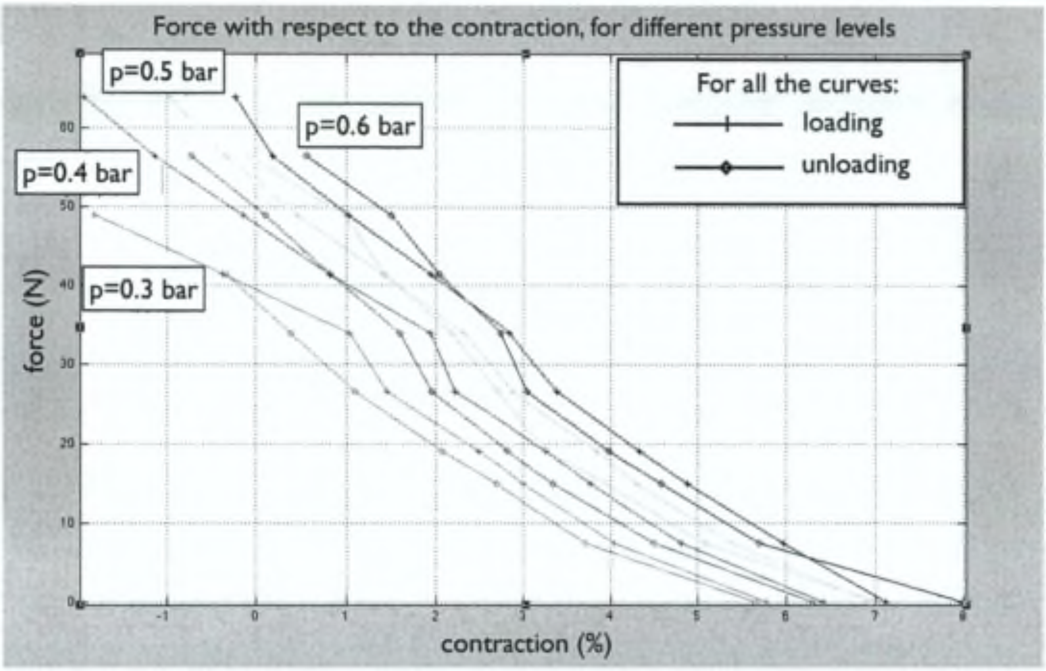

Figure 7.20: First miniaturized PPAM: developed force F with respect to the contraction ϵ, for different pressure levels p. As can be seen, the muscle presents some hysteresis and for forces above about 41 N, the loading curves pass under the unloading curves. The maximum contractions range between 5.7 % and 8 % and as the pressure increases, the maximum contraction increases. This is due to the fact that the areas located near the end fittings slightly unfold when the pressure is increased and this contributes to increase the enclosed volume of the muscle and the contraction. Figure adapted from [27].

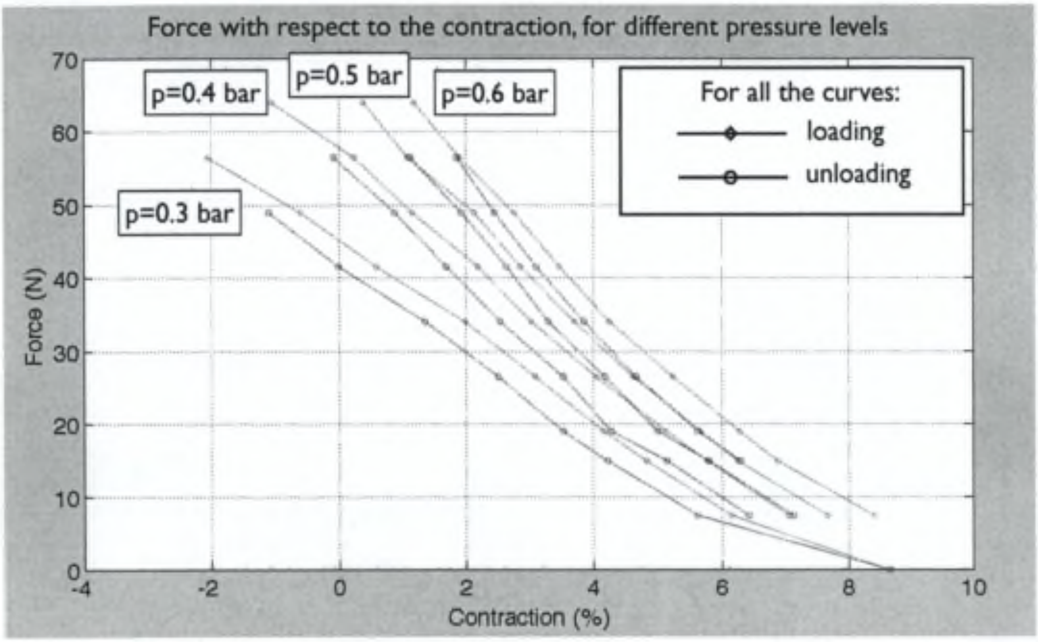

Figure 7.21: Second miniaturized PPAM: developed force F with respect to the contraction ϵ, for different pressure levels p. As can be seen, the muscle presents some hysteresis and the loading curves always stay above the unloading curves. Besides, the maximum contractions seem to be higher than for the first miniaturized PPAM, for the same pressure levels. Figure adapted from [27].

Fig. 7.22 compares the first and the second miniaturized PPAMs and presents their developed force F with respect to the contraction ϵ, for $p = 0.6$ bar; both curves are loading curves. As is shown in the figure, for given pressure and contraction, the second muscle develops a larger force. This is probably due to the better regularity of the muscle folds.

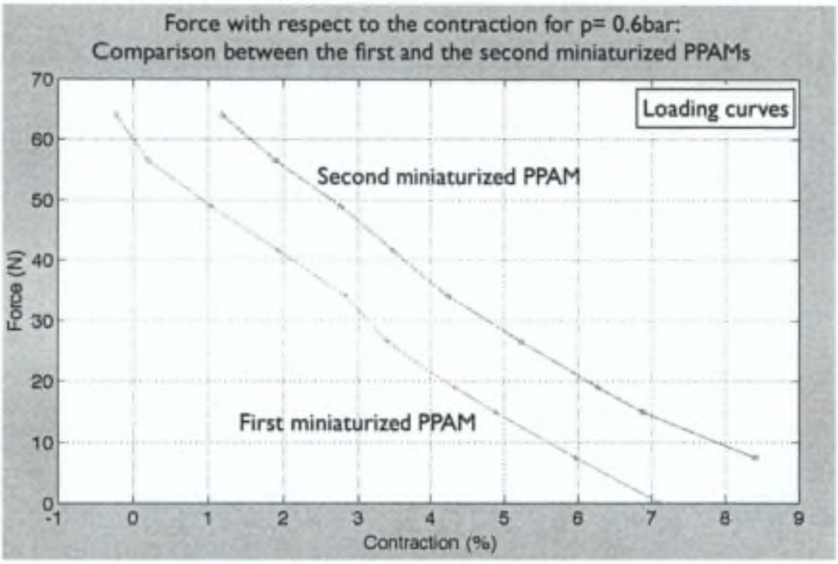

Figure 7.22: Developed force F with respect to the contraction ϵ, for $p = 0.6$ bar: comparison between the first and the second miniaturized PPAMs. Both curves are loading curves. As it is shown in the figure, for given pressure and contraction, the second muscle develops a higher force than the first one. Figure adapted from [27].

Fig. 7.23 compares theoretical curves to the experimental curve of the second miniaturized PPAM, for $p = 0.6$ bar. The theoretical curves have been achieved with the traction model which takes the number of folds into account (see equation (7.6)). $R = 3.5$ mm is the initial radius of the miniaturized PPAM; it is the radius at which the fibres are placed. $l = 50$ mm is the initial length of the membrane while $l = 40$ mm is the length of the membrane when the areas located near the end fittings and which do not unfold, are not taken into account in the length of the membrane. As illustrated by the figure, for given pressure and contraction, the force developed by the second muscle is smaller than the force predicted by the theoretical curves, even if the unfolded areas near the end fittings are not taken into account. Besides, the maximum contraction achieved experimentally is also smaller than the predicted ones. This can be explained by the fact that the membrane of the miniaturized muscle does not allow to reach an enclosed volume that is large enough. Indeed, the membrane counts 16 folds of 5 mm; hence, when totally unfolded, its circumference equals 16×5 mm $= 80$ mm and the corresponding equatorial diameter is $D = 25.5$ mm. The miniaturized muscle has a slenderness $\frac{l}{R}$ of about 14. As shown by Fig. 7.5, for a slenderness $\frac{l}{R} = 10$ and thus close to 14, the maximum value of the dimensionless diameter function $d(\epsilon, \frac{l}{R})$ equals about 0.9. With the initial muscle length $l = 50$ mm, the theoretical model thus predicts a maximum equatorial diameter $D = 45$ mm. Hence, the maximum equatorial diameter that can be achieved with the miniaturized muscle is nearly twice as low as recommended by the theoretical model. In conclusion, deeper folds would be necessary to correct this but another solution is to opt for a shorter length for which a maximum

equatorial diameter $D = 25.5$ mm would be enough to fully expand.
As explained before, equation (7.1) expresses the theoretical maximum pulling force that a muscle can develop for a given pressure and a given contraction. For given pressure and contraction, if the unfolding of the pleats has involved a volume increase dV that is smaller than the one predicted by the models, the corresponding force will, according to equation (7.1), also be smaller than the predicted one. Hence, the fact that the miniaturized muscle develops a force smaller than the predicted one can probably also be explained by the fact that the folds of the miniaturized PPAM do not allow it to expand enough in comparison with the expansion recommended by the models. In addition to this, the difference between the force measurements and the force predictions may also be due to the fact that the muscle needs a non-negligible amount of energy to expand and/or that there are energy losses, by friction for example.

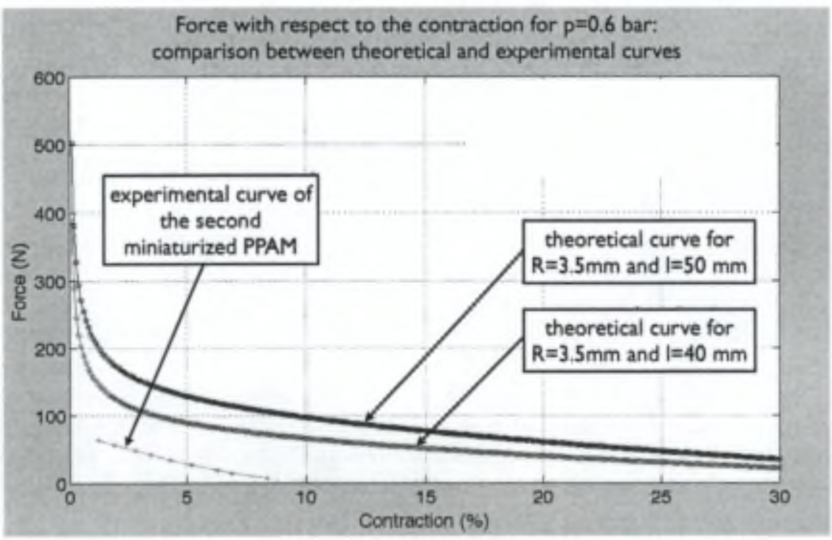

Figure 7.23: Developed force F with respect to the contraction ϵ, for $p = 0.6$ bar: comparison between theoretical curves and the experimental curve of the second miniaturized PPAM. The theoretical curves have been achieved with the traction model which takes the number of folds into account (see equation (7.6)). $R = 3.5$ mm is the initial radius of the miniaturized PPAM; it is the radius at which the fibres are placed. $l = 50$ mm is the initial length of the membrane while $l = 40$ mm is the length of the membrane when the areas located near the end fittings and which do not unfold, are not taken into account in the length of the membrane. As illustrated by the figure, for given pressure and contraction, the force developed by the second muscle is smaller than the force predicted by the theoretical curves, even if the unfolded area near the end fittings are not taken into account. Besides, the maximum contraction achieved experimentally is also smaller that the predicted ones. Both observations can be explained by the fact that the membrane of the miniaturized muscle does not allow to reach an enclosed volume that is large enough. Figure adapted from [27].

Remark: A third miniaturized PPAM has been tested. It differs from the first and second ones by its membrane which has been manufactured in resin by stereolithography. The membrane has a thickness of 0.3 mm and the chosen resin presents some flexibility at such a thickness (the ribbed parts of this muscle have also been manufactured by stereolithography in another resin). The advantage of this membrane is that its folds have been achieved by a method which offers a better precision than the manual folding. Hence the folds are very regular and the unfolding of the membrane is uniform when it is pressurized. In addition, the assembly of the muscle is easier with this membrane. However, this membrane is more rigid than the combination of adhesive tape and polyester and requires more energy to be unfolded. As a consequence, the achieved contractions are smaller for a given pressure and the muscle has a higher pressure threshold. Besides, the membrane is fragile and after some pressurization-depressurization cycles, cracks have appeared in the membrane making the muscle unusable.

7.4 Conclusions and perspectives

Pleated Pneumatic Artificial Muscles (PPAMs) differ from the other pneumatic artificial muscles by the design of their membrane. This membrane presents pleats which need a very low amount of energy to unfold when the membrane is pressurized. This confers good characteristics to the PPAMs such as a low hysteresis, a low pressure threshold, larger developed forces and contractions.

A miniaturization work has been performed on the third generation PPAMs developed at the VUB, in order to reach a size that would allow to use them in flexible medical instruments. For example, for applications in Minimally Invasive Surgery, instruments must have a diameter less than 10 mm [66] in order to pass through the trocars, while the diameter of catheters can be as low as 1 mm or less [60].
For this first miniaturization work, the target was to develop a miniaturized muscle able to develop a force of about 100 N and having a diameter at rest of about 1 cm. No specific objective was set concerning the stroke of the muscle.

The achieved miniaturized muscles have a design similar to that of the third generation PPAMs developed at the VUB and present a total length of about 90 mm and an outer diameter at rest of about 15 mm. They are twice as small as the third generation PPAM of the VUB. Two miniaturized muscles have been characterized experimentally. They have been subjected to loading-unloading cycles with weights up to 64 N. Both muscles present an irregular unfolding involving a radial displacement but these behaviours diminish after some pressurization-depressurization cycles. The manual folding of the membrane is the cause of these phenomena because the pleats are irregular and the string tension is not the same in all the folds hollows. Besides, both muscles present some hysteresis and when they are pressurized, two areas, each one located near one of the end fittings, are not unfolded at all and do not contribute to the contraction of the muscles. However, when the inner pressure of the muscles increases, the pleats unfold more in these areas which thus decrease and consequently the maximum contraction of the muscles increases. For pressure levels ranging between 0.3 bar and 0.6 bar, the maximum contractions of the first muscle range between 5.7 % and 8 %. The second muscle presents better characteristics than the first one and this is due to the better regularity of its folds. Indeed, for given pressure and contraction, the second muscle develops a larger force than the first one. Besides, it better goes back to its initial cylindrical shape when it is depressurized and for the same pressure levels as the first muscle, its maximum contractions seem to be larger.
The first miniaturized PPAM has also been pressurized at $p = 1$ bar and it was able to develop a pulling force $F = 100$ N while producing a contraction $\epsilon = 4$ %. Hence, it can be concluded that the miniaturization objectives have been reached concerning the developed force while the diameter should be reduced further.
Comparing the second muscle to the theoretical traction model, it has been noticed that the force developed by the muscle is smaller than the force predicted by the theoretical curve. Besides, the maximum contraction achieved experimentally is also smaller that the predicted

one. Both observations can probably be explained by the fact that the membrane of the miniaturized muscle does not allow to reach an enclosed volume that is large enough. In conclusion, deeper folds would be necessary to correct this but another solution is to opt for a shorter muscle length for which the maximum equatorial diameter allowed by the membrane would be enough to fully expand.
In addition to this, the difference between the force measurements and the force predictions may also be due to the fact that the muscle needs some amount of energy to expand and/or that there are energy losses, by friction for example.

Other tests on other miniaturized muscles are necessary to verify the repeatability of the results, to study more thoroughly the hysteresis of the muscle, to assess its life duration and to determine the maximum force and contraction the muscle can produce and the maximum pressure it can bear. Besides, dynamical tests could be performed to determine the dynamical characteristics of the miniaturized muscles.

Regarding a further miniaturization while keeping the same muscle design, it can be concluded that:

- Decreasing the diameter of the muscle also means decreasing the diameter of the membrane and thus the size of the folds, if one wants to keep their number. However, the manual folding of the membrane limits the folds depth that can be achieved. The membrane thickness could be decreased to ease the folding but it would also decrease the membrane stiffness. Tests would have to be performed to assess the influence of this change on the muscle performances. Another solution would be to find a manufacturing method that would allow the realization of small regular pleats while keeping sufficient membrane stiffness, flexibility and solidity. Plastic injection or heat-forming of a thermoplastic membrane in a ribbed mold could be tracks to investigate. Another idea to reduce the diameter of the membrane, would be to keep folds of 5 mm but to reduce their number.

- The size of the end fittings parts could be further reduced by micro-manufacturing methods. The fastenings have been achieved by classical manufacturing methods and their size could probably be reduced using micro-manufacturing methods. However, if the diameter of the hole foreseen for the air feeding of the muscle is decreased, the pressurization of the muscle may become more difficult due to pressure losses in this small hole. Again, tests would be necessary to assess this.
  According to the manufacturer of the ribbed parts, the Selective Laser Melting has reached its limits with these parts and it is not sure whether thinner teeth and closer teeth could be achieved with this method; tests would be necessary to evaluate this. The stereolithography would allow to decrease further the thickness of the teeth and the space between the teeth but the resin could become quite fragile.

- Decreasing the sizes of all the muscle parts would make the assembly more difficult.

Simplifying the design and reducing the number of parts is another solution that can be considered to miniaturize the muscle further. For example, since the required pulling forces are quite small ($100 - 200$ N compared to more than 1000 N for the third generation PPAMs developed at the VUB), the string could be removed. The muscle design would then be the same as that of the first generation PPAMs developed at the VUB. Besides, the design of the end fittings could be reconsidered and a fastening and the corresponding inner ribbed part could be merged into one part.

To simplify the design, one could think of replacing the folded membrane by an elastic membrane reinforced by axial fibres. The muscle equipped with such a membrane would need energy to deform the elastic membrane and would have thus a force output lower than that of the PPAM. However, this muscle could maybe be able to develop the required forces even if it does not present characteristics as good as those of the PPAM. Such a miniaturized muscle has been developed by [81]. It is made of a silicone rubber tube reinforced by axial aramid fibres (see Fig. 7.24). Its diameter equals 10 mm while its length is about 14 mm. This muscle is able to produce a 0.17 N pulling force for a pressure of 8 kPa. Since the rubber is very elastic, its resistance to pressure is limited and therefore, the developed forces are limited and too low in comparison with the required force of 100 – 200 N.

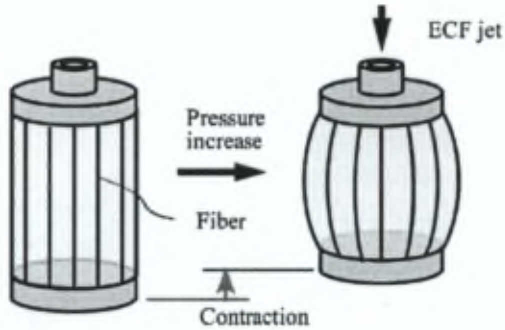

Figure 7.24: Micro artificial muscle made of a silicone rubber tube reinforced by axial aramid fibres. The actuation fluid is an electro-conjugate fluid (ECF). When the muscle is pressurized, it contracts. Figure from [81].

Fig. 7.25 presents a graph coming from [45]. It compares different kinds of actuators by presenting their actuation stress with respect to the actuation strain. The heavy lines are the upper right corner of the performance space of each class of actuator. The first miniaturized PPAM has been placed on this graph for a pressure $p = 0.6$ bar.

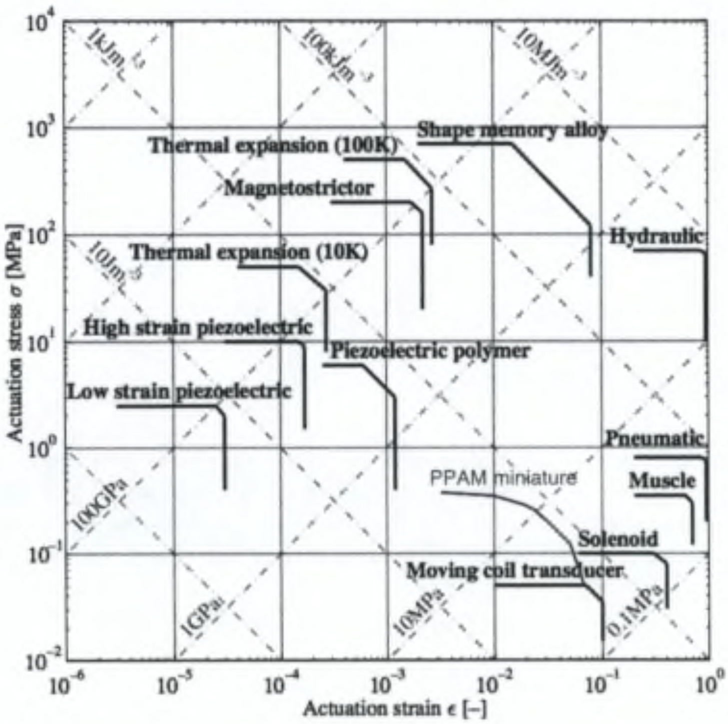

Figure 7.25: Comparison between different kinds of actuators: the actuation stress is presented with respect to the actuation strain. The heavy lines are the upper right corner of the performance space of each class of actuator. The first miniaturized PPAM has been placed on this graph for a pressure $p = 0.6$ bar. Figure adapted from [45].

Chapter 8

Conclusions and perspectives

8.1 Conclusions

This work proposes a study of a specific kind of actuators: the Flexible Fluidic Actuators. These are driven by fluid, i.e. gas or liquid, and present a flexible structure, i.e. an elastically deformable and/or inflatable structure. These actuators could be used to develop flexible instruments which could answer the need expressed by the medical community for such instruments. Hence this study is performed with a view to medical applications.

A review of the existing flexible fluidic actuators has been performed. It shows that there exist actuators able to stretch themselves, to shorten, to bend themselves or to develop a rotational motion and some of them present several DOFs. Two different methods to achieve bending have been identified. The first technique is based on "internal chambers differently pressurized" and the other one on "anisotropic rigidity". Besides, two methods to generate a rotational motion have also been identified. The actuators based on the first technique present a structure reinforced in places (with fibres or by increasing the material thickness) in such a way that when the actuators are pressurized, their structure involves a rotation. The second method to generate a rotational motion consists in an articulated structure in which one or several flexible fluidic actuators are inserted. When the actuators are pressurized, they actuate the structure which involves a rotation.
There exists a multitude of flexible fluidic devices and additional actuators can be obtained by combining different principles, in order to achieve more or less DOFs. Hence, this review can helps to develop medical flexible instruments based on flexible fluidic actuators. Indeed, according to the number and types of degrees of freedom required for the application, this review can help to choose a design. Besides, tools to be placed at the tips of the instruments could also be designed and based on flexible fluidic actuators.

According to the bulkiness that is allowed for the instrument in the targeted application, it will be necessary to assess the miniaturization potential of the actuators presented in the review. In this respect, actuators presenting a simple structure with a small number of parts will be better candidates to design miniature instruments. Since, miniaturizing the actuators also means miniaturizing their peripherics, some solutions have been presented in this respect.

Flexible fluidic actuators present interesting characteristics regarding an application inside the human body such as their compliance that allows them to handle delicate objects and to adapt themselves to their environment during contacts. Among the interesting features linked to the use of these actuators, one has caught our eye. Indeed, in [79], the "Flexible Microactuator" (FMA) is presented and it is suggested that the measurements of the fluid

pressure and of the volume of supplied fluid allow to determine and control the position of the actuator and the force it develops. This property has been called the "Pressure-Volume-Force-Position principle" or "PVFP principle" and it means being able to determine the displacement of a flexible fluidic actuator and the force it develops without using a displacement sensor or a force sensor [79].
This concept is particularly interesting for applications, such as medical ones, where the space is limited and where a miniaturization effort is required. This is for example the case in Teleoperated MIS where it is necessary to measure the force applied by the tools to the organs to ensure a force feedback of good quality. Obtaining this measurement is not straightforward. Indeed, if the force sensor is placed on the tool, outside the body of the patient, the measurement will be polluted by the friction of the trocar. To solve this problem, some researchers propose to place the sensor at the end of the tool inside the body but this raises the challenge to develop a small and sterilizable force sensor [64]. Using flexible fluidic actuators to actuate the surgical tools and exploiting the PVFP principle would allow to measure the force applied to the organs without the need for a force sensor.

A test bench has been developed to study and implement the PVFP principle and to characterize flexible fluidic actuators. It is basically a syringe-pump connected to the actuator to be studied. In practice, this syringe-pump is implemented with a linear motor that drives the piston of a cylinder whose output is connected to the actuator. This system uses a constant quantity of driving fluid and allows to pressurize the studied actuator. The test bench is equipped with different sensors that allow to measure the displacement of the cylinder piston, the pressure inside the actuator and the displacement(s) of its tip and weights are used to load the actuator. For the implementation of the PVFP principle, the volume of fluid supplied to the actuator is considered to be the volume swept by the cylinder piston and since this swept volume is proportional to the piston displacement, the latter will be the variable of interest instead of the swept volume.

To study and implement the PVFP principle, a flexible fluidic actuator called "Pneumatic Balloon Actuator" (PBA) has been used. This actuator, invented by [50], has been selected in the actuators review because it has a simple design, one DOF and because it is easily manufactured.

The implementation of the PVFP principle has consisted in characterizing the actuator by establishing experimental models of its behaviour. These models have then allowed to predict the displacements of the actuator tip and the weight attached to it, on the basis of the measurements of the piston displacement and of the pressure inside the actuator. This experimentally validates the PVFP principle in the case of the PBA. Concerning the quality of the predictions provided by the PVFP principle implemented on the flexible fluidic actuator, it to be evaluated with respect to a targeted application. Indeed, the predictions can be accurate enough for a given application but not for another one.
Hysteresis tests have been performed and it can be concluded that some of the PBA variables present some hysteresis; this hysteresis is not properly modeled by the experimental models. However, before modeling the hysteresis, it has to be assessed whether this hysteresis is problematic or not with respect to the targeted application. Indeed, for a given application, the hysteresis may be small enough to be negligible; in this case, there is no need to model the hysteresis. On the other hand, for another application, the same hysteresis may be too large to be ignored; in this case, it has to be modeled properly and this requires the elaboration of new experimental models of the PBA.

A numerical model of the PBA has been established by modeling the physics that seem to rule it. This model has been built in collaboration with the PMA department of the

KUL. The actuator is modeled as the combination of a membrane and a beam. A PBA modeled with the numerical model will be less stiff than its real counterpart and some of the assumptions on which the model rests are not verified in reality; this leads to large differences between the predictions provided by the model and the measurements performed on the prototypes (the PBA described in [50] and the PBA developed for the test bench). However, the numerical model is able to predict the bidirectional behaviour of a PBA and allows to better understand the physics underlying. The bidirectional behaviour is due to the pressure applied to the beam and to the force applied by the pressurized membrane to the beam. If the force applied by the membrane is predominant, the PBA free end moves upwards while if the pressure is predominant, it moves downwards.
It has to be mentioned that the numerical model seems to predict that all PBAs show this bidirectional behaviour while in practice, this behaviour has been reported for PBAs completely made of the same material and it is not established whether this behaviour happens for PBAs whose layers are made of different materials.
However, at this stage, it is not possible to conclude whether the numerical model could be used to predict the qualitative effects, on the tip displacements, of the change of a PBA parameter.

A miniaturization work has been performed on a particular kind of flexible fluidic actuator: the Pleated Pneumatic Artificial Muscle (PPAM). This actuator has been developed at the Department of Mechanical Engineering of the Vrije Universiteit Brussel (VUB).
According to theoretical models, miniaturized PPAMs, whose dimensions are small enough to be inserted into MIS medical instruments, could be able to develop the forces required to allow the instruments to perform most surgical actions. Therefore, the PPAMs have been studied in order to assess their miniaturization potential. This miniaturization work has been performed by Nhat-Quang CAO as a Master's thesis, in collaboration with the VUB.
The miniaturization work has been performed on the third generation PPAMs developed at the VUB and for this first attempt, the target was to develop a miniaturized muscle able to develop a force of about 100 N and having a diameter at rest of about 1 cm. No specific objective was set concerning the stroke of the muscle.
The achieved miniaturized muscles have a design similar to that of the third generation PPAMs developed at the VUB and present a total length of about 90 mm and an outer diameter at rest of about 15 mm. They are twice as small as the third generation PPAM of the VUB. Two miniaturized muscles have been characterized experimentally. For pressure levels ranging between 0.3 bar and 0.6 bar, the maximum contractions of the first muscle range between 5.7 % and 8 %. The second muscle presents better characteristics than the first one and this is due to the better regularity of its folds. Indeed, for given pressure and contraction, the second muscle develops a larger force than the first one. Besides, it better goes back to its initial cylindrical shape when it is depressurized and for the same pressure levels as the first muscle, its maximum contractions seem to be larger.
The first miniaturized PPAM has also been pressurized at $p = 1$ bar and it was able to develop a pulling force $F = 100$ N while producing a contraction $\epsilon = 4$ %. Hence, it can be concluded that the miniaturization objectives have been reached concerning the developed force while the diameter should be further reduced.

For the PBAs as well as for the PPAMs, it is not possible to impose the actuator displacement(s) and the force it develops at the same time. In practical applications, a choice will have to be made between imposing the force and imposing the displacements, according to the task to be performed.

8.2 Perspectives

The PVFP principle has been experimentally validated with the PBA, i.e. an actuator presenting only one DOF. With such an actuator, the applied force can be predicted at only one precise point and along only one precise direction. However, the principle can probably be applied to more complex structures presenting several chambers to be pressurized.

The PVFP principle could be implemented in a control loop in order to control the displacement of a flexible fluidic actuator tip or the force it develops, without using a displacement or a force sensor.

To implement this principle in a real medical application, it needs to be robust to the external perturbations such as a change in the ambient atmospheric pressure or temperature. Concerning the PBA, the PVFP principle seems applicable to this actuator with an incompressible or a compressible actuation fluid. Besides, if the PVFP principle is implemented on the PBA with an incompressible fluid and if a gauge pressure is used to measure the actuator pressure, it seems that the predictions provided by the PVFP principle implemented on the actuator will not be influenced by the changes of the atmospheric pressure and of the temperature.
For medical applications, a physiological saline solution can be used as incompressible fluid all the more that gas leakages are forbidden in some applications.

Replacing gas by liquid brings also the advantage that the system gets rid of the compressibility of the actuation fluid and this may decrease the establishing time of the pressure in the fluidic circuit. Indeed, during the experiments presented in this work, it has been noticed that the gas pressure takes several minutes to stabilize after a piston displacement.The fact that the pressure needs a long time to stabilize can be accredited to the gas compressibility, to the elasticity of the pneumatic tubes and to the elasticity of the flexible fluidic actuator. Studying the quantitative effect of each of these three causes would help to determine which action to take in order to reduce the establishment time of the pressure in the fluidic circuit and to increase the bandwidth of the system. However, before performing this study, it would be interesting to study the sensibility of the actuator displacements with regard to the pressure establishment. Indeed, it has a small effect on the actuator displacements, it may be superfluous to make a thorough study of the pressure dynamics.

Replacing gas by liquid implies larger pressure losses whose effect has to be studied. Besides, a flexible fluidic actuator filled with liquid will be heavier and as a consequence it will develop smaller displacements, for a given pressure level, than the same actuator filled with gas. Hence, the actuator will probably present a pressure threshold because a minimum pressure level will be required to compensate the weight of the liquid. An actuator filled with liquid will also be less compliant. All these aspects could be studied in future works.

Concerning the numerical model of the PBA, it could be modified in order to predict the displacements of the actuator tip rather than the displacements of the cavity tip. This would allow a better comparison between the predictions of the numerical model and the measurements performed on Konishi's PBA and the test bench PBA.
More experimental validations should be made with prototypes whose parameters are perfectly known in order to determine whether the numerical model could be used to predict the qualitative effects, on the tip displacements, of the change of a PBA parameter.

Concerning the miniaturized PPAMs, other tests on other miniaturized muscles will be necessary to verify the repeatability of the results, to study more thoroughly the hysteresis of the muscle, to assess its life duration and to determine the maximum force and contraction the muscle can produce and the maximum pressure it can bear. Besides, dynamical tests could be performed to determine the dynamical characteristics of the miniaturized muscles. Regarding a further miniaturization of the muscles, propositions have been made and could be tested in future works.

Appendix A

Test bench

A.1 Design of the syringe-pump test bench: comparison of the different considered solutions

A syringe-pump design is chosen for the test bench. The flexible fluidic actuator will be connected to the output of the syringe-pump and this will create a fluidic circuit composed of the chamber of the syringe-pump, the connection tubes and the flexible fluidic actuator. When the piston of the syringe-pump will be actuated, the pressure in the fluidic circuit will increase or decrease according to the actuation direction and the actuator will be actuated. In practice, a cylinder will be used as the syringe (see no. 5 in Fig. A.1). Besides, although a syringe-pump design can be used with gas or liquid, air will be used as fluid. Indeed, this will ease the use of the test bench because air is a readily available source, it can be freely evacuated in the ambient air [71] and possible leakages will not risk damaging the test bench (e.g. the electrical connections).

The volume of fluid supplied to the actuator is considered to be the volume swept by the piston of the syringe-pump. Hence, this volume is proportional to the displacement of the cylinder piston and in practice, the piston displacement is the variable that will be used instead of the swept volume.

The principle of the test bench is presented in Fig. A.1 and consists in the actuation of the cylinder piston (no. 4 in Fig. A.1) by an actuator (no. 1 in Fig. A.1). This actuator will be equipped with a position sensor to measure the displacement of the cylinder piston.

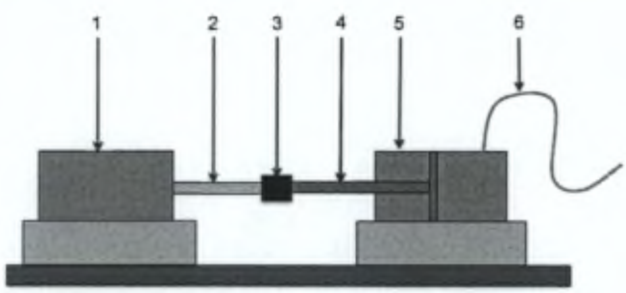

Figure A.1: Scheme of the syringe-pump test bench: 1) actuator + position sensor 2) shaft of the actuator 3) linking part 4) pneumatic cylinder piston 5) pneumatic cylinder 6) pneumatic tube (it connects the flexible fluidic actuator to the output of the cylinder)

Four possible solutions have been considered for the implementation of the test bench; they are presented here and compared regarding the implementation difficulty.

A.1.1 Basic solution: nothing is integrated, all the components are chosen separately and assembled together

Description

Fig. A.2 presents the first solution. A DC or stepper motor (no. 2 in Fig. A.2), equipped with an encoder, is coupled to a ball screw (no. 4 in Fig. A.2), supporting a ball nut (no. 5 in Fig. A.2). This nut is linked to the slider (no. 10 in Fig. A.2) of a linear guide (no. 11 in Fig. A.2) and the slider is linked to the piston of the cylinder (no. 7 in Fig. A.2). When the motor rotates, it drives the ball screw. The nut moves along the ball screw, the slider is driven along the linear guide and the cylinder piston is displaced. The encoder measures the rotation of the motor and allows to compute the displacement of the cylinder piston.

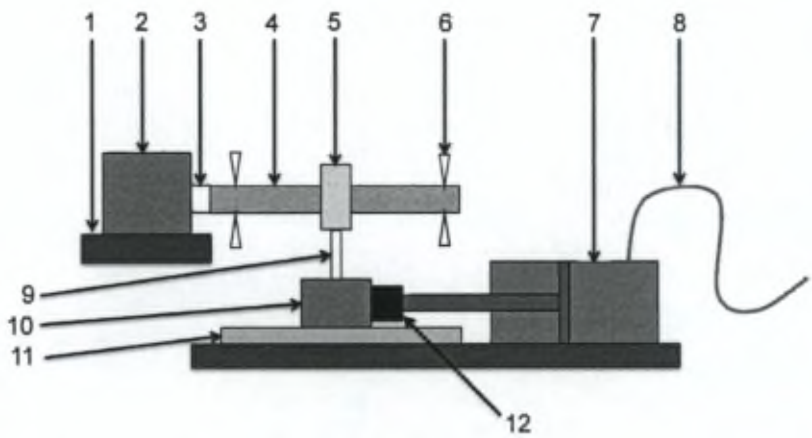

Figure A.2: First solution to implement the syringe-pump test bench: nothing is integrated, all the components are chosen separately and assembled together. 1) mounting parts of the motor 2) DC or stepper motor + encoder 3) coupling parts 4) ball screw 5) ball nut 6) support bearings of the ball screw 7) pneumatic cylinder 8) pneumatic tubes 9) linking part between the ball nut and the slider 10) slider 11) linear guide 12) linking part between the slider and the cylinder piston

Discussion

With this solution, nothing is integrated and all the parts are chosen separately. To assemble them, extra parts need to be ordered or designed and manufactured. Indeed, :

- To be fixed, the motor needs mounting parts (no. 1 in Fig. A.2). These parts need to be manufactured.
- To assemble the motor and the ball screw, coupling parts are necessary (no. 3 in Fig. A.2). These can be chosen off the shelf.
- The ball screw needs support bearings (no. 6 in Fig. A.2). These can be chosen off the shelf.

- The part linking the ball nut and the slider needs to be manufactured (no. 9 in Fig. A.2). This part will be subjected to shear and needs to be correctly designed to bear these stresses.
- The part linking the slider and the cylinder piston needs to be manufactured (no. 12 in Fig. A.2).

Besides,

- The motor and the ball screw need to be correctly aligned as well as the ball screw and the linear guide and the linear guide and the cylinder piston, to avoid out-of-axis efforts. Indeed, the motor, the linear guide and the cylinder piston can bear limited out-of-axis efforts and moreover, these efforts could cause friction and loss of positioning accuracy.
- The ball screw has a limited maximum rotational speed.
- The rotational motor can bear a limited axial load and a limited radial load.
- The slider sliding in the linear guide can bear limited efforts (forces and torques).
- The backlash resulting from the assembly of all the parts of the system needs to stay acceptable with regard to the wanted positioning accuracy.

In conclusion, the implementation of this first solution is quite difficult because of all the components limitations that have to be taken into account and because of the large number of parts that need to be selected or designed and manufactured.

A.1.2 The motor and the ball screw are integrated

Description

There exist motors already combined with a ball screw supporting a nut. For example, Maxon Motor [16] proposes "Modular spindle drives" (see Fig. A.3)

Figure A.3: "Modular spindle drive" proposed by Maxon Motors. Figure from [7].

The second solution is thus the same as the first solution apart from that the motor and the ball screw are integrated.

Discussion

This second solution brings the following advantages in comparison with the first solution:

- The integrated module "motor + ball screw" is designed to support higher axial loads than classical motors.
- The coupling between the motor and the ball screw is already done. As a consequence, no coupling part needs to be chosen and ordered.
- The alignment between the motor and the ball screw is already done.

A.1.3 The ball screw and the linear guide are integrated

Description

There exist devices including the ball screw and the linear guide into one linear module. For example, the THK company [21] proposes "LM guide actuators Model KR". As can be seen in Fig. A.4, these devices present:

- mounting parts for the motor
- a ball screw
- a ball train that slides in a rail
- support bearings for the ball screw

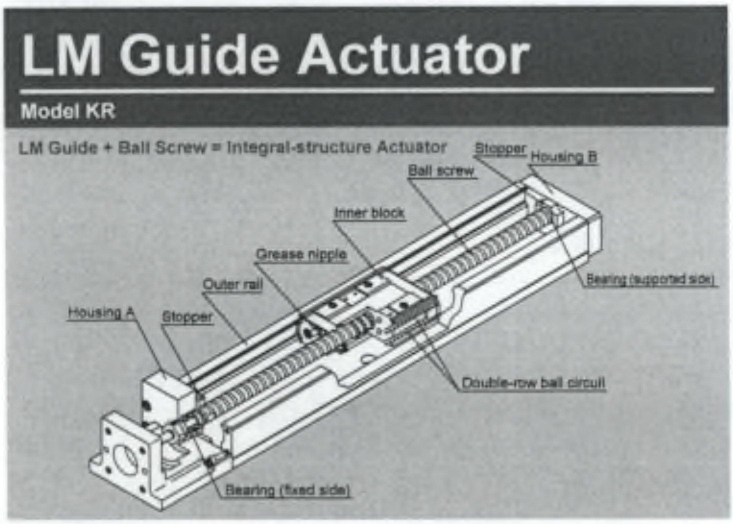

Figure A.4: "LM guide actuator Model KR" proposed by THK. Figure from [15].

Fig. A.5 presents a scheme of the implementation of the test bench based on such a linear module. As can be seen, in addition to selecting a linear module (parts no. 1, 4, 6, 7 and 8 in Fig. A.5 are integrated into the linear module), implementing this solution requires to select coupling parts (no. 3 in Fig. A.5) and a motor equipped with an encoder (no. 2 in Fig. A.5), to design and manufacture a linking part (no. 5 in Fig. A.5) for the ball train (no. 7 in Fig. A.5) and the cylinder piston (no. 9 in Fig. A.5) and to align the linear module and the cylinder piston.

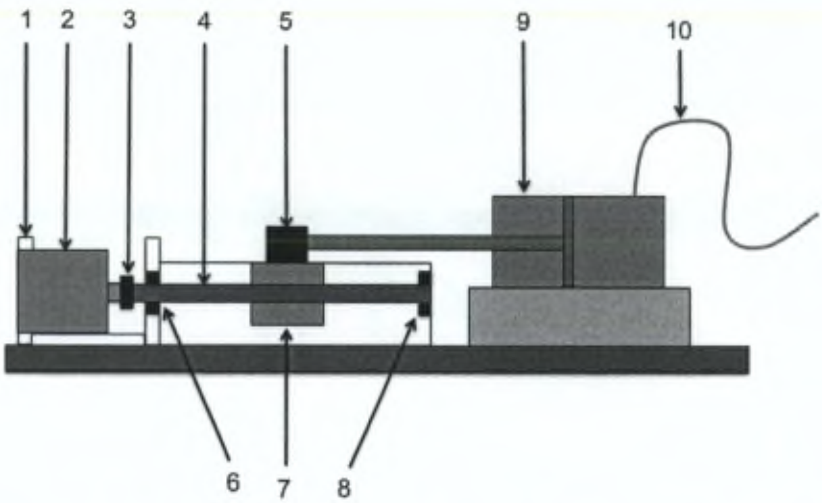

Figure A.5: Third solution to implement the syringe-pump test bench: 1) mounting parts of the motor 2) DC or stepper motor + encoder 3) coupling parts 4) ball screw 5) linking part between the ball train and the cylinder piston 6) support bearings 7) ball train 8) support bearings 9) pneumatic cylinder 10) pneumatic tubes. Parts no. 1, 4, 6, 7 and 8 are integrated into a linear module.

Discussion

With such an integrated unit, the third solution presents the following advantages in comparison with the first solution:

- The support bearings of the ball screw are already provided.
- Mounting parts are already provided for the motor.
- A linking part between the ball screw and the linear guide is no longer needed since the ball train slides in the guide.
- The alignment between the ball screw and the linear guide is already done.
- The alignment between the motor and the ball screw is easily performed since the motor only needs to be placed in the mounting parts.
- The linear module limits the risk of backlash in comparison with the first design solution.

A.1.4 Linear actuator

Description

A fourth solution consists in using a linear actuator to actuate the cylinder piston. A linear actuator can be a linear motor, such as those proposed by the LinMot company [14] (see Fig. A.6), or an integrated system "motor - screw - sliding shaft" such as those provided by the Danaher Motion company[1] [10] (see Fig. A.7).

[1] Danaher Motion describes its electric linear actuators as follows: "The design of an electric linear actuator is quite basic. An electric motor - through either a timing belt, a gear drive or via in-line direct coupling - rotates a ball screw or acme screw, which translates the torque into axial force through the extension tube" [5].

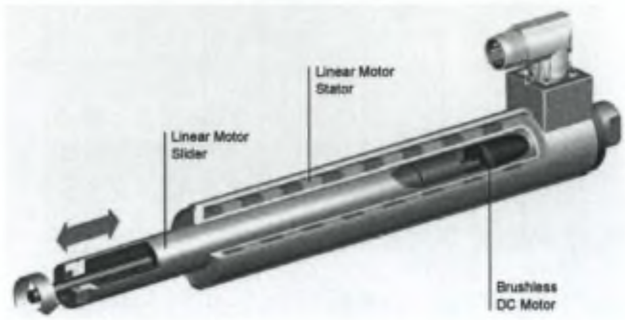

Figure A.6: Linear motor proposed by LinMot. Figure from [1].

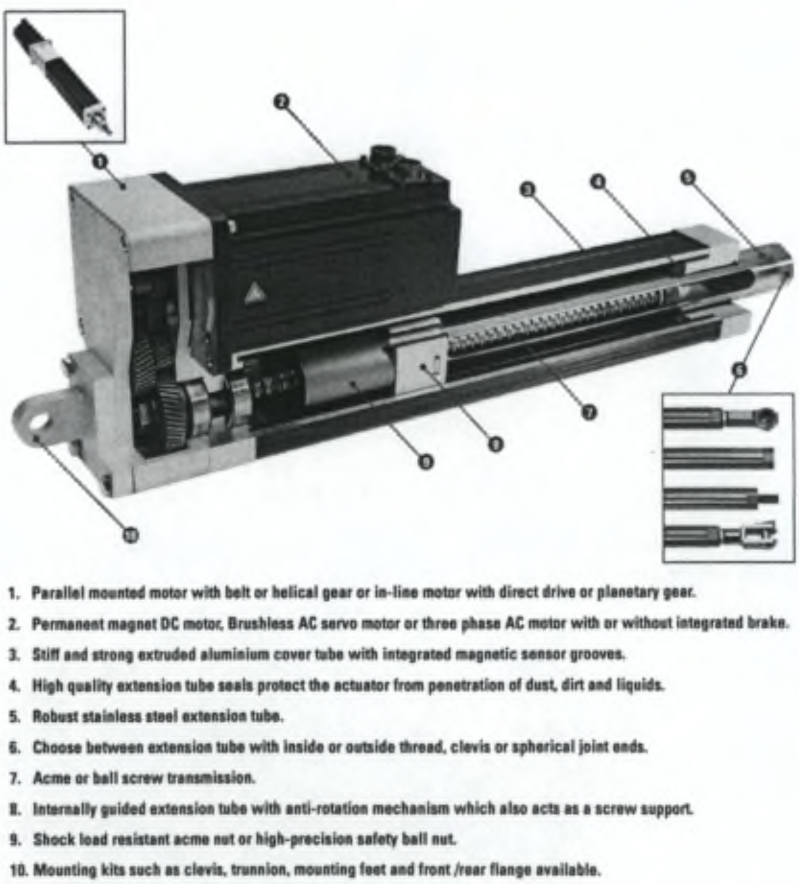

Figure A.7: "Electric linear actuator" proposed by Danaher Motion. Figure from [5].

As shown in Fig. A.8, to set up this fourth solution, the linear actuator equipped with a position sensor (no. 1 in Fig. A.8) only needs to be aligned with the cylinder piston (no. 4 in Fig. A.8) and a part (no. 3 in Fig. A.8) linking the cylinder piston and the sliding shaft of the linear actuator (no. 2 in Fig. A.8) needs to be manufactured.

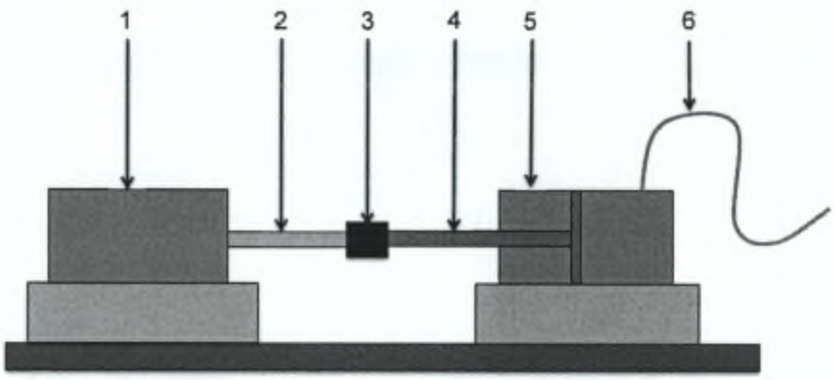

Figure A.8: Fourth solution to implement the syringe-pump test bench: 1) linear actuator + position sensor 2) sliding shaft of the linear actuator 3) part linking the shaft of the linear actuator and the piston of the pneumatic cylinder 4) piston of the pneumatic cylinder 5) pneumatic cylinder 6) pneumatic tubes

Discussion

Since they are designed to produce linear motions, linear actuators can presumably bear higher axial loads than the motors of the first and third solutions. Moreover, among the linear actuators, the linear motors have presumably a better positioning accuracy because they are composed only of a magnetic slider sliding in a stator while the other types of linear actuators are made of several parts assembled together.
Among the four considered solutions, the fourth one is the easiest to implement.

A.1.5 Conclusions

To ease the setting up of the test bench, the fourth solution has been chosen because most of its parts are already integrated. Besides, a linear motor has been preferred to another type of linear actuator in order to have a better positioning accuracy.

A.2 Linmot linear motor

A.2.1 List of all the ordered Linmot components (motor + accessories)

Technical components
AL-Profiles
Linear motors
Pneumatic units
Conveyors
Special Bearings
Axes
Machine Design

4A, Z.I. In den Allern
L-9911 TROISVIERGES

Tél.: 00352/99 89 06
Fax : 00352/26 95 73-73

profilex@pt.lu
www.profilex-systems.com

UNIVERSITE LIBRE DE BRUXELLES
Mad.De Greef
Av. F.D. Roosevelt, 50 CP 165/55
B-1050 BRUSSEL 0

OFFRE 280201
Personne de contact : Manfred Backes

Fax : +32-2-650-47-24

Date	Page	Client	N° TVA	Référence : Offre de prix actualisée
20/06/08	1 de 1	ULB1	BE0407.626.464	

Pos	N° article	Désignation	Dimens.	Unité	Quant.	Prix unit.	Rab %	Montant
		Nous vous remercions de votre demande de prix aimable et avons le plaisir de vous offrir:						
1	L0150-1943	POWER SUPPLY 72V/600W/ S01-72/600		pc	1	757,940	15,0	644,25
2	L0150-1381	SLIDER PL01-28x410/330 F.LIN.MOTOR 4		pc	1	817,500	15,0	694,88
3	L0150-1219	LINEAR MOTOR STATOR PS01-48x240-C		pc	1	637,920	15,0	542,23
4	L0150-1975	MOUNTING FLANGE PF01-48x240		pc	1	74,200	15,0	63,07
5	L0150-5051	Fan cooling for H01-37/48 & PF01-48		pc	1	28,460	15,0	24,19
6	L0150-1801	CABLE K15-W/C-04M EXTENSION/IP67-I		pc	1	165,620	15,0	140,78
7	L0150-1685	CONTROLLER B 1100 VF 48-72V/8A		pc.	1	349,730	15,0	297,27
8	L0150-3087	FIXED END WASHER SET FOR 28 MM SI		pc	1	5,280	15,0	4,49
9	L0150-3094	PLL01-28 FLOATING BEARING F.28 MM		pc	1	35,970	15,0	30,57
10	L0150-1840	MAGNET SENSOR 1µm, A/B(for 1 mm pit		m	1	394,520	15,0	335,34
11	L0150-1963	MAGNETIC STRIP MB01-1000 , 1MM PIT	0,2700	m	1	346,000	15,0	79,41
12	TRANS	PORT		pc	1	17,720		17,72
13	ASSU	ASSURANCE TRANSPORT		pc	1	10,440		10,44
		Délai : 7-10 jours						
		Payement: endans 30 jours date de facture net.						
		Validité : 60 jours						

TVA		Base	Montant
G	0 %	2.884,64	0,00

Total remise 504,08 €

Total hors TVA	2.884,64
Total TVA	0,00
TOTAL EUR	2.884,64

[illegible]

Signature client, date et cachet
Handtekening klant, datum en stempel
Kundenunterschrift, Datum und Stempel

Figure A.9: Order of the linear motor and its accessories

A.2.2 The S and SS strokes of the Linmot motors

The Linmot linear motors are characterized by two kinds of strokes (see Fig. A.10):

- a maximum stroke S: it is the maximum displacement that the slider can reach.
- a shortened stroke SS: it is the part of the stroke S on which the motor can develop its maximum peak force.

The evolution of the peak force along the stroke has a trapezoidal shape and the centre of the stroke range is called the "zero position (ZP)". The available peak force is thus dependent on the slider position but it is also dependent on the maximum current from the servo controller.

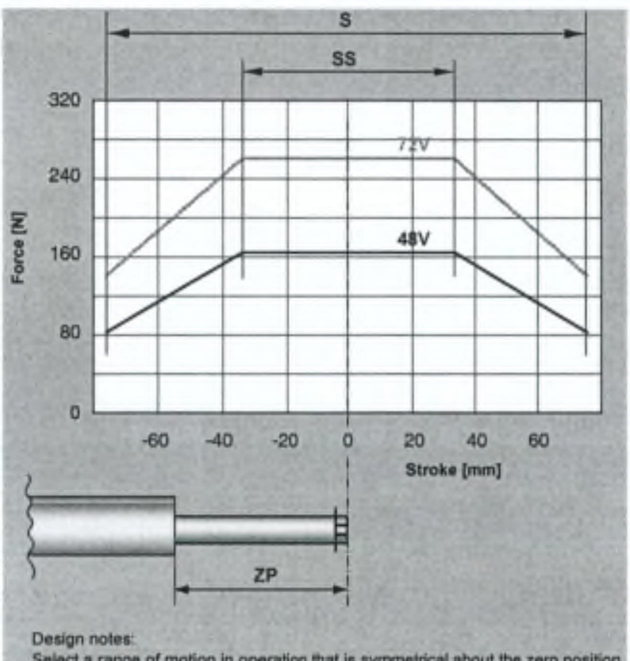

Figure A.10: Linmot linear motors: description of the maximum stroke S, of the shortened stroke SS and of the zero position ZP. The evolution of the peak force along the stroke has a trapezoidal shape. Both curves correspond to different servo controllers. Figure from [1].

A.2.3 Characteristics of the Linmot motor chosen for the test bench

The characteristics of the chosen Linmot motor are presented in Fig. A.11.

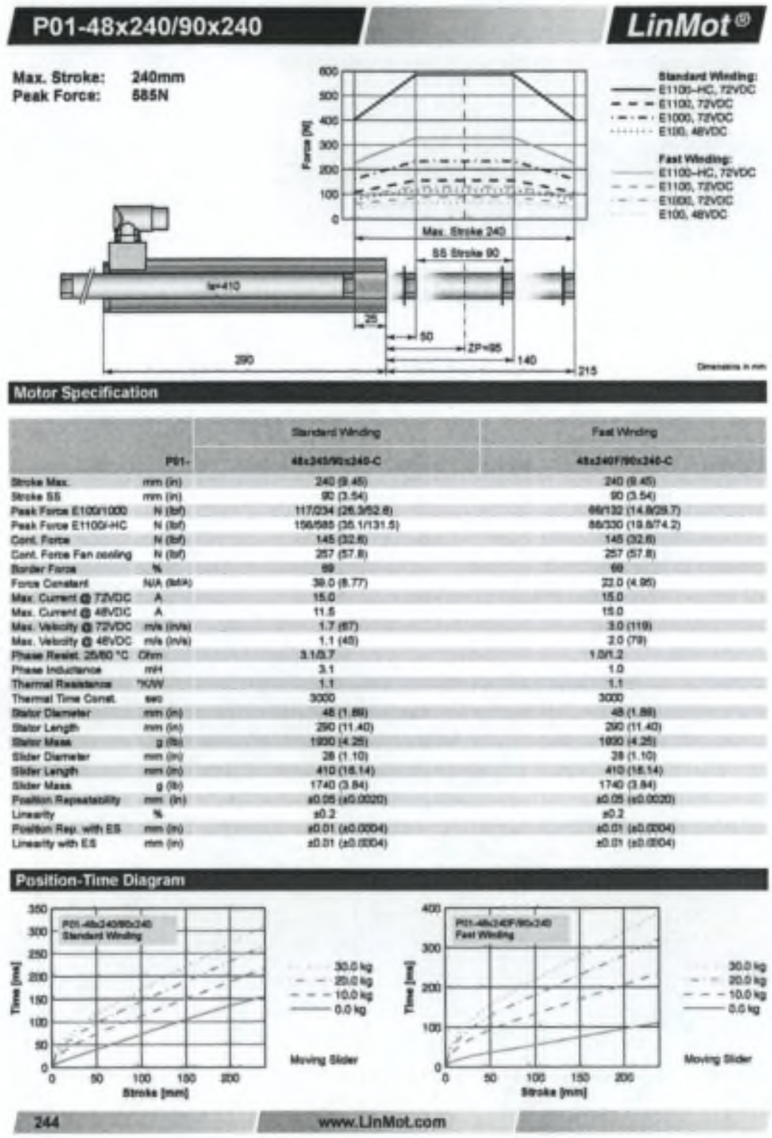

		Standard Winding	Fast Winding
	P01-	48x240/90x240-C	48x240F/90x240-C
Stroke Max.	mm (in)	240 (9.45)	240 (9.45)
Stroke SS	mm (in)	90 (3.54)	90 (3.54)
Peak Force E100/1000	N (lbf)	117/234 (26.3/52.6)	66/132 (14.8/29.7)
Peak Force E1100/-HC	N (lbf)	156/585 (35.1/131.5)	88/330 (19.8/74.2)
Cont. Force	N (lbf)	145 (32.6)	145 (32.6)
Cont. Force Fan cooling	N (lbf)	257 (57.8)	257 (57.8)
Border Force	%	69	69
Force Constant	N/A (lbf/A)	39.0 (8.77)	22.0 (4.95)
Max. Current @ 72VDC	A	15.0	15.0
Max. Current @ 48VDC	A	11.5	15.0
Max. Velocity @ 72VDC	m/s (in/s)	1.7 (67)	3.0 (119)
Max. Velocity @ 48VDC	m/s (in/s)	1.1 (45)	2.0 (79)
Phase Resist. 25/80 °C	Ohm	3.1/3.7	1.0/1.2
Phase Inductance	mH	3.1	1.0
Thermal Resistance	°K/W	1.1	1.1
Thermal Time Const.	sec	3000	3000
Stator Diameter	mm (in)	48 (1.89)	48 (1.89)
Stator Length	mm (in)	290 (11.40)	290 (11.40)
Stator Mass	g (lb)	1930 (4.25)	1930 (4.25)
Slider Diameter	mm (in)	28 (1.10)	28 (1.10)
Slider Length	mm (in)	410 (16.14)	410 (16.14)
Slider Mass	g (lb)	1740 (3.84)	1740 (3.84)
Position Repeatability	mm (in)	±0.05 (±0.0020)	±0.05 (±0.0020)
Linearity	%	±0.2	±0.2
Position Rep. with ES	mm (in)	±0.01 (±0.0004)	±0.01 (±0.0004)
Linearity with ES	mm (in)	±0.01 (±0.0004)	±0.01 (±0.0004)

Figure A.11: Characteristics of the PO1-48X240/90X240 Linmot linear motor. Figure from [1].

The motor is installed in a flange (see Fig. A.12) and is cooled by a fan (see Fig. A.13).

Figure A.12: Linear motor equipped with a flange (black part). Figure from [1].

Optional Fan for PF01-48

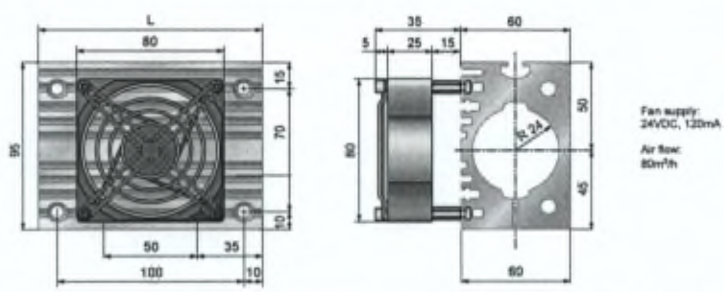

Item	Description	Part Number
HV01-37/48	Fan kit for H01-48, B01-48 and PF01-48	0150-5051

Figure A.13: Fan of the Linmot linear motor. Figure from [1].

Besides, it is equipped with an external position sensor (see Fig. A.14 and A.15).

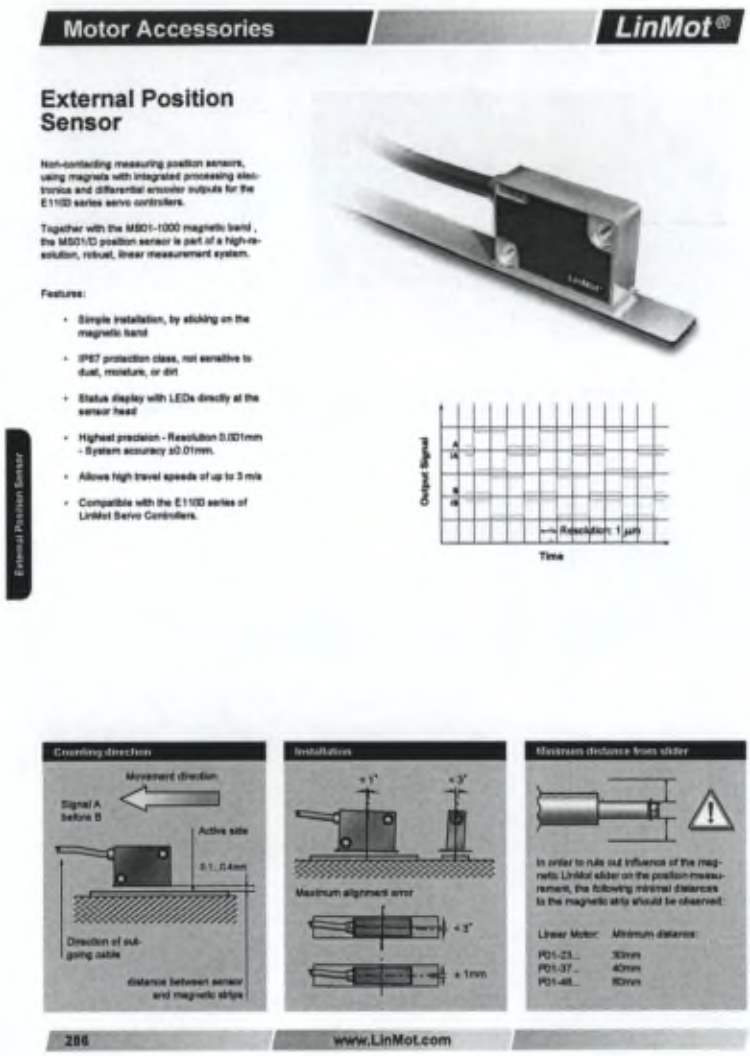

Figure A.14: External position sensor and magnetic strip. Figure from [1].

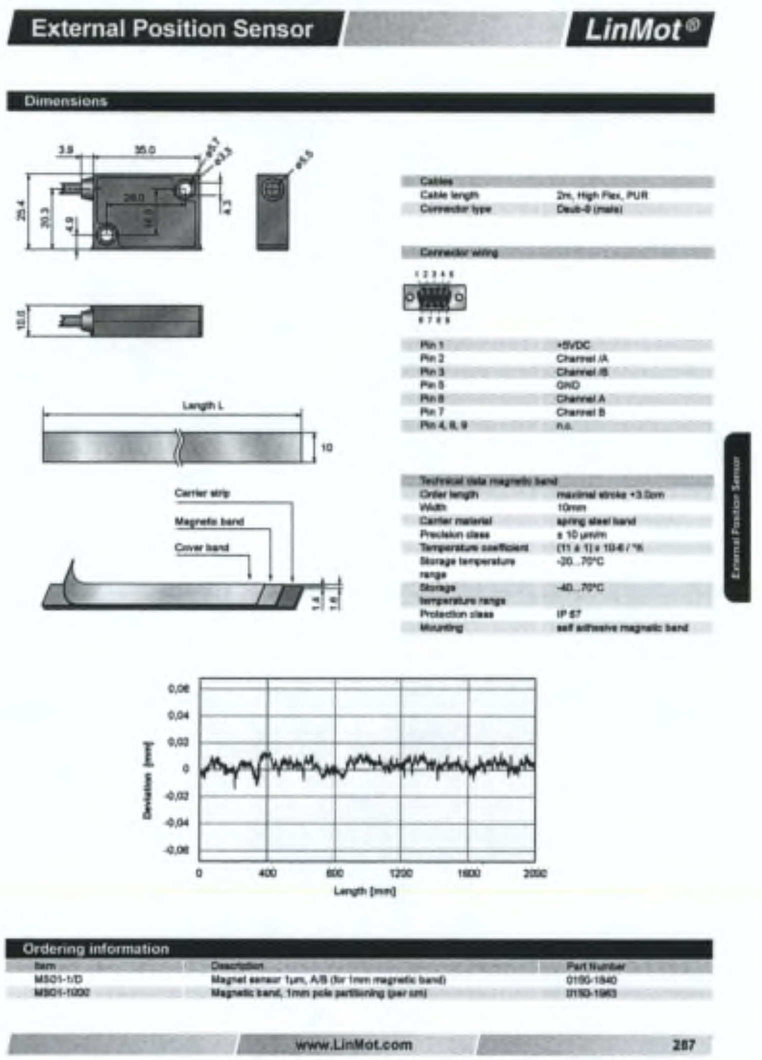

External Position Sensor — LinMot®

Dimensions

Cables	
Cable length	2m, High Flex, PUR
Connector type	Dsub-9 (male)

Connector wiring	
Pin 1	+5VDC
Pin 2	Channel /A
Pin 3	Channel /B
Pin 5	GND
Pin 6	Channel A
Pin 7	Channel B
Pin 4, 8, 9	n.c.

Technical data magnetic band	
Order length	maximal stroke +3.0cm
Width	10mm
Carrier material	spring steel band
Precision class	± 10 µm/m
Temperature coefficient	(11 ± 1) x 10-6 / °K
Storage temperature range	-20...70°C
Storage temperature range	-40...70°C
Protection class	IP 67
Mounting	self adhesive magnetic band

Ordering information

Item	Description	Part Number
MS01-1/D	Magnet sensor 1µm, A/B (for 1mm magnetic band)	0150-1840
MS01-1000	Magnetic band, 1mm pole partitioning (per cm)	0150-1963

www.LinMot.com 287

Figure A.15: External position sensor and magnetic strip. Figure from [1].

A B1100-VF controller (see Fig. A.16, A.17 and A.18) has been chosen for the motor.

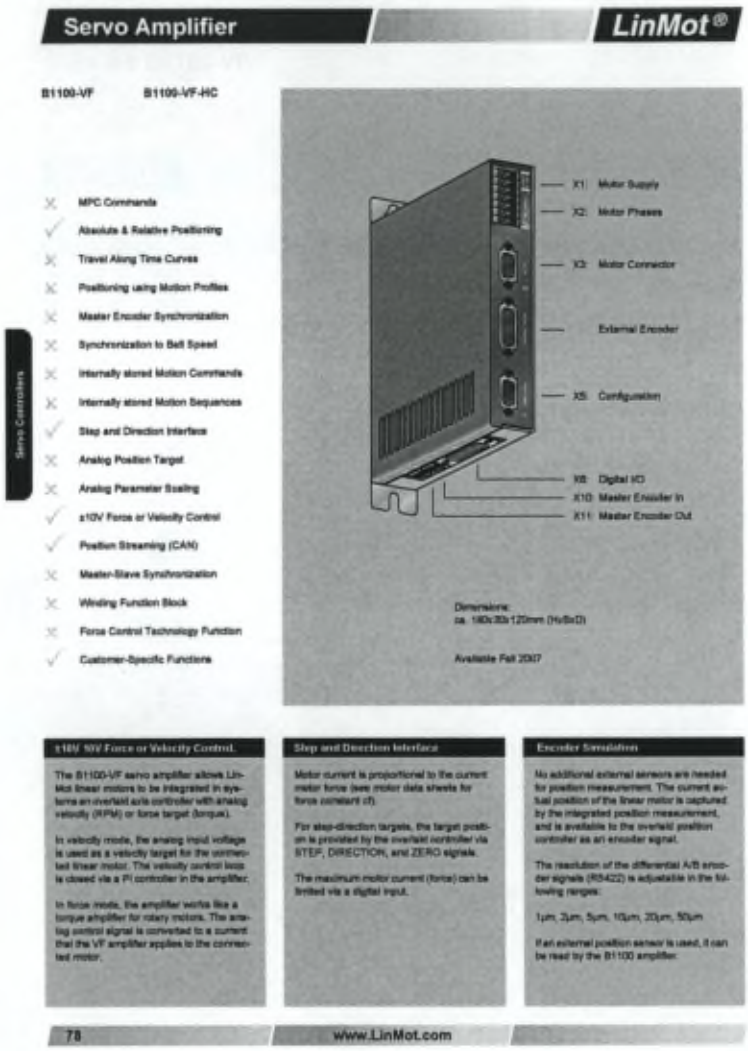

Servo Amplifier

LinMot®

B1100-VF B1100-VF-HC

Servo Controllers

- ✗ MPC Commands
- ✓ Absolute & Relative Positioning
- ✗ Travel Along Time Curves
- ✗ Positioning using Motion Profiles
- ✗ Master Encoder Synchronization
- ✗ Synchronization to Belt Speed
- ✗ Internally stored Motion Commands
- ✗ Internally stored Motion Sequences
- ✓ Step and Direction Interface
- ✗ Analog Position Target
- ✗ Analog Parameter Scaling
- ✓ ±10V Force or Velocity Control
- ✓ Position Streaming (CAN)
- ✗ Master-Slave Synchronization
- ✗ Winding Function Block
- ✗ Force Control Technology Function
- ✓ Customer-Specific Functions

X1: Motor Supply
X2: Motor Phases
X3: Motor Connector
External Encoder
X5: Configuration
X8: Digital I/O
X10: Master Encoder In
X11: Master Encoder Out

Dimensions:
ca. 180x30x120mm (HxBxD)

Available Fall 2007

±10V 10V Force or Velocity Control.

The B1100-VF servo amplifier allows LinMot linear motors to be integrated in systems an overlaid axis controller with analog velocity (RPM) or force target (torque).

In velocity mode, the analog input voltage is used as a velocity target for the connected linear motor. The velocity control loop is closed via a PI controller in the amplifier.

In force mode, the amplifier works like a torque amplifier for rotary motors. The analog control signal is converted to a current that the VF amplifier applies to the connected motor.

Step and Direction Interface

Motor current is proportional to the current motor force (see motor data sheets for force constant cf).

For step-direction targets, the target position is provided by the overlaid controller via STEP, DIRECTION, and ZERO signals.

The maximum motor current (force) can be limited via a digital input.

Encoder Simulation

No additional external sensors are needed for position measurement. The current actual position of the linear motor is captured by the integrated position measurement, and is available to the overlaid position controller as an encoder signal.

The resolution of the differential A/B encoder signals (RS422) is adjustable in the following ranges:

1µm, 2µm, 5µm, 10µm, 20µm, 50µm

If an external position sensor is used, it can be read by the B1100 amplifier.

78 www.LinMot.com

Figure A.16: Datasheet of the B1100-VF controller. Figure from [1].

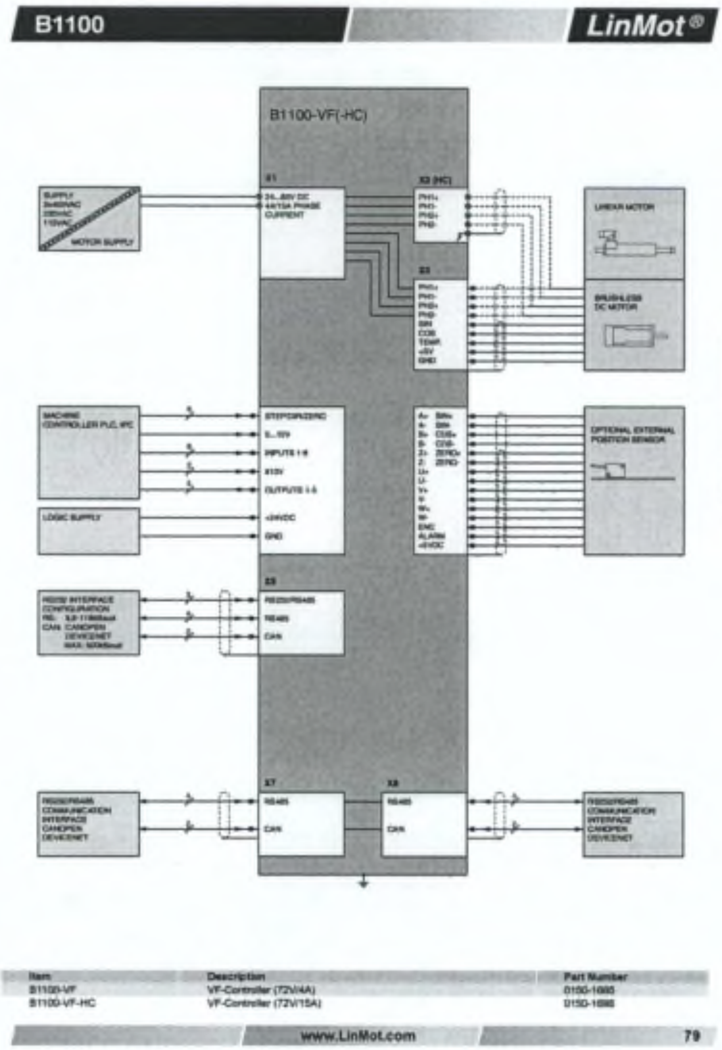

Figure A.17: Datasheet of the B1100-VF controller. Figure from [1].

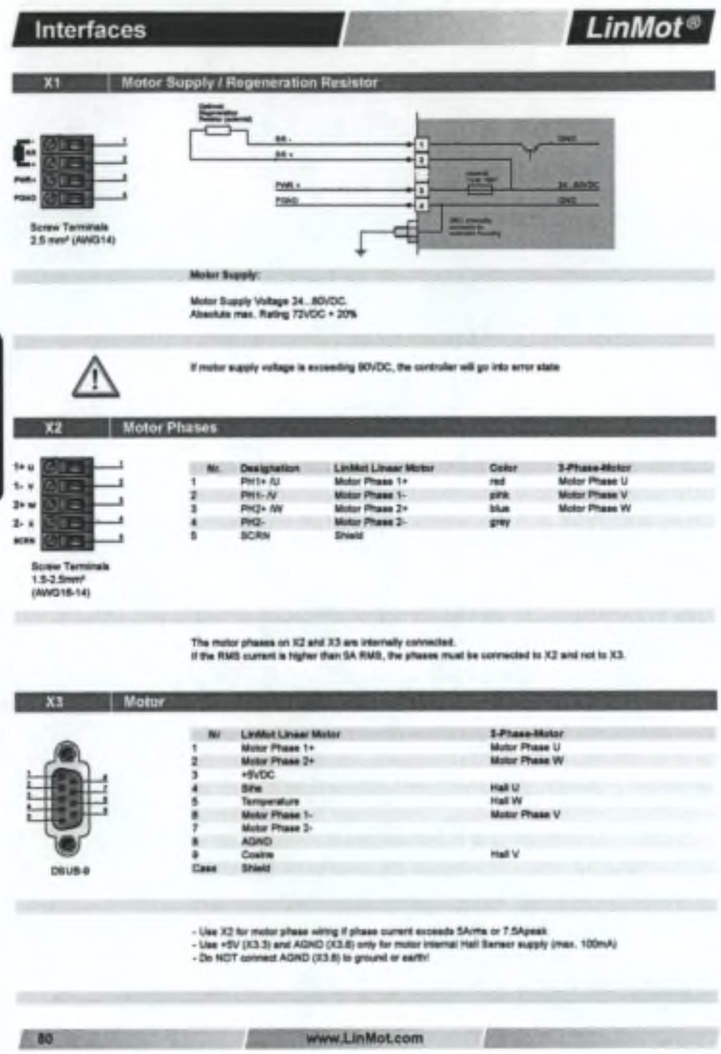

Figure A.18: Datasheet of the B1100-VF controller. Figure from [1].

Fig. A.19 and A.20 present the datasheets of the 72 V/600 W power supply of the linear motor.

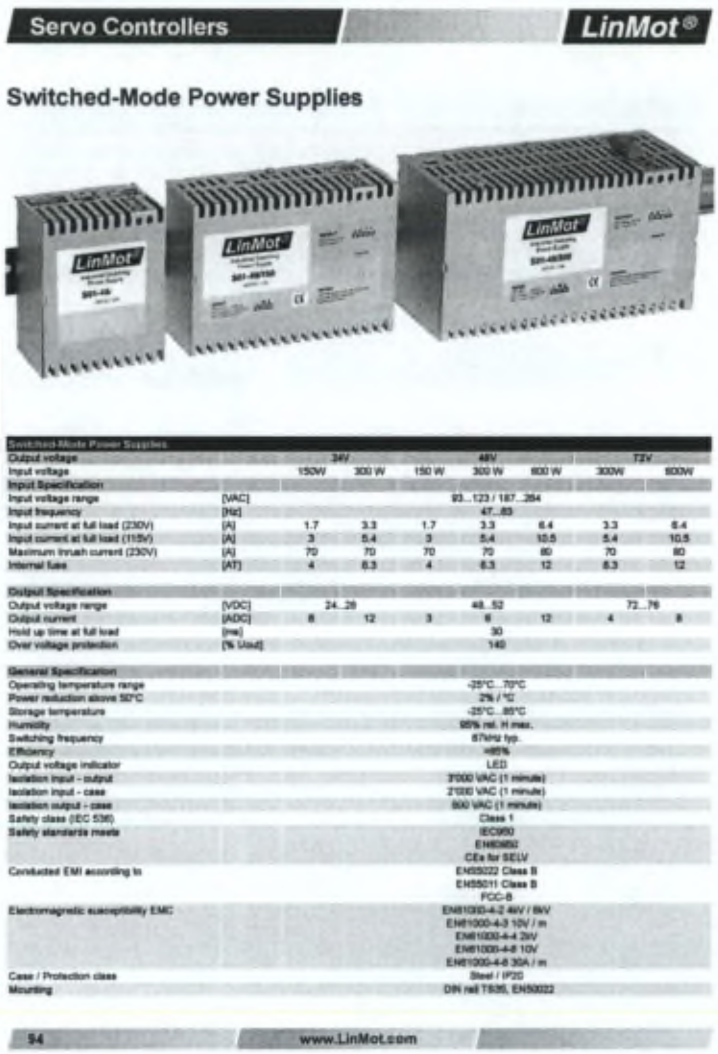

Servo Controllers LinMot®

Switched-Mode Power Supplies

Servo Controller Accessories

Switched-Mode Power Supplies								
Output voltage		24V		48V			72V	
Input voltage		150W	300 W	150 W	300 W	600 W	300W	600W
Input Specification								
Input voltage range	[VAC]	93...123 / 187...264						
Input frequency	[Hz]	47...63						
Input current at full load (230V)	[A]	1.7	3.3	1.7	3.3	6.4	3.3	6.4
Input current at full load (115V)	[A]	3	5.4	3	5.4	10.5	5.4	10.5
Maximum inrush current (230V)	[A]	70	70	70	70	80	70	80
Internal fuse	[AT]	4	6.3	4	6.3	12	6.3	12
Output Specification								
Output voltage range	[VDC]	24...28		48...52			72...76	
Output current	[ADC]	6	12	3	6	12	4	8
Hold up time at full load	[ms]	30						
Over voltage protection	[% Uout]	140						
General Specification								
Operating temperature range		-25°C...70°C						
Power reduction above 50°C		2% / °C						
Storage temperature		-25°C...85°C						
Humidity		95% rel. H max.						
Switching frequency		67kHz typ.						
Efficiency		>85%						
Output voltage indicator		LED						
Isolation input - output		3'000 VAC (1 minute)						
Isolation input - case		2'000 VAC (1 minute)						
Isolation output - case		500 VAC (1 minute)						
Safety class (IEC 536)		Class 1						
Safety standards meets		IEC950 EN60950 CEs for SELV						
Conducted EMI according to		EN55022 Class B EN55011 Class B FCC-B						
Electromagnetic susceptibility EMC		EN61000-4-2 4kV / 8kV EN61000-4-3 10V / m EN61000-4-4 2kV EN61000-4-6 10V EN61000-4-8 30A / m						
Case / Protection class		Steel / IP20						
Mounting		DIN rail TS35, EN50022						

94 www.LinMot.com

Figure A.19: Datasheet of the 72 V/600 W power supply of the linear motor. Figure from [1].

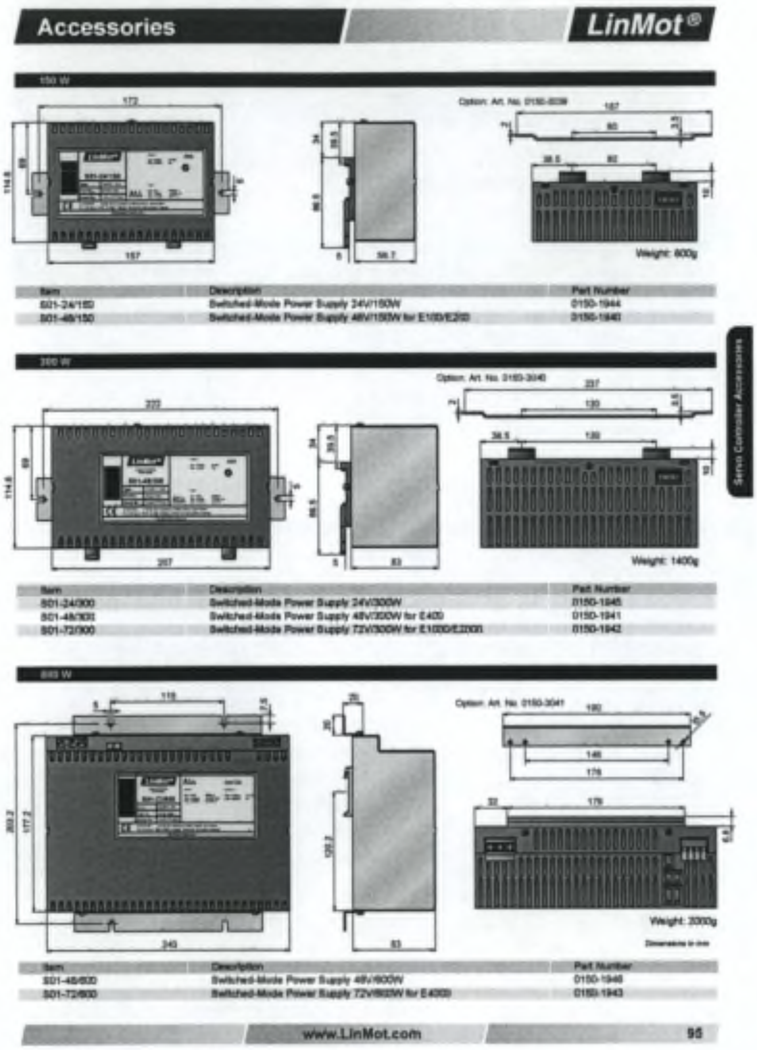

Accessories

LinMot®

150 W

Option: Art. No. 0150-3039

Weight: 600g

Item	Description	Part Number
S01-24/150	Switched-Mode Power Supply 24V/150W	0150-1944
S01-48/150	Switched-Mode Power Supply 48V/150W for E100/E200	0150-1940

300 W

Option: Art. No. 0150-3040

Weight: 1400g

Item	Description	Part Number
S01-24/300	Switched-Mode Power Supply 24V/300W	0150-1945
S01-48/300	Switched-Mode Power Supply 48V/300W for E400	0150-1941
S01-72/300	Switched-Mode Power Supply 72V/300W for E1000/E2000	0150-1942

600 W

Option: Art. No. 0150-3041

Weight: 3000g

Dimensions in mm

Item	Description	Part Number
S01-48/600	Switched-Mode Power Supply 48V/600W	0150-1946
S01-72/600	Switched-Mode Power Supply 72V/600W for E4000	0150-1943

www.LinMot.com 95

Figure A.20: Datasheet of the 72 V/600 W power supply of the linear motor. Figure from [1].

Fig. A.21 presents the linear guides available in the Linmot catalog [1]. Such guides should be used if the slider is subjected to radial loads, if the rotation of the slider or the 0.5 mm gap between the slider and the stator causes inconvenience.

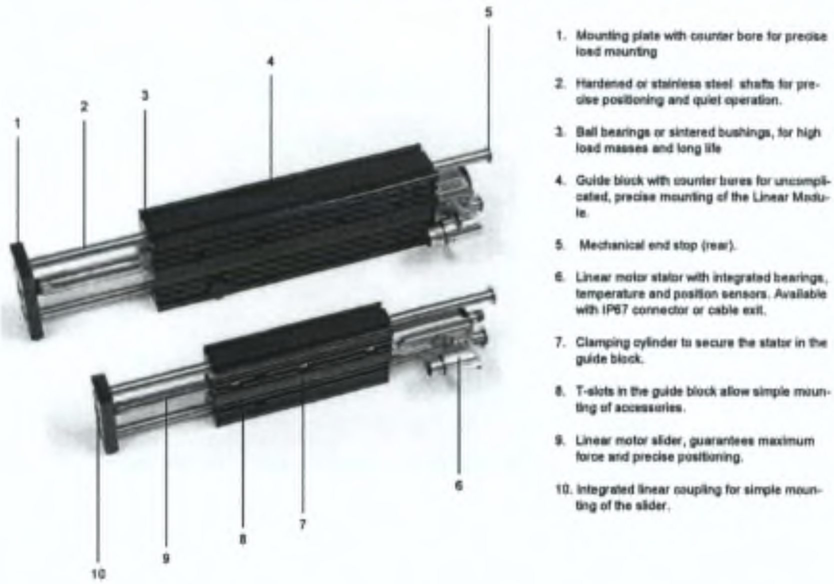

Figure A.21: Linear guides proposed in the Linmot catalog. Figure from [1].

A.2.4 Linmot Designer software: list of the parameters encoded to perform the dynamic study of the "cylinder - linear motor" combination

To perform the dynamic study of the "cylinder - linear motor" combination, a motor sizing software called "Linmot Designer" has been used (this software is available for download on the LinMot website [14]).
To study an application case with this design program, the following data must be provided:

- the global motor settings
  - the motor type and the number of motors: this specifies the short stroke SS, the maximum stroke S, the maximum peak force, the slider mass, the stator mass, etc.
    For our study, the motor type is: PO1-48X240/90X240 and there is one motor.
  - the slider mounting: regular or reversed (see Fig A.22 and A.23)
    For our study, the slider mounting is regular.
  - the cooling method: flange only or flange+fan
    For our study, a fan is used in addition to a flange.
  - the servo controller type: this automatically specifies the maximum current available for the linear motor.
    For our study, a B1100VF controller is chosen since two types of commands can be given to it. Indeed it is possible to give a current command or a slider position command.

Figure A.22: "Regular" slider mounting. Figure from [1].

Figure A.23: "Reversed" slider mounting. Figure from [1].

- the power supply voltage.
  For our study, a 72 V*DC power supply is chosen.*
- the type and length of the cable linking the motor and the controller: indeed, the resistance of the cable can reduce the force limit.
  For our study, the cable type is K15 and the cable length is 4 m.

• the global load settings

- the start position of the motor: it can be set automatically by an auto centering function so that the motion will be symmetrical relative to the centre of the stroke range, i.e. to the Zero Position (ZP, see Fig. A.10). Indeed, according to the Linmot Designer Tutorial [3], such a motion will give the best performance.
- the mass the linear motor has to displace anytime it is actuated. Concerning the mass of the moving part of the motor, it is automatically added by the program (it is just necessary to specify whether it is the slider or the stator mass that needs to be added).
  For our study, the mass of the slider of the linear motor is automatically added by the program while the mass of the cylinder piston needs to be specified. This mass has been computed thanks to the data found in the Festo catalog and equals 243 g.
- the constant external force applied to the linear motor
  For our study, no constant external force is applied.
- the dry and viscous frictions applied to the slider
  For our study, dry friction exists in the pneumatic cylinder and it equals 10 kPa *applied to the section of the piston. Since the diameter of the piston is* 32 mm, *the friction equals* 8 N.
- the angle the linear motor presents relative to the horizontal
  For our study, this angle equals 0°.
- the spring zero position and spring constant: these parameters have to be specified if a mechanical spring is used.
  For our study, no mechanical spring is used.

• the motor layout: "moving slider" (the slider moves while the stator is fixed, see Fig. A.24) or "moving stator" (the stator moves while the slider is fixed, see Fig. A.25).
For our study, a moving slider layout is chosen.

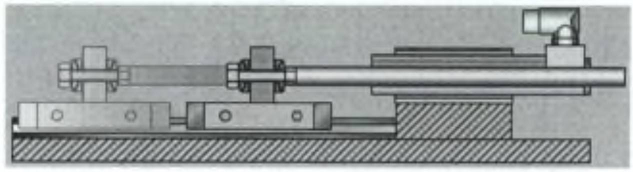

Figure A.24: "Moving slider" layout: the slider moves while the stator is fixed. Figure from [1].

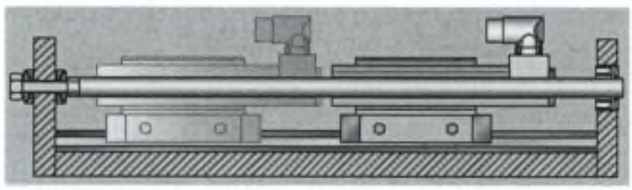

Figure A.25: "Moving stator" layout: the stator moves while the slider is fixed. Figure from [1].

Once all these data are provided to the program, the motion of the linear motor can be specified. To do so, it is segmented, i.e. it is divided into movement sections called "segments" (e.g. forward movement, backward movement, standstill). For each segment, the curve settings and the local load settings are specified:

- the curve settings
  - the curve type for the displacement, the velocity and the acceleration: sine, standstill, point to point, limited jerk or minimal jerk. According to the selected curve type, only a few of the following parameters need to be specified. Besides, it is also possible to import custom curves.
  - the segment duration
  - the covered stroke
  - the maximum velocity
  - the acceleration and deceleration
  - the maximum acceleration and maximum deceleration
  - the jerk
- the local load settings: while the global load settings are valid for any motion of the motor, the local load settings are only valid for the considered motion segment and come in addition to the global load settings.
  - the mass
    For our study, no extra mass is displaced by the motor during the considered motion segment.
  - the external force (for a regular mounting, the sign convention for the force is given in Fig. A.26)
    For our study, an external force F_{ext} is applied during the considered motion segment. It is the force applied by the pressurized gas to the cylinder piston.

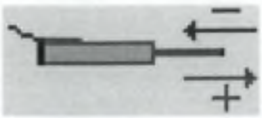

Figure A.26: Sign convention for the external force: a negative (positive) force tends to push (pull) the slider inside (out of) the stator. Figure from [3].

- the dry and viscous frictions
  For our study, no extra dry or viscous friction is applied to the slider during the considered motion segment.
- the spring start position and spring constant
  For our study, no spring is used during the considered motion segment.

If the linear motor combined with the controller and the cylinder, is not able to perform the proposed motion cycle, warnings are indicated by the Linmot Designer software. These warnings notify, for example, that the dynamic force the motor has to produce exceeds the peak force limits of the "motor - servo controller" combination.

For each application case of Table 3.2,

- a start position is specified for the motor. In practice, the slider and the cylinder piston will be connected so that only the 90 mm SS stroke of the linear motor will be used (see Section A.2.2 for a definition of the SS stroke).
  The start position is defined relatively to ZP and is thus computed as follows:

$$start\_position = 45 \text{ mm} - L, \tag{A.1}$$

  so that after a displacement of L, the slider is located at the right limit of the SS stroke (see Fig. A.10).

- the following motion cycle is studied:
  1. a forward motion of stroke L with an external force $F_{ext} = -F_{max\_statics}$ and a maximum velocity $v_{max} = 0.9$ m/s
  2. a backward motion of stroke L with an external force $F_{ext} = -F_{max\_statics}$ and a maximum velocity $v_{max} = 0.9$ m/s

The constraint on the velocity is due to the pneumatic cylinder. Indeed, according to the Festo support, a velocity larger than 0.9 m/s could damage the flexible cushioning rings/pads placed at both ends of the chosen cylinder.
The goal of the dynamic study is to approach a duration time of 0.05 s for the forward motion and the backward motion, respectively. With this target in mind, a search is done for each application case in order to find a curve type and the values of the corresponding parameters so that the motor, combined with the controller and the cylinder, would be able to perform the motion cycle.

Remark: In the software, the external force $F_{ext} = -F_{max\_statics}$ is applied continuously to the cylinder piston during the motion. However, in practice, when the cylinder piston is displaced and the actuator is pressurized (depressurized), the external force increases (decreases) and its intensity finally becomes equal to $F_{max\_statics}$ (0 N), at the end of the displacement. Hence, considering that $F_{ext} = -F_{max\_statics}$ during all the motion overestimates the real external force.

A.3 MiniTec profiles

The MiniTec company [17] proposes different types of profiles and fastening elements that can be combined to easily build structures. The MiniTec components used for the test bench are:

- 45X45 F profiles of different lengths (see Fig. A.27)
- 45 GD-Z angles (see Fig. A.28)
- Power-Lock fasteners (see Fig. A.29)
- screws, square nuts and square nuts with spring metal (see Fig. A.30)
- a thread former M8: it is used to form threads in the profile holes, in order to use Power-Lock fasteners as in the last configuration shown in Fig. A.29.

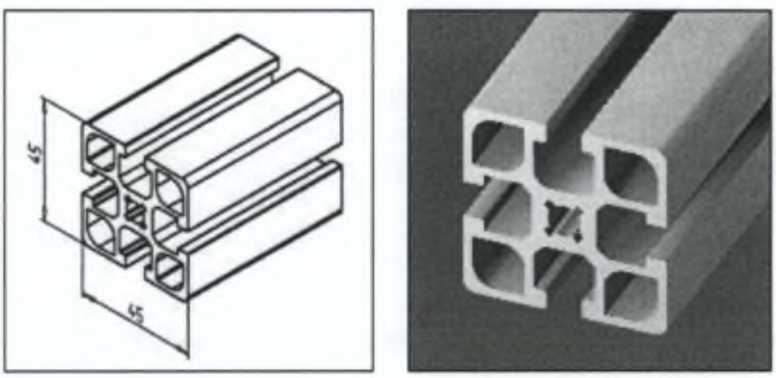

Figure A.27: 45X45 F MiniTec profiles. Figure from [2].

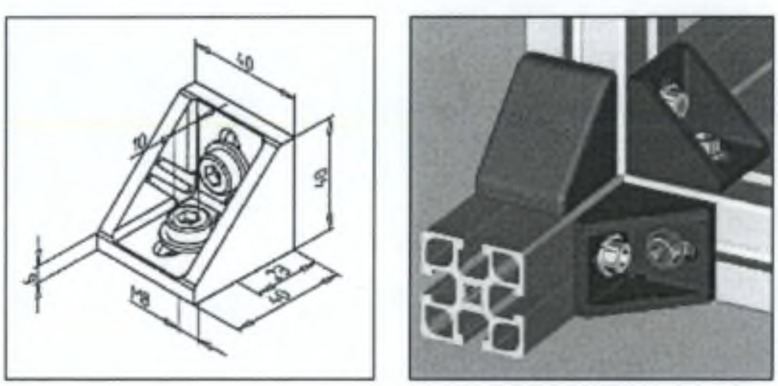

Figure A.28: 45 GD-Z MiniTec angles. Figure from [2].

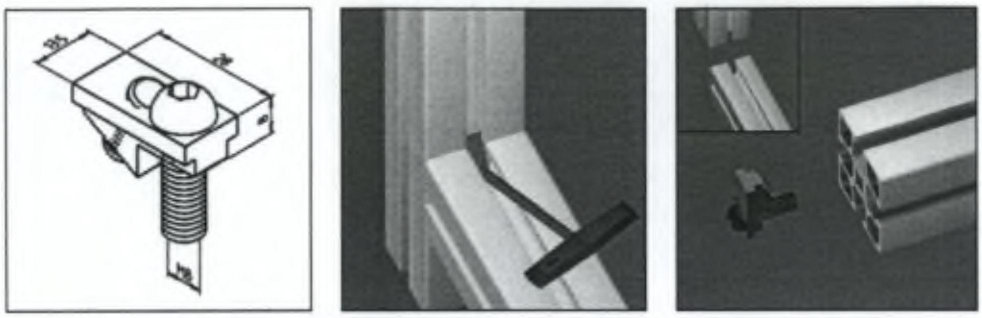

Figure A.29: MiniTec Power-Lock fasteners and different ways to use them to fasten MiniTec profiles to each other. Figure from [2].

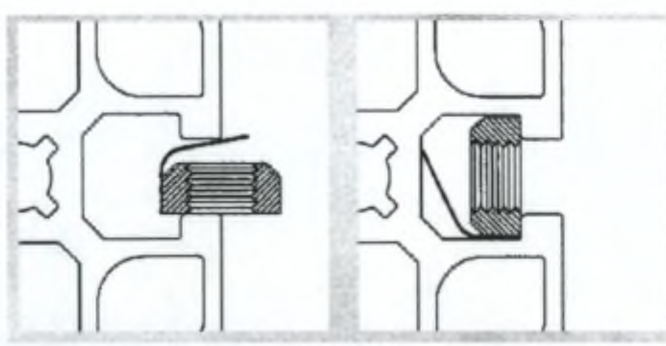

Figure A.30: View of the cross-section of a MiniTec profile in which a square nut with spring metal is inserted. Figure from [2].

A.4 National Instruments platform for measurement and control: detailed list of the components of the platform

NATIONAL INSTRUMENTS

National Instruments Belgium SA
Ikaroslaan 13 B-1930 Zaventem
Tel : 02/757.00.20 Fax : 02/757.03.11
BTW BE 445.807.706 HRB 582.093
KB 436-6252841-86

ULB
Mme Aline De Greef
Fac. Sciences Appliquées
Av. F.D. Roosevelt 50 CP165/14
1050 Bruxelles

Date 26-08-2008

Offre de prix N° 933400 - 1

Pour consulter la ou les configurations proposées, rendez-vous sur http://ni.com/advisors/retrieve.
ID de configuration : PX676261

Poste	Qté	Article	Description	Prix p/u	Remise	Prix Net
1	2	186381-02	SH68-C68-S 68-Pin VHDCI to 68-Pin, D-Type, 2m Pays d'origine : Mexico	89,00	10.00%	160,20 Eur
2	2	192061-02	SHC68-68-EPM Shielded Cable, 68-D-Type to 68 VHDCI Offset, 2 m Pays d'origine : China	109,00	10.00%	196,20 Eur
3	1	763067-01	Power Cord, 240V, 10A, Euro, Right Angle Pays d'origine : China	9,00	10.00%	8,10 Eur
4	1	776844-01	SCB-68 Noise Rejecting, Shielded I/O Connector Block Pays d'origine : Hungary	269,00	10.00%	242,10 Eur
5	1	778636-01	NI PXI-1042 8-Slot 3U Chassis with Universal AC Power Supply Pays d'origine : China	1.799,00	10.00%	1.619,10 Eur
6	1	778998-01	NI PXI-6723 32-Channel Analog Output Board Pays d'origine : Hungary	1.149,00	10.00%	1.034,10 Eur
7	1	779114-01	NI PXI-6224, M Series DAQ (32 Analog Inputs, 48 Digital I/O) with NI-DAQmx driver software. Pays d'origine : Hungary	679,00	10.00%	611,10 Eur
8	2	779475-01	SCC-68 I/O Connector with 4 SCC Module Slots Pays d'origine : Hungary	269,00	10.00%	484,20 Eur
9	1	779888-02	NI PXI-8106 Core 2 Duo 2.16 GHz Controller with Windows Vista Pays d'origine : Hungary	3.549,00	10.00%	3.194,10 Eur
10	1	960597-08	PXI 8-Slot Factory Installation Service and Extended Warranty Pays d'origine : Hungary	729,00		729,00 Eur
11	2	779302-1024	1 GB DDR2 RAM for NI 8106, NI 8105 and NI 8104 Controllers Pays d'origine : USA	219,00	10.00%	394,20 Eur
			Sous-Total			8.672,40 Eur
			Transport			100,19 Eur
			Total			8.772,59 Eur

Figure A.31: Order of the National Instruments platform for measurement and control

A.5 Detailed description of the connections between the motor controller, the motor fan and the different power supplies

Fig. A.32 explains how the controller of the linear motor has to be connected. As can be seen, the controller is connected to two power supplies: the linear motor supply (72 VDC) and the logic supply (24 VDC).

Power Supply and Grounding

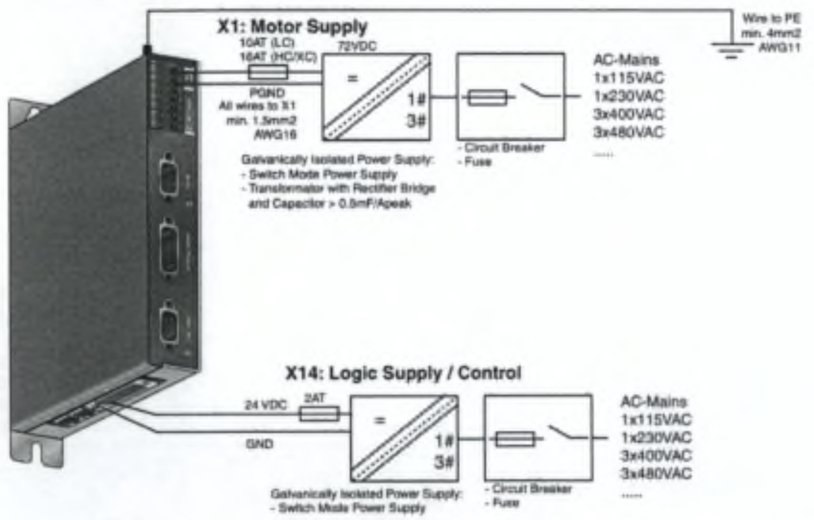

*Inside of the B1100 controller the *PWR motor GND* and *PWR signal GND* is connected together and to the GND of the controller housing. It is recommended that the *PWR motor GND* is NOT grounded at another place than inside of the controller to avoid circular currents.

In order to assure a safe and error free operation, and to avoid severe damage to system components, **all system components* must be well grounded to either a single earth or utility ground**. This includes both LinMot and all other control system components to the same ground bus.

Each system component* should be tied directly to the ground bus **(star pattern)**, rather than daisy chaining from component to component. (LinMot motors are properly grounded through their power cables when connected to LinMot controllers.)

Power supply connectors must not be connected or disconnected while DC voltage is present. Do not disconnect system components until all LinMot controllers LEDs have turned off. (Capacitors in the power supply may not fully discharge for several minutes after input voltage has been disconnected). Failure to observe these precautions may result in severe damage to electronic components in LinMot motors and/or controllers.

Do not switch Power Supply DC Voltage. All power supply switching and E-Stop breaks should be done to the AC supply voltage of the power supply. Failure to observe these precautions may result in severe damage to controller.

Figure A.32: Explanations about how to connect the motor controller to the 72 VDC motor supply and the 24 VDC logic supply. Figure from [8].

The 24 VDC logic supply was not provided with the linear motor. Hence, a 24 VDC power supply has been bought and its main characteristics are summarized in Table A.1.

24 VDC logic supply of the linear motor controller	
brand	SIEMENS
type	SITOP modular 5A 1/2phasig 6EP1 333-3BA00
output DC voltage	$24VDC \pm 1\%$
direct output current	$0-5$ A
power consumption (active power)	140 W
rated input voltage	$120VAC$ / $230VAC-500VAC$, 50/60 Hz
input current at 230 V	1.2 A_{rms}
can be installed on DIN rail	yes

Table A.1: Main properties of the 24 VDC logic supply of the linear motor controller

Following the explanations of Fig. A.32, the connections between the controller, the 72 VDC motor supply, the 24 VDC logic supply, the fan and its supply have been made as shown in Fig. A.33.

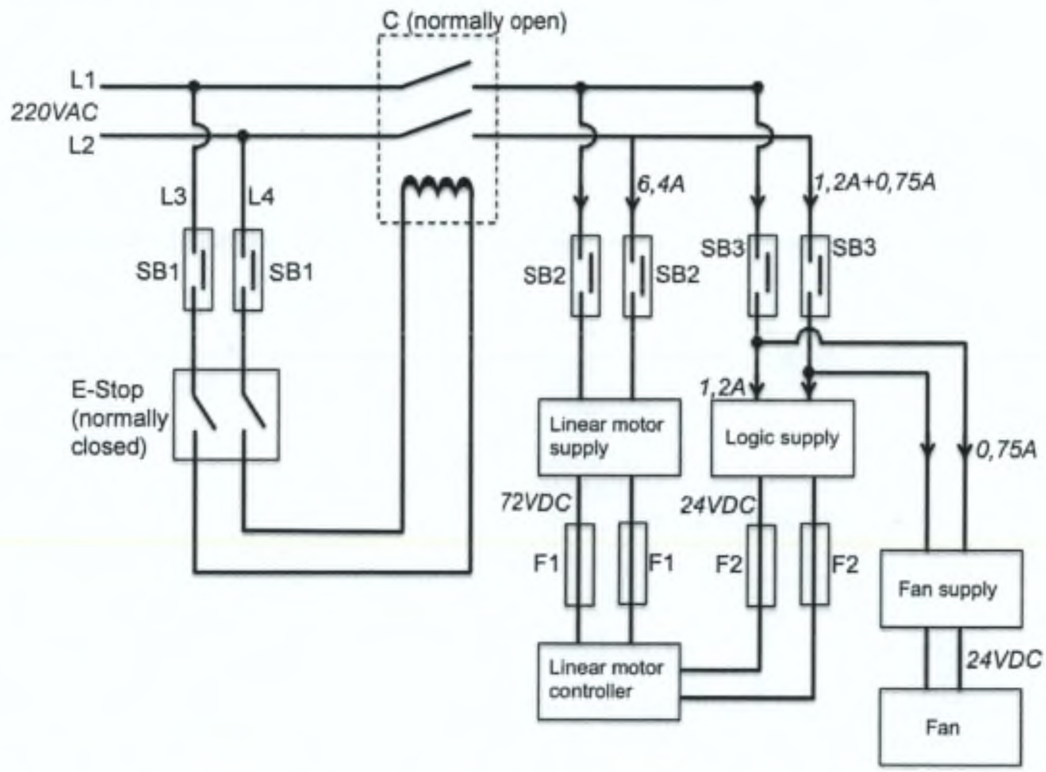

Figure A.33: Connections between the controller, the 72 VDC motor supply, the 24 VDC logic supply, the fan and its supply. "F", "SB", "L" and "C" stand for "fuse", "switching break", "line" and "contactor", respectively.

The fuses, the switching breaks, the E-Stop button, the contactor and the fan supply of the circuit have the following characteristics:

- F1 is a $10AT$ fuse[2] (as suggested by Fig. A.32) under $72VDC$ but it is able to bear $550VAC$ and $250VDC$. It protects the controller and the linear motor supply.

- F2 is a $2AT$ fuse (as suggested by Fig. A.32) under $24VDC$ but it is able to bear $550VAC$ and $250VDC$. It protects the controller and the logic supply.

- SB1 is a switching break whose limit current equals $2A$. It is under $220VAC$ but it is able to bear $440VAC$ and $60VDC$. It protects the E-stop button, which can bear up to $3A$, and the coil of the contactor C. As the contactor consumes $70VA$ and is under $220VAC$, the current in its coil equals $\frac{70VA}{220VAC} = 0.3A$. A switching break whose limit current is larger than $0.3A$ but close to 0.3 A has been looked for and the best match found is a switching break offering a limit current of $2A$.

- SB2 is a switching break whose limit current equals $10A$. It is under $220VAC$ but it is able to bear $440VAC$ and $60VDC$. It protects the linear motor supply, which consumes up to $6.4A$ (= "input current at full load ($230V$)", see Section A.2.3, in Fig. A.19). Hence, the best match found for the switching break is a limit current of $10A$.

- SB3 is a switching break whose limit current equals $2A$. It is under $220VAC$ but it is able to bear $440VAC$ and $60VDC$. It protects the logic supply and the fan supply. The logic supply consumes $1.2A$ (see Table A.1) while the fan supply consumes 0.75 A (see Table A.2). This makes 1.2 A + 0.75 A = 1.95 A. The best match found for this switching break is a limit current of $2A$.

- An E-Stop button is combined with a contactor C so that when the E-Stop button is pressed, the contactor opens the lines L1 and L2 and the circuit is no more provided with current.
  The contactor is composed of a coil and two breaks, which are placed in the lines L1 and L2. The chosen contactor is normally open. This means that when the coil is not (is) put under voltage, the lines L1 and L2 are open (closed).
  The E-Stop button is normally closed. This means that when the E-Stop button is not (is) pressed, the lines L3 and L4 are closed (open).
  Hence, when the E-Stop button is pressed, lines L3 and L4 open, thus the coil of the contactor is no more under voltage, this involves the opening of lines L1 and L2 and the rest of the circuit is no more put under voltage.
  In the lines L1 and L2 a current of $8.35A$ runs ($6.4A$ for the linear motor supply + $1.2A$ for the logic supply + $0.75A$ for the fan supply). The E-Stop button can bear $3A$ and is thus not able to open the lines L1 and L2.
  This is why a contactor has been combined with the E-Stop. This contactor is under $220VAC$ (but is able to bear $440VAC$) and is able to open a line travelled by a current of $10A$. The E-Stop commands the opening of lines L1 and L2 but in practice, it is the contactor that opens the lines.

- The fan of the linear motor requires a supply providing $24VDC$ and $120mA$, as can be seen in Section A.2.3, in Fig. A.13. This supply is not provided with the linear motor and has been bought separately. Its characteristics are summarized in Table A.2.

- Limit switches are interesting devices to add to the test bench as they can help to increase the safety of operation of the linear motor. Indeed, as the motor has a much

[2] The notation x AT for a fuse means that the fuse is going to blow if the current exceeds xA. "T" stands for "temporized" and means that when the current achieves the limit, the fuse is not going to blow immediately, but after a certain period of time.

24VDC fan supply	
brand	RS
type	DR-45 series 282-473
output DC voltage	$24VDC \pm 1\%$
rated output current	2 A
output rated power	48 W
input voltage range	85 ~ 264 VAC or 120 ~ 370 VDC, 47 ~ 63 Hz
input typical AC current at 230VAC	0.75 A
can be installed on DIN rail	yes

Table A.2: Main properties of the 24VDC fan supply

larger stroke than the pneumatic cylinder, limit switches can be used to shut down the motor supply when the displacement of the motor slider risks exceeding the cylinder stroke. The limit switches used for the test bench are presented in Fig. A.34. When the metallic bar is pressed downwards (is at rest), it pushes (doesn't push) on the A button and the connection between COM and NO (normally open) (COM and NC (normally closed)) is established.

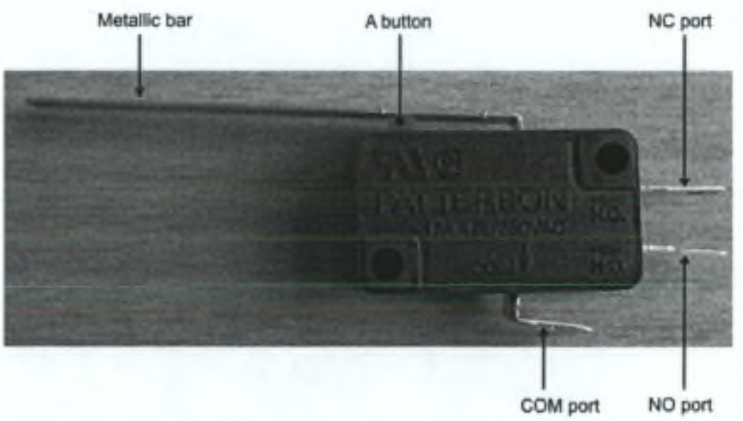

Figure A.34: Picture of the limit switches used in the test bench

The limit switches could be installed in series with the E-Stop button. Hence, if a limit switch is pressed, the circuit lines L1 and L2 open and the motor supply is shut down. Afterwards, as soon as the limit switch is no more pressed, lines L1 and L2 close and the motor supply switches on again. Since it was preferred that an external manual action was required to switch on the power again, another solution has been implemented. Indeed, as shown in Fig. A.35, the limit switches (LS1 and LS2) have been connected to a shunt itself bond (with a physical bond) to two switching breaks SB4 placed in the lines L1 and L2. When a limit switch is pressed, the shunt is put under voltage, it opens the switching breaks and this shuts the power off. A manual action is then necessary to close the SB4 switching breaks in order to put the power on again.

- Earth connectors to be fixed to DIN rails (see Fig. A.36) are placed at different locations in the circuit to allow the connection of the different components to the earth.

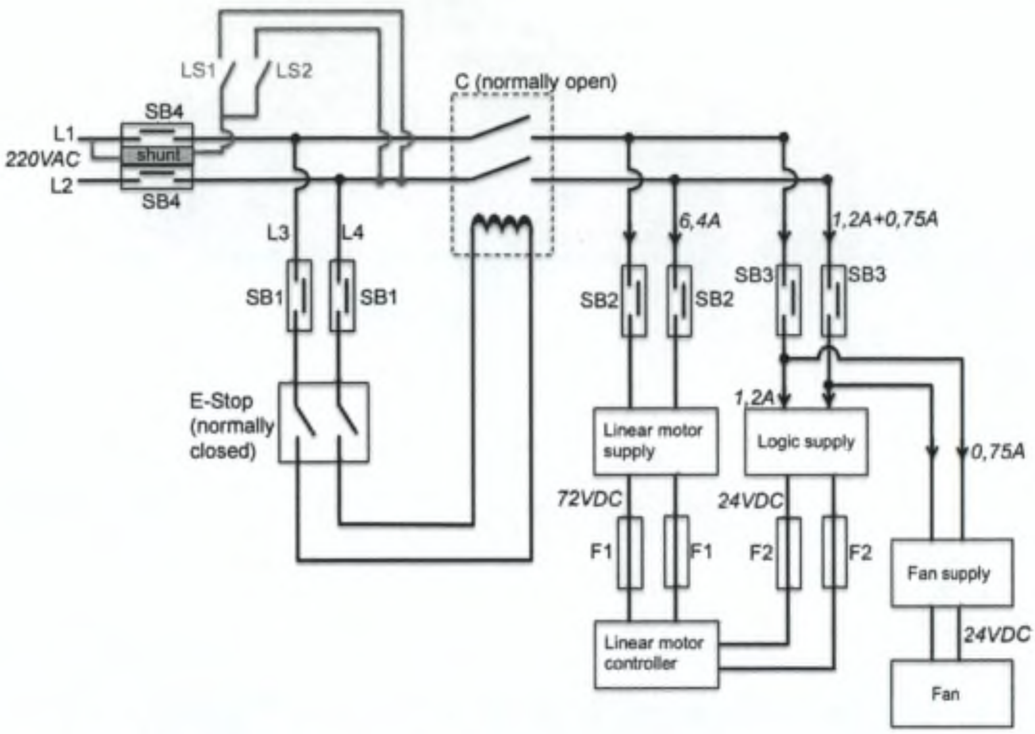

Figure A.35: Connections between the controller, the 72 VDC motor supply, the 24 VDC logic supply, the fan and its supply, the shunt and the limit switches. "F", "SB", "L", "C" and "LS" stand for "fuse", "switching break", "line", "contactor" and "limit switch", respectively.

Figure A.36: Earth connector

The main characteristics of the fuses, the fuse holders, the switching breaks, the limit switches, the E-Stop button, the earth connectors, the shunt and the contactor are summarized in Tables A.3 and A.4.

fuses F1	brand: GE Power Controls part number: NIT10 current rating: $10A$ max. voltage rating ac: $550V$ max voltage rating dc: $250V$ fuse technology: T; HBC fuse type: A1
fuses F2	brand: GE Power Controls part number: NIT2 current rating: $2A$ max. voltage rating ac: $550V$ max voltage rating dc: $250V$ fuse technology: T; HBC fuse type: A1
fuse holders	brand: Cooper Bussmann part number: CM32FC current rating: $32A$ fuse type: A1 installation on DIN rails: yes
switching breaks SB1 and SB3	brand: ABB part number: S201D2 current rating: $2A$ rated voltage: $440VAC/60VDC$ tripping characteristics: type D number of poles: 1 short circuit capacity: $6kA$ installation on DIN rails: yes
switching breaks SB2	brand: ABB part number: S201D10 current rating: $10A$ rated voltage: $440VAC/60VDC$ tripping characteristics: type D number of poles: 1 short circuit capacity: $6kA$ installation on DIN rails: yes
switching breaks SB4	brand: ABB part number: S203D10 current rating: $10A$ rated voltage: $440VAC$ tripping characteristics: type D number of poles: 3 short circuit capacity: $6kA$ installation on DIN rails: yes

Table A.3: Main characteristics of the fuses, the fuse holders and the switching breaks

limit switches LS1 and LS2	brand: Patterson maximum current: $12A$ rated voltage: 125 $250VAC$
E-stop button	brand: Telemecanique part number: XAL-K174F turn to release AC current under 240V: $3A$ contact configuration: 2N/C
earth connectors	brand: RS part number: 1212.2 installation on DIN rails: yes
shunt	brand: ABB part number: S2C-A2 operating current at $230VAC$: $1A$ installation on DIN rails: yes
contactor	brand: RS part number: 135-020 contact configuration: 2 NO and 2 NC coil voltage: 50/60 Hz - $230V$ installation on DIN rails: yes

Table A.4: Main characteristics of the limit switches, the E-Stop button, the earth connectors, the shunt and the contactor

A.6 Sensors

Before the measurements of the pressure sensors are acquired by the NI PXI platform, they pass through anti-aliasing filters whose electronic circuit is presented in Fig. A.37. The characteristics of this circuit components are given in Table A.5.

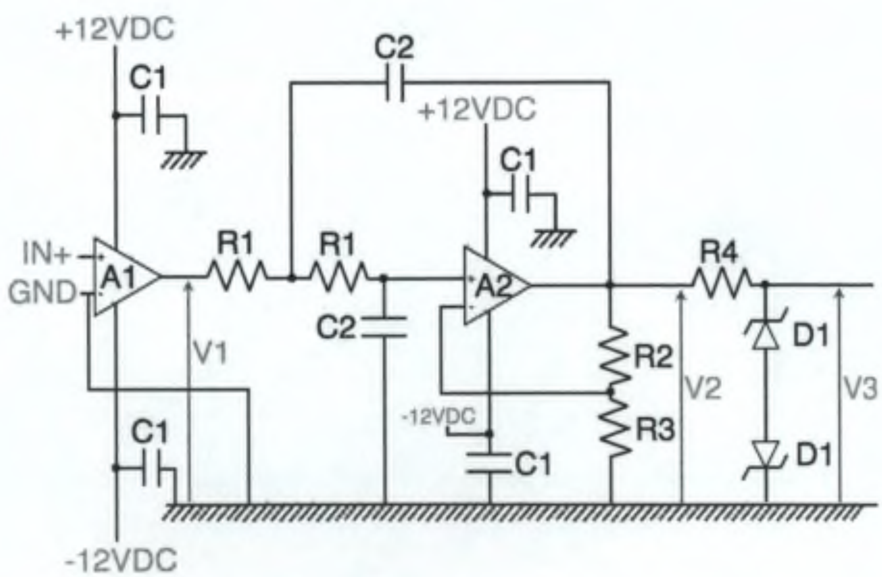

Figure A.37: Electronic circuit of the anti-aliasing filters

Component	Characteristics
A1	instrumentation amplifier AD620AN
A2	operational amplifier TLE 2061
C1	decoupling capacitor $C1 = 100\ nF$
C2	capacitor $C2 = 22\ nF$
R1	resistor $R1 = 7.15\ k\Omega$
R2	resistor $R2 = 1.21\ k\Omega$
R3	resistor $R3 = 2.05\ k\Omega$
R4	resistor $R4 = 1\ k\Omega$
D1	Zener diode maximum power $= 0.4\ W$ breakdown voltage $= 9.1V$

Table A.5: Components of the anti-aliasing circuits

The electronic cards of the anti-aliasing circuits have been manufactured as follows:

1. The electronic circuit is drawn as a block diagram with the EAGLE software.
2. According to the block diagram, the EAGLE software draws the tracks that will connect the electronic components.
3. The produced EAGLE file is provided to a numerically controlled machine.
4. A copper coated plate is placed in the numerically controlled machine.
5. The machine draws the electronic tracks by removing copper and it makes holes in the plate to allow the fixing of the electronic components.
6. The electronic components are welded on the card.

Fig. A.38 and A.39 present the EAGLE block diagrams of the anti-aliasing filter described above. Fig. A.40 and A.41 present the corresponding electronic tracks drawn by the EAGLE software.

Three anti-aliasing filters have been manufactured. Two of them correspond to Fig. A.38 and A.40 and are the filters of the pressure sensors, while the third filter corresponds to Fig. A.39 and A.41. This third filter had been dedicated to a force sensor which was finally not used. However, this filter contains a TML 10212 which is an electronic component that produces the supply voltages ($+12\ VDC$ and $-12\ VDC$) used for the instrumentation and the operational amplifiers of the three filters. This explains why this anti-aliasing filter has been kept although the force sensor is not used anymore.

The circuit controlling the solenoid valve (see Chapter 4) and the anti-aliasing filters have been placed into plastic boxes to protect them from the dust and to prevent that someone touches the electronic cards with its fingers (see Fig. A.42).

The connections between the pressure sensors, the solenoid valve and the circuit controlling it (see Chapter 4), the NI PXI platform, the supplies and the anti-aliasing filters

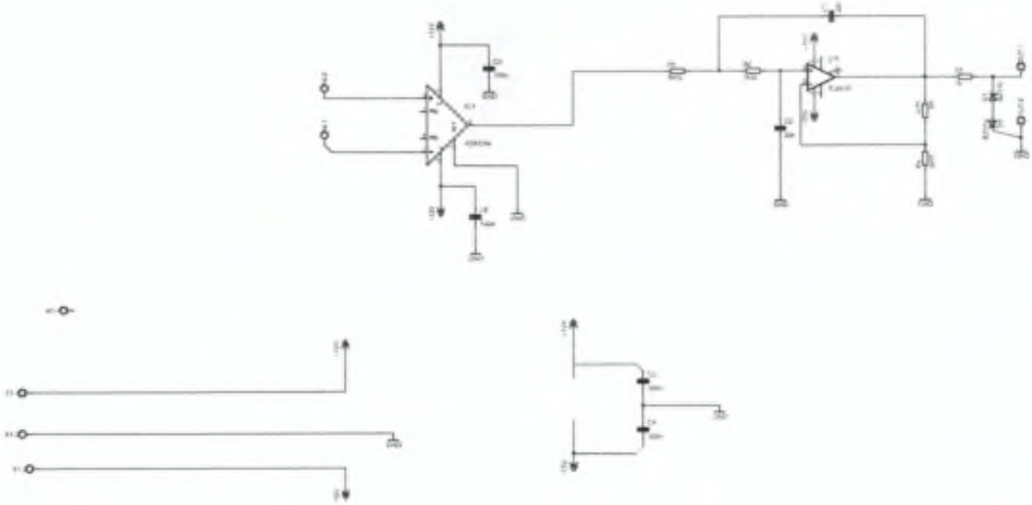

Figure A.38: Block diagram of the anti-aliasing filter, drawn with the EAGLE software

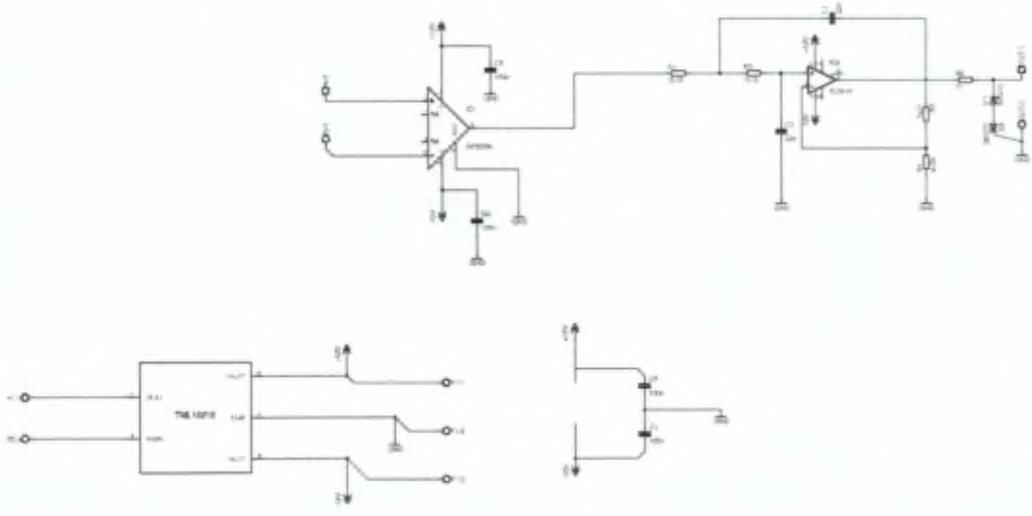

Figure A.39: Block diagram of the anti-aliasing filter, drawn with the EAGLE software. The component TML 10212 produces +12 VDC and −12 VDC voltages. These voltages are used as supply voltages for the instrumentation and the operational amplifiers.

have been organized around a central set of screw terminals (see Fig. A.43). Each element is connected to it using shielded cable and the connections between the elements are made by connecting electric wires between the different screw terminals. The shielded cables are connected to the plastic boxes thanks to female and male DB connectors.

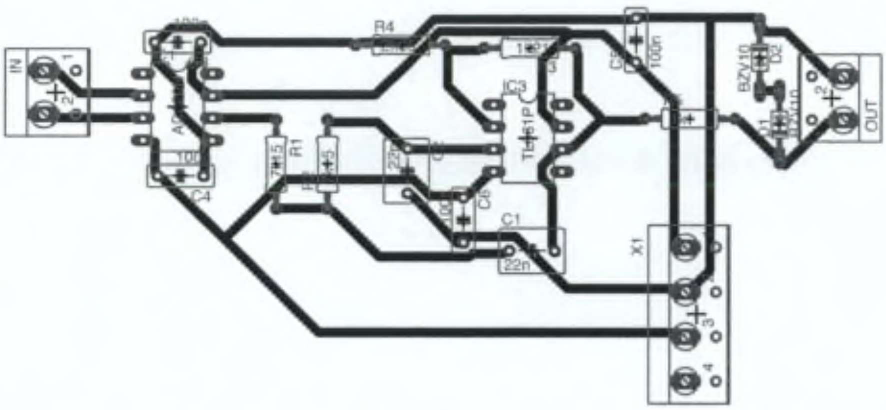

Figure A.40: Electronic tracks of the anti-aliasing filter, generated by the EAGLE software

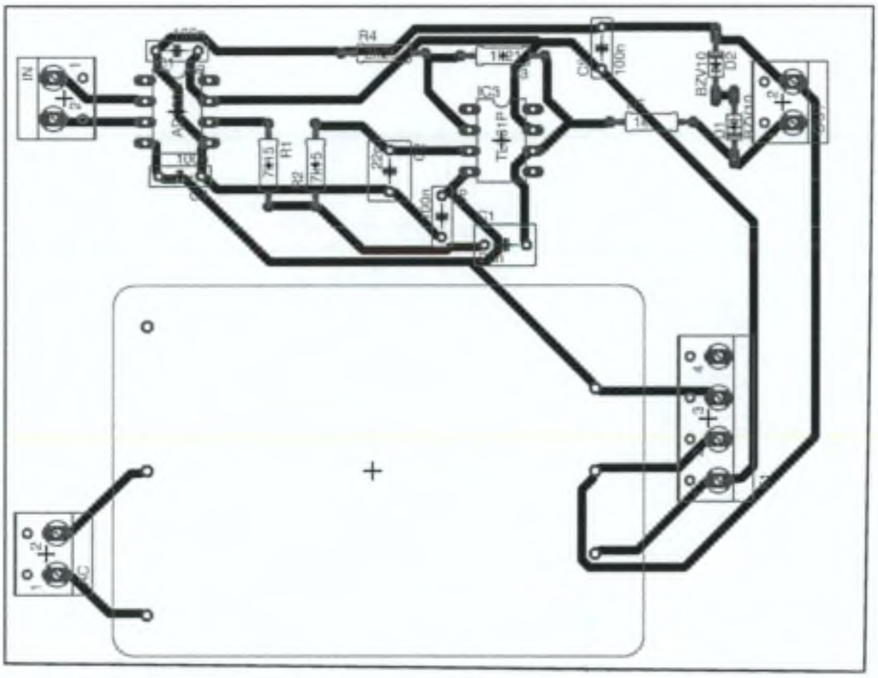

Figure A.41: Electronic tracks of the anti-aliasing filter, generated by the EAGLE software. The large rectangle component is a TML 10212 that produces +12 VDC and −12 VDC voltages. These voltages are used as supply voltages for the instrumentation and the operational amplifiers.

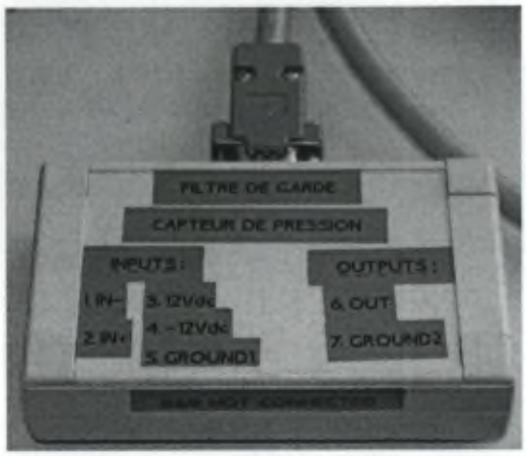

Figure A.42: Picture of one of the plastic boxes in which the electronic cards are placed.

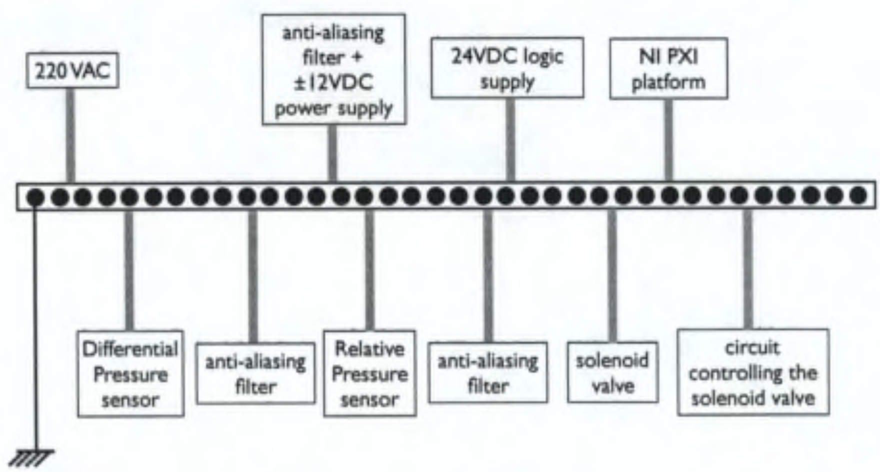

Figure A.43: Connections between the pressure sensors, the solenoid valve and the circuit controlling it, the NI PXI platform, the supplies and the anti-aliasing filters: they are organized around a central set of screw terminals. Each element is connected to it using shielded cable (= grey lines in the figure) and the connections between the elements are made by connecting electric wires between the different screw terminals. The boxe noted "anti-aliasing filter + ±12 VDC power supply" is the third anti-aliasing filter that contains an electronic component producing $+12$ VDC and -12 VDC voltages.

Appendix B

Pneumatic balloon actuators

B.1 Home-made manufacturing methods of the "Pneumatic Balloon Actuator"

As explained before (see Section 4.2.2), a Pneumatic Balloon Actuator (PBA) can be obtained simply by gluing to one another two plastic squares of different rigidities along their surrounding edge in order to form a cavity. Hence, as manufacturing these actuators seemed very easy, different methods have been tested to manufacture home-made PBAs. However, as each of the three tested methods (gluing, latex moulding and welding) presented disadvantages, it was eventually decided to look for a company to manufacture the PBAs.

B.1.1 Gluing

Principle

Two plastic squares showing different rigidities (a very flexible one and a stiffer one) are glued to one another along their surrounding edge with a glue dedicated to rubbers and plastics (a LOCTITE 406 glue). A syringe equipped with a needle is then used to pierce one of the films and to inject air in the cavity.

Results

The results were not concluding as there were leakages difficult to totally suppress by adding glue.

B.1.2 Moulding

Principle

Another idea is to mould a PBA in Latex. A mould has then been fabricated in balsa wood. The mould is made of six parts as can be seen in Fig. B.1.
Parts 1 to 5 are made of balsa while part 6 is made of polystyrene. Parts 2, 3 and 5 are glued on part 1. Before fixing part 4, a dry lubricant with PTFE is sprayed on the walls of the future cavity, on parts 1 and 4. Part 4 is then fixed to part 1 thanks to screws and nuts, as shown in Fig. B.2. Part 6 is hung in the cavity by screws and nuts (see Fig. B.3). Washers are strung on these screws and are used to position part 6 so that the distances between parts 1 and 6 and between parts 4 and 6 are different. The mould is then filled with latex and the latex dries then with the contact of air. After 36 hours, the PBA is dry and it is removed

from the mould. Latex sticks quite well to the wood but absolutely not to the polystyrene part.

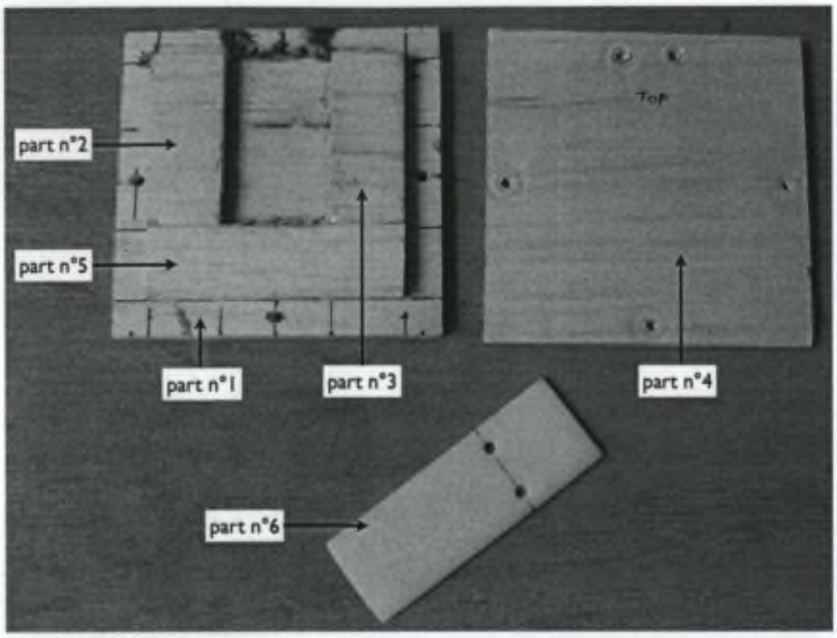

Figure B.1: Balsa mould developed to mould a PBA in Latex. Parts 2, 3 and 5 are glued on part 1.

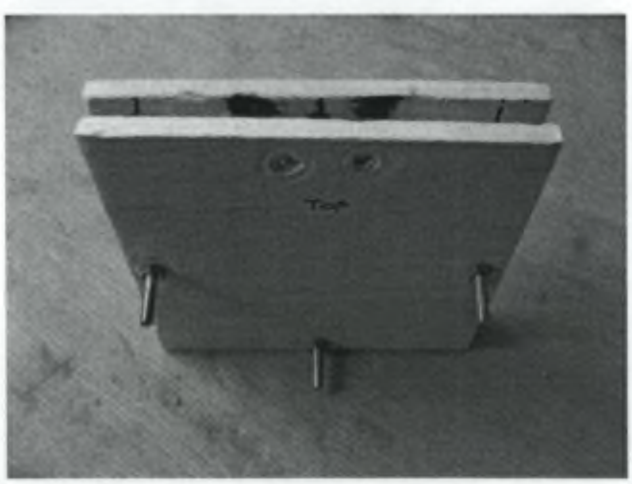

Figure B.2: Balsa mould developed to mould a PBA in Latex. The mould is here assembled without part 6.

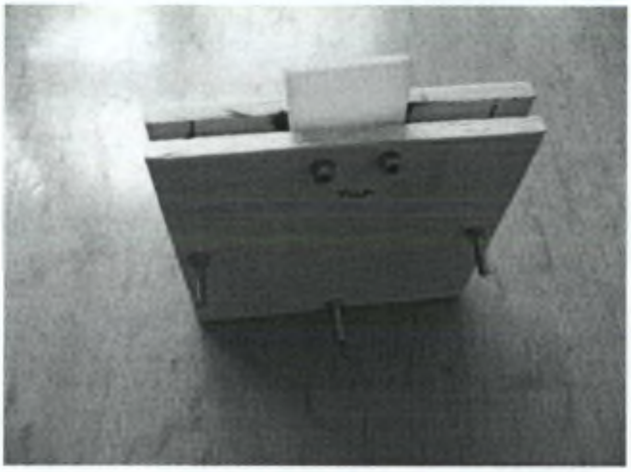

Figure B.3: Balsa mould developed to mould a PBA in Latex. The mould is here completely assembled.

Results

The achieved PBA is satisfying since it is airtight. To test it, it is clamped as a cantilever so that the size of the cavity is 30 mm × 30 mm and so that the upper cavity layer is the thinner one. Air is then injected in the cavity with a syringe equipped with a needle. As can be seen in Fig. B.4, when the PBA is pressurized, its free extremity deflects upwards but from a given pressure level, it begins to displace downwards. This bidirectional behaviour has also been noticed in [51] also for PBAs completely made of the same material.

In conclusion, the proposed moulding method allows to manufacture airtight latex PBAs. However, another manufacturing method has been looked for because the manufactured PBA does not present a channel for the air supply. Indeed, the air supply is done by piercing the latex with a needle and by injecting air with a syringe. However, to insert the latex PBA in a test bench, it would be easier to have a channel to which the air supply could be properly connected. Obtaining such a channel is difficult with this moulding method. Indeed, part 6 is used to form the cavity in the PBA and it is removed before using the PBA. However, if a narrow channel is foreseen, removing part 6 after the drying of the PBA will not be possible anymore.
The welding of plastic films, whose thicknesses are guaranteed by the supplier, is then considered in section B.1.3. Indeed, this solution can solve the drawback of the moulding method if a channel is foreseen, to which a tube can be connected for the air supply.

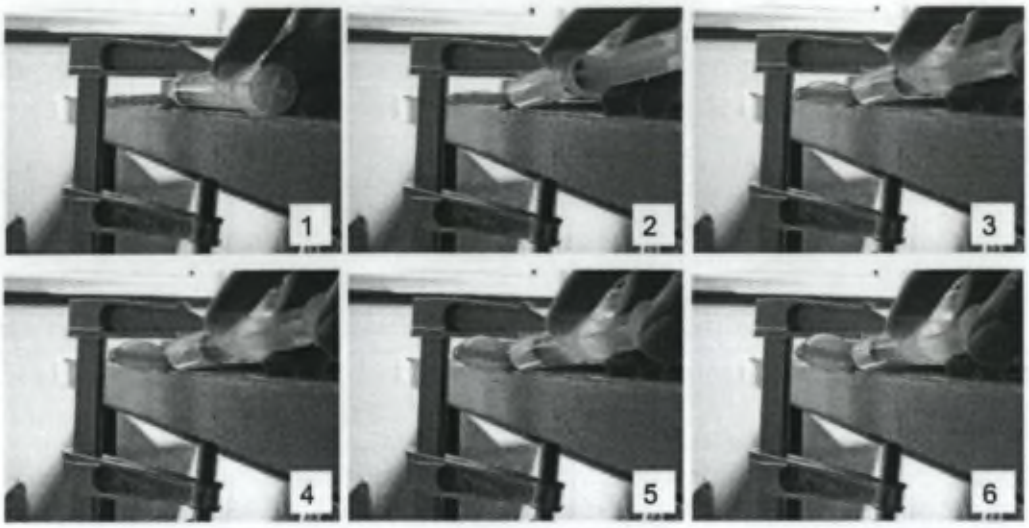

Figure B.4: Behaviour of the pressurized latex PBA. The PBA is fixed as a cantilever and air is injected in its cavity with a syringe equipped with a needle. When the PBA is pressurized, its free extremity deflects upwards but from a given pressure level, it begins to displace downwards (the downwards motion is not visible on the pictures).

B.1.3 Welding

Principle

The idea is to weld to each other two plastic films of different rigidities. To do so, films of thermoplastic elastomers (TPEs) are used. Indeed, elastomers are very elastic and will allow the inflation of the PBA while thermoplastics have the particularity to melt when they are heated [41]. Among the TPEs, it has been chosen to use thermoplastic polyurethane (TPU) since TPU exists under the form of films or sheets. Samples of TPU films of different thicknesses (50 μm, 100 μm and 200 μm) have been provided by the PLAST NEDERLAND B.V. company.
The goal is thus to weld two plastic films of different thicknesses (and thus rigidities) to each other and to obtain weldings whose shape is presented in Fig. B.5.

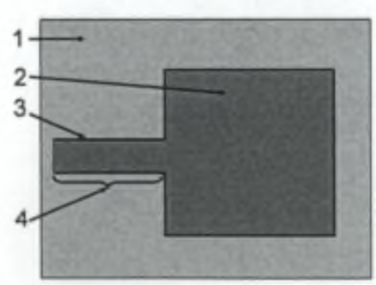

Figure B.5: PBA obtained by welding two TPU films to one another 1) TPU films 2) PBA 3) Weldings 4) Channel for the air supply

To do that, the films are pressed against an electronic card whose copper tracks are travelled by a current. The heating of the tracks involves then the melting and the welding of the films.
This card has been manufactured by lithography and Fig. B.6 presents the shape of its copper tracks. Electrodes are connected to points Z and Z' and all the copper tracks have the same thickness. Once the weldings are made, the TPU films are cut along the welded edges and a PBA is obtained.

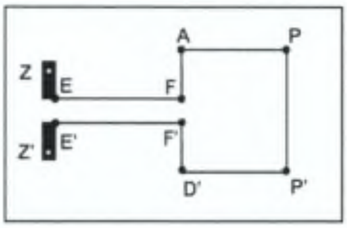

Figure B.6: Drawing of the electronic card used to manufacture PBAs by welding TPU films to each other. All the copper tracks have the same thickness.

Results

In practice, achieving a uniform welding is not easy and several trials are necessary before obtaining an airtight PBA.
Remark: A soldering iron has also been tested to weld two plastic films to one another but it is delicate to obtain a uniform welding of good quality with this method. Indeed, holes are made in the films if the soldering iron is pressed for too long on them.

B.2 PBA developed by the PRONAL company

Fig. B.7 shows the PBAs developed by the PRONAL company.

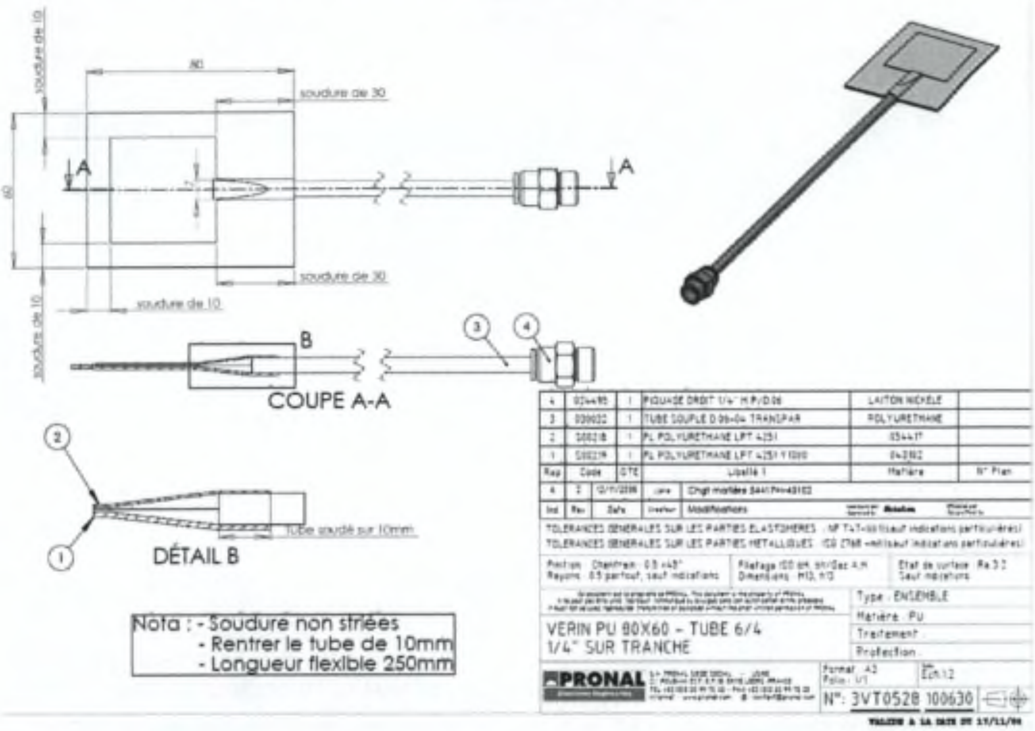

Figure B.7: Drawing of the PBA proposed by the PRONAL company. The dimensions of the cavity are 40 mm × 40 mm.

B.3 Particularities of the test bench

The relative and differential pressure sensors used to measure the pressure inside the PBAs are integrated into the fluidic circuit presented in Fig. B.8. This circuit is composed of the pneumatic cylinder chamber, the flexible fluidic actuator to be studied, the pressure sensors, a solenoid valve and the fittings and tubes connecting all these components. Table B.1 gives a description of the components of this fluidic circuit.

The solenoid valve is a 2/2-way valve presenting two pressure ports; when it is open/closed, the ports are/are not connected. The solenoid valve is normally closed. This means that when it is not powered, it is closed. On the other hand, as soon as power is supplied, it commutes and opens itself. To control the closing/opening of the valve with the NI PXI platform (see Section 3.5.2), the electronic circuit presented in Fig. B.9 has been built. *NI GND* and *NI command* are signals generated by the NI PXI platform:

- *NI GND* = 0 V.
- *NI command* = 0 V or 2 V. When *NI command* = 2 V (*NI command* = 0 V), the potential of point A is set to 0 V (24 V) and the solenoid valve sees a potential difference

of 24 V (0 V) between its terminals A and B, it is thus supplied (not supplied) and it opens itself or stays open (it closes itself or stays closed).

Remark: The electronic card of the circuit controlling the solenoid valve has been hand-made: the components have been welded on a board already presenting a network of parallel and perpendicular copper tracks.

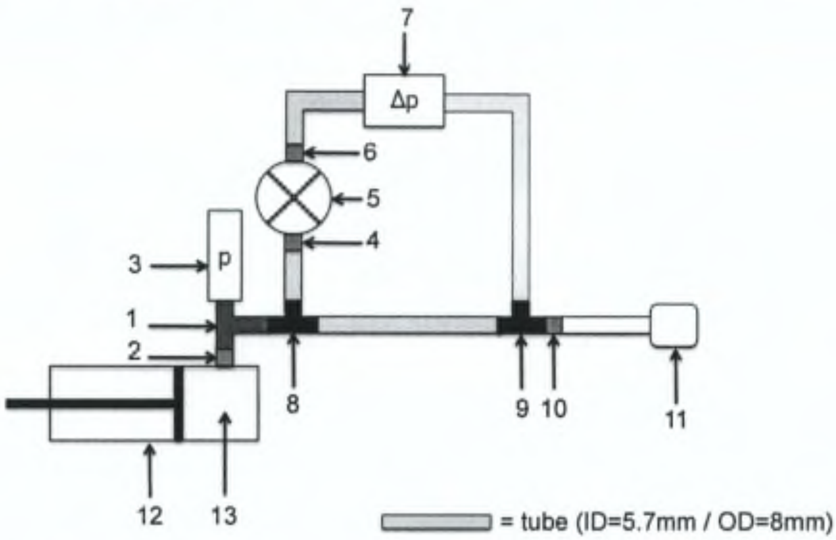

Figure B.8: Fluidic circuit implemented to study the PBAs: 1) threaded T-fitting 2) double nipple 3) relative pressure sensor 4) push-in fitting 5) solenoid valve 6) push-in fitting 7) differential pressure sensor 8) multiple distributor (one threaded fitting and two push-in fittings) 9) multiple distributor (one threaded fitting and two push-in fittings) 10) sleeve 11) PBA 12) pneumatic cylinder 13) pneumatic cylinder chamber. The light grey areas represent the tubes used to link the circuit components: ID=inner diameter and OD=outer diameter. All the fittings are equipped with seals.

Components of the fluidic circuit implemented to study the PBAs	
Component	Description
1) threaded T-fitting	brand: Festo type: NPFB - T - 3G14 - F pressure ports: G1/4 female + G1/4 female + G1/4 female
2) double nipple	brand: Festo type: NPFB - D - G18 - G14 - M pressure ports: G1/4 male + G1/8 male
3) $0-1$ *bar* relative pressure sensor	see Table 3.7 pressure port: G1/4 male
4) and 6) push-in fittings	brand: Festo type: QS - G1/8 - 8 pressure ports: G1/8 male + push-in fitting for tubes with OD = 8 mm
5) solenoid valve	brand: Burkert type: 2/2-way valve, normally closed / number: 126091 pressure ports: G1/8 female + G1/8 female
7) $0-10$ *mbar* differential pressure sensor	see Table 3.8 pressure ports: Φ 6.6 X 11, for flexible tubes with ID = 6 mm
8) and 9) multiple distributors	brand: Festo type: QSLV2 - G1/4 - 8 pressure ports: G1/4 male + 2 push-in fittings for tubes with OD = 8 mm
10) sleeve	brand: Festo type: NPFB - S - 2G14 - F pressure ports: G1/4 female + G1/4 female
11) PBA	pressure port: G1/4 male
12) pneumatic cylinder	pressure port: G1/8 female
tubes	brand: Festo type: PUN - 8 - SI - 25 - CB ID = 5.7 mm and OD = 8 mm
seals	already provided with the fittings or ordered separately and added to the fittings types of the ordered Festo seals: OL - 1/8 and OL - 1/4

Table B.1: Description of the components of the fluidic circuit implemented to study the PBAs. The numbers make reference to Fig. B.8.

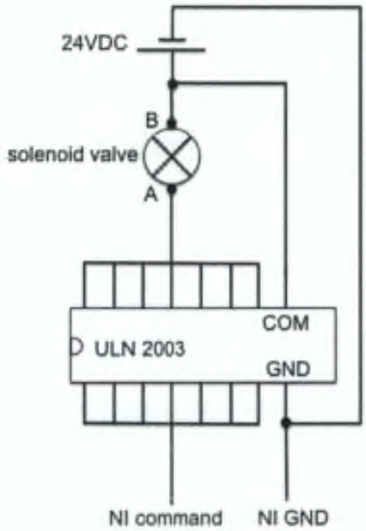

Figure B.9: Electronic circuit allowing to control the closing/opening of the solenoid valve with the NI PXI platform. This platform generates the *NI GND* and *NI command* signals. $NI\ GND = 0$ V and $NI\ command = 0$ V or 2 V. When $NI\ command = 2$ V ($NI\ command = 0$ V), the potential of point A is set to 0 V (24 V) and the solenoid valve sees a potential difference of 24 V (0 V) between its terminals A and B, it is thus supplied (not supplied) and it opens itself or stays open (it closes itself or stays closed).

Appendix C

List of Publications

Journal papers

- Aline De Greef, Pierre Lambert and Alain Delchambre. Towards Flexible Medical Instruments: Review of Flexible Fluidic Actuators. *Precision Engineering*, 33: 311-321, October 2009.
- Marie Blondeau, Aline De Greef, Pierre-Alexis Douxchamps, Benjamin Genêt, Marc Haelterman, Cyrille Lenders, Erwan Leroy, Pascal Nardone, Vincent Raman, Aliénor Richard and Frédéric Robert. Apprentissage par projet : Réalisation d'une éolienne urbaine en matériaux de récupération. *J3EA*, 8, 2009.

Proceedings of conferences

- Thomas Delwiche, Laurent Catoire, Michel Kinnaert and Aline De Greef. Experimental study of position-position and force-position control methods in teleoperation. In *Proceedings of the "25th Benelux Meeting on Systems and Control"*, pp108, 13-15 March 2006, Heeze, The Netherlands, ISBN-10 90-386-2558-8 ISBN-13.
- Aline De Greef, Thomas Delwiche, Laurent Catoire and Michel Kinnaert. Experimental study of position-position and force-position control methods in teleoperation. In *Proceedings of Mechatronics 2006 - 4th IFAC - Symposium on Mechatronics Systems*, pp 301-306, 12-14 September 2006, Heidelberg, Germany.
- Aline De Greef, Pierre Lambert and Alain Delchambre. A Minimally Invasive Surgery Actuator Based on a Flexible and Inflatable Structure. In *Proceedings of the First Annual symposium of the IEEE/EMBS Benelux Chapter*, 7-8 December 2006, Brussels, Belgium.
- Thierry Leloup, Aline De Greef, Sylvie Bantuelle, Wissam El Kazzi, Guy Mannaert, Nadine Warzée, Frédéric Schuind and Alain Delchambre. Design of an Articulated Mini-Fixation Device for Proximal Interphalangeal Joint Finger Fractures. In *Proceedings of the Annual Symposium of the IEEE/EMBS Benelux Chapter*, 6-7 December 2007, Heeze, The Netherlands.
- Marie Blondeau, Aline De Greef, Pierre-Alexis Douxchamps, Benjamin Genêt, Marc Haelterman, Cyrille Lenders, Erwan Leroy, Pasquale Nardone, Vincent Raman, Aliénor Richard and Frédéric Robert. Apprentissage par projet : Réalisation d'une éolienne urbaine en matériaux de récupération. *Proceedings of the "7ème Colloque sur*

l'Enseignement des Technologies et des Sciences de l'Information et des Systèmes - CETSIS 08", 27-29 October 2008, Brussels, Belgium.

- Patricia Van Dale, Aline De Greef, Cyrille Lenders and Nadine Warzée. Biomedical engineer and phlebologist: a midship frame. In *International Angiology - Proceedings of the XVI World Congress of the Union Internationale de Phlebologie (31 August - 4 September 2009)*, 28: 138, 2009.

- Aline De Greef, Pierre Lambert, Thomas Delwiche, Cyrille Lenders, Bruno Tartini and Alain Delchambre. Flexible Fluidic Actuators: Determining Force and Position Without Force or Position Sensors. In *Proceedings of the IEEE ISAM2009 conference*, 17-20 November 2009, Suwon, Korea

Miscellaneous

- Aline De Greef. *Etude d'un actionneur à structure flexible et gonflable*, DEA, Université Libre de Bruxelles, 2006.

- Aline De Greef, Pierre Lambert and Alain Delchambre. Les actionneurs fluidiques flexibles : caractérisation et application à la mesure de force sans capteurs. poster presentation at *7èmes Journées Nationales de la Recherche en Robotique JNRR'09*, 4-6 November 2009, Sologne, France.

Bibliography

[1] Industrial linear motors (edition 14) - linmot catalog.

[2] Profile system - minitec catalog.

[3] Tutorial linmot designer 1.5, 2006.

[4] European course on laparoscopic surgery - solid organs - new technology, university hospital saint-pierre, brussels, belgium, 2007.

[5] Precision linear actuators - danaher motion catalog, 2007.

[6] The lee company - website - http://www.theleeco.com/leeweb2.nsf, 2008.

[7] Modular spindle drives - maxon motor catalog, 2008.

[8] Servo controller installation guide (version 1.2/ro/june 2008) - linmot guide, 2008.

[9] Airpot corporation - website - http://www.airpot.com/, 2010.

[10] Danaher motion - website - http://www.danahermotion.com/, 2010.

[11] Design-expert 8 - website - http://www.statease.com/dx8descr.html, 2010.

[12] dspace - website - http://www.dspace.com/ww/en/pub/start.cfm, 2010.

[13] Kern & sohn gmbh - website - http://www.kern-sohn.com/, 2010.

[14] Linmot - website - http://www.linmot.com/, 2010.

[15] Lm guide actuator (model kr) - thk catalog, 2010.

[16] Maxon motor - website - http://www.maxonmotor.com/, 2010.

[17] Minitec - website - http://www.minitec.co.uk/, 2010.

[18] National instruments - website - http://www.ni.com/, 2010.

[19] Newport corporation - website - http://www.newport.com/, 2010.

[20] Pronal elastomer engineering - website - http://www.pronal.com/, 2010.

[21] Thk - website - http://www.thk.com/, 2010.

[22] Arthur W. Adamson and Alice P. Gast. *Physical Chemistry of Surfaces.* John Wiley and Sons, 6^{th} edition, 1997.

[23] C. Anthierens. *Conception d'un micro robot à actionneur asservi électropneumatique pour l'inspection intratubulaire.* PhD thesis, Institut National des Sciences Appliquées de Lyon, 1999.

[24] T. Belèndez, M. Pèrez-Polo, C. Neipp, and A. Belèndez. Numerical and experimental analysis of large deflections of cantilever beams under a combined load. *Phys. Scr.*, T118:61–65, 2005.

[25] A. M. Bertetto and M. Ruggiu. A novel fluidic bellows manipulator. *J. Robotics Mechatronics*, 16(6):604–612, 2004.

[26] P. Beyl, B. Vanderborght, R. Van Ham, M. Van Damme, R. Versluys, and D. Lefeber. Compliant actuation in new robotic applications. In *Proceedings of the NCTAM06 - 7th National Congress on Theoretical and Applied Mechanics, DVD*, 29-30 May 2006.

[27] N.-Q. Cao. Master's thesis - "miniaturisation de muscles artificiels". Master's thesis, Université libre de Bruxelles, 2009.

[28] M. C. Cavusoglu, I. Villanueva, and F. Tendick. Workspace analysis of robotic manipulators for a teleoperated suturing task. In *Proceedings of the IEEE/RSJ International Conference on Intelligent Robots and Systems (IROS 2001), Maui, HI*, volume 4, pages 2234–2239, October 29-November 3 2001.

[29] F. Daerden. *Conception and realization of Pleated Pneumatic Artificial Muscles and their use as Compliant Actuation Elements.* PhD thesis, Vrije Universiteit Brussel, 1999.

[30] F. Daerden and D. Lefeber. The concept and design of pleated pneumatic artificial muscles. *International Journal of Fluid Power*, 2(3):41–50, 2001.

[31] F. Daerden and D. Lefeber. Pneumatic artificial muscles: actuators for robotics and automation. *Eur. J. Mech. Env. Eng.*, 47(1):10–21, 2002.

[32] F. Daerden, D. Lefeber, B. Verrelst, and R. Van Ham. Pleated pneumatic artificial muscles: Compliant robotic actuators. In *Proceedings of the IEEE/RSJ International Conference on Intelligent Robots and Systems (IROS 2001), Maui, Hawaii, October-November 2001*, pages 1958–1963, 2001.

[33] R. J. Damiano, H. A. Tabaie, M. J. Mack, J. R. Edgerton, C. Mullangi, W. P. Graper, and S. M. Prasad. Initial prospective multicenter clinical trial of robotically-assisted coronary artery bypass grafting. *The Annals of Thoracic Surgery*, 72:1263–9, 2001.

[34] M. De Volder, J. Peirs, D. Reynaerts, J. Coosemans, R. Puers, O. Smal, and B. Raucent. Production and characterization of a hydraulic microactuator. *J. Micromech. Microeng.*, 15(7):15–21, 2005.

[35] S. Dohta, Y. Ban, and H. Matsushita. Application of a flexible strain sensor to a pneumatic rubber hand. In *Proceedings of the FLUCOME 2000 : the 6th Triennal International Symposium on Fluid Control, Measurement and Visualization, Sherbrooke, Canada, CD-ROM*, August 2000.

[36] E. Dombre, M. Michelin, P. Poignet, P. Bidaud, G. Morel, D. Sallé, P. Médéric, P. Gravez, M. Karouia, and N. Bonnet. Projet marge: Modélisation, apprentissage et reproduction du geste endochirurgical. In *Actes des Journées ROBEA: Journées Bilan du Programme Interdisciplinaire ROBEA'02, Toulouse, France*, pages 47–51, 24-25 October 2002.

[37] K. Donovan, C. Penninger, A. Plinta, and A. Rashid. Microfingers for micromanipulation, 2004.

[38] Festo. Fluidic muscle dmsp, with press-fitted connections / fluidic muscle mas, with screwed connections (festo catalog), 2005.

[39] F. Frey. *Traité de Génie Civil de l'école polytechnique de Lausanne : Analyse des structures et milieux continus (volume 2)*. 2000.

[40] Aline De Greef, Pierre Lambert, and Alain Delchambre. Towards flexible medical instruments: Review of flexible fluidic actuators. *Precis. Eng.*, 33:311–321, October 2009.

[41] C. A. Harper. *Handbook of Plastics, Elastomers and Composites*. 1992.

[42] Y. Hayama. Flexible actuator, patent: Publication number jp2004181569, 2004.

[43] S. Hirai, T. Masui, and S. Kawamura. Prototyping pneumatic group actuators composed of multiple single-motion elastic tubes. In *Proceedings of the IEEE International Conference on Robotics and Automation, Seoul, Korea*, volume 4, pages 3807–3812, May 2001.

[44] L. L. Howell. *Compliant Mechanisms*. Interscience, July 2001.

[45] J. E. Huber, N. A. Fleck, and M. F. Ashby. The selection of mechanical actuators based on performance indices. In *Proceedings: Mathematical, Physical and Engineering Sciences*, volume 453, pages 2185–2205, 1997.

[46] K. Ikuta, H. Ichikawa, K. Suzuki, and T. Yamamoto. Micro hydrodynamic actuated mutiple segments catheter for safety minimally invasive therapy. In *Proceedings of the 2003 IEEE International Conference on Robotics and Automation, Taipei, Taiwan*, pages 2640–2645, 14-19 September 2003.

[47] P. Joli and Z.-Q. Feng. Modélisation adaptée pour une simulation interactive d'un actionneur hydraulique. In *7ème colloque National en Calcul des Structures, Gies, France*, may 2005.

[48] H.-W. Kang, I. H. Lee, and D.-W. Cho. Development of a micro-bellows actuator using micro-stereolithography technology. *Microe. Eng.*, 83:1201–1204, 2006.

[49] G. K. Klute. *Artificial Muscles: Actuators for Biorobotic Systems*. PhD thesis, University of Washington, 1999.

[50] S. Konishi, F. Kawai, and P. Cusin. Thin flexible end-effector using pneumatic balloon actuator. *Sensors and Actuators A*, 89:28–35, 2001.

[51] S. Konishi, M. Nokata, O. C. Jeong, S. Kusuda, T. Sakakibara, M. Kuwayama, and H. Tsutsumi. Pneumatic micro hand and miniaturized parallel link robot for micro manipulation robot system. In *Proceedings of the 2006 IEEE International Conference on Robotics and Automation, Orlando, Florida*, pages 1036–1041, May 2006.

[52] S. Konishi, M. Nokata, O.C. Jeong, T. Sakakibara, S. Kusuda, M. Kuwayama, and H. Tsutsumi. Merging micro and macro robotics toward micro manipulation for biomedical operation. In *Proceedings of the 36th International Symposium on Robotics (ISR 2005)*, 2005.

[53] S. Konishi, S. Sawano, S. Kusuda, and T. Sakakibara. Fluid-resistive bending sensor compatible with a flexible pneumatic balloon actuator. *J. Robotics Mechatronics*, 20(3):436–440, 2008.

[54] M. Lazeroms, A. La Haye, W. Sjoerdsma, W. Scheurs, W. Jongkind, G. Honderd, and C. Grimbergen. A hydraulic forceps with force-feedback for use in minimally invasive surgery. *Mechatronics*, 6(4):437–446, 1996.

[55] Y. K. Lee and I. Shimoyama. A mutli-channel micro valve for micro pneumatic artificial muscle. In *Proceedings of the Fifteenth IEEE International Conference on Micro Electro Mechanical Systems, Las Vegas, USA*, pages 702–705, 2002.

[56] Y.-W. Lu and CJ Kim. Characterization of balloon-jointed micro-fingers. In *Proceedings of the 2003 ASME International Mechanical Engineering Congress and Exposition (IMECE), Washington DC, USA*, pages 311–316, 15-21 November 2003.

[57] W. McMahan, B. A. Jones, V. Chitrakaran, M. Csencsits, M. Grissom, M. Pritts, C. D. Rahn, and I. D. Walker. Field trials and testing of the octarm continuum manipulator. In *Proceedings of the International Conference on Robotics and Automation, Orlando, Florida*, pages 2336–2341, May 2006.

[58] A. Menciassi, M. Quirini, and P. Dario. Microrobotic technologies in endoluminal applications. In *presentation at the IARP - IEEE / RAS - EURON Joint Workshop on "Micro and Nano Robotics", Paris, France*, 23-24 October 2006.

[59] J. M. Morrison. Remotely controlled arm, patent: Publication number gb2100826, 1983.

[60] Y. Muyari, Y. Haga, T. Mineta, and M. Esashi. Development of hydraulic suction type active catheter using super elastic alloy tube. In *Proceedings of the 20th Sensor Symposium*, pages 57–60, 2003.

[61] T. Noritsugu, M. Kubota, and S. Yoshimatsu. Development of pneumatic rotary soft actuator made of silicone rubber. *J. Robotics Mechatronics*, 13(1):17–22, 2001.

[62] D. J. O'Brien and D. M. Lane. 3d force control system design for a hydraulic parallel bellows continuum actuator. In *Proceedings of the 2001 IEEE International Conference on Robotics and Automation, Seoul, Korea*, pages 2375–2380, 21-26 May 2001.

[63] J. Ok, M. Chu, and CJ Kim. Pneumatically driven microcage for micro-objects in biological liquid. In *Proc. of IEEE MEMS*, pages 459–563, 17-21 January 1999.

[64] J. Peirs, J. Clijnen, D. Reynaerts, H. Van Brussel, P. Herijgers, B. Corteville, and S. Boone. A micro optical force sensor for force feedback during minimally invasive robotic surgery. *Sensors and Actuators A*, 115:447–455, 2004.

[65] G. Picinbono and J.-C. Lombardo. Extrapolation: a solution for force feedback? In *Virtual Reality and Prototyping, Laval, France*, pages 117–125, June 1999.

[66] P. Poignet and G. Poisson. La conception de robots pour l'assistance aux gestes médicaux et chirurgicaux. In *5èmes journées nationales de la recherche en robotique, Guidel, Morbihan, France*, October 2005.

[67] C. Prelle. *Contribution au contrôle de la compliance d'un bras de robot à actionnement électropneumatique.* PhD thesis, Institut National des Sciences Appliquées de Lyon, 1997.

[68] A. Ruzzu, K. Bade, J. Fahrenberg, and D. Maas. Positioning system for catheter tips based on an active microvalve system. *J. Micromech. Microeng.*, 8:161–164, 1998.

[69] D. Salle. *Conception Optimale d'Instruments Robotisés à Haute Mobilité pour la Chirurgie Mini-Invasive.* PhD thesis, Université Paris 6, 2004.

[70] S. Schulz, C. Pylatiuk, and G. Bretthauer. A new ultralight anthropomorphic hand. In *Proceedings of the 2001 IEEE International Conference on Robotics and Automation (ICRA 2001), Seoul, Korea*, volume 3, pages 2437–2441, 2001.

[71] S. T. Smith and R. M. Seugling. Sensor and actuator considerations for precision, small machines. *Precis. Eng.*, 30:245–264, 2006.

[72] K. Suzumori. Elastic materials producing compliant robots. *Robotics and Autonomous Systems*, 18:135–140, 1996.

[73] K. Suzumori, S. Iikura, and H. Tanaka. Development of flexible microactuator and its applications to robotic mechanisms. In *Proceedings of the 1991 IEEE International Conference on Robotics and Automation, Sacramento, California, USA*, volume 2, pages 1622–1627, April 1991.

[74] K. Suzumori, S. Iikura, and H. Tanaka. Flexible microactuator for miniature robots. In *Proceedings of the 1991 IEEE Micro Electro Mechanical System, Nara, Japan*, pages 204–209, 30 January - 2 February 1991.

[75] K. Suzumori, S. Iikura, and H. Tanaka. Applying a flexible microactuator to robotic mechanisms. *IEEE Control Systems Magazine*, 12:21–27, 1992.

[76] K. Suzumori, A. Koga, and R. Haneda. Microfabrication of integrated fmas using stereo lithography. In *Proceedings of the 1994 IEEE Micro Electro Mechanical System, Oiso, Japan*, pages 136–141, January 1994.

[77] K. Suzumori, A. Koga, F. Kondo, and R. Haneda. Integrated flexible microactuator systems. *Robotica*, 14:493–498, 1996.

[78] K. Suzumori, T. Maeda, H. Wantabe, and T. Hisada. Fiberless flexible microactuator designed by finite-element method. *IEEE-ASME Trans. Mechatron.*, 2, issue 4, December 1997.

[79] K. Suzumori, T. Matsumaru, and S. Iikura. Elastically deformable fluid actuator, us patent 4,976,191, 11 December 1990.

[80] P. Taillard. Guide de dimensionnement - la production d'énergie pneumatique. *Technologie*, (110):21–25, novembre - décembre 2000.

[81] K. Takemura, S. Yokota, and K. Edamura. Development and control of a micro artificial muscle cell using electro-conjugate fluid. *Sensors and Actuators A*, Article in press, 2006.

[82] G. Thomann. *Contribution à la chirurgie minimalement invasive: conception d'un coloscope intelligent.* PhD thesis, National Institute of Applied Sciences in Lyon, 2003.

[83] L. Toledo, D. Gossot, S. Fritsch, Y. Revillon, and C. Reboulet. Etude des forces subies et de l'espace de travail des instruments de chirurgie endoscopique. *Annales de Chirurgie*, 53(7), 1999.

[84] B. Verrelst. *A dynamic walking biped actuated by pleated pneumatic artificial muscles: Basic concepts and control issues.* PhD thesis, Vrije Universiteit Brussel, 2005.

[85] Q. Yang, L. Zhang, G. Bao, S. Xu, and J. Ruan. Research on novel flexible pneumatic actuator fpa. In *Proceedings of the 2004 IEEE Conference on Robotics, Automation and Mechatronics, Singapore*, volume 1, pages 385–389, 1-3 December 2004.

[86] S. Diaz Zagal. *Conception et Développement d'un Mini-Actionneur à Muscle Artificiel. Application à la Robotique Médicale.* PhD thesis, Institut National des Sciences Appliquées de Toulouse, 2007.